Department of Civil Engineering
Nottingham Transportation Engineering Centre

Enhancing Pavements for Thermal Applications

By

Pejman Keikhaei Dehdezi

Thesis submitted to the University of Nottingham
for the degree of Doctor of Philosophy

March 2012

To my family

ABSTRACT

Renewable energy combined with energy efficiency can offer a viable and influential solution to minimise the harmful consequences of both fossil fuel depletion and increases in the cost of power generation. However, in most cases renewable energy technologies require high initial investments that may deter potential users. Pavement Energy Systems (PES) potentially offer a low-cost solution to sustainable and clean energy generation by utilising the thermo-physical properties and design features of new/existing pavement infrastructure. Within the PES, fluid-filled pipes are buried in the pavement at varying depths and transfer heat to and from the surrounding material, for application as a solar energy collector and/or thermal storage media. The fluid in the pipes can absorb/reject heat to the pavement and deliver useful energy to nearby buildings as well as benefiting the pavement structure and pavement users (in terms of reduced rutting, winter road maintenance, etc.). A significant advantage of such systems is that the pipes can be installed within pavements that are already needed for structural reasons and need not to be installed as single-function elements, as do conventional thermal utilisation systems.

In this project, the effect of pavement materials and layer design optimisations on the performance of PES was investigated both theoretically and experimentally. The thermo-physical properties and load-bearing performance of concrete and asphalt pavements, consisting of conventional and unconventional components, were determined. In addition, pseudo 3D transient explicit finite-difference software was developed for modelling and performance analysis of the PES under various operating conditions and configurations. This software is capable of predicting the outlet fluid temperature and temperature distributions within the pavement structure. Furthermore, large-scale physical models of the PES were designed and constructed to compare the performance of the thermally modified pavement structures with those of conventional ones and also to validate the model. The physical

model consisted of copper pipes embedded in pavements which were irradiated (causing surface heating) using halogen lamps.

The results of thermo-physical optimisation of pavement materials, coupled with mechanical testing, showed that it was possible to achieve a wide range of thermally-modified pavements that can also meet the rigorous functional requirements of an airfield pavement. The experimental comparison between the thermally modified and unmodified concrete pavements revealed that there was potential to enhance both the heat collection and storage capability of concrete pavement structures. In addition, the model's predicted temperatures in concrete pavements were in good agreement with the experimental ones with a mean error of less than 1°C. A similar comparison on asphalt pavements showed that although the surface temperature was lowered by asphalt modification, there were significant discrepancies between the measured and predicted surface temperatures for both modified and unmodified pavements. Further study was conducted on the pipe/pavement interface using X-Ray Computed Tomography (XRCT). The X-ray images revealed improper bonding between the pavement's matrix and the pipe that was evidenced by the presence of air voids accumulation around the pipe perimeter, and could explain the significant discrepancy in the modelled temperatures.

Furthermore, the validated model was used, for genuine temperature patterns, to simulate the relative influence of both the thermo-physical properties of pavement materials and the pavement layer sequences on the performance of the PES and to determine the implications for pavement design. It was concluded that the enhancements could allow pipes to be installed deeper within the pavement without having any negative effect on their thermal performances. Pipe installation deeper in the pavement is expected to reduce 'reflective cracking' under traffic loading as well as enabling future resurfacing of the pavement without damaging the pipe network.

PUBLICATIONS

The following is a list of the papers have been submitted to or published by the author during preparation of this thesis.

- **Keikhaei Dehdezi, P**., M. R. Hall., A. R. Dawson (2011). "Thermo-Physical optimisation of specialised concrete pavement materials for surface heat energy collection and shallow heat storage applications". Transportation Research Record: Journal of the Transportation Research Board, **2240** (1): 96-106.

- Hall, M., **P. Keikhaei Dehdezi.**, A. Dawson., J. Grenfell and R. Isola (2012). "Influence of the thermo-physical properties of pavement materials on the evolution of temperature depth profiles in different climatic regions." Journal of Materials in Civil Engineering, **24**(1): 32-47.

- **Keikhaei Dehdezi, P**., M. R. Hall., A. R. Dawson., S. Casey (2011). "Thermal, mechanical, and microstructural analysis of concrete containing microencapsulated phase change materials". International Journal of Pavement Engineering, (Provisionally Accepted for publication).

- **Keikhaei** Dehdezi, P., M. R. Hall., A. R. Dawson (2011). "Enhancement of soil thermo-physical properties using microencapsulated phase change materials for ground source heat pump applications", Applied Mechanics and Materials, **110-116**, 1191-1198.

- A. R. Dawson., **P. Keikhaei Dehdezi**., M. R. Hall., J. Wang., R. Isola (2011). "Enhancing thermo-physical properties of asphalt materials for pavement energy system (PES) applications". Road Materials and Pavement Design, (Under Review).

- A. R. Dawson., **P. Keikhaei Dehdezi**., M. R. Hall., J. Wang, R. Isola (2012). "Thermo-physical optimisation of asphalt pavement materials." In Transportation Research Board, 91th Annual Meeting, 23rd-27th January, Washington DC, USA.

- **Keikhaei Dehdezi, P**., M. R. Hall., A. R. Dawson (2010). "Concrete Pavements as a Source of Heating and Cooling." Proc 11th International Symposium on Concrete Roads, 13th-15th October, Seville, Spain.

- **Keikhaei Dehdezi, P**., A. R. Dawson., M. R. Hall., S. Casey (2012). "Investigate the feasibility of using asphalt pavements as a source of heating." 2nd International Symposium on Asphalt Pavements & Environment, 1st-3rd October, Fortaleza, Brazil, (Abstract Accepted, Paper Under Review).

- **Keikhaei Dehdezi, P**., A. R. Dawson., M. R. Hall (2012). "Pavements as a source of heating and cooling." Transport Research Arena 2012, 23rd-26th April, Athens, Greece. (First prize winner in the "Young Research Arena 2012" competition).

DECLARATION

The research reported in this thesis was conducted at the University of Nottingham, Department of Civil Engineering, Nottingham Transportation Engineering Centre, between October 2008 and March 2012. I declare that the work is my own and has not been submitted for a degree at another university.

Pejman Keikhaei Dehdezi

Nottingham

March 2012

ACKNOWLEDGEMENTS

TABLE OF CONTENTS

LIST OF FIGURES

LIST OF TABLES

LIST OF ABBREVIATIONS

AC	Asphalt Concrete
ADD	Additives
ASHRAE	American society of heating, refrigerating and air conditioning
BS	British standard
BSE	Backscattered electron
C	Celsius
CEM	Cement
COP	Coefficient of performance
CRCP	Continuously reinforced concrete pavement
CT	Computed tomography
D	Dimensional
DBM	Dense bitumen macadam
DSC	Differential scanning calorimetery
EDS	Energy dispersing spectrometer
Eq	Equation
FA	Fine aggregate
FDG-ESEM	Field emission gun environmental scanning electron microscopy
FHWA	Federal highway administration
GSHP	Ground source heat pump
h	Hour
HCP	Hardened cement paste
HF	Heat flow
HFM	Heat flow meter
HMA	Hot mix asphalt
HRA	Hot Rolled Asphalt
HWA	Heavy weight aggregate
HWM	Hot wire method
ISO	International organization for standardization
ITFT	Indirect tensile fatigue test
ITSM	Indirect tensile stiffness modulus
ITZ	Interfacial transition zone
IZ	Interfacial Zone
J	Joule
JRC	Jointed reinforced concrete
K	Kelvin
KJ	Kilo joule
KN	Kilo Newton
KPa	Kilo Pascal
LMC	Lean mix concrete
LTPP	Long term pavement performance
LVDT	Linear variable differential transformers
LWA	Light weight aggregate
m	Meter
Max	Maximum
min	Minutes
Min	Minimum
ml	Millilitre
mm	Millimetre
MPa	Mega Pascal
ms	Millisecond
MS	Microsoft
NAT	Nottingham asphalt tester

NTEC	Nottingham transportation engineering centre
PCC	Portland cement concrete
PCM	Phase change material
PES	Pavement energy system
PQC	Pavement quality concrete
PSHS	Pavement source heat store
RES	Road energy system
RH	Relative humidity
RLAT	Repeated load axial test
RMSE	Root mean-squared errors
s	second
SE	Secondary electron
SEM	Scanning electron microscopy
SHRP	Strategic highway research program
SMP	Seasonal monitoring program
TA	Thermal analysis
TPS	Transient plane source
TRL	Transport research laboratory
TW	Tetra Watt
UHI	Urban heat island
UK	United Kingdom
USA	United States of America
UV	Ultraviolet
VBA	Visual basic for applications
VHC	Volumetric heat capacity
W	Watt
XRCT	X-ray computed tomography
μm	Micron

LIST OF SYMBOLS

A	Surface area (m^2)
A_{pipe}	Inside surface area of the pipe (m^2)
AP	Apparent porosity (-)
a	Surface absorptivity (-)
C_{fluid}	Specific heat capacity of the fluid (J/kg K)
c_p	Dry-state specific heat capacity at constant pressure (J/Kg K)
c_p^*	Wet-state specific heat capacity at constant pressure (J/Kg K)
D_i	Internal pipe diameter (m)
dl	Length of pipe section (m)
d_{pipe}	Wall thickness of the pipe (m)
f_c	Compressive strength (MPa)
f_{fl}	Flexural strength (MPa)
F_o	Fourier number ($=\alpha \times \Delta t/l^2$) (-)
h_c	Convective heat transfer coefficient (W/m^2 K)
H_{melt}	Latent heat (KJ/kg)
i	Counter for time step ($i=0$ corresponding to specific initial condition)
k	Calibration constant for the HFM apparatus
k	Thermal conductivity of air (W/m K)
l	Node distance in 3D model ($=\Delta z=\Delta x$)
L	Peak load in ITSM test (N)
L_c	Characteristic length (m)
l_s	Thickness of slab in HFM apparatus (mm)
m	Number of nodal points (1, 2, …n)
N_f	Number of cycles to failure
N_u	Nusselt number (-)
P	Maximum applied load in ITFT test (N)
P_r	Prandtl number(-)
Q	Rate of heat transfer (W)
q	Heat flux (W/m^2)
R	Specific thermal resistance (m^2 K/W)
R_a	Surface roughness (μm)
R_e	Reynolds number (-)
s_m	Stiffness modulus of bituminous mixture (MPa)
T	Temperature (°C)
T_0	Surface temperature (K)
T_{dp}	Dew point temperature (K)
T_{inlet}	Inlet fluid temperature (K)
T_{melt}	Melting point temperature (°C)
T_{outlet}	Outlet fluid temperature (K)
T_{sky}	Sky temperature (K)
T_{surr}	Surrounding temperature (K)
U_{pipe}	Overall heat transfer coefficient for the pipe (W/m^2 K)
v_w	Wind velocity (m/s)
w	Weight (kg)
α	Wet-state thermal diffusivity (m^2/s)
α^*	Wet-state thermal diffusivity (m^2/s)
β	Dry-state thermal effusivity ($J/s^{0.5}$ m^2 K)
β^*	Wet-state thermal effusivity ($J/s^{0.5}$ m^2 K)
Δt	Time increment in finite difference grid (s)
Δz	Depth increment in finite difference grid (m)
ε	Surface emissivity (-)
ε_{max}	Maximum horizontal tensile strain (-)

λ	Dry-state thermal conductivity (W/m K)
λ^*	Wet-state thermal conductivity (W/m K)
λ_{pipe}	Thermal conductivity of pipe materials (W/m K)
v	Kinematic viscosity of air (m^2/s)
ρ_d	Dry density (kg/m^3)
ρ_{ssd}	Saturated surface dry density (kg/m^3)
σ	Stefan-Boltzmann constant (=5.67×10^{-8} W/m^2 K^4)
σ_{max}	Maximum horizontal tensile stress (KPa)
μ	Dynamic viscosity of the fluid (Pa-s)
ν	Poisson's ratio (-)
$\dot{m}$	Mass flow rate (kg/s)

1 INTRODUCTION

1.1. Energy Needs

With the increase in world population and industrialization, there has been a continuous increase in consumption of energy. Therefore, this important question is raised; will fossil energy resources (i.e. coal, oil, and gas) in the future account for the energy needed to survive and develop? Although opinions differ as to when fossil fuels will be depleted, the fact is that they are limited. Oil as one of the most consumable types of fossil fuels, is being consumed about one million times faster than it was made (Armstrong and Blundell 2007). In addition, environmental pollution is a serious threat to vegetation, wild life, and human health. Generating energy from fossil fuels increases the level of carbon dioxide into the upper earth atmosphere and causes anthropogenic climate change; an acceleration of the 'greenhouse effect' (Armstrong and Blundell 2007). The depletion of oil reserves, the need to arrest global warming, climate change, or ozone layer depletion caused by the combustion of fossil fuels, all mandate new thinking from all those with concerns for the future.

In order to avoid further impacts of these phenomena, the alternative is to replace fossil fuel usage as much as possible with environmentally friendly, clean, and renewable energy sources. Among the renewable sources, solar energy comes at the top of the list due to its abundance and more even distribution in nature than any other renewable energy type, such as wind, hydro, wave, and tidal energies. Approximately, half of the world's incoming solar energy is absorbed by the earth's surface (Budikova et al. 2010). Most obviously, the sun provides solar energy to our planet's surface on an annual basis at a rate of about 100, 000 TW; therefore, the energy from one hour of sunlight is equivalent to all the energy mankind currently uses in a year (Armstrong and Blundell 2007).

Due to the nature of solar energy, two components are required to have a functional solar energy system; a collector and a storage unit. The collector simply collects the radiation that falls on it and converts it to other forms of energy such as electricity and/or heat. The storage unit is required because of the non-constant nature of solar energy. The acceptance of solar energy to provide hot water, electricity, heating and cooling for homes, businesses, and industries will depend on the cost of the equipment needed to collect and/or store it. Even though sunlight is free, one must pay a capital charge for amortisation of the collecting equipment which is the most important and the most expensive single component of an active solar energy system (Rabl 1985).

1.2.   Pavement Energy Systems

Pavements comprise large areas of our infrastructure and include roads, pedestrian pathways and parking areas. They are already required for structural reasons and need not to be installed as additional elements as do conventional thermal energy utilisation systems. In addition, many buildings that have a high heating and/or cooling load are built adjacent to large pavement areas (e.g. airport terminals, shopping malls, factories, warehouses, school buildings, and retail outlets). Therefore, there is a great opportunity to turn pavements into a ubiquitous and inexpensive source of energy. The pavement structure can be equipped with fluid-filled pipes (known as 'loops') in order to be served as a solar energy collector and/or storage media. The fluid in the pipe can absorb/reject heat to the pavement and deliver useful energy to nearby buildings. If such a system is installed at the time of pavement construction or rehabilitation, it might incur only a marginal cost as the cost of the pavement construction would probably be already funded from a separate budget (i.e. a budget for transportation rather than energy purposes).

Previous attempts to recover heat energy from pavements have been extremely limited but there are two studies, one in the UK and one in the Netherlands, which both employ loops buried in the pavement to extract heat. The Ooms 'Road Energy System' (RES) developed a

quick and simple process for an asphalt energy collection system which, the authors claim, enables pipes to be placed close to the surface of the asphalt without the disadvantages of stress concentration induced by the presence of holes (the pipe) (de Bondt 2003). Another major instrumented trial of the solar energy collector and storage technique was undertaken by Transport Research Laboratory (TRL) in the UK (Carder et al. 2007). The TRL 'Interseasonal Heat Transfer' system collects the solar heat from the asphalt pavement surface in the summer, storing it in shallow insulated ground heat stores for subsequent re-using (e.g. ice prevention on the road surface during winter and building heating). These two systems have already been tested, partly commercialised, and have become applicable in practice.

Installing loops in pavements could also have other benefits for the environment and pavement itself. High temperature of pavements has a significant impact on the environment and increases the temperature of the near-surface air in urban areas. The Urban Heat Island (UHI) effect leads to an increase in power consumption for cooling of buildings adjacent to pavements and a deterioration of the air quality (Wong and Chen 2009). Moreover, rutting is a major temperature-related distress in asphalt pavements that occurs as a result of high temperature. Collecting heat from the pavement could reduce the UHI effect and rutting potential of the asphalt pavement (Mallick et al. 2009; Wu et al. 2011).

Applications of Pavement Energy Systems (PESs) are not limited to those mentioned in above. Pavements, by installing loops at shallower depths, might also be used as a heat source during winter and as a heat sink during summer (similar application to Ground Source Heat Pump). A 'Pavement Source Heat Store' (PSHS) would exploit the fact that the seasonal temperature variation under the pavement is much less than the temperature fluctuation of ambient air because of the high thermal mass of the pavement. Figure 1-1 depicts different applications of the PESs.

The use of pavements to collect and/or store solar energy is relatively new subject that is still at an early age of development. Very little work has been reported, either experimentally or theoretically, on the PESs and determination of factors affecting their performances, especially factors that are related to the civil engineering materials (e.g. effect of thermo-physical properties of pavement materials, the pavement/pipe interface, and the depth of embedded pipe). It is therefore, necessary and timely to conduct research into PESs' performance and attempt to enhance this by material and design optimisation. In addition, materials' optimisation of PESs for their thermal characteristics and load bearing would also allow intelligent design and material specification that could lead to improved performance and longevity of pavements.
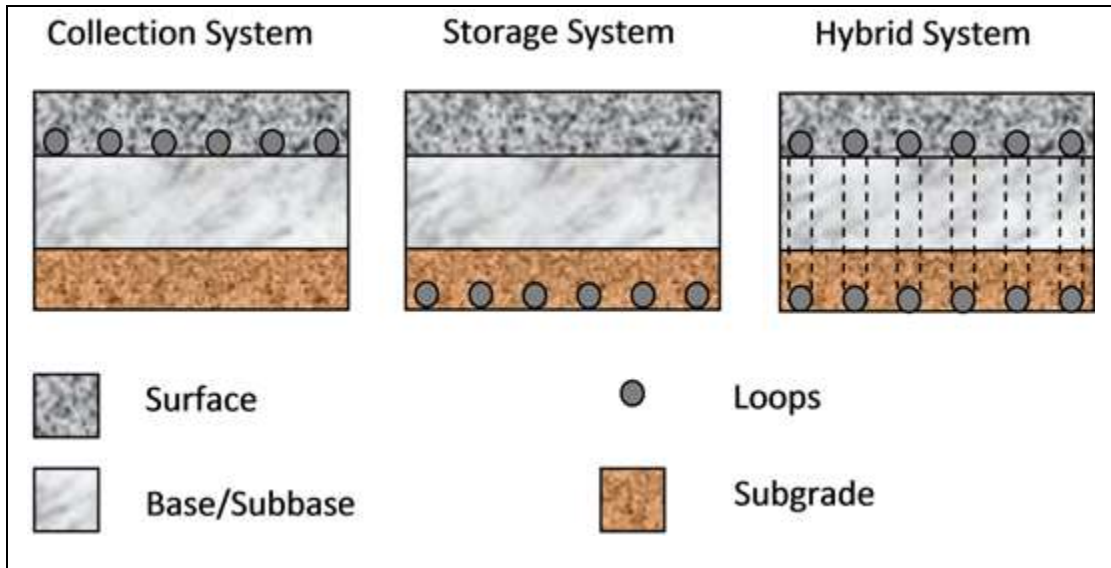
Figure 1-1 Applications of Pavement Energy Systems (PESs)

1.3. Aim and Objectives

1.3.1. General Aim

The aim of this study is to optimise a pavement's materials and structure in order to serve as a solar energy collector and/or storage, particularly for locations where the energy can be delivered to nearby buildings (directly or in conjunction with heat pumps). The specific driver to this study is the potential for heating and/or cooling of airport buildings by installing loops into the pavements of adjacent infrastructure that has been funded for

structural purposes (principally car parks and aircraft aprons) (see Figure 1-2), but it is anticipated that the project outputs should have much wider applicability than this specific situation.
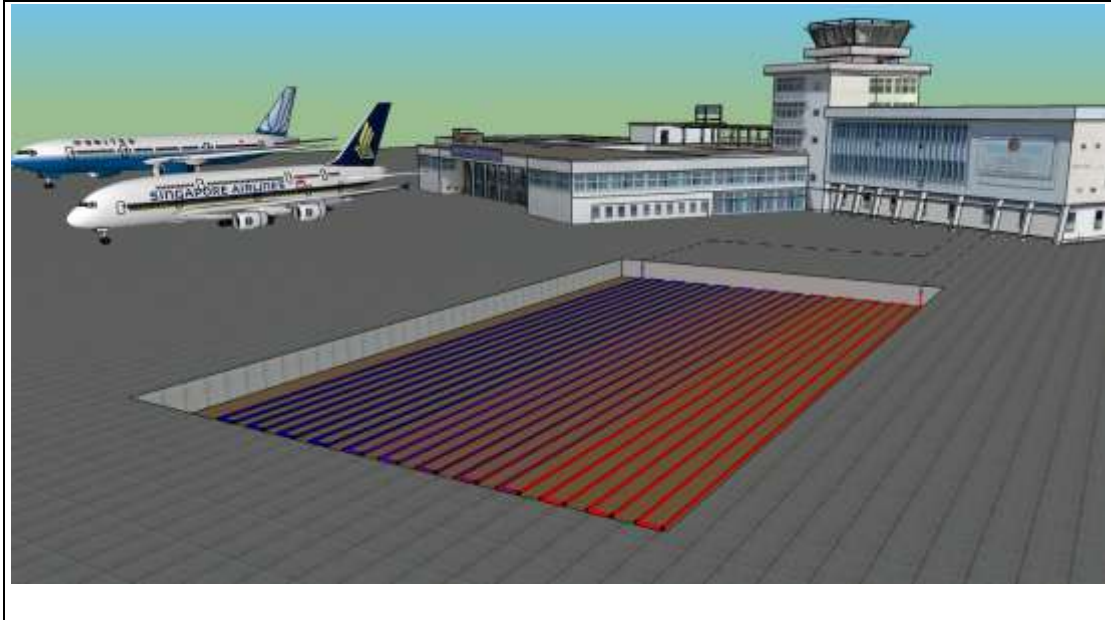
Figure 1-2 A Pavement Source Heat Store (PSHS)

1.3.2. Objectives

To achieve this aim, the following research objectives have been identified:

1) To study what is currently known about using pavement materials and structures as solar energy collectors and storage media and to appraise the factors affecting their design and performance.

2) To experimentally determine the potential for optimisation of pavement materials for thermo-physical properties (i.e. by measuring thermal conductivity, thermal diffusivity, thermal effusivity, and heat storage) while maintaining comparable mechanical performance of the pavement.

3) To develop appropriate techniques to calculate temperature profile within the pavement structure and also to predict the performance of different Pavement Energy Systems (PESs) (see Figure 1-1) by numerical modelling and experimental testing.

4) To design and construct large-scale PESs and carry out laboratory testing to determine their performance and also to validate the model (See Objective 3).

5) To analyse the performance of the PESs for structures with various thermo-physical properties (See Objective 2) and climatic conditions by using the validated model (See Objectives 3 and 4).

1.4.   Scope of the Study and Thesis Layout

The objectives of this research are linked together and organised in seven chapters, as shown in Figure 1-3, in order to complete the research. After this introductory chapter, the other chapters are organised as follows:

Chapter 2 provides a background to the project. It includes a basic understanding of pavement materials and structures as well as discussions on the PESs and their design considerations. This chapter also reviews the applications of Phase Change Materials (PCM) in building constructions for latent heat storage. Finally, the factors affecting thermo-physical properties of pavement mixes and their measuring techniques are described.

Chapter 3 presents and discusses the measured thermo-physical and mechanical properties of concrete and asphalt pavements. Thermal conductivity, specific heat capacity, density, thermal diffusivity, thermal effusivity as well as basic mechanical tests on concrete and asphalt mixes are performed. This chapter also investigates the feasibility of using PCMs in pavement mixes.

Chapter 4 outlines the development of a one-dimensional (1D) transient model of temperature distributions in pavements and its validation using the U.S. Long Term Pavement Performance (LTPP) database and field validation using data from Sutton Bonington (UK).

Chapter 5 describes the construction and instrumentation of large-scale physical models of the PESs. In this chapter, the performance of the thermally modified PES are monitored and compared with those of conventional ones. In addition, this chapter covers the development and validation of pseudo 3D transient explicit finite-difference software to simulate the performance of the PES.

In **Chapter 6**, the performance of the PESs under various conditions (e.g. pavements' thermo-physical properties, layer sequences, climatic conditions, etc.) is evaluated using the validated model.

The final chapter, **Chapter 7**, details the conclusions and recommendations for further research work.
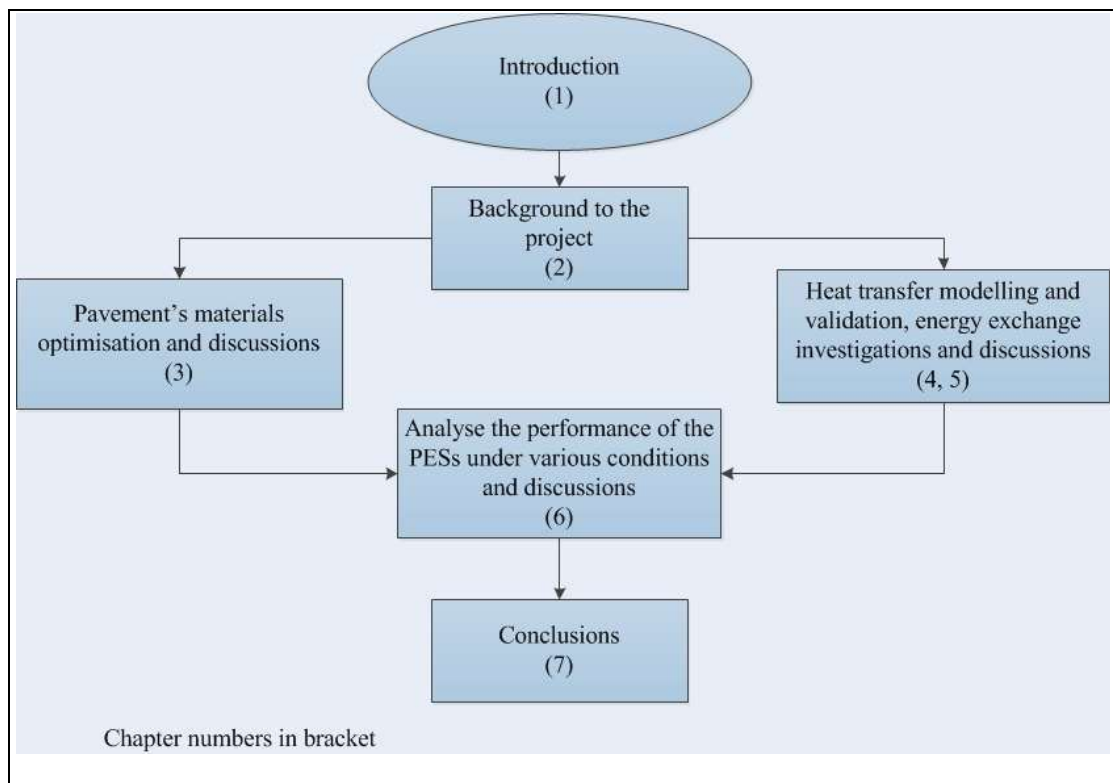
Figure 1-3 Project flowchart

2   BACKGROUND TO THE PROJECT

2.1.   Overview

This chapter aims to detail the background information required for the subsequent chapters. The chapter is divided into six main sections and begins with Section 2.2 exploring pavement types and materials. This section is required in order to provide a correct understanding of pavement structures and materials before utilising them as a source of energy. Section 2.3 presents the basics of the heat transport mechanisms in materials. Section 2.4 explores applications of pavement as a 'heat collector system' as well as highlighting the factors affecting their design considerations. This section will also review commercial systems applied to recover heat energy from pavements. Section 2.5 reviews 'ground source heat pump' systems and it covers the principles and different types of the system. Section 2.6 will be based on a review on the application of Phase Change Materials (PCM) in building materials to improve latent heat storage. This literature review will finish, in Section 2.7, with a presentation on the thermo-physical properties of pavements' materials and it covers measuring techniques and factors affecting their capabilities.

2.2.   Pavement Types

The main structural function of a pavement is to provide an adequate support to withstand the imposed loads upon it and distribute them over a relatively wide area of soil. For discussion purposes, pavements can be categorised into two groups; flexible pavements (those which are surfaced with bituminous materials) and rigid pavements (those which are surfaced with Portland Cement Concrete (PCC)). There are also combinations of two types, which are termed rigid or flexible composite pavements.

2.2.1. Concrete Pavements and Mixes

Concrete in its simplest is formed by mixing aggregates (coarse$> 4mm$ and fine$\leq 4mm$), water, and cement. Concrete pavements have been used for airports, highways, streets, local roads, heavy-duty industrial floor slabs, parking lots, and other types of infrastructure. The cross-section of a concrete pavement is most usually composed of a cement concrete slab which is normally termed Pavement Quality Concrete (PQC) on top of a base and/or subbase (both terms of 'base' and 'subbase' have been used in the literature to describe the layer under a concrete pavement).

Concrete Pavement Layers

The PQC must be strong enough to provide an economical pavement thickness as well as a durable and weather resistant surface. Three forms of PQC are currently used in civil engineering projects namely; plain concrete, Jointed Reinforced Concrete (JRC), and Continuously Reinforced Concrete Pavement (CRCP). The plain concrete is the most commonly used type of concrete pavement because of the economic reasons (Delatte 2008). It is widely used in airfield aprons, taxiways and runways, and heavily trafficked highway pavements in tropical countries (Griffiths and Thom 2007). The layer under the PQC is usually a low strength concrete which is normally termed Lean Mix Concrete (LMC) (Defence Estates 2006).

Concrete Mixes

The PQC mix design parameters, for an airfield pavement, recommended by Defence Estate (2005; 2006) are summarised in Table 2-1.

Table 2-1 Mix design parameters for the PQC

Parameters	Recommendations
Cement Type	CEM I, Strength class 42.5 N/mm^2 or above
Minimum cement contents	350 kg/m^3
Maximum free water/cement ratio	0.45
28-day characteristic compressive strength	>40 MPa
28-days flexural strength	>4.5 MPa
Coarse aggregate grading	20/40, 10/20, or 4/10 single sized according to BS EN 12620 (2008)
Fine aggregate grading	According to Table 3.3 in Defence Estate (2005)

The LMC mix design parameters recommendations for an airfield pavement are summarised

in Table 2-2 (Williams 1986; Defence Estates 2005; Delatte 2008).

Table 2-2 Mix design parameters for the LMC

Parameters	Recommendations
Cement content	118-208 kg/m^3
Maximum Aggregate/Cement ratio	15/1
Water/(Aggregate+Cement)	5-7%
7-day characteristic compressive strength	>15MPa
Water/Cement ratio	Around unity

Table 2-1 and Table 2-2 have been used as the basis for design of concrete specimens (see

Section 3.3).

2.2.2. Asphalt Pavements and Mixes
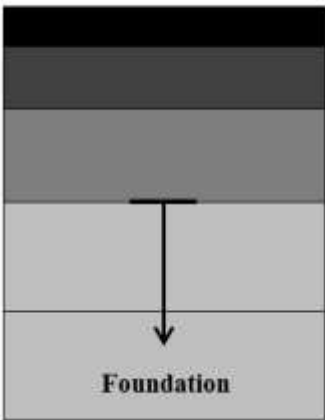
Asphalt in its simplest form consists of aggregates which are bound together by means of a

binder (i.e. bitumen). The term 'visco-elastic' is normally used to indicate that bituminous

materials have both viscous and elastic behaviour; viscous at high temperature and elastic at

low temperature. Therefore, because of the 'visco-elastic' behaviour of asphalt pavement,

they are very susceptible to permanent deformation (i.e. rutting) at the high temperatures

and/or longer loading time (i.e. stationary or slow moving vehicle).

High susceptibility to permanent deformation, caused by high tyre pressure of standing

aircraft, as well as other factors such as low resistance to fuel and oil spillages will limit the

use of asphalt pavements for aircraft parking (i.e. apron). In certain circumstances, however, when the frequency of use is very low, asphalt surfacing may be an alternative to concrete pavements (Defence Estates 2008). In addition, asphalt pavements are the most common construction for car park lots around the world.

Asphalt Pavement Layers

A typical asphalt pavement consists of surface, base and sub-base built over a compacted subgrade as shown in Figure 2-1. The surface course (sometimes subdivided into surfacing and binder course) is the layer in contact with traffic loads, it protects the lower layers from weather and provides characteristics such as friction, smoothness, noise control, and drainage. Base course is immediately beneath the surface course, it is the main structural layer which provides the major part of the strength and load distributing properties of the pavement. Subbase course is between the base course and the subgrade. The primary function of it is to act as structural support, particularly during construction of higher layers. Subgrade is the natural soil or manmade ground on which the pavement is built.

Asphalt pavement		Material type
	Surfacing	A thin asphalt surface
	Binder course	Asphalt
	Base	Asphalt/Unbound granular material
	Sub-base	Unbound granular material/Bitumen or cement stabilised material
Foundation	Subgrade	In-situ compacted material/cement stabilised/unbound granular material

Figure 2-1 Typical structure of asphalt pavement

Asphalt Mixes

Regarding how bituminous materials are mixed, there are two known groups, namely Hot Mix Asphalt (HMA) and cold mix asphalt. HMA is a mixture in which all materials are mixed at high temperature. Two well-known examples of HMA are Asphalt Concrete (AC)

(formerly known as Dense Bitumen Macadam (DBM)) and Hot Rolled Asphalt (HRA). The AC is a continuously graded mixture and contains all the aggregate sizes from the maximum down to filler, (i.e. <0.063mm). The use of a relatively low amount of soft bitumen as well as a good aggregate interlock result in this material having very good load-spreading properties and a high resistance to permanent deformation. Therefore, AC is recommended to use in places with slow moving traffics, e.g. uphill (O'Flaherty 2002) and at locations subjected to stationary traffic, e.g. car parks and aircraft stands (Defence Estates 2008). Specifications for a car park pavement or an airfield parking apron (with a very low frequency of use) surface course are summarised in Table 2-3.

Table 2-3 Specifications for car park pavements surface course

Parameters	Recommendations
Bitumen content	4.9±0.4%
Bitumen type	100/150
Air void	4±1.5%
Aggregate grading	According to Table 5.2 in Defence Estates (2008)

Table 2-3 has been used as the basis for design of asphalt specimens (see Section 3.6).

2.3. Transport of Heat

Basic mechanisms of heat transfer are reviewed here and details about the modelling of heat transfer in pavements will be discussed in Chapter 4. Heat is defined as "*the form of energy that can be transferred from one system to another as a result of temperature difference*" (Cengel 2002). Temperature difference is the driving force for heat transfer and the larger the temperature difference, the larger the rate of heat transfer. Heat, in the presence of a temperature difference, can be transferred in three different modes: 'conduction', 'convection', and 'radiation' and all modes are from a high-temperature medium to a lower-temperature one.

2.3.1. Conduction

"Conduction is the transfer of energy from the more energetic particles of a substance to the adjacent less energetic ones as a result of interaction between particles" (Cengel 2002).

Heat conduction in solids is normally due to the motion of free electrons (case for metals) and vibration of the molecules in a lattice (case for non-metals). The rate of conductive heat transfer through a plane layer (Figure 2-2) of thickness Δx, temperature difference of $\Delta T = T_2 - T_1$ and a cross section of A is governed by 'Fourier's law' and is given by:

$$Q_{conduction} = \lambda A \frac{T_1 - T_2}{\Delta x} = -\lambda A \frac{\Delta T}{\Delta x}$$

Eq. 2-1

where,

$Q_{conduction}$= Rate of heat conduction (W)

A= surface area (m^2)

λ= Thermal conductivity of the material (W/m K)

$\frac{\Delta T}{\Delta x}$ = Temperature gradient in the direction of heat flow for one-dimension (1D) (K/m)
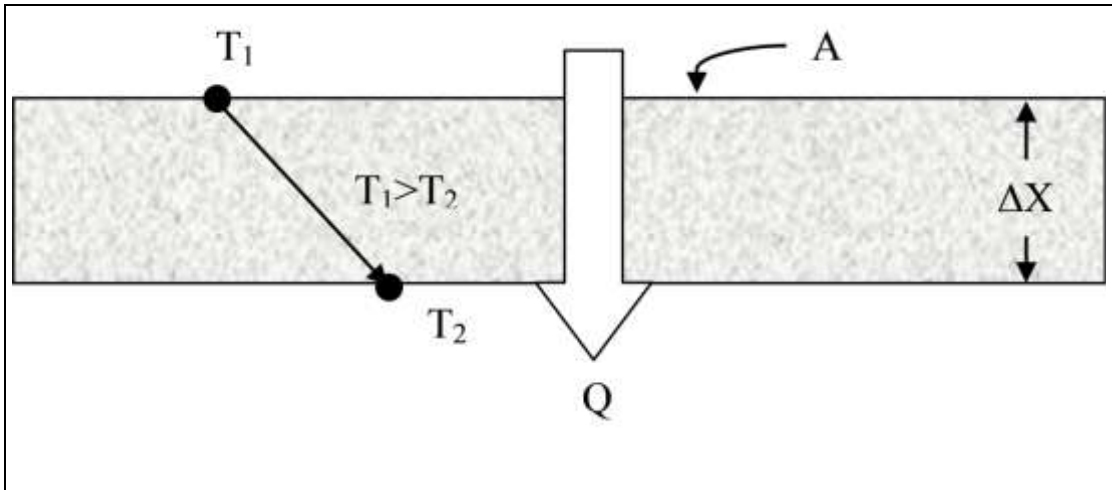
Figure 2-2 Heat conduction through a plane layer

2.3.2. Convection

"Convection is the mode of energy transfer between a solid surface and the adjacent liquid or gas that is in motion" (Cengel 2002). The rate of heat transfer by convection is determined by 'Newton's law of cooling' as follows:

$$Q_{convection} = h_c A (T_0 - T_f)$$

Eq. 2-2

where,

$Q_{convection}$= rate of heat transfer by convection (W)

h_c= convective heat transfer coefficient (W/m^2 K)

T_0= surface temperature (K)

T_f= fluid temperature (K)

Convection can be classified as 'natural' (or free) and 'forced convection'. In free convection the flow is induced by buoyancy forces, which are due to the rise of warmer fluid and the fall of the cooler fluid. In contrast, forced convection occurs when the flow is caused by external means such as by a pump, a fan or atmospheric wind. Convection is also classified as 'external' and 'internal', depending on whether the fluid is forced to flow over a surface or in a pipe. Water flow in pipes is an example of internal convection which will be discussed in Chapter 5.

2.3.3. Radiation

"Radiation is the energy emitted by matter in the form of electromagnetic waves (or photons) as a result of the changes in the electronic configurations of the atoms or molecules" (Cengel 2002). Radiation heat transfer unlike convection and conduction does not require a medium and can even be transferred across a perfect vacuum.

'Thermal radiation' can be defined as electromagnetic radiation emitted from a body due to its temperature and occurs at wavelengths between 0.1 and 100 µm on the 'electromagnetic spectrum' (see Figure 2-3). Thermal radiation includes the entire visible and infrared (IR) radiation as well as a portion of the ultraviolet (UV) radiation. The heat emitted by an ideal radiator or 'blackbody' is determined by the 'Stefan-Boltzmann's law' as follows:

$$Q_{thermal} = \sigma A T_0^4$$

where,

$Q_{thermal}$= rate of heat radiated (W)

σ= Stefan-Boltzmann constant= 5.67×10^{-8} W/m^2 K^4

The radiation emitted by a real surface is less than that of a blackbody. Therefore, the term emissivity (ε) will introduce to the Stefan-Boltzmann equation to take account for the real

surface. The emissivity value in general depends on the surface material and finish and ranges from 0 to 1.

$$Q_{thermal} = \sigma \varepsilon A T_0^4$$

<div align="right">**Eq. 2-3**</div>

The electromagnetic radiation emitted by the sun is known as 'solar radiation', and nearly all of it falls into the wavelength band 0.3–3 μm. Almost half of solar radiation is light with the remaining being UV and infrared. The amount of solar radiations that absorbed by the surface depends on the solar absorptivity and it can be calculated from equation below.

$$Q_{absorbed} = aAQ_{incident}$$

<div align="right">**Eq. 2-4**</div>

where,

$Q_{absorbed}$: absorbed radiation flux (W)

a: absorptivity ($0 < a \leq 1$)

$Q_{incident}$: radiation flux incident on a surface (or, irradiation) (W)
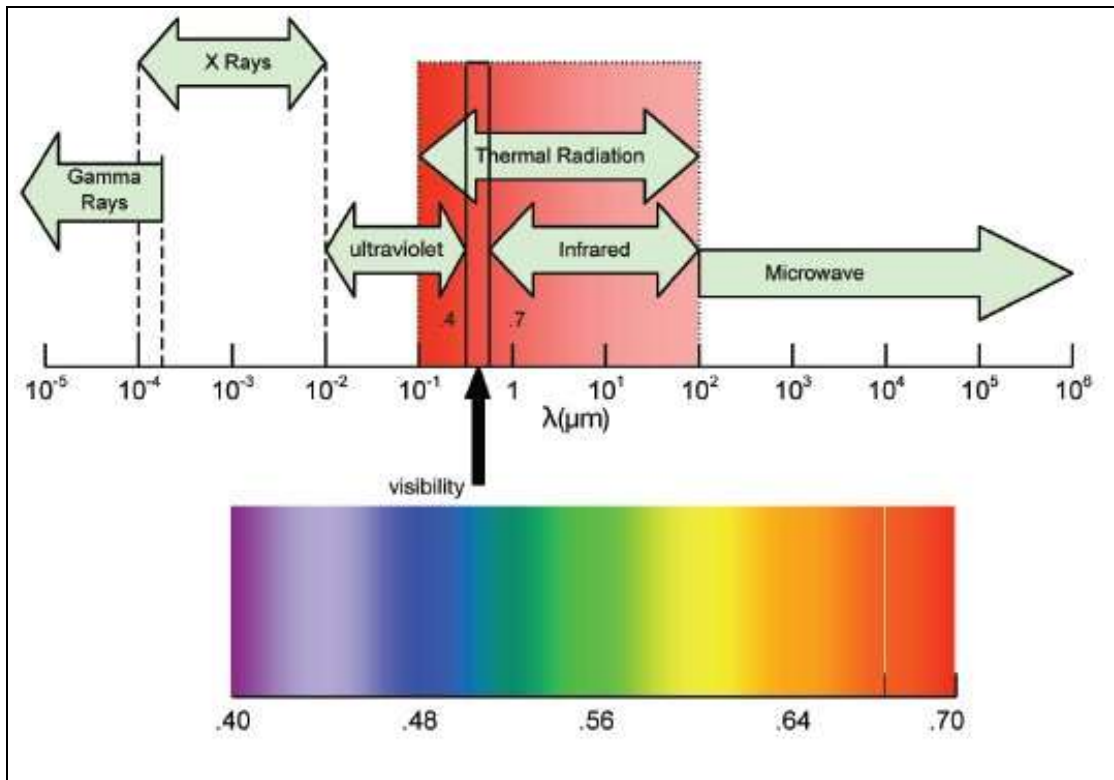
Figure 2-3 The electromagnetic wave spectrum (PTB 2010)

2.4.   Pavement Heat Collector Systems

Asphalt pavements can heat up to 70°C due to solar irradiation in summertime because of their excellent heat-absorbing properties (Wu et al. 2011). Solar energy absorbed by a pavement's surface could be collected by installing loops under the pavement. The collected heat from the pavement could be used for different applications such as; to store heat in an underground water reservoir (de Bondt 2003) or under the pavement structure (Carder et al. 2007) for heating adjacent building and/or de-icing of roads in winter, to supply hot water (Sedgwick and Patrick 1981), or to convert the energy to a transmittable form using a thermo-electric generator (Hasebe et al. 2006). The heat collected from the pavement could also reduce the Urban Heat Island (UHI) effect and the rutting potential of the asphalt pavement (Mallick et al. 2009; Wu et al. 2011).

2.4.1.   Applications and Design Considerations

A first application of pavement solar collectors in the literature seems to be that of Sedgwick and Patrick (1981). They experimentally studied swimming pool heating in summer by use of a grid of plastic pipes laid at 20 mm under an asphalt surface in a tennis court in the UK. The air temperature and solar radiation for the period of the experiment reached 22°C and 610 W/m^2, respectively. They found that the system can provide heating to swimming pools which are usually operated at between 20°C and 27°C, hence, concluded that the system was technically feasible, for UK conditions, and cost effective compared to a conventional swimming pool solar heater. Turner (1986; 1987) studied, theoretically, the performance of a pavement heat collector in winter (maximum pavement surface temperature of 15°C) and summer (maximum pavement surface temperature of 70°C) for applications varying from de-icing of roads and bridges to water heating for heat pumps and swimming pools. He did some analysis (using a simple 1D steady-state model) and found that pavement heat collector systems may be suitable for the application was aiming towards.

Nayak et al. (1989) carried out experimental studies on a roof solar concrete collector, with glazing at the top, used for providing domestic hot water. They embedded PVC tubes at 10mm under the concrete which was painted in black to increase its solar absorptivity. They concluded that solar concrete collectors can be used as a cost-effective alternative to conventional systems (e.g. flat-plate collectors) under the climate where the experiment was performed (maximum air temperature and solar radiation reached 35°C and 1000 W/m^2 respectively). In addition, they studied the effect of flow arrangement (parallel and series) on the performance of the system and found that the performance of both collectors under different flow arrangements was similar. Similarly, Chaurasia (2000) experimentally studied the performance of a concrete solar collector by laying down a network of aluminium pipes in a building's roof (with no glazing at the top), in India (maximum air temperature and solar radiation reached 27°C and 650 W/m^2 respectively), to supply hot water for domestic use. They concluded that at an inlet water temperature of 15°C-28°C, hot water at temperature 36°C to 58°C can be obtained during the daytime in winter.

Hasebe et al. (2006) experimentally investigated an asphalt solar collector to produce electric power. The electric power was produced by temperature differences between warm water (coming out of the embedded pipe in the pavement) and cool water (supplied from a river) at a thermoelectric generator. They investigated the effects of outlet temperature of the warm water on generated electricity and found that the output power significantly increases as outlet water temperature increases.

Studies in recent years have aimed to improve the efficiency of pavement heat collector systems. Mallick et al. (2009) experimentally and theoretically studied asphalt pavement for applications of harvesting energy and reducing the UHI effect. They theoretically (using a finite- element model) showed that near-surface air temperature could be reduced as much as 10°C by running water through the embedded pipes placed at about 40 mm under the pavement. In addition, they performed a small-scale laboratory testing on asphalt pavement

samples. Their results showed that black acrylic paint on the asphalt surface and replacing

limestone aggregates with aggregates containing high percentages of quartz could increase

the efficiency (rise in water temperature) of the system by 50% and 100%, respectively. Wu

et al. (2011) performed a similar study on small-scale asphalt pavement slabs (see Figure 2-4

top) and concluded that the pavement surface temperature could be significantly reduced as

water flows in the embedded pipes. In another study, Wu et al. (2009) experimentally

investigated the use of graphite powders in asphalt pavement to improve the thermal

conductivity and energy exchange efficiency. They concluded that the addition of graphite

could slightly increase the outlet water temperature (see Figure 2-4 bottom) however, they

realised a longer piping and a larger area of heat transfer is necessary to realize a meaningful

temperature rise. In addition, the lubricant effect of graphite may have a negative effect on

the mechanical performance of the asphalt pavements.
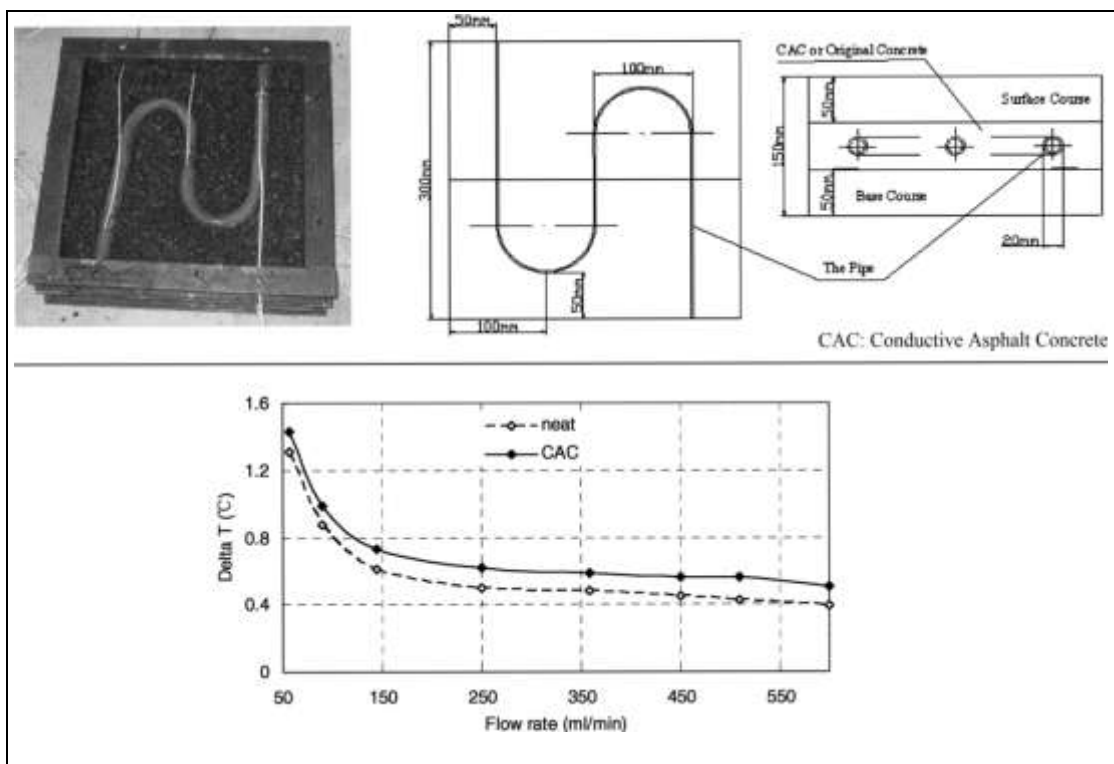
**Figure 2-4 Tested asphalt slabs (top) and temperature rise as a function of flow rate (bottom)
for normal and conductive asphalt slabs, Adapted from (Wu et al. 2009)**

2.4.2. Commercial Systems

Previous attempts to recover heat energy from pavements have been extremely limited but there are some commercialised systems which employ loops buried in the pavement to extract/reject heat. These systems are briefly described in the following paragraphs.

Road Energy Systems® (RES) asphalt solar collector (see Figure 2-5), is a system for extracting energy from asphalt pavements. This system have been developed and partly commercialised in the Netherlands by Ooms Avenhorn Holding bv (de Bondt 2003; Sullivan et al. 2007). The RES works as follows; in summer, cold water from an aquifer is pumped up and circulated through plastic pipes buried in the upper layer of asphalt pavement. Due to the effect of the sun, the water gets warm and the warm water is then transported into another underground reservoir and held at this location until required. In winter, the system works in the opposite way (the stored heat flows from the hot storage medium to the asphalt pavement). The system has the potential of cooling the pavement in summer, which can reduce the deformation of asphalt (rutting), and heating the pavement in winter, which can eliminate icy driving conditions (de Bondt 2003). The system is also linked with a heat pump to provide heating and cooling for adjacent buildings (see Figure 2-5).
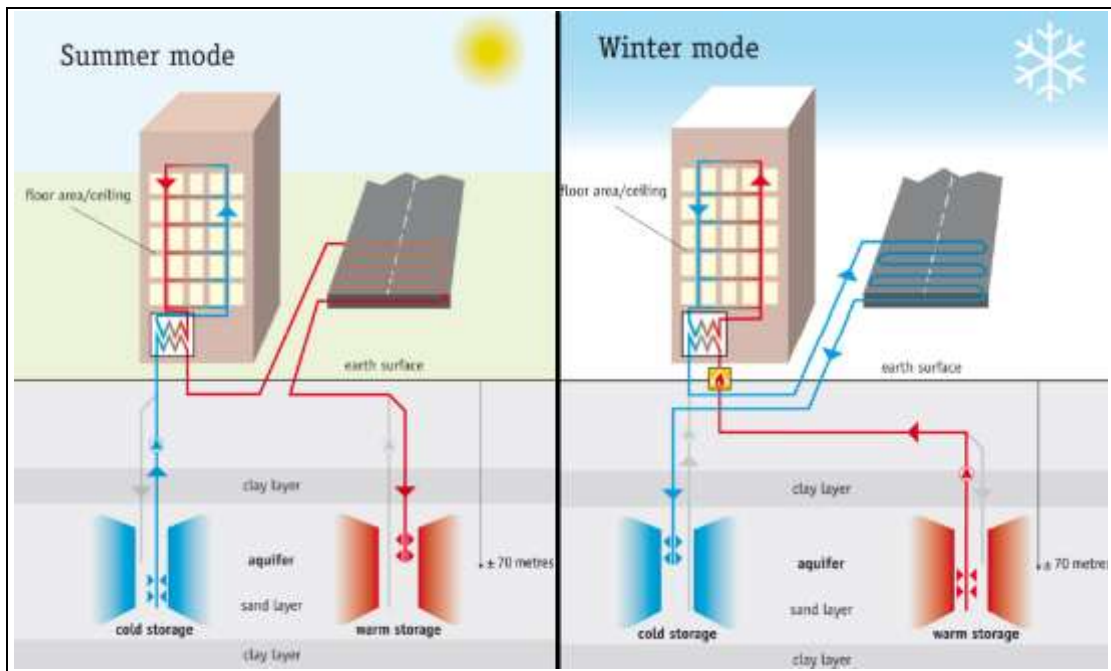
Figure 2-5 Road Energy System innovated by Ooms Avenhorn Holding bv (de Bondt 2003)

In order to commercialise the RES system, Ooms have conducted different experiments to investigate possible detrimental effects of pipes on the lifetime of the pavement as well as the effect of the asphalt compaction process on the plastic pipes. van Bijsterveld and de Bondt (2002) experimentally showed that the presence of pipes in the asphalt has negative effects on the durability of asphalt structure and that is because of concentrated stresses near the pipes which can lead to crack initiation. To prevent this phenomenon, they have developed a three-dimensional reinforcing grid to fix and protect the pipes during the laying and compaction of the asphalt mixture and reduce the stresses around the pipes (see Figure 2-6). In addition, a special polymer modified bitumen (known as Sealoflex®) was developed to achieve high quality asphalt mixture in between the pipes and the grid. The RES has been successfully installed in the Netherlands and UK (Sullivan et al. 2007).
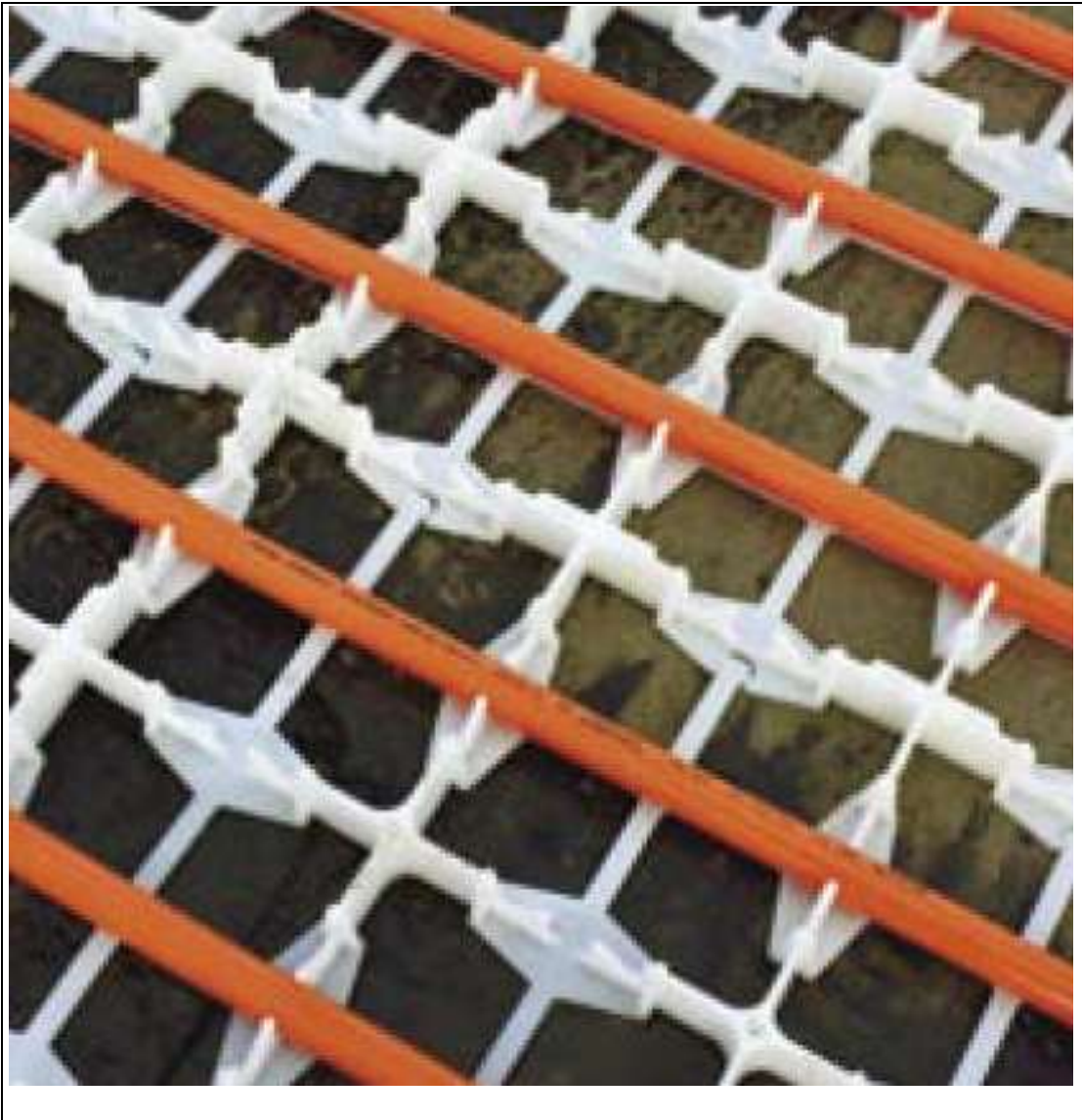
Figure 2-6 Three-dimensional reinforcing grid developed by Ooms Avenhorn Holding bv (van Bijsterveld and de Bondt 2002) carrying water pipes (in red)

Another major instrumented trial of the solar energy collector from asphalt pavements was undertaken by Icax[TM] Limited (Carder et al. 2007) in the UK. The Icax system is very similar to the Ooms system since both of the systems can be considered as 'hybrid systems' (collect the solar energy and store it until required). In the Icax system heat, absorbed by the asphalt pavement, will be collected through upper loops installed below the asphalt surface. The warm water in the upper loops will then be circulated and stored through lower loops installed below the asphalt surface (see Figure 2-7). Carder et al. (2007) found that at the end of a full season of heat recovery (from May to September), ground temperature in the centre of the heat store remained about 9°C higher than that of the control area of the pavement (i.e.

without any loops and insulation). Moreover, they carried out winter maintenance of the

pavement from the heat recovered in the heat store. They found that the heated section of the

road was maintained at a temperature about 3°C hotter than the unheated area.
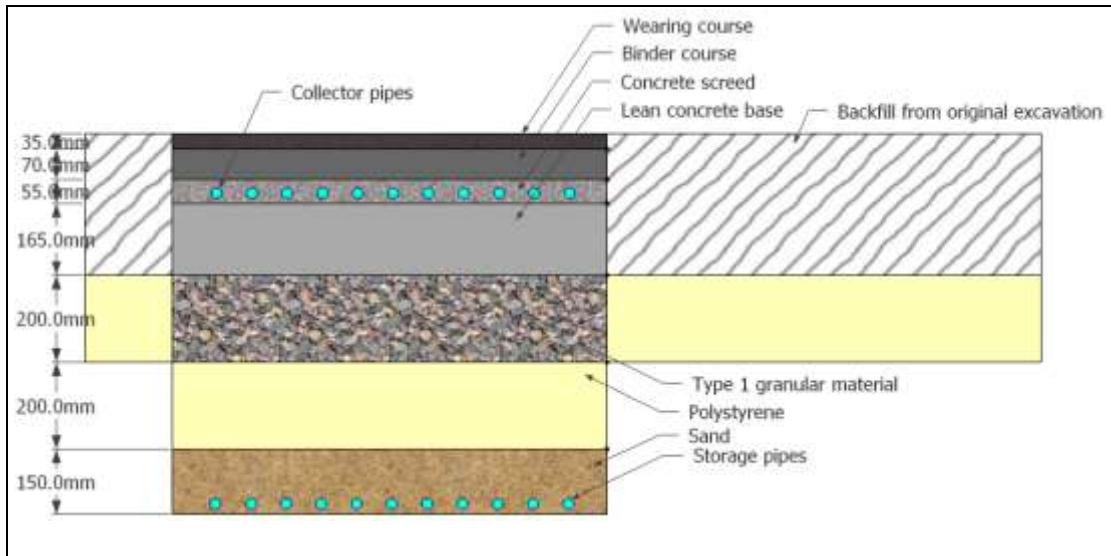
Figure 2-7 Cross-section of collector and storage loops in the Icax system, Adapted from (Carder et al. 2007)

2.5.   Ground Source Heat Pump Systems

First of all, ground source heat and 'geothermal energy' must be distinguished from each

other. Ground source heat is referred to the occurrence, movement, and exploitation of low-

temperature (temperature of less than 30°C) heat in the relatively shallow (depths of down to

200m) geosphere (Banks 2008). On the other hand, geothermal energy is the high-

temperature energy provided by the earth's deep interior which can be found either in very

deep boreholes and/or in certain specific locations in the earth's crust (Banks 2008). Ground

source heat may contain a component of genuine geothermal energy from deep-earth heat

flux, but will usually be dominated by solar energy that has been absorbed and stored in the

ground.

2.5.1.   Principle of the System

The idea of thermal storage dates back to ancient civilization. In 400 BC, Persian engineers

had mastered the technique of ice storage in the middle of summer in the desert. They

recognised that the underground is significantly cooler than the air during summer and could

be used to slow down the rate at which the ice melted. Therefore, in winter the ice was brought from nearby mountains and stored in a specially designed, passively cooled refrigerator, called a Yakhchal (meaning: ice store). 'Ice houses' and ice stores were also commonly used, in a similar manner, in the Europe before the invention of the refrigerator.

The Temperature of the Ground

In summer, the surface of the earth heats up due to solar radiation. This heating effect, due to the high heat capacity of rocks and soils, moves slowly in the ground. Therefore, below a few metres depth, the temperature of the subsurface is remarkably stable, at a value approximating to the long-term annual average surface temperature. Figure 2-8, which is an example for typical UK ground temperature variations, shows that annual temperature cyclic variations reduce as the depth into the ground increases and the peak become offset due to the slow movement of heat through the ground.
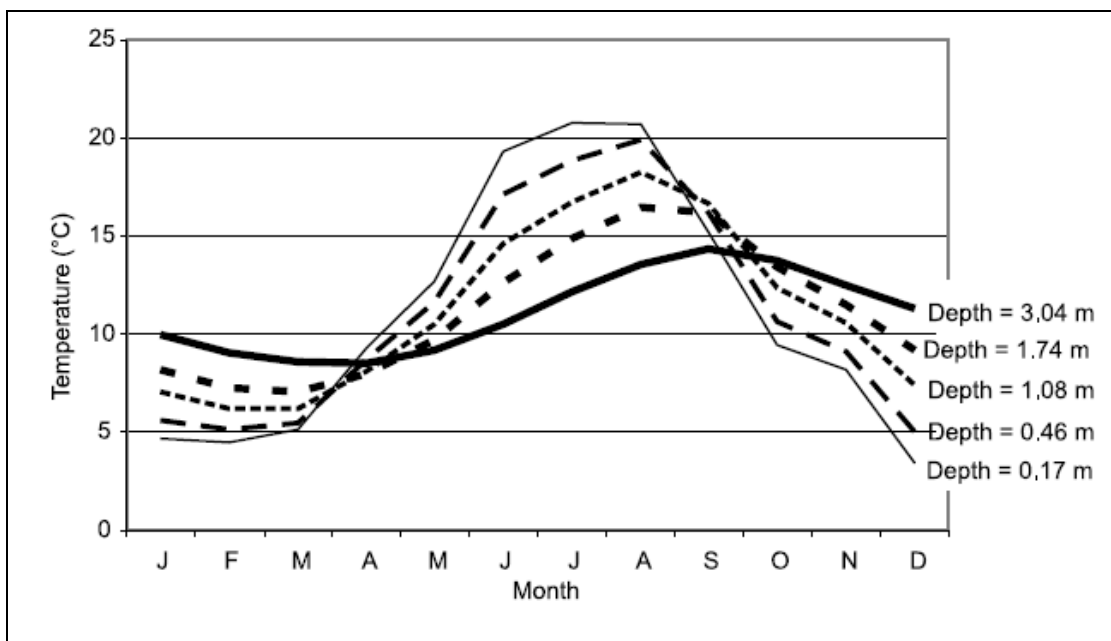
Figure 2-8 Seasonal temperature fluctuation at various depths (Banks 2008)

The use of rocks and soils in the subsurface as a huge thermal energy storage system allows storing solar energy and other surplus heat (e.g. heat loss from a building, discharged heat via water to the sewers, etc.) until a time when they are needed. In other words, the ground can be manipulated as a heat store; it can preserve summer heat until winter and winter cold until summer. Loops are installed underground to extract heat during winter (i.e.

underground temperature, in winter, is higher than ambient air) or reject heat during summer (i.e. underground temperature, in summer, is lower than ambient air). The transmitted heat to buildings can be used, either directly or in conjunction with a heat pump which is a device to transfer heat from a low temperature to a high temperature using mechanical work.

Types of Ground Source Heat Pump System

Ground Source Heat Pump (GSHP) systems can be classified generally as open or closed systems. In open systems groundwater is used as a heat carrier, and is brought directly to the heat pump, however, in summer (i.e. cooling mode) a heat pump does not necessarily need to be used and cool groundwater at 11°C can be circulated in a building to provide 'free' or 'passive' cooling (Banks 2008). The Ooms system, described in Section 2.4.2, is an example of an open system. On the other hand, closed systems normally consist of high strength polyethylene or polybutylene pipes and are located underground. A working fluid (a mixture of water and antifreeze) is circulated within the loops transporting heat from the ground to a heat pump (or vice versa). Closed-loop systems are of two types: direct circulation (Figure 2-9 right) and indirect circulation (Figure 2-9 left). In addition, closed loops, from a configuration point of view, could also be installed as a vertical system (i.e. boreholes) or horizontal system.
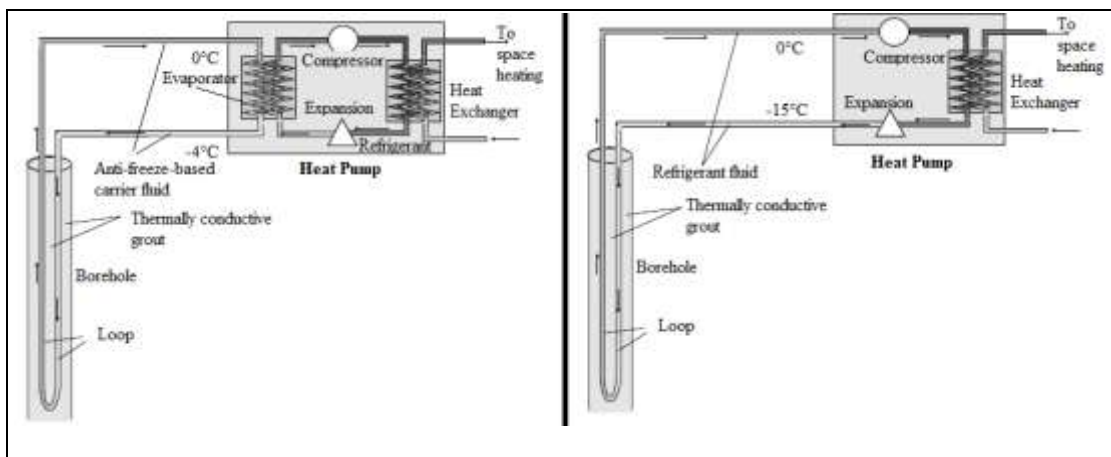
Figure 2-9 Schematic diagrams of an indirect (left) and direct closed-loop (right) installed in a borehole, Adapted from (Banks 2008)

2.5.2. Vertical Systems

Vertical loops, shown in Figure 2-9, are well suited when a land surface is limited or when minimum disruption of the landscaping is desired. Vertical boreholes are normally drilled to a depth of 45-150m and occupied with one or two U-bend loops at the bottom and then backfilled with thermal conductive grout to enhance heat transfer. Vertical systems are very efficient because the ground temperature is more constant deeper in the ground (see Figure 2-8). However, they are more expensive to install due to high drilling costs.

2.5.3. Horizontal Systems and Design Considerations

Higher cost associated with installation of a GSHP system is one of the main causes that prevents the wide adoption of these systems in the UK (Wu et al. 2010b). Therefore, horizontal systems have become increasingly important since they can reduce installation cost compared to that of vertical systems. In horizontal systems no drilling is necessary and horizontal loops, illustrated in Figure 2-10, are placed in trenches typically at a depth of 1 to 2 m (Banks 2008).

Although at many sites ground area is at a premium, but if a large amount of available space at a development site is available, horizontal trenched installations may be the cheapest means of installing a ground loop (Banks 2008; Egg and Howard 2011). Figure 2-11 shows that for a specific capacity of a heat pump, the cost of a 'slinky' horizontal system is significantly lower than that of vertical closed-loop systems (i.e. boreholes). Moreover, a report, produced by Edberg et al (2011), for the Department of Energy and Climate Change showed that for a 10kW capacity heat pump, horizontal slinky systems cost 65% less than vertical systems. In spite of having lower cost, horizontal systems have some disadvantages over vertical systems that need to be considered in their design processes. Those are: 1) horizontal systems are subjected to seasonal temperature variation at shallow depths, 2) a large ground area is required for adequate heat transfer, 3) the thermal properties of soil surrounding the loops fluctuate with seasons and influence the heat exchange efficiency.
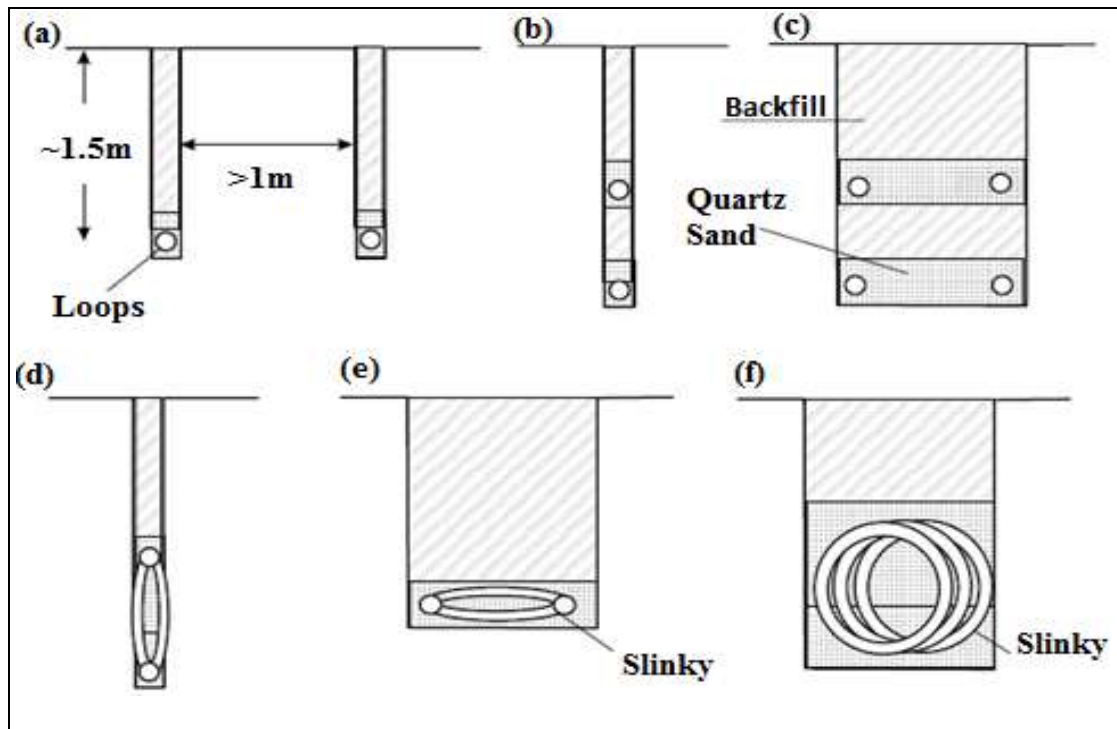
Figure 2-10 Possible configurations of horizontal ground loops in trenches: (a) single pipes in parallel trenches; (b) vertically installed double pipe system (flow and return); (c) 'square' four-pipe system (two flow, two return); (d) vertically installed slinky; (e) horizontally installed slinky; and (f) three-dimensional spiral slinky, Adapted from (Banks 2008)
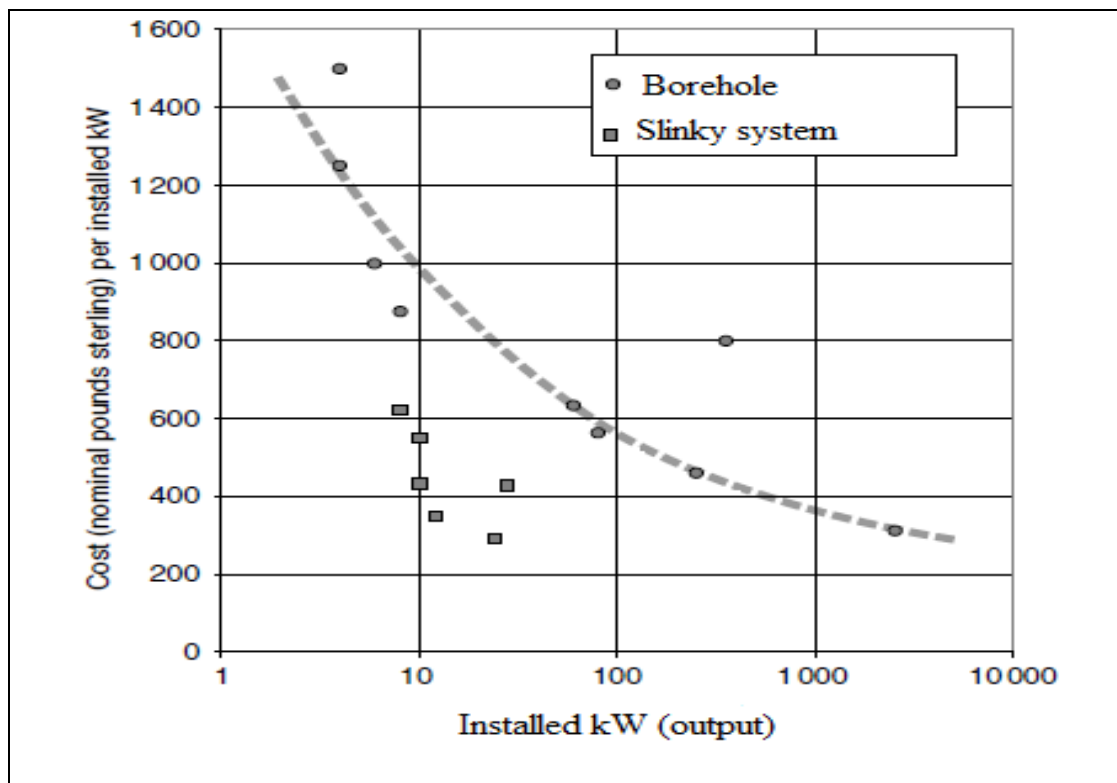
Figure 2-11 The cost, per installed kW, of borehole and horizontal (slinky) systems, Adapted from (Banks 2008)

Design Considerations

The performance of a heat pump is usually expressed in terms of its Coefficient Of Performance (COP) which is the ratio of energy output to supplied energy (electricity for the compressor, pump, etc.) of a GSHP. A typical heat pump has a COP of around 4 which indicates that the heat pump produces four units of heating energy for every unit of electrical energy input. GSHPs are generally considered as three major parts namely: heat pump, ground loops, and an interior heating or cooling distribution system. There are many parameters that influence the COP and the installation cost of the system. The effects of parameters on the ground loops part of the system are discussed in below.

Depth of pipe burial

Horizontal loops should be buried at an optimum depth such that loops are isolated from diurnal temperature fluctuations and frost formation (Banks 2008). In addition, for all horizontal systems in heating-only mode, the main thermal recharge is provided by the solar radiation falling on the ground surface; therefore, it is important not to cover the ground surface above the loops. Inalli and Esen (2004) carried out experimental measurements of a horizontal GSHP system in selected depths of 1 and 2 m in Turkey. They found that, after running the system for heating from November 2002 to April 2003, deeper loop installation can improve the COP of the system by 5%.

The required pipe length

The require pipe length in a GSHP system is important because it dictates the materials and land needed to install the system and therefore, affecting the installation cost. A parameter used to calculate the required length of a trench (or borehole) is the specific heat extraction, expressed in Watt per meter length. Typical values are in the range from 40 to 70 W/m for vertical systems, depending on soil thermal conductivity, heat pump annual operation, and number of neighbouring boreholes (European Geothermal Energy Council 2008).

Typical values for horizontal systems can be obtained from Figure 2-12 for different loop configurations (see Figure 2-10 for loop configuration) (Banks 2008). Figure 2-12 shows

that single pipes may extract 20-30 W/m at 1m spacing, while slinky pipes may support 50-100 W/m at 3-5m spacing. In addition, Wu et al. (2010b) by numerical simulation found that heat extraction per meter length of soil drops significantly at the beginning of system operations. However, heat extraction rate reaches a steady-state where it ranges from 25 to 35 W/m for an extended slinky loop (i.e. coils not overlap) and 15-20 for a single loop at 1m spacing (see Figure 2-13). It must be noted that, these values are representative of a normal soil and the extracted heat per unit length of a trench may increase by enhancing the heat transfer between loops and surrounding materials.
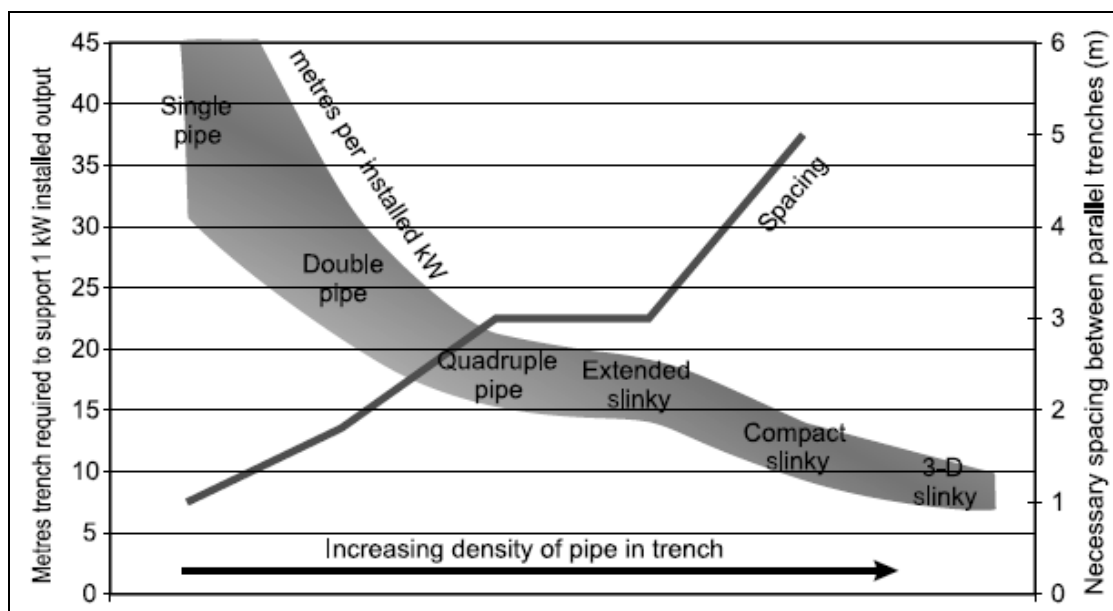
Figure 2-12 A relationship between the lengths of meters of trenches and heat extraction for different loop configuration, Adapted from (Banks 2008)
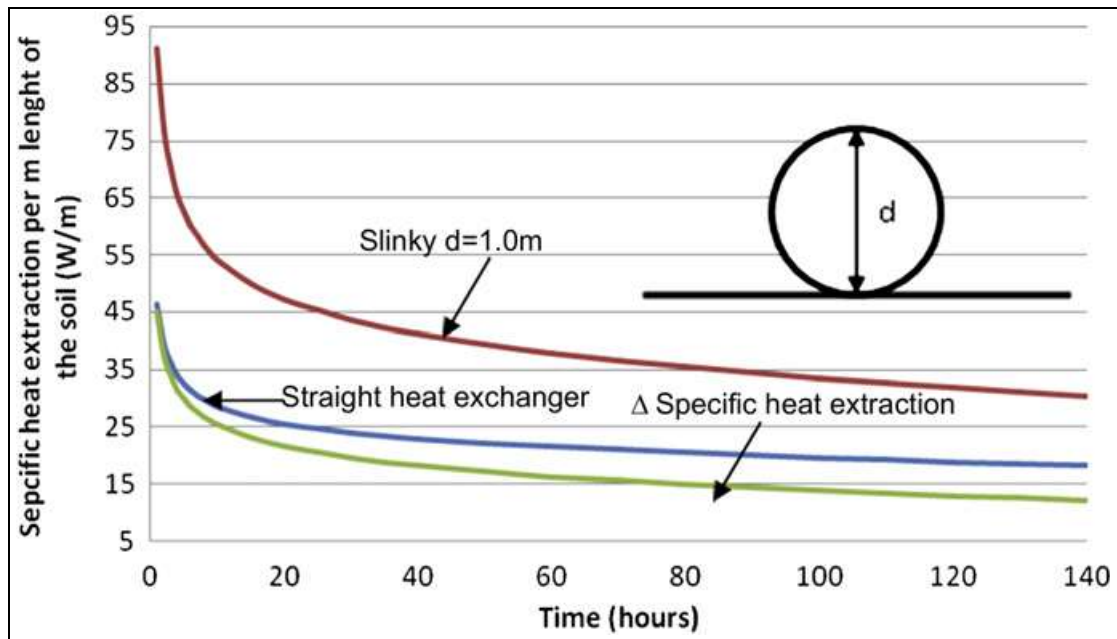
Figure 2-13 Variation of the heat extraction per meter length of soil by straight and slinky loops, Adapted from Wu et al. (2010b)

Tarnawski et al. (2009b) simulated COP of a GSHP with a single pipe of variable length buried at the depths of 0.5 and 1.0 m (see Figure 2-14). They concluded that although the COP increases with the pipe length, there is an optimum length beyond which it is not cost-effective to increase the pipe length. For example, in Figure 2-14, the COP rise associated with a 1000 m length compared to length of 300m is only 10%, while the pipe length increase is 233%.
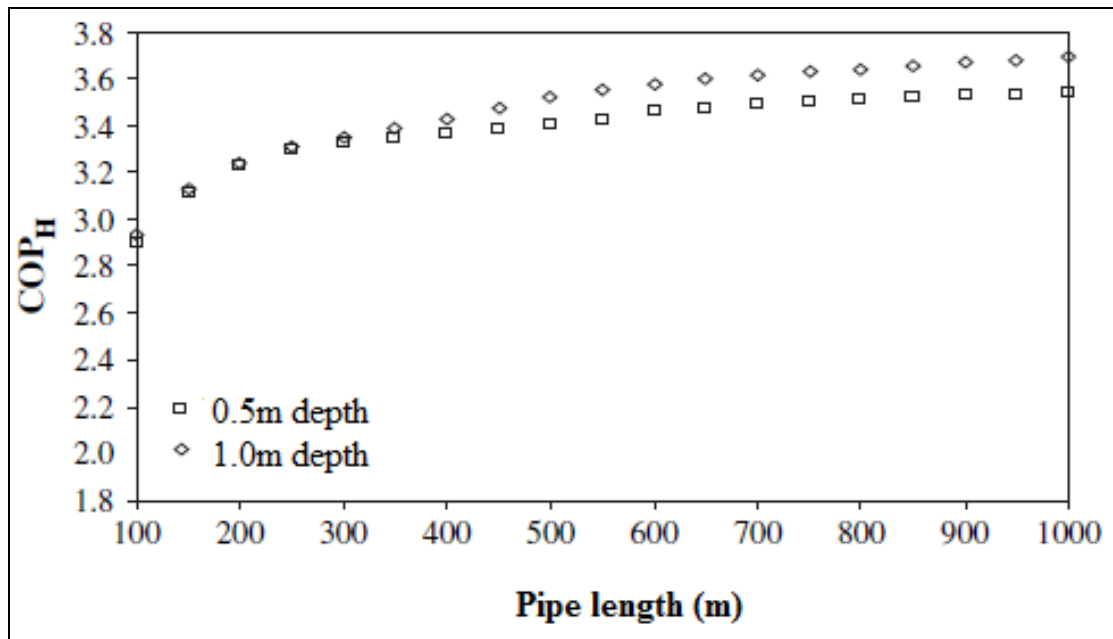
Figure 2-14 COP variation with pipe length and burial depth, Adapted from (Tarnawski et al. 2009b)

<u>Soil thermal properties</u>

Heat transfer process between the ground and the loops is an important aspect of ground loop design. However, it is the least understood aspect of GSHP system design because there are many factors affecting the ground's thermal properties and so few measured data available (ASHRAE 1995; Rawlings and Sykulski 1999). The rate of heat extraction, and ultimately the size of the loop and cost of the system, significantly depends on the thermal properties of the soil. The transfer of heat between the loops and the surrounding soil is primarily by heat conduction and to a certain degree by moisture migration (Leong et al. 1998). The higher the conductivity of the soil, the higher the rate of energy extraction from the soil and therefore, a smaller loop size will be required. The thermal conductivity of soils depends on many factors such as; mineral composition, porosity and water content, size, shape, texture, and arrangement of particles.

Quartz has a thermal conductivity, at around 8 W/m K, several times higher than that of other common rocks forming minerals (Banks 2008). Thus, the thermal conductivity of rocks and soils depends to a large extent on their quartz content. The higher the quartz

content of a soil, the higher the thermal conductivity of the soil (Leong et al. 1998; Côté and

Konrad 2005; Tarnawski et al. 2009a).

Moisture content of soil is another important factor that affects the thermal properties of soil

and subsequently, the performance of a GSHP system. Ewing and Horton (2007) illustrated

that (Figure 2-15) the added water to soil provides a thermal bridge between particles and

therefore, increases the total heat transfer. Leong et al. (1998) have simulated the effect of

soil type and moisture content on the heat extraction rate in the GSHP systems. A graph

from their study is shown in Figure 2-16. They concluded that the average heat extraction

and hence the performance of a GSHP system significantly increases as moisture content

and quartz content in the soil increase. They added that alteration of soil moisture content

from complete dryness to 12.5% saturation strongly influences the GSHP performance, and

any decrease of soil moisture in this range has a devastating effect on the COP.
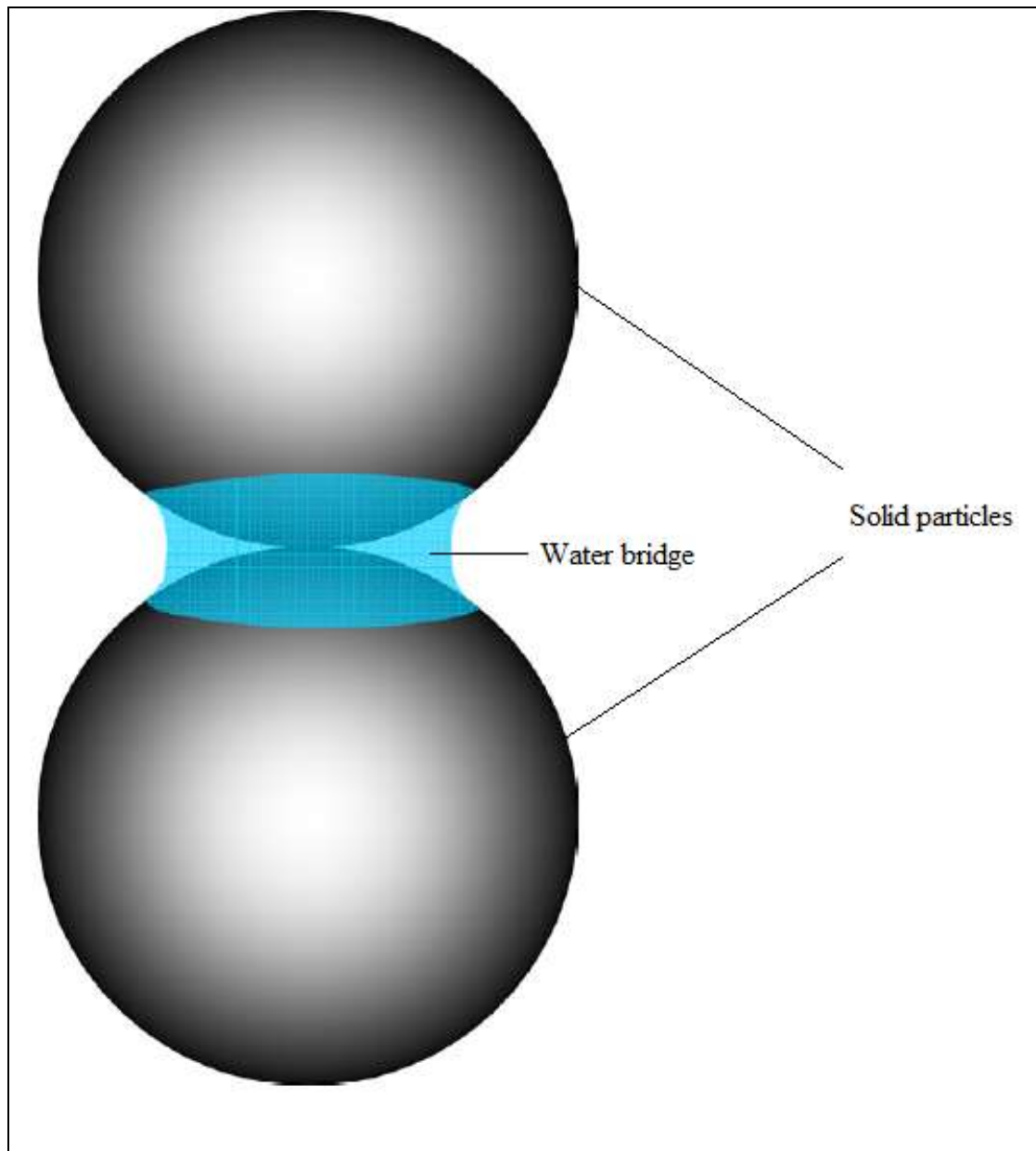
Figure 2-15 A capillary bridge between two touching solid particles, Adapted from (Ewing and Horton 2007)
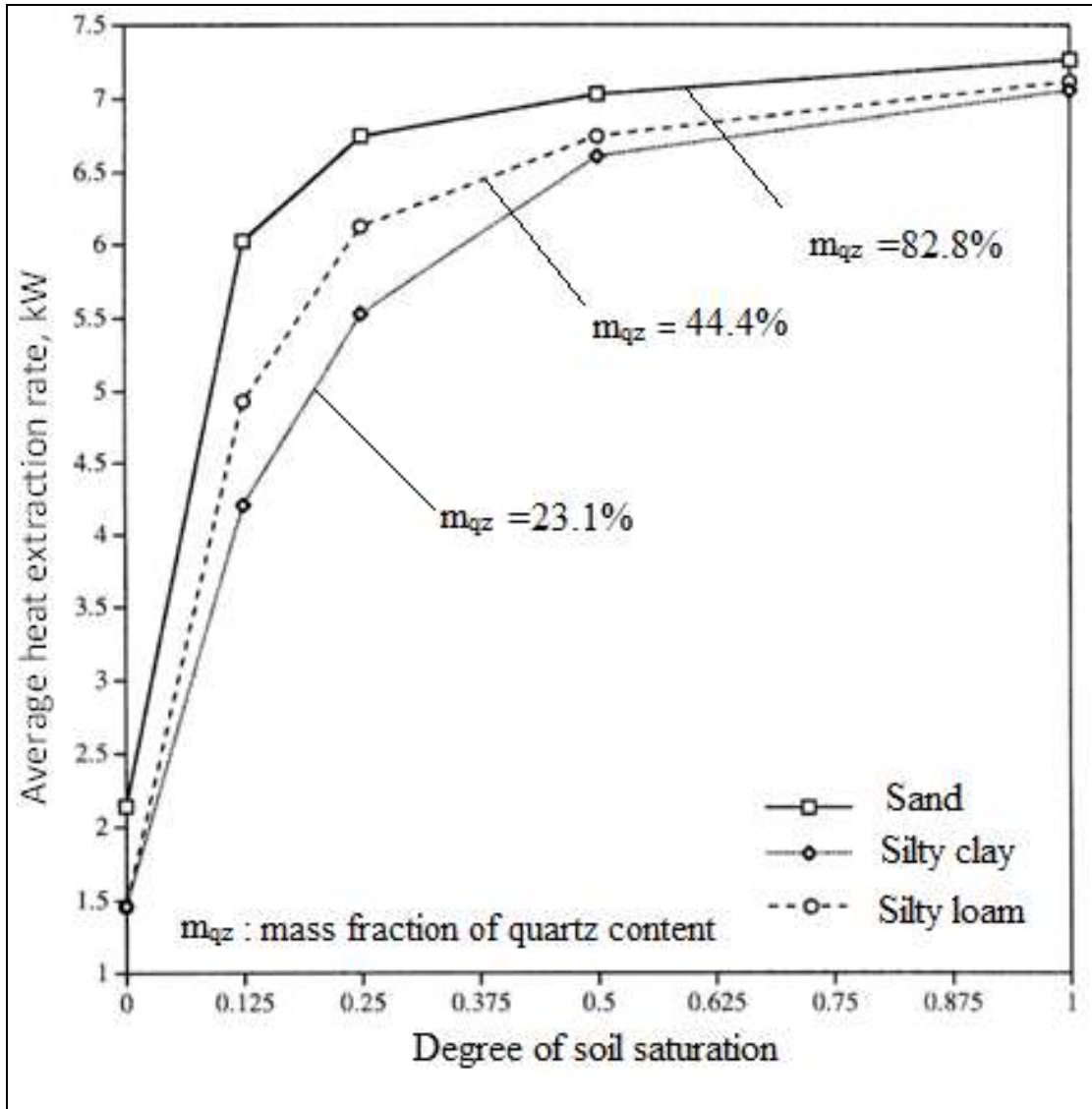
Figure 2-16 Variation of the average heat extraction rate versus soil type and moisture content, Adapted from (Leong et al. 1998)

2.6. Other Heat Storage Technique

Physical thermal energy storage technologies can be divided into two categories; sensible and latent (Mehling and Cabeza 2008). Sensible heat storage is by far the most common method for heat storage, which is by changing the temperature of a storage material (see Figure 2-17), for example high-grade heat storage (e.g. hot water, steam) or low-grade GSHP system described in Section 2.5. Heat may also be absorbed, stored or released from a material at an almost constant temperature (see Figure 2-17) due to the high latent heat of solid-liquid phase change.
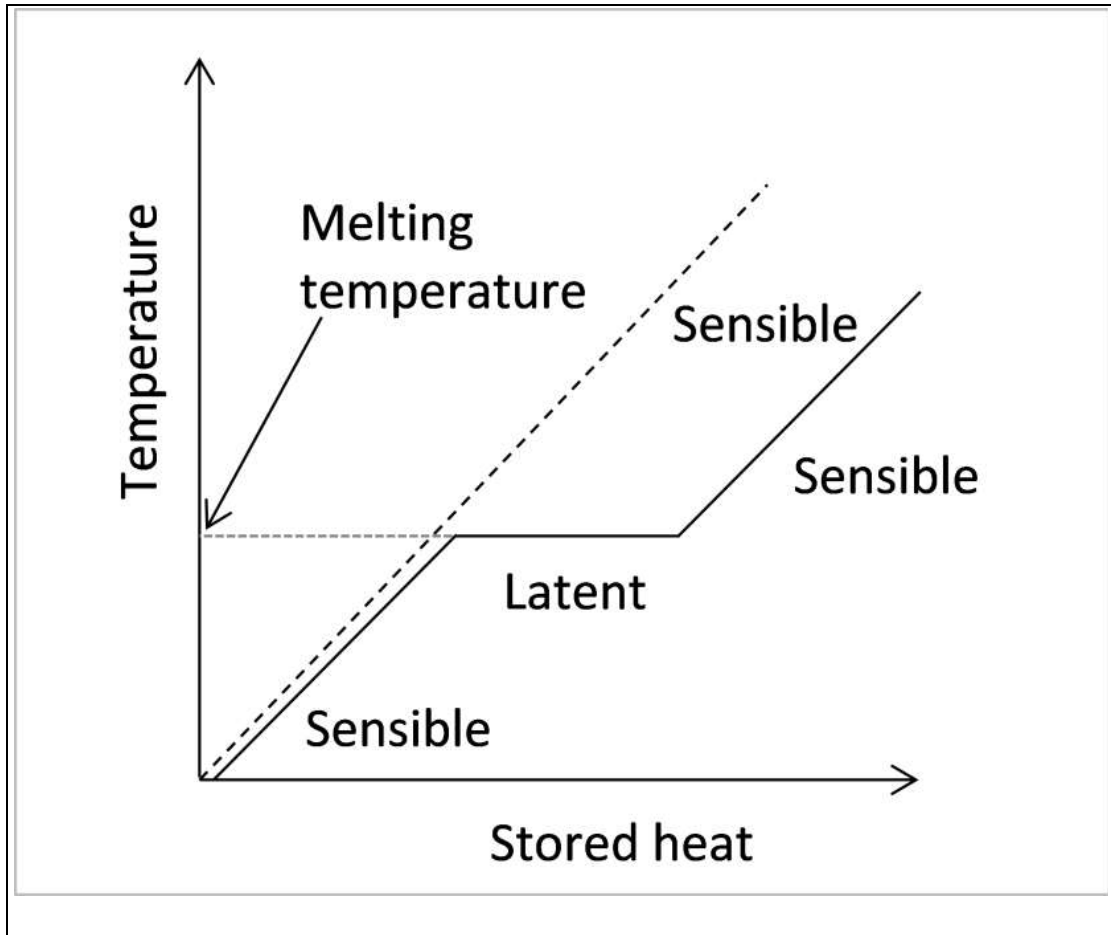
Figure 2-17 Sensible and latent heat storage, Adapted from (Mehling and Cabeza 2008)

2.6.1. Phase Change Materials (PCMs)

Phase Change Materials (PCMs) are substances with a high 'latent heat', H_{melt} (i.e. heat of fusion) which control the melting and solidifying at a certain temperature (i.e. 'melting point', T_{melt}). They are capable of storing and releasing large amounts of energy at a narrow characteristic temperature which can be selected to suit operating temperatures in any particular engineering application.

In the context of this research, PCMs are limited to materials that change their state from solid to liquid and back again. PCMs are generally classified as organic, inorganic, and eutectic (a mixture of organic and inorganic). Although inorganic PCMs have a much greater thermal storage capacity over organics ones, but they are not normally used in conjunction with metals and building construction materials because of their corrosion

potential (Mehling and Cabeza 2008). On the other hand, organic materials including paraffin and non-paraffin based materials are widely used in building materials. Organic PCMs can be manufactured with melting temperatures ranging from about 5°C to 200°C and latent heat ranging from 150 to 350 kJ/kg.

Table 2-4 gives a comparison between typical storage densities of different energy storage methods. As Table 2-4 shows, PCM can store about 2 to 4 times more heat per volume than is stored as sensible heat in liquids or solids over a temperature interval of 20°C.

Table 2-4 Comparison of typical storage densities of different energy storage methods, Adapted from (Mehling and Cabeza 2008)

Material	Sensible heat (kJ/kg)	Latent heat (kJ/kg)	Temperature (°C)
Granite (density~2650 kg/m^3)	17	-	$\Delta T = 20°C$
Water (density~1000 kg/m^3)	84	330	$\Delta T = 20°C$ $T_{melt} = 0°C$
Paraffin (density~900 kg/m^3)	-	~200	$T_{melt} = 5°C-130°C$

PCMs, in most cases, need to be encapsulated in order to hold the liquid phase of PCM and to avoid contact of the PCM with the environment. Encapsulations are usually classified by their size into macro- and microencapsulation. Macroencapsulation means filling the PCM in a macroscopic containment that fit amounts from several ml up to several litres. Microencapsulation is the encapsulation of solid or liquid particles of 1 μm to 1000 μm diameter with a solid shell, which can either be in bulk powder form or in colloidal suspension.

2.6.2. Applications of PCMs

The use of PCM for energy storage in GSHP systems, described in Section 2.5, has not been reported however, some similar applications of PCMs for energy storage will be reviewed. Potential applications for PCMs include stabilisation of temperature as well as storage and

supply of heat at relatively small temperature differential. PCMs have been in use for many years, from their use in the transport of food, beverages, medicine and electronic equipment (Mehling and Cabeza 2008), to being used as thermo regulators in textiles (Sánchez et al. 2010). PCMs have been considered for thermal storage and temperature regulation in building materials since before 1980. They can be impregnated into gypsum wallboards (Athienitis et al. 1997), and concrete (Zhang et al. 2004; Bentz and Turpin 2007; Cabeza et al. 2007; Hunger et al. 2009; Entrop et al. 2011).

Athientis et al. (1997) showed that utilisation of gypsum board containing 25wt.% Butyl stearate as a PCM material in passive solar buildings can reduce maximum room temperature by about 4°C during the daytime. In addition, Cabeza et al. (2007) presented an experimental study of two full size concrete test buildings, one of which included 5wt.% microencapsulated PCM (H_{melt} = 250 kJ/kg, T_{melt} = 26°C) in the concrete walls. They found that, the concrete room without PCM had a maximum indoor dry bulb air temperature about 1°C higher than the room with PCM, and a minimum temperature 2°C lower (see Figure 2-18).

Bentz and Turpin (2007) proposed the idea of using PCM-modified concrete to reduce the number of freeze/thaw cycles in concrete bridge decks. They showed, by numerical simulations, that 15wt.% microencapsulated PCM-modified concrete (H_{melt} = 250 kJ/kg, T_{melt} = 5° C) could potentially reduce the number of freeze/thaw cycles by up to ~30% compared to a plain concrete (control). Hunger et al. (2009) investigated the mixing rheology, hydration, and post-hardening properties of self-compacting concrete modified with microencapsulated PCM. Numerical modelling and experimental results showed that the peak hydration temperature in concretes could be reduced by up to ~28% with 5wt.% PCM addition (H_{melt} = 100 kJ/kg, T_{melt} = 23° C).

Entrop et al. (2011) studied the use of microencapsulated PCMs to store solar energy in concrete floors and to save energy in Dutch houses. They experimentally compared the floor temperature variations in a control concrete and in a 5 wt.% PCM-modified concrete (H_{melt} = 110 kJ/kg, T_{melt} = 23ºC) and concluded that the application of PCMs in concrete floors resulted in a reduction of maximum floor temperatures up to 16% and an increase of minimum temperatures up to 7%.
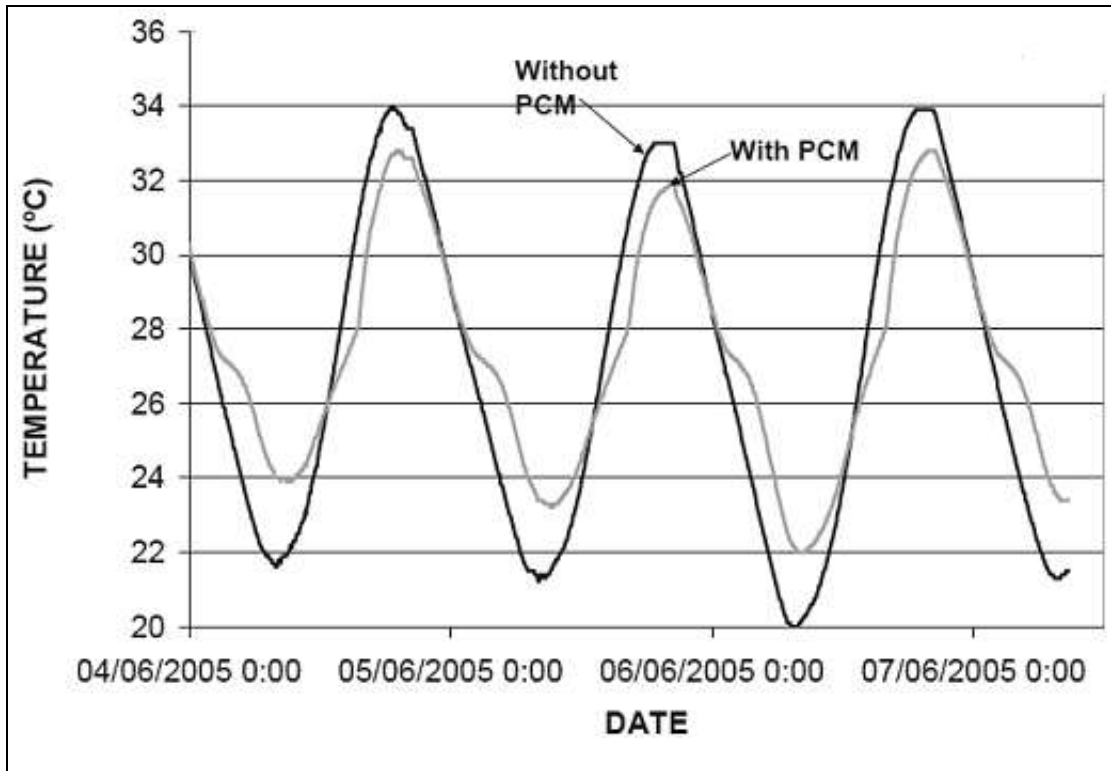
Figure 2-18 Temperature buffering using PCM in a concrete wall (Cabeza et al. 2007)

2.7. Thermo-physical Properties of Pavements Materials and Measuring Techniques

The rate at which heat energy is transferred to the loops depends on the materials' thermo-physical properties. The three most important properties of a material in a thermal analysis are the thermal conductivity, specific heat capacity, and density. Factors affecting the thermo-physical properties of pavement materials and mixes as well as their measuring techniques are reviewed.

2.7.1. Thermal Conductivity

As mentioned in Section 2.3.1, Page 12 thermal conductivity describes a material's ability to conduct heat and can be defined as *"the rate of heat transfer through a unit thickness of the material per unit area per unit temperature difference"* (Cengel 2002). A material with high thermal conductivity will allow heat to conduct easily (Conductor), while one with a low value will hinder the conduction (Insulator).

Measurement of Thermal Conductivity

According to 'Fourier's law' (see Eq. 2-1, Page 13) the measurement of thermal conductivity always involves the measurement of the heat flux and temperature difference. Two classes of methods are normally used to measure the thermal conductivity of building materials; steady-state methods and transient methods. Steady-state techniques perform a measurement when the temperature across a sample does not change with time while the transient techniques perform a measurement during the process of heating up. Many different types of apparatus for measuring thermal conductivity have been reported in the literature that it would be impractical to review all of them here. Instead, some typical apparatus used to measure thermal conductivity of concrete, asphalt, and crushed aggregates are reviewed here.

Steady-state methods

Mrawira and Luca (2002) designed an apparatus, based on the steady-state method, to measure the thermal conductivity of asphalt pavement slabs. In their apparatus, the slab with known dimensions was placed between a heat emitter and a heat receiver plate and insulated from the other edges. They measured the thermal conductivity of the slab based on the 'Fourier's equation' (Eq. 2-1) from knowing the dimension of the slab, magnitude of heat flux generated by heat emitter, and temperature gradient across the specimen.

Somerton (1992) and Côté and Konrad (2005) applied a comparative technique to measure the thermal conductivity of crushed aggregates. In their apparatus, shown in Figure 2-19, a

sample of known dimensions is sandwiched between two samples of known dimensions and thermal conductivities. Knowing the dimensions of sample, dimensions of the reference materials, thermal conductivities of reference materials and temperature gradient across them, the thermal conductivity of sample can be calculated by using the equation shown on Figure 2-19.

The accuracy of steady-state methods, explained in above, largely depends on controlling edge heat losses/gains. In addition, sample preparation is usually time consuming and needs careful consideration. Somerton (1992) added that steady-state methods require long periods of time to achieve equilibrium conditions but results are generally more accurate than transient methods.

$$\lambda = \lambda_{ref} \, (\Delta T_{ref}/d_{ref}) \, (d/\Delta T)$$
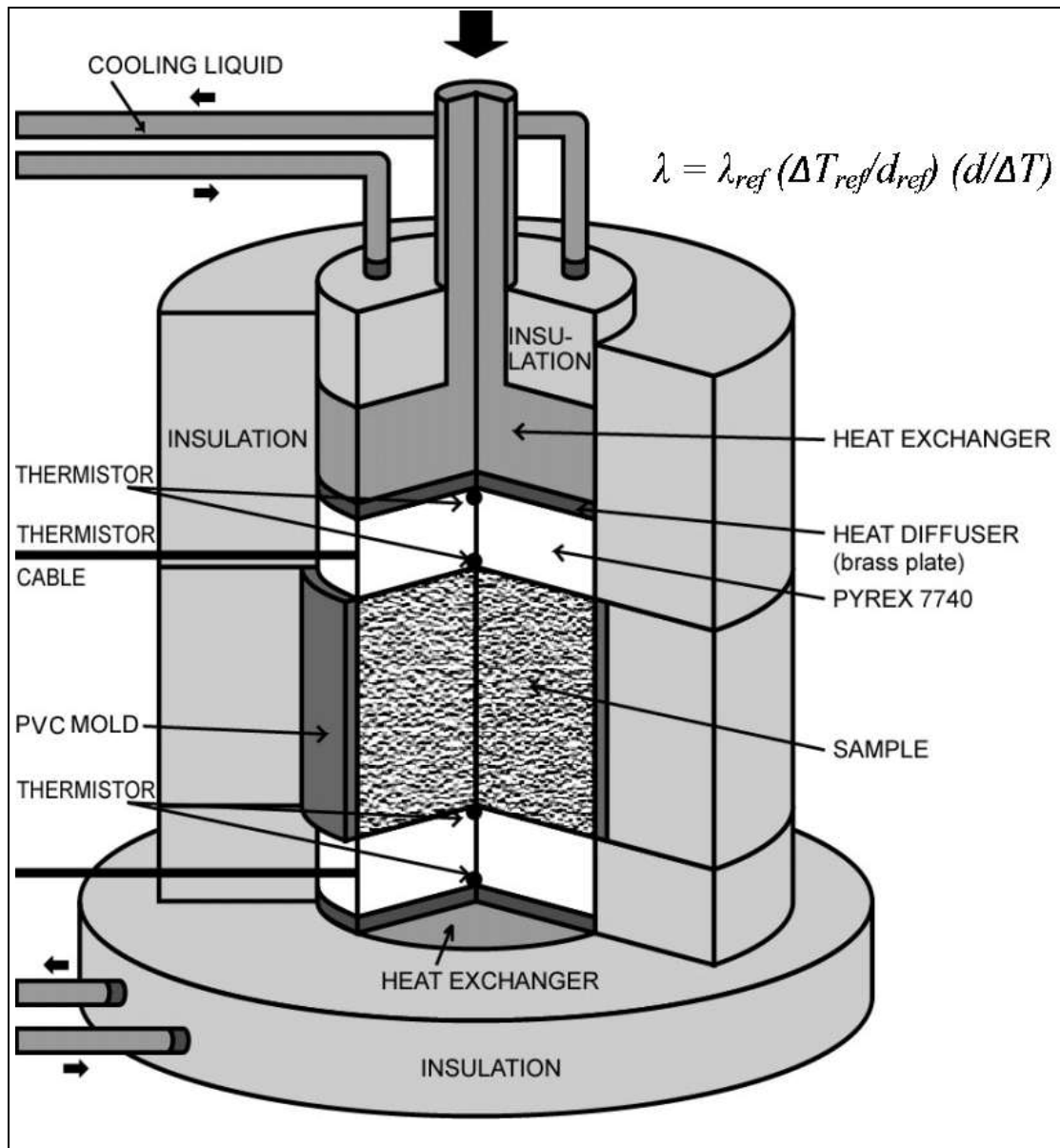
Figure 2-19 Comparative technique to measure the thermal conductivity, Adapted from (Côté and Konrad 2005)

<u>Transient methods</u>

Hot Wire Method (HWM) and Transient Plane Source (TPS) method are transient techniques for measuring the thermal conductivity of materials. The HWM has been used by some researchers to measure the thermal conductivity of concrete (Demirboga and Gül 2003; Uysal et al. 2004; Demirboga 2007). In this method an electrically heated wire is inserted into a material and heat flows out radially from it. The thermal conductivity of material can then be computed from the relationship between the wire temperature and the

time passed since starting. In the TPS method, heat flow emanates from a circular heating

element and temperature is monitored over time (Benazzouk et al. 2008).

All transient methods normally suffer from contact resistance problems, especially in

applications where it is necessary to drill a hole to insert the probe (Somerton 1992).

Transient methods also have the disadvantage of being unsuitable for non-homogeneous

materials (Hilton Ltd 1994) and may not give a representative thermal conductivity value of

the whole sample.

Heat Flow Meter (HFM) method

The HFM method, introduced in ISO 8301 (1996), is a comparative technique and uses the

steady-state approach to measure the thermal conductivity of building materials. In this

method, a specimen is placed between a hot plate and a heat flow meter which is attached to

a cold plate (see Figure 2-20). The hot and cold plates are maintained at suitable constant

temperatures, measured by surface thermocouples. Thermal conductivity will be measured

by a set of calibration constants, derived from testing a sample of known thermal

conductivity, as well as heat flow meter output and the mean temperature the hot and cold

plates. Hall and Allinson (2008; 2009) and Phillipps (2007) applied this technique to

measure the thermal conductivity of pavement materials. The advantage of the HFM method

over the conventional steady-state method is that the heat flow through the specimen is

measured directly and no estimation of the heat loss/gain is necessary. Therefore, the limits

of accuracy of the thermal conductivity values measured by the HFM apparatus are

considered to be ±2-3% of the absolute magnitude. In this study, the HFM method is

selected to determine the thermal conductivity of pavement materials and mixes, more detail

of the test is given in Section 3.4.
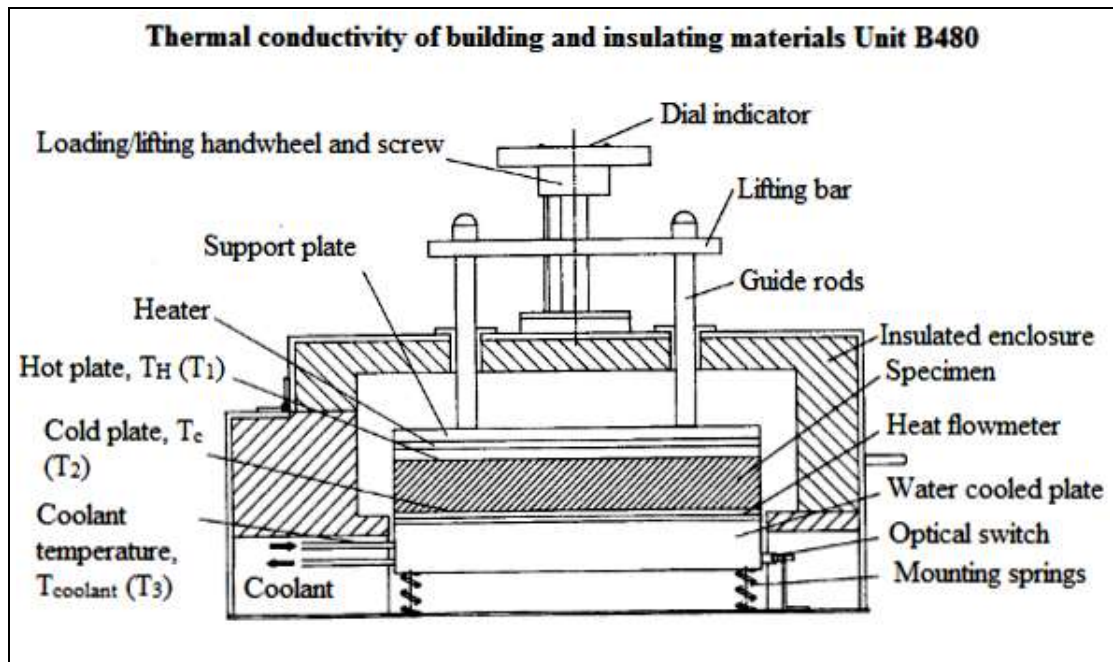
Figure 2-20 Cross-sectional diagram of the B480 heat flowmeter apparatus, Adapted from (Hilton Ltd 1994)

Indirect method

Thermal conductivity of building materials could also be determined indirectly by measuring the thermal diffusivity, specific heat capacity, and density of the materials. This method is explained in Section 2.7.3.

Factors Affecting Thermal Conductivity

Aggregate type and content

A large proportion of a pavement structure is constituted of aggregate; therefore, they have a significant effect on the thermal conductivity of pavement mixes. As mentioned in Section 2.5.3, Page 25, quartz has the highest thermal conductivity in rock forming minerals. Higher quartz content in aggregates will increase the thermal conductivity of aggregates and subsequently the pavement. The thermal conductivity of the aggregates that are commonly used in pavement structures (O'Flaherty 2002) along with other pavement constituents are tabulated in Table 2-5.

Table 2-5 Thermal conductivity of some pavement constitutions (Sundberg 1988; Somerton 1992; Read and Whiteoak 2003; Banks 2008; Busby et al. 2009)

Aggregates/Pavement constituents	Range of thermal conductivity (W/m K)
Quartzite	5.5-7.5
Granite	3.0-4.0
Limestone	1.5-3.0
Basalt	1.3-2.3
Bitumen	0.15-0.17
Cement	0.29
Water	0.6
Air	0.024

An experiment was carried out by Khan (2002) on the influence of coarse aggregate on thermal conductivity of concrete. The experimental values show that quartzite aggregates produced the most conductive concrete and that is ~50% more conductive than limestone concrete. In addition, Côté and Konrad (2005) investigated the thermal conductivity of compacted coarse base-course materials used in pavements. Figure 2-21, is a graph taken from their study, and shows for similar dry density, thermal conductivity of compacted aggregates largely depends on the thermal conductivity of solid particles and quartzite aggregates produced the highest thermal conductivity.
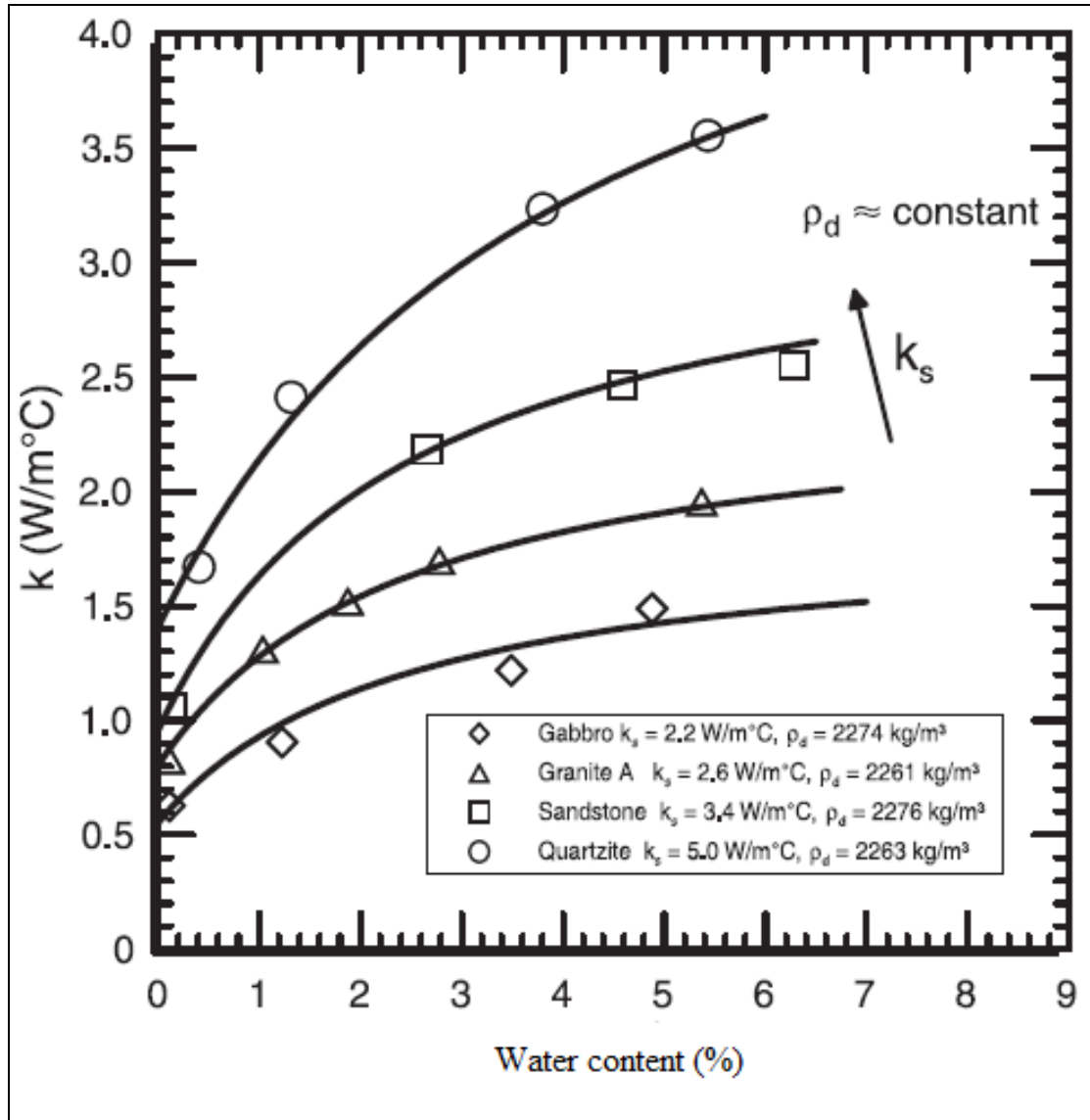
Figure 2-21 Thermal conductivity of base-course pavement materials as a function of water content and thermal conductivity of solid particles (Côté and Konrad 2005)

Use of Light-Weight Aggregates (LWA) (aggregates with an average particle density <2000 kg/m³) in concrete productions can offer many advantages such as reduction of dead load (i.e. lower density) and high thermal insulation. Such aggregates, due to their process of formation, have a high pore volume which has the potential to provide concrete and asphalt with a higher thermal resistance than with low porosity/non-porous aggregates. Research has shown that the thermal conductivity of light-weight concretes (i.e. concretes produced with LWA) is considerably lower than that of normal concretes (Demirboga and Gül 2003; Ünal et al. 2007).

Amount of aggregate in a mixture is another factor that influences the thermal conductivity of pavement mixes. Results of an experiment carried out by Kim et al. (2003) showed that the thermal conductivity of concrete specimens is positively related to the volume fraction of aggregate in the mix.

Additions and admixtures

Cook and Uher (1974) investigated the effect of copper and steel fibre (0.8 mm in diameter and 25 mm long) on the thermal conductivity of concrete. The results indicated that copper fibres significantly increase the density and thermal conductivity of the concrete while steel fibres have a lesser effect (see Figure 2-22). In addition, Lie and Kodur (1996) experimentally showed that 1.7 wt.% steel fibres (0.9 mm diameter and 50 mm long) increases the thermal conductivity of concrete from 1.4 to 2.1 W/m K. On the other hand, Fu and Chung (1997) experimentally found that the addition of 0.5-1 wt.% short carbon fibre (10 μm in diameter and 5 mm long) to cement paste did not increase the thermal conductivity of the cement paste due to the increase of air void content (reduction in density) in the cement paste.
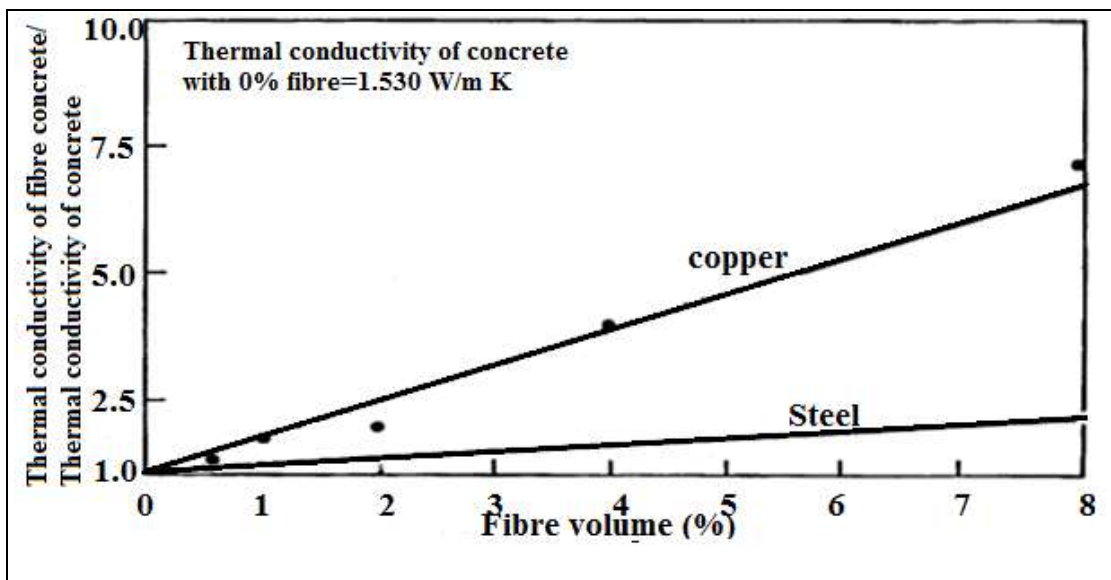
Figure 2-22 Effect of steel and copper fibre reinforcement on thermal conductivity of concrete, Adapted from (Cook and Uher 1974)

Although addition of metallic fibres could enhance the thermal conductivity in pavements, some researchers found that the addition of conductive metallic particles has not improved

the thermal conductivity of pavements. Phillipps (2007) found that the addition of raw iron shots in asphalt mixes had no significant effect on the thermal conductivity improvement of the mix. A similar conclusion was achieved by Mallick et al. (2008) where they added copper powder into an asphalt mix. Mallick et al. (2008) added that it could be because of the copper was covered with asphalt during mixing and also was partially oxidized during the heating of the aggregates prior to mixing.

<u>Density and porosity</u>

Thermal conductivity, for the same materials and mixes, increases with an increase of density and decrease of porosity (air voids) (Côté and Konrad 2005; Canakci et al. 2007; Benazzouk et al. 2008). The increase of density in a mix will increase the contact surface between the aggregate particles and, hence, this can be expected to increase the thermal conductivity.

<u>Moisture content</u>

As previously mentioned, in Section 2.5.3 (see Figure 2-15, Page 32), thermal conductivity increases as moisture content in pavement materials and mixes increases (Kim et al. 2003; Côté and Konrad 2005; Canakci et al. 2007; Hall and Allinson 2009). This can be attributed to changes in air voids filled with water, whose thermal conductivity is superior to that of air.

2.7.2. Specific Heat Capacity

The specific heat capacity is defined as the energy required to raise the temperature of a unit mass of a substance by one degree. The relationship between change in heat content and change in temperature of a body of mass, m (kg) is generally expressed as follows:

$$\Delta Q = mc_p\Delta T \qquad \qquad \text{Eq. 2-5}$$

where;

ΔQ=Heat gain or loss (J)

m= Mass (kg)

c_p= Specific heat capacity (J/kg K)

ΔT=Temperature change (k)

The specific heat capacity can also be expressed in terms of Volumetric Heat Capacity (VHC) (J/m^3 K) as follows:

VHC= Density (ρ) $\times$ Specific heat capacity (c_p)

Measurement of Specific Heat Capacity

The specific heat capacity of pavement materials and mixes can simply be measured by means of a colorimeter and monitoring heat fluxes and temperature changes (Asaeda et al. 1996).

The specific heat capacity can also be accurately measured using a Differential Scanning Calorimeter (DSC) (Xu and Chung 2000; Vosteen and Schellschmidt 2003). The advantage of this technique is a higher accuracy of determination of the heat capacity of materials (Mehling and Cabeza 2008). By using this technique, the temperature-dependant specific heat capacity of materials can also be determined. In this study, the DSC technique is selected to determine the specific heat capacity of pavement materials, therefore more detail of the test is given in Section 3.4.

Specific heat capacity of a specimen could also be determined from its value of thermal conductivity, thermal diffusivity, and density (dos Santos 2003) (see Section 2.7.3 for more details). The accuracy of the specific heat capacity value using this method largely depends on the methods used to determine the values of other thermal properties.

The total specific heat capacity of a mixture can then be calculated as the sum of the heat capacities of the constituent parts weighed by their relative proportions (Sundberg 1988; Somerton 1992; Hall and Allinson 2008).

2.7.3. Thermal Diffusivity

Thermal diffusivity (α) is the coefficient that expresses the rapidity of temperature change when a material is exposed to a fluctuating thermal environment and is calculated as:

$$\alpha = \frac{\lambda}{\rho c_p}$$

Eq. 2-6

where

α= thermal diffusivity (m^2/s)

ρ= density (kg/m^3)

The larger the thermal diffusivity, the faster the propagation of heat into the medium. A small value of thermal diffusivity (i.e. high volumetric heat capacity and low thermal conductivity) means that heat is mostly absorbed by the material and a small amount of heat will be conducted further.

Asaeda et al. (1996) and Mrawira and Luca (2002) applied an experimental setup (see Figure 2-23) to measure the thermal diffusivity of pavement mixtures. In this method at least three thermocouples are positioned at equal distances. By applying the heat source on top of the specimen and recording the temperature change with time, the thermal diffusivity could be calculated using the following equation.

$$\alpha = \frac{(T_m^{i+1} - T_m^i)}{(T_{m+1}^i + T_{m-1}^i - 2 \times T_m^i)} \times \frac{\Delta z^2}{\Delta t}$$

Eq. 2-7

where

α= thermal diffusivity (m^2/s)

Δz= depth increment (m)

Δt= time increment (s)

i= time node

m=depth node
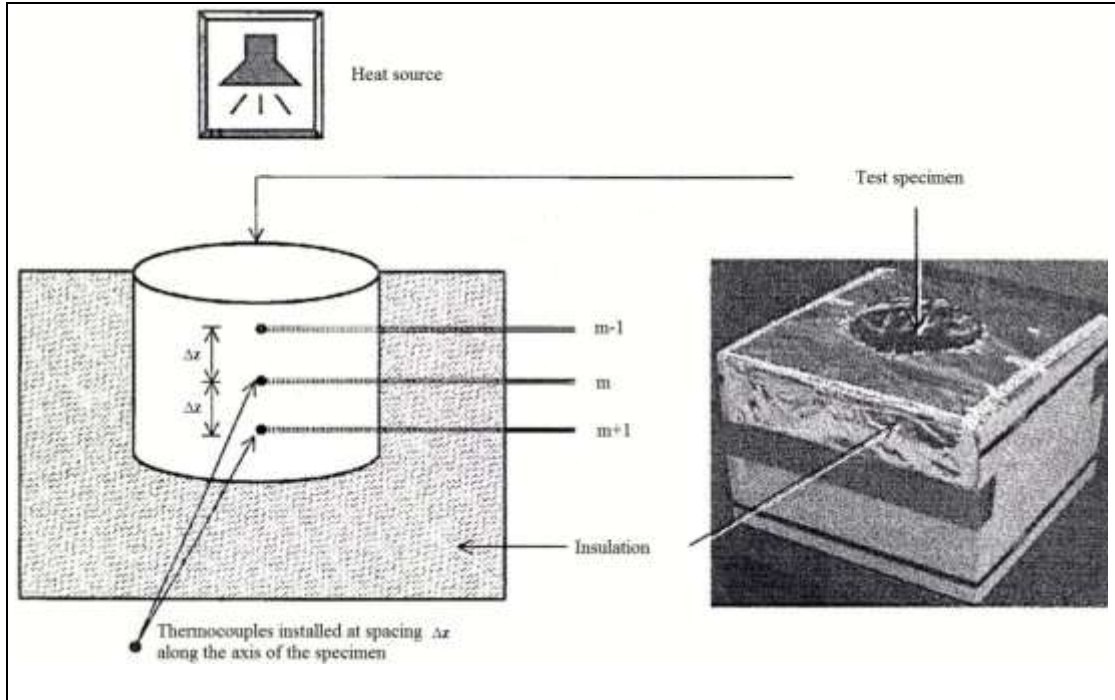
Figure 2-23 Test setup for thermal diffusivity measurement, Adapted from (Mrawira and Luca 2002)

2.7.4. Thermal Effusivity

Thermal effusivity (β), also known as the coefficient of heat storage, is a measure of material's ability to exchange heat with its surroundings and is calculated as follows:

$$\beta = \sqrt{\lambda \times \rho \times c_p}$$

Eq. 2-8

where

β= Thermal effusivity (J/s$^{0.5}$m^{2}K)

A large value of thermal effusivity indicates both large storage capacity and efficient heat transfer.

2.8. Discussions and Summary

The following key points have been drawn based on the literature search reported in this chapter and some information given earlier in Chapter 1 of this thesis:

- Renewable energy technologies are likely to become more important as other energy sources become depleted and the cost of power generation using fossil fuels rises.

Pavements, already required for structural purposes, have great potential to be used as a solar-energy collector and/or storage medium.

- The applications of pavement materials and structure to collect and/or store solar energy have been discussed. It is evident that a small number of studies have focused on these applications and clearly more research is required to address the factors affecting the performance and efficiency of the PESs. Most notably, factors that are related to the design of the civil engineering material (e.g. ability of pavement materials to absorb and conduct heat, the pavement/pipe interface, the depth of embedded pipe) have, to date, received very little attention and therefore, are also appropriate to study in this thesis.

- Acceptance of renewable energies as a successful alternative to conventional energies depends on many factors, cost being one of the important ones. Reviews on the Ground Source Heat Pump (GSHP) systems indicated that horizontal systems can reduce installation cost compared to that of the vertical systems; however, the large area required for their loop installation is still an obstacle. Large areas of pavements that are already required for transportation purposes and located close to high-energy demand buildings might be utilised as a low cost and high performance alternative to GSHP. Therefore, the use of Pavement Source Heat Store (PSHS) and factors affecting their performance are investigated.

- Phase Change Materials (PCMs) have a narrow characteristic temperature range over which melting occurs, and which can be selected to suit operating temperatures in specific engineering applications. PCMs are widely used in building applications for storing energy and maintaining the room temperature closer to the desired temperature. However, the potential application of PCM to improve the energy storage and control temperature in the ground and pavement structure has not been extensively studied to date. Therefore, the mechanical and thermo-physical properties of pavement materials modified with PCM are measured and their effects

on the performance of PSHS and other implications for pavement design are investigated in this thesis.

- The rate at which heat energy is transferred to the loops depends on the material's thermo-physical properties (i.e. thermal conductivity, specific heat capacity, density, thermal diffusivity, and thermal effusivity) which are mainly influenced by aggregate types, porosity (i.e. inter particle contact), and moisture content. The thermo-physical properties of pavement materials are therefore studied in later chapters and their effects on the performance of PESs, and other implications to help pavement design, are determined.

3 THERMAL, PHYSICAL, AND MECHANICAL PROPERTIES OF MODIFIED PAVEMENTS

3.1. Overview

The previous chapter (see Section 2.5.3, Page 25) showed that the thermo-physical properties of the soil surrounding the loops are an important aspect of horizontal Ground Source Heat Pump (GSHP) design. It is therefore anticipated that the thermo-physical properties of pavement materials might also affect the performance of the Pavement Energy Systems (PESs). In this chapter the thermo-physical and mechanical properties of concrete and asphalt pavements consisting of conventional and unconventional components are measured and discussed.

The individual effects of pavement's thermo-physical properties on the variation of maximum and minimum pavement surface temperature have been proven to be significant (Gui et al. 2007). However, changes in thermo-physical properties alone may be contentious and their effect needs to be considered as a whole. Moreover, the accuracy of temperature prediction relies heavily on the quality of the thermo-physical input parameters used in the heat transfer model. In this chapter, the thermo-physical properties of pavement mixtures consisting of conventional and unconventional components, for the first time, are measured using accurate and reliable methods such as a Heat Flow Meter (HFM) for measuring thermal conductivity and a Differential Scanning Calorimeter (DSC) to measure specific heat capacity.

Crucially, changing pavement composition in order to modify a pavement's thermal properties cannot be performed in isolation from the effect on the other properties, specifically on the mechanical properties. The potential for optimisation of pavement materials for thermo-physical and mechanical properties is a very significant point which

was largely missing from the previous studies. Therefore, in this study it was decided to determine the potential for optimisation of pavement materials for thermo-physical properties and for their load-bearing performance (the second objective of this study).

The thermo-physical properties, measured in this study, could also be used for the other applications where these parameters are critical, e.g. predicting freeze-thaw cycles in a pavement due to fluctuating environmental conditions (Dempsey and Thompson 1970; Mrawira and Luca 2002); predicting the Urban Heat Island (UHI) effect (Gui et al. 2007; Mallick et al. 2009); determining optimum binder content in flexible pavements (Solaimanian and Kennedy 1993); road-condition forecasting for timely application of de-icing and anti-icing salt for winter road maintenance.

3.2.   Materials Selection

A wide range of heavy-weight, light-weight, and normal aggregates (see Figure 3-1), as well as other additives were used to produce concrete and asphalt pavements that might deliver beneficial thermo-physical properties for the PESs. Aggregates used to produce pavement mixes were selected, as far as possible, from the waste materials that are currently utilised in building constructions. Pavements composed of waste materials have a lower environmental impact and could complement the PES application which is already considered as an environmentally friendly system.

3.2.1. Light-weight Aggregates

Use of light-weight aggregates (LWA) can offer many advantages such as reduction of dead load (i.e. lower density) and higher thermal insulation. LWA can be either naturally occurring low-density materials such as pumice (Demirboga and Gül 2003), or diatomite (Ünal et al. 2007) or they can be formed from coarse grade bottom ashes that self-sinter during the combustion process such as incinerator bottom ash (Cheeseman et al. 2005). They can also be artificially manufactured from the expansion or pelletisation of clay (e.g. Leca$^{©}$) or from industrial by-product such as fly ash (e.g. Lytag$^{©}$) (Cheeseman et al. 2005). Such

aggregates, due to their process of formation, have a high pore volume which has the potential to provide concrete and asphalt with a lower thermal conductivity. In this study, sintered pulverised fuel ash lightweight aggregate (provided by Lytag Ltd) was used due to its availability, consistency, and relatively high strength compared to the other LWA (Cheeseman et al. 2005). The raw material used in the manufacture of Lytag is fly ash, which is the waste material produced from electricity production in coal-fired power stations.

3.2.2. Heavy-weight Aggregates

Aggregates with an average particle density >3000 kg/m^3 are considered as Heavy-weight Aggregates (HWA) (Smith and Collis. 2001). HWA may be classified as either natural or artificial materials. The most widely used natural HWA in building construction are barites and iron ores such as haematite (Smith and Collis. 2001). The artificial HWA that can be used in building construction are iron shot, lead shot, or metal slags (Smith and Collis. 2001). The slag is a by-product of smelting ore to separate the metal fraction from the unwanted fraction. Examples of the slags used in construction buildings are iron, steel, copper, tin, lead, zinc, and phosphorus slags. The high particle density of slag and remaining metallic content may mean that they have a greater thermal conductivity and heat storage ability than conventional aggregates. In this study, air cooled copper slag (provided by Hodge Clemco Ltd) and chilled iron shot (known as Ferag$^{©}$) (provided by Civil & Marine Ltd) were used due to their availability, and wide use in concrete productions. It is estimated that about 2.2 tonnes of slag is generated for every tonne of copper production and approximately 5.56 million tons of slag are generated in Europe, and 24.6 million tons worldwide every year (Gorai et al. 2003). Copper slag is largely used in pavement constructions as the granular road base materials (FHWA 2011), replacement for aggregate and cement in concrete (Tixier et al. 1997; Al-Jabri et al. 2006; Wu et al. 2010a), and as fine aggregates in bituminous mixtures (Pundhir et al. 2005; Hossam and Al-Jabri 2011). 'Ferag' is produced during the process of iron production. Air cooled iron slag contains some iron-

based materials (i.e. 'Ferag') that are separated by an electromagnet. Concrete containing iron shots is broadly used in the construction of radiation shielding structures due to its high density (Kan et al. 2004).

3.2.3. Normal Aggregates

Aggregates with an average particle density of 2000-3000 kg/m^3 are considered as normal-weight aggregates (Smith and Collis. 2001). In this study, limestone and quartzite are used for the production of concrete and asphalt. Limestone is a sedimentary rock which is primarily formed of calcium carbonate ($CaCO_3$). In 2004, it was estimated that a total 225 million tons of limestone were produced (British Geological Survey 2006). Limestone is the most widely used aggregate in pavement construction. In Great Britain, it provides 54% of the crushed rock aggregate produced (British Geological Survey 2006) and is recommended by Defence Estate for use in asphalt and concrete pavements (Defence Estates 2006; Defence Estates 2008). Quartzite is a kind of metamorphic rock primarily formed of silicon dioxide (Sio_2). Quartzite aggregates due to their high elastic modulus (Wu et al. 2001; Beshr et al. 2003) and high thermal conductivity (Côté and Konrad 2005; Tarnawski et al. 2009a) might deliver useful thermo-physical and mechanical properties.

3.2.4. Other Additives

Phase Change Material (PCM) (supplied by CIBA Specialty Chemicals), copper fibre, and chipped tyre rubber (supplied by J. ALLCOCK & SONS Ltd) are additives that were used to manufacture pavement mixes in this study. The PCM was selected in order to improve latent heat storage. It was a microencapsulated paraffin wax in the form of a dry powder comprising an acrylic outer shell, where melting point $T_{melt} = 26°C$, and latent heat $H_{melt} = 160$ kJ/kg. Copper fibres were selected in order to increase thermal conductivity of the pavement mixes. The fibres used were copper wire 1mm in diameter and 50mm long. The rubber was used in concrete production in order to gain possible improvement of concrete insulation properties.

Figure 3-1 Illustration of aggregates and additives used in the study

3.3.   Concrete Mix Design and Specimen Preparation

Pavement Quality Concrete (PQC) and Lean Mix Concrete (LMC) mixes were designed (see Table 3-1) according to the airfield concrete pavement design guidelines (as given in Table 2-1 and Table 2-2 in Section 2.2.1, Page 9). The control mix for PQC used is a 10/20 single sized limestone aggregate and 4mm down natural sand in compliance with BS EN 12620 (2008) as well as high-strength Portland cement (CEM I, 52.5 N/mm^2). The control mix for LMC used is an all-in limestone aggregate and the same cement. Particle density and water absorption coefficients of the materials (see Table 3-2) were experimentally

determined according to BS EN 1097-6 (2000). Based on these values, the volumetric

replacement method was used in calculating the mixture proportions.

Table 3-1 Mix design for control mixes

Concrete	Saturated Surface Dry Aggregates (kg/m³)		Cement (kg/m³)	Free Water (kg/m³)
	Coarse	Fine		
PQC	985	828	370	200
LMC	2100		110	115

Table 3-2 Particle density and water absorption coefficients of the materials

Aggregates	Saturated surface dry Particle density (gr/cm³)		Water absorption (%)	
	Coarse(≥4mm)	Fine(<4mm)	Coarse(≥4mm)	Fine(<4mm)
Limestone	2.69	2.68	0.74	0.26
Quartzite	2.61	2.62	0.27	0.30
Lytag	1.64	1.72	30.4	24.4
Copper slag	3.68	3.64	0.35	0.41
Natural sand	-	2.65	-	0.58
Rubber	1.12	-	0.69	-
Iron shot	-	7.86	-	-
PCM	-	0.91	-	-

24 hours before mixing, all aggregates were dried in an oven and extra water to account for

their water absorption was added to make them saturated-surface dry. In this condition,

coarse aggregates in the concrete mix can absorb no water and thus require no alteration in

the quantity of mixing water. In mixing, the dry ingredients (cement, sand and coarse

aggregate) were initially blended for 2 min. Then, the water was gradually added and mixed

together for another 3 min. For the fibre-reinforced mixes, the fibres were then added and

mixed for an additional 3-5 min. The fibres were carefully sprinkled by hand in small

amounts on the surface of the mix to avoid fibre balling, and thus achieve uniform fibre

distribution. After the mixing process, the fresh concrete was filled into steel moulds in two

layers and then consolidated by using a vibration table. The concrete in the moulds was then

covered with plastic sheet to prevent excessive surface moisture loss and left for 24h in

laboratory conditions. The concrete specimens were de-moulded after that and immediately placed in a water tank at 20±2 ˚C for a period of ~28 days.

3.4. Tests Performed on Concrete Mixes and Components

<u>Compressive strength</u>

At least three 100mm cubes were used for the determination of unconfined compressive strength (f_c) according to BS EN 12390-3 (2009a).

<u>Flexural strength</u>

At least three 100×100×500mm prisms were used for the determination of four-point flexural strength (f_{fl}) of concrete mixes, according to BS EN 12390-5 (2009b).

<u>Apparent porosity</u>

Apparent Porosity (*AP*) of specimens was assessed using the following expression (Hunger et al. 2009):

$$AP(\%) = \frac{w_s - w_o}{w_s - w_w} \times 100$$

            Eq. 3-1

where

w_s= weight of the specimen at the saturated condition,

w_w= weight of the specimen in water under saturated conditions

w_o= weight of oven-dried specimen

<u>Thermal conductivity</u>

Two types of apparatus were used to measure the thermal conductivity of pavement mixes. A computer-controlled P.A. Hilton B480 uni-axial Heat Flow Meter (HFM) apparatus with downward vertical heat flow which complies with ISO 8301 (1996) and a modified transient plane source thermal conductivity analyser (Mathis TCi, C-Therm Technologies Ltd). The thermal conductivity of pavement mixes was measured using the HFM apparatus due to its higher accuracy and being suitable for non-homogeneous mixtures (as described in Section 2.7.1, Page 38). The thermal conductivity of individual aggregates was measured using the transient plane source apparatus.

The thermal conductivity tests were performed, following immersion in water (λ^*) and oven-dried (λ) conditions, on concrete slabs with dimensions of 300×300mm and a thickness of approximately 60 mm. The concrete slab specimens were placed inside the apparatus between a temperature-controlled hot plate and a water-cooled cold plate connected to a separate chiller device (see Figure 3-2). Under steady-state conditions, the thermal conductivity of the specimen is calculated using (Hilton Ltd 1994):

$$\lambda \ (or \lambda^*) = \frac{l_s \cdot \left[\left(k_1 + (k_2 \cdot \bar{T})\right) + \left((k_3 + (k_4 \cdot \bar{T})) \cdot HFM\right) + \left((k_5 + (k_6 \cdot \bar{T})) \cdot HFM^2\right) \right]}{dT}$$

<div align="right">**Eq. 3-2**</div>

where

k_1-k_6= calibration constants of the apparatus determined separately (from testing a sample of known thermal conductivity)

$\bar{T} = \frac{T_{hot} + T_{cold}}{2}$= average temperature of hot & cold plate (°C)

$dT = T_{hot} - T_{cold}$

HFM= heat flowmeter output (mV)

l_s= thickness of the specimen (mm)

Steady state conditions are deemed to occur when the percentage variation in heat flux throughout the sample is ≤3%. The sample interval of the heat flow meter is given by:

Max (300s; $\rho \ C_p \ l_s$ R)

where

ρ= density of the specimen (kg/m^3),

R= specific thermal resistance of the material (m^2 K/W)

Two slabs were prepared for each mix design and then the mean value of three independent readings was obtained for each slab specimen at oven-dried and wet states. For thermal conductivity measurement in a wet state, the concrete slabs were removed from the curing tank water at the end of their 28-day curing period and sealed in a vapour-tight envelop to prevent a change in moisture content. The influence of the thin envelop on the thermal

conductivity of the slab specimens is negligible when measuring thermal conductivity at a steady-state variance of ± 2-3%, as prescribed by ISO 8301 (1996). In the dry state, all the specimens were dried in an oven for 24h and then cooled in a desiccator.

Figure 3-2 Heat flowmeter apparatus for thermal conductivity measurement

The Mathis TCi™ system, shown in Figure 3-3, was utilised in this study to perform the thermal conductivity measurements on aggregates. The test was performed on three individual aggregates of each type on which five independent readings were obtained. The aggregates were polished, to achieve a flat surface, and dried prior to testing. The Mathis TCi™ system is based on the modified transient plane source technique. It uses a heat reflectance sensor (see Figure 3-3) that applies a momentary, constant heat source to the sample. The sample is tested by placing it in contact with the heating element of the sensor. A known current is applied to the sensor's heating element providing a small amount of heat which results in a rise in temperature at the interface between the sensor and the sample. This temperature rise at the interface induces a change in the voltage drop of the sensor element (Harris and Sorensen 2007). Since the rate of the temperature rise at the heating

element is inversely proportional to the thermal conductivity of the material, this material property can be determined by measuring the rate of the voltage rise when a constant current is applied. The voltage increase can be correlated with thermal conductivity through a calibration with reference materials having known thermal conductivity.

Figure 3-3 Mathis TCi thermal conductivity analyser

Specific heat capacity

The specific heat capacity of each concrete mix was calculated as the sum of the specific heat capacities of the constituent parts weighted by their relative mass proportions. Therefore, the specific heat capacity of Hardened Cement Paste (HCP) was first measured and then the specific heat capacity of Coarse Aggregates (CA), Fine Aggregates (FA), and Additives (ADD) were added proportionally. It was assumed that air in the samples had a negligible contribution to the heat capacity of the total concrete since it has a density of approximately ~1.2 kg/m^3 at ambient temperatures compared to ~2300 kg/m^3 for the

concrete solids. The specific heat capacity of concrete in both the dry (c_p) and wet (c_p^*) states are calculated from equations Eq. 3-3 and Eq. 3-4, respectively.

$$c_p = \frac{1}{w_{total}} [w_{HCP}c_{HCP} + w_{CA}c_{CA} + w_{FA}c_{FA} + w_{ADD}c_{ADD}]$$ **Eq. 3-3**

$$c_p^* = c_p + \frac{AP * \rho_{water}}{w_{total}} * c_{water}$$ **Eq. 3-4**

where:

w= mass proportion of the concrete constituents (kg)

c= specific heat capacities of the concrete constituent (J/kg K)

HCP denotes 'Hardened Cement Paste'; *CA* denotes 'Coarse Aggregates'; *FA* denoted 'Fine Aggregates' and ADD denoted 'Additives'.

A TA Instrument Q10 Differential Scanning Calorimeter (DSC) (see Figure 3-4) was used to determine the specific heat capacity of the concrete constituents according to BS EN ISO (2009) and BS ISO (2005). A DSC operates on the principle that, *the difference between the rate of heat flow into a specimen and that into a reference crucible is measured as a function of temperature and/or time while the specimen and the reference are subjected to the same temperature-control programme under a specified atmosphere* (BS EN ISO 2009).

Testing was carried out in 4 steps as follows:

1) Introducing a temperature profile

Temperature profile was first equilibrated at -15°C and maintained isothermal for 10 minutes. The temperature was then ramped to 60°C at a rate of 5°C/min. Finally, the temperature was held isothermal at 60°C for another 10 minutes to complete the test run.

2) DSC calibration

Heat flow into an empty aluminium sample crucible (see Figure 3-4) was measured using the temperature profile to achieve a 'baseline'.

3) Heat flow into a reference specimen

Heat flow was measured into a reference specimen with known specific heat capacity. A certified reference specimen of pure Sapphire (α-Al$_2$O$_3$) was used to achieve a 'reference line'.

4) Heat flow into concrete constituents

The heat flow was measured, under the specific temperature profile, for all the concrete constituents and it was repeated three times for each specimen.

Figure 3-4 A TA Instruments Q10 Differential Scanning Calorimeter

An example of heat flow curves and temperature profiles is shown in Figure 3-5. The specific heat capacity of the test specimen can then be calculated using Eq. 3-5 (BS ISO 2005).
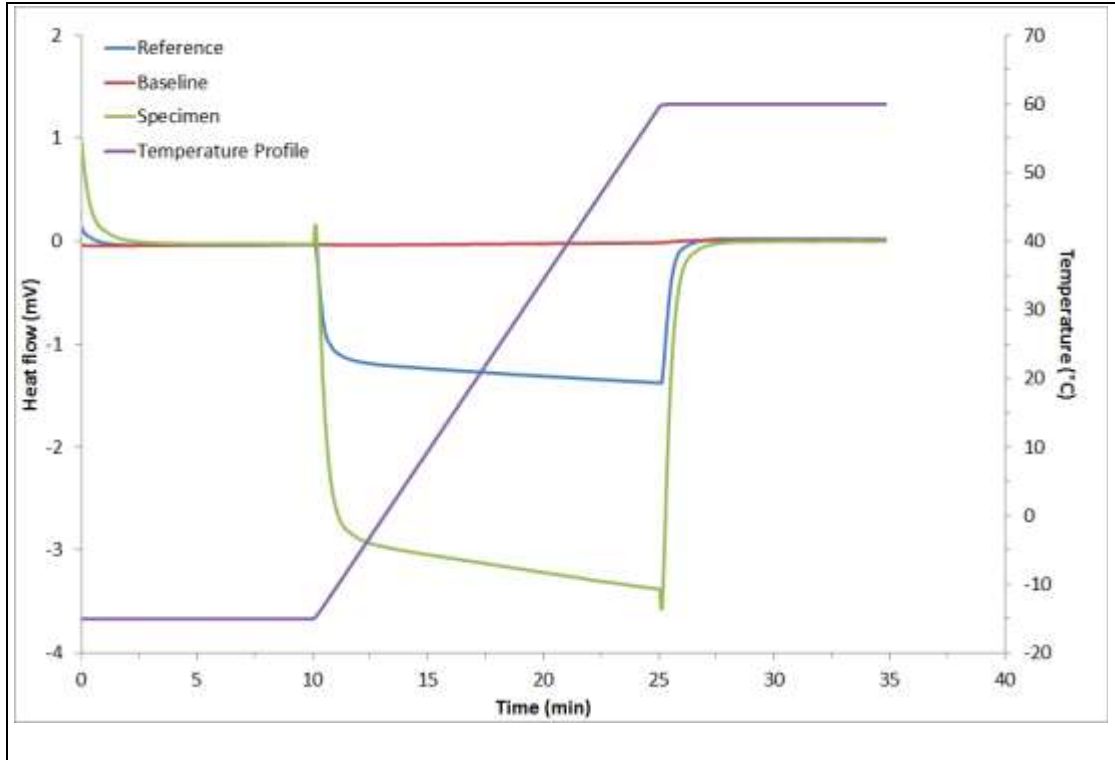
Figure 3-5 Characteristic heat flow curve from DSC analysis

$$c_p^{sp} = c_p^{ref} \times \frac{m^{ref}\left(HF_{specimen} - HF_{baseline}\right)}{m^{sp}\left(HF_{reference} - HF_{baseline}\right)} \qquad \text{Eq. 3-5}$$

where:

sp denotes 'specimen'; ref denotes 'reference'; m is mass and HF is the heat flow readings.

<u>Microstructural Investigation using Scanning Electron Microscopy</u>

Scanning Electron Microscopy (SEM) is a microscopic imaging technique that uses a high energy electron beam to scan a specimen under high vacuum. Electrons are accelerated down a column towards the sample at energies ranging from a few hundred to tens of thousands of electron volts to generate a variety of signals at the surface of a specimen. The signals that derive from the interaction of electron and atoms at the surface of the sample reveal information about the sample, including external morphology (texture), chemical composition, and crystalline structure and orientation of materials making up the sample. The types of signals produced by an SEM include Secondary Electrons (SE), Back-Scattered Electrons (BSE), and characteristic X-rays which can be detected by an Energy Dispersing

Spectrometer (EDS). Detectors collect these X-rays, BSE, and SE and convert them into a signal that is sent to the screen and produces the final image.

The SEM instrument has many applications across different industry sectors. The extremely high magnification images together with localised chemical information mean the instrument is capable of solving a great deal of common industrial issues such as particle analysis, defect identification materials and metallurgical problems. It is widely recognised that the mechanical behaviour of concrete can be directly related to its microstructure. In concrete, microscopy analysis is generally undertaken in order to characterize micro cracks and the Interfacial Transition Zone (ITZ), which represents a small region next to the particles of coarse aggregate and exists as a thin shell, typically 10 to 50 μm thick around the large aggregate (Erdem et al. 2011). For instance, Figure 3-6 can give a good picture of the microstructure of concrete. Both the concrete specimens shown in Figure 3-6 demonstrate evidence of bonding between cement paste and aggregate that could be related to the mechanical and thermal performance of the concrete.
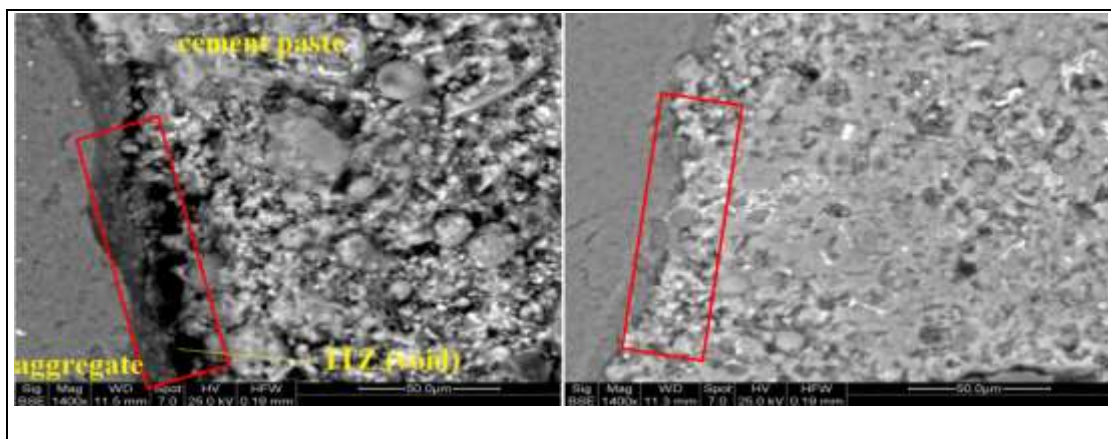
Figure 3-6 SEM micrographs of the concrete, showing ITZ between cement paste and aggregate, Adapted from (Erdem et al. 2011)

In this study, SEM analysis was conducted using a Philips XL-30 Field Emission Gun Environmental Scanning Electron Microscope (FEG-ESEM) equipped with Oxford Instruments Inca model Energy Dispersive Spectrometer (EDS). Micrographs were recorded in high vacuum mode using an Everhart-Thornley type SE detector and a Back Scattered Electron (BSE) detector supplied by K.E. Developments. Elemental mapping was also

performed on the samples using EDS spectral analysis at 113eV resolution. Samples were prepared by taking small pieces from the crushed specimens. The samples were then placed on aluminium stubs and were fixed in place using adhesive carbon cement. For good imaging, samples need to be conductive as those that are non-conductive can 'charge' under scanning and produces poor quality images. Therefore, samples were first coated using the sputter coating technique where platinum powder was applied to the surface of the sample and then placed onto the SEM unit.

Microstructural Investigation using X-ray Computed Tomography

X-ray Computed Tomography (CT) is a non-destructive technique for visualizing interior features within solid objects, and for obtaining digital information on their 3D geometries and properties. The principle of X-ray CT is, when X-rays pass through an object, they are absorbed or attenuated by absorption and scatter depending on the density of materials scanned. The portion of radiation that penetrates through the object will form a projective image that will indicate the presence of the internal structure and constituent materials' distribution. The variation in darkness of captured image is interpreted to provide information concerning the internal features of the structure. The colour differences in the final image show the differences in materials density of the object in a 2D image (Masad et al. 2002). Figure 3-7 illustrates the X-ray CT components where the specimen is placed between the X-ray source and the detector. X-rays pass through the specimen along several directions producing a 2D image (i.e. slice) after a full rotation of the specimen. The specimen is then shifted vertically by a fixed amount (slice spacing) and the entire procedure is repeated to generate additional slices. The X-ray image consists of 256 levels of grey intensity that correspond to different densities within a specimen (Masad et al. 2002). In a typical 2D slice from a pavement mixture, the aggregate is the brightest followed by paste and the darkest is air void (see Figure 3-8). To identify any mixture constituents (e.g. aggregate, air void, paste), a threshold grey intensity must be chosen. For instance, using a threshold value, the original image can be transformed to a binary image of black (i.e. air voids) and white (aggregate and paste) phases, as shown in Figure 3-9. Image analysis

software can be used to obtain information about the selected component (in this case air voids) that existed on each slice. In this study, the specimens were scanned using a Venlo H 225/350 X-Ray CT, available in the Nottingham Transportation Engineering Centre (NTEC), at 83 micron resolution and 340 kV accelerating voltage. The freely available Image J software was used to analyse the images.
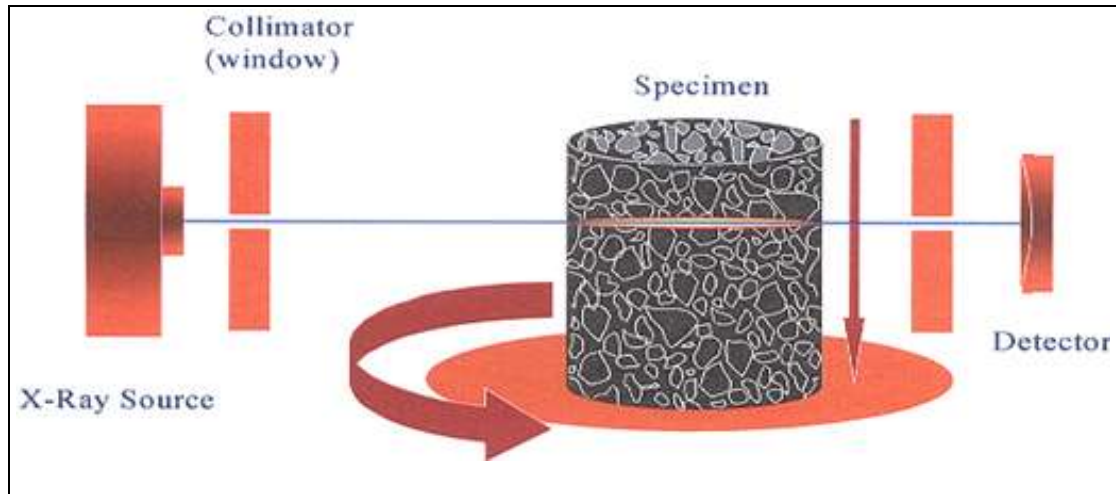
Figure 3-7 Components of x-ray computed tomography system (Masad et al. 2002)
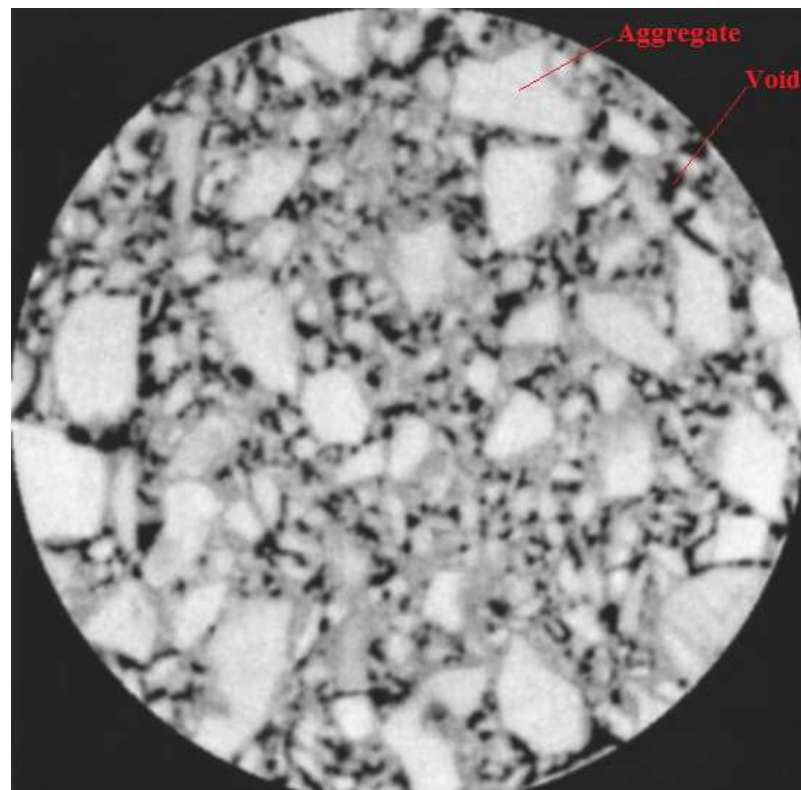
Figure 3-8 2D x-ray tomography image of asphalt concrete, Adapted from (Masad et al. 2002)
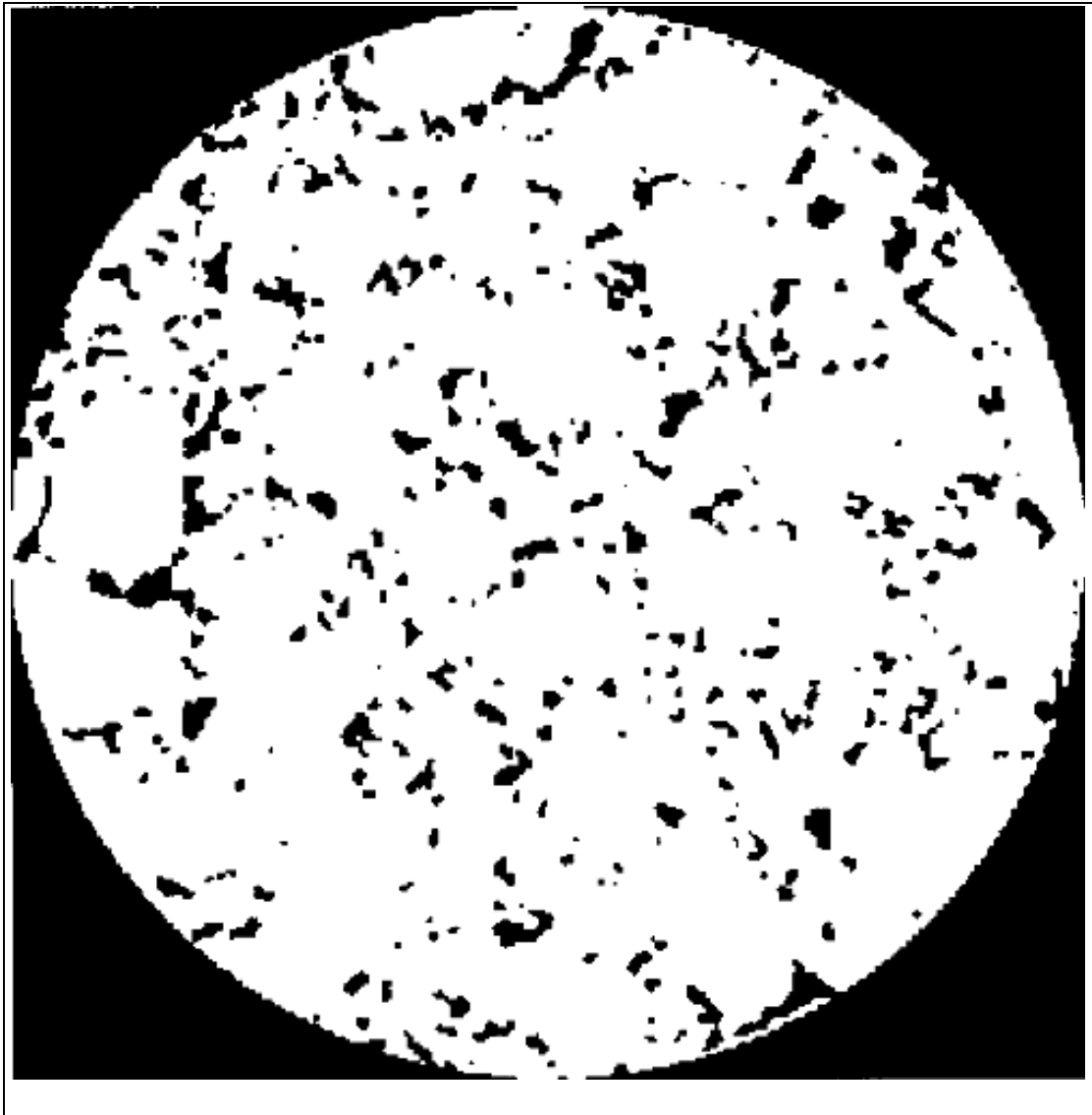
Figure 3-9 Image threshold to isolate air voids (black) from solids (white) (Masad et al. 2002)

3.5. Test Results and Discussions on the Aggregates and Concrete Mixes

The results of tests on the pavement materials and their components are presented and discussed in the next three sections as follows:

3.5.1. Aggregate Test Results

The mean values of specific heat capacity and thermal conductivity of the pavement components are presented in Table 3-3 and Figure 3-10, respectively.

Table 3-3 Mean values of dry-state specific heat capacity of pavement componenets (Max variation of ±7%)

Components	c_p (J/kg K)							
	-10°C	0°C	7°C	17°C	27°C	37°C	47°C	57°C
Limestone	793	838	859	878	892	904	917	931
Quartzite	609	629	642	659	675	693	709	724
Copper slag	628	670	679	691	701	712	723	734
Natural sand	610	637	655	679	698	711	721	734
Lytag	620	712	741	767	778	787	799	812
Rubber	1194	1292	1326	1369	1406	1444	1485	1523
Hardened Cement Paste	877	1021	1094	1241	1458	1714	1978	2300
Ferag	521	552	562	575	586	589	609	618
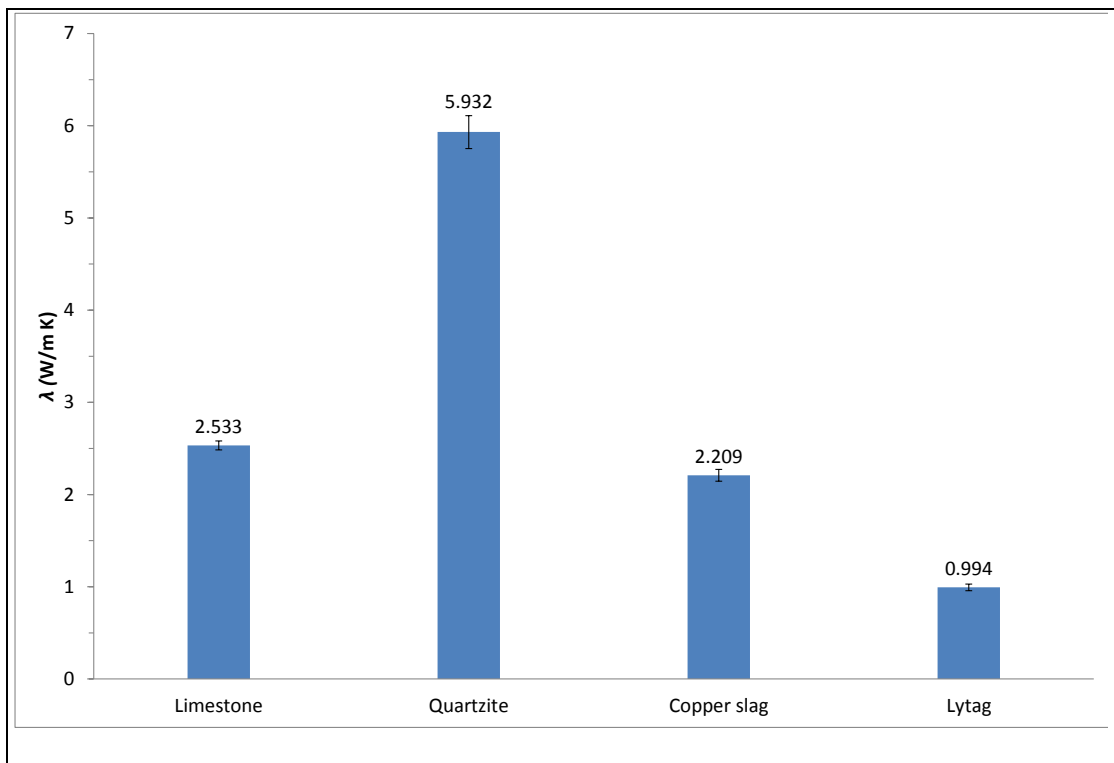
Figure 3-10 Dry-state thermal conductivity of pavement components including 95% confidence limit

Table 3-3 shows that the specific heat capacity of the aggregates increases as temperature rises, consistent with the findings reported by Somerton (1992). In addition, Table 3-3 shows that, limestone aggregates can produce slightly higher specific heat capacity among the natural aggregates. Somerton (1992) also reported that the specific heat capacity of limestone, due to its calcite content, is higher than that of quartzite which is mainly consisted of quartz minerals.

Figure 3-10 shows that quartzite aggregates exhibited the highest value of thermal conductivity among the tested aggregates followed by limestone and copper slag. A low thermal conductivity value for Lytag is due to its higher porosity because it is formed as a result of incomplete densification during the sintering process at high temperatures. Erdem et al (2011) experimentally found that porosity of the Lytag is about 52.7% compared to 1.62% for the natural aggregates.

3.5.2. Test Results of Modified Concrete Mixes

The mean values of all measured physico-mechanical and thermo-physical properties of the concrete mixes are tabulated in Table 3-4 and Table 3-5, respectively. Thermal diffusivity (α) and Thermal effusivity (β) are calculated using Eq. 2-6 (in Page 48) and Eq. 2-8 (in Page, 49), respectively. The wet-state thermal diffusivity (α^*) and thermal effusivity (β^*) of concretes were also calculated by inserting the wet values in the above equations.

Table 3-4 Physical and mechanical properties of modified concretes

Sample No	Concrete		ρ_d (kg/m³) dry density	ρ_{ssd} (kg/m³) saturated density	f_c (MPa) compressive strength	f_{fl} (MPa) flexural strength	AP (%) Apparent porosity
	Coarse Aggregate	**Fine Aggregate**					
1	Limestone	Natural sand	2190	2320	52±1	5.4±0.2	12.9
2	Quartzite	Natural sand	2250	2387	52±2	5.1±0.1	13.7
3	Quartzite	Quartzite	2268	2343	51±2	5.1±0.1	7.5
4	Quartzite	Quartzite+1%cu-fibre	2431	2573	55±1	6.5±0.3	14.2
5	Copper slag	Natural sand	2638	2755	53±2	5.3±0.1	11.6
6	Copper slag	Copper slag	2985	3105	49±2	4.6±0.1	11.9
7	80%Limestone +20%Rubber	Natural sand	2079	2231	35±0	3.8±0.2	15.1
8	50%Limestone +50%Rubber	Natural sand	1929	2096	14±0	1.6±0.1	16.5
9	20%Limestone +80%Rubber	Natural sand	1712	1901	8	-	18.8
10	Rubber	Natural sand	1531	1730	3	-	20.1
11	Lytag	Natural sand	1699	1948	39±1	4.3±0.2	24.3
12	Lytag	Lytag	1412	1706	37±3	4.2±0.3	29.4
13	Copper slag	Ferag	4258	4354	47±1	4.4±0.2	9.6
14[a]	Limestone	Limestone	2258	2378	25±3	-	-
15[a]	Lytag	Lytag	1568	1788	14±2	-	-
16[a]	Quartzite	Quartzite	2295	2415	23±1	-	-

[a] (LMC mixes)

Table 3-4 shows that almost all of the concrete mixes (except those containing high percentages of rubber) meet mechanical requirements to be used in heavily trafficked areas such as an airfield apron pavement (refer to Table 2-1 and Table 2-2, Page 10, for the required compressive and flexural strength). Using Lytag aggregates resulted in a reduction in compressive strength of about 23% compared to the control mix (i.e. limestone+natural sand), consistent with the findings by Kayali et al (2003). The reduction of compressive strength of concrete incorporating Lytag can be attributed to lower impact value (softness) of these aggregates compared to natural aggregates (Erdem et al. 2011). Therefore, as a result of this, cracks in the Lytag concrete mix took place through the aggregates. On the other hand, the other concrete mixes (e.g. limestone, quartzite, copper slag) obtained almost similar compressive strength. In these mixes, the weakest link observed to be the link

between aggregates and cement paste where failure took place. The flexural strength of the concrete mixes also shows that they have potential to be used as concrete pavements in heavily trafficked areas. The flexural strength of all concrete mixes almost follow the well-known relationship that exists between the flexural strength and compressive strength of concrete mixes (i.e. f_{fl}=8%-11%$\times f_c$) (Neville 1995).

Table 3-5 Thermo-physical properties of modified concretes

Sample No	Concrete		λ (W/m K) dry-state thermal conductivity	λ^* (W/m K) wet-state thermal conductivity	C_p (J/kg K) dry-state specific heat capacity	C_p^* (J/kg K) wet-state specific heat capacity	$\alpha (\times 10^{-7})$ (m²/s) dry-state thermal diffusivity	$\alpha^* (\times 10^{-7})$ (m²/s) wet-state thermal diffusivity	B (J/s$^{0.5}$m² K) dry-state thermal effusivity	β^* (J/s$^{0.5}$m² K) wet-state thermal effusivity
	Coarse Aggregate	Fine Aggregate								
1	Limestone	Natural sand	1.12±0.07	1.36	953	1114	5.4	5.3	1529	1875
2	Quartzite	Natural sand	2.64±0.23	2.81	870	1031	13.5	11.4	2273	2630
3	Quartzite	Quartzite	2.98±0.18	3.08	852	948	15.4	13.9	2400	2616
4	Quartzite	Quartzite+1%cu_fibre	3.46±0.32	3.84	845	1026	16.8	14.5	2666	3184
5	Copper slag	Natural sand	1.18±0.16	1.42	854	986	5.2	5.2	1630	1964
6	Copper slag	Copper slag	0.81±0.15	0.94	837	958	3.2	3.2	1423	1672
7	80%Limestone+20%Rubber	Natural sand	0.81±0.14	0.97	987	1180	3.9	3.7	1289	1598
8	50%Limestone+50%Rubber	Natural sand	0.44±0.16	0.61	1043	1263	2.2	2.3	941	1271
9	20%Limestone+80%Rubber	Natural sand	0.27	0.40	1110	1369	1.4	1.5	716	1020
10	Rubber	Natural sand	0.22	0.36	1160	1444	1.2	1.4	625	948
11	Lytag	Natural sand	0.94±0.05	1.07	935	1285	5.9	4.3	1222	1637
12	Lytag	Lytag	0.46±0.11	0.71	1009	1481	3.2	2.8	810	1339
13	Copper slag	Ferag	1.21±0.14	1.31	729	800	3.9	3.8	1938	2136
14[a]	Limestone	Limestone	0.92±0.09	1.16	983	1227	4.1	4.1	1429	1840
15[a]	Lytag	Lytag	0.59±0.01	0.88	953	1574	3.9	3.1	939	1574
16[a]	Quartzite	Quartzite	2.58±0.12	2.91	754	1040	14.9	11.6	2113	2703
17	Grade 310 Stainless Steel		11.61±0.50	-	-	-	-	-	-	-
18	Acrylic sheet		0.18±0.02	-	-	-	-	-	-	-

[a] (LMC mixes), [b] Samples with known thermal conductivity tested to check heat flowmeter accuracy

It is evident from the data presented in Table 3-5 that the degree of saturation correlates to an increase in the thermal conductivity and specific heat capacity for each concrete material that was tested. The increase in thermal conductivity can be attributed to changes in air voids filled with water, whose thermal conductivity is superior to that of air. However, it was also observed that the thermal conductivity of the concrete was directly and positively related to that of the aggregate. Quartzite aggregate, for example, has a conductivity of ~6.0 W/m K and produced concrete with a conductivity of ~2.8 W/m K in this study, whereas limestone which has a conductivity of ~2.5 W/m K produced concrete with a conductivity of ~1.4 W/m K, this is also the case for synthetic alternative aggregates such as Lytag and chipped rubber. In addition, chipped rubber modified concrete is known to have problematic ITZ (Segre and Joekes 2000) (see Figure 3-11) which increases the porosity around aggregate and is likely to augment reductions in thermal conductivity. This point is illustrated in Figure 3-12 that shows an inverse relationship between the apparent porosity and both the dry and wet thermal conductivity for chipped rubber-modified concretes. Figure 3-12 shows that the thermal conductivity increases as the apparent porosity decreases. This can occur as a result of enhanced inter-particle contact when the void ratio is minimised.

Table 3-4 and Table 3-5 show that within the limitation of materials and mix design used in this study, it is feasible to provide mechanically acceptable PQC and LMC mixes to have a thermal conductivity range from ~0.5 to ~4 W/m K and with VHC (ρc_p) ranging from 1.9×10^6 to 3.3×10^6 (J/m^3 K). The measured thermal conductivity and VHC can provide concrete with a thermal diffusivity range from ~2×10^{-7} to ~16×10^{-7} m^2/s. Thermal diffusivity of the concrete can effectively be reduced by using the LWA (i.e. overall reduction of the concrete thermal conductivity) and/or to some extent by using the HWA (i.e. overall increase of the concrete's VHC). On the other hand, it seems that increasing the thermal conductivity of concrete by using high conductive aggregates is the way to increase the concrete's thermal diffusivity. In addition, concrete's thermal effusivity increases with

increase in the thermal conductivity and it ranges from ~1000 to ~3000 $J/s^{o.5} m^2 K$ for

concretes.
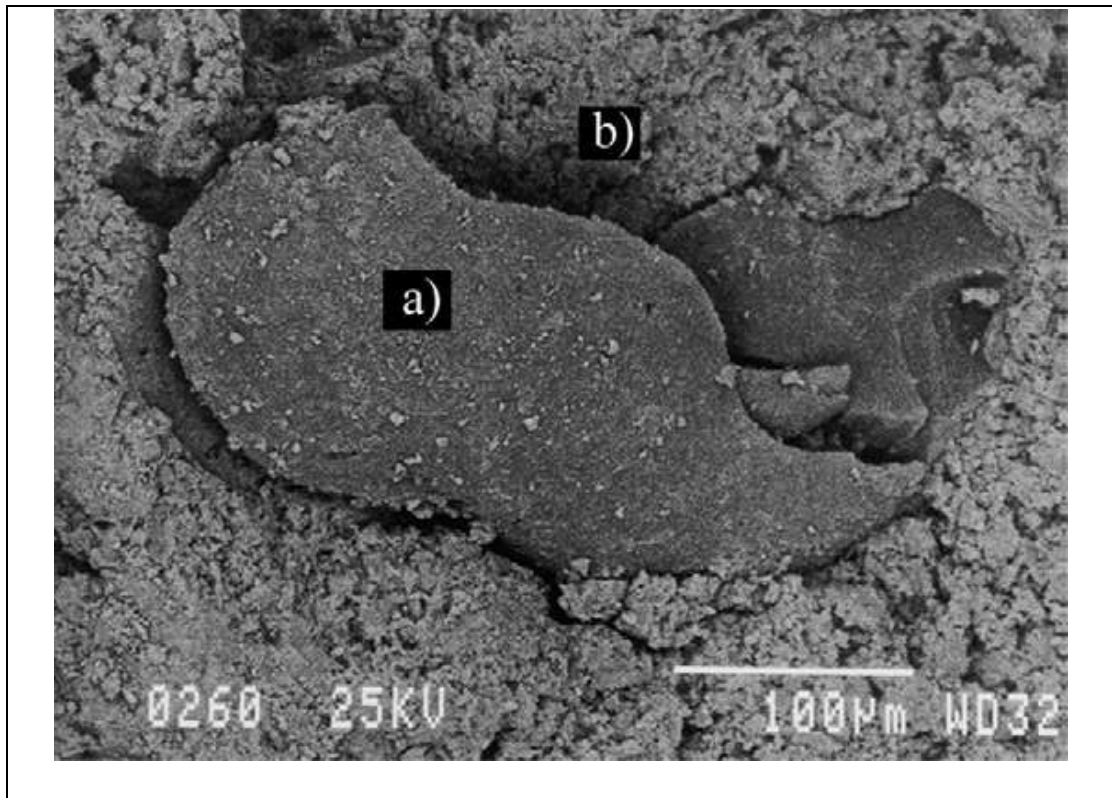
Figure 3-11 SEM micrograph (using BSE detector) of cement paste with rubber aggregate: (a) rubber particles and (b) cement paste (Segre and Joekes 2000)
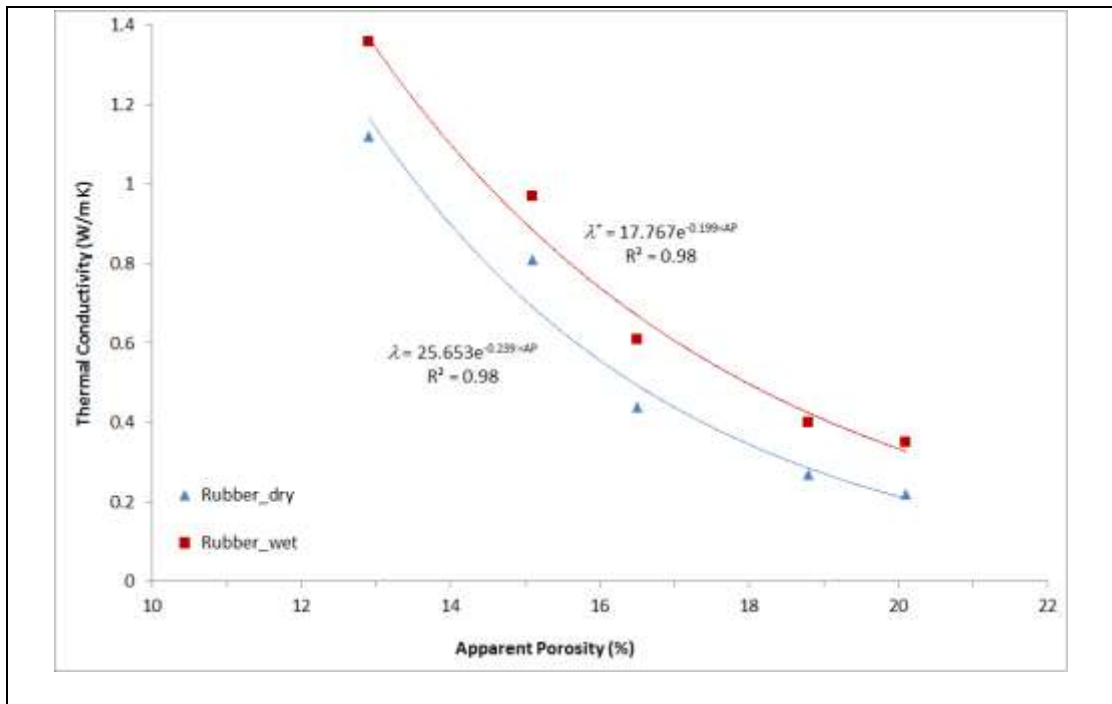
Figure 3-12 Relationship between Apparent Porosity of chipped rubber-modified concretes with wet and dry thermal conductivity

Interestingly, the addition of cooled iron shot particles had a minimal effect on the thermal conductivity of the concrete mix. The thermal conductivity of cast iron is known to be approximately 45 W/m K at 25 °C (Incropera et al. 2007). However, when loose cooled iron shot particles were tested using the TCi modified transient plane source device, the thermal conductivity was determined to be only 1.4 W/m K in the dry state. This reduction must be a reflection of the very limited inter-particle contact. Figure 3-13 (left), is an X-ray CT cross-sectional image through a concrete core taken from the concrete slab containing cooled iron shot particles. It shows that even though there are some clusters of Ferag which might deliver a conductivity of 1.4 W/m K, these clusters are not well interconnected further reducing their opportunity to convey heat energy effectively through concrete. Comparison of λ values in Table 3-5 for 'with' and 'without' iron shot particles (see Mix#13 and Mix#5 respectively) will illustrate this. The poor interconnection (i.e. not continuous conductive path) between iron particles, observed in Figure 3-13, can also explain why iron shot and copper powder additives, used by other researchers (Phillipps 2007; Mallick et al. 2008), did not improve the thermal conductivity of asphalt mix.

On the other hand, the results of copper fibre-reinforced concrete in this study as well results of experiments carried out by Cook and Uher (1974) (see Figure 2-22 in Section 2.7.1) proved that the addition of metallic fibres in concrete can improve the thermal conductivity of the concrete. Figure 3-13 shows that the addition of metallic fibre in concrete can develop many continuous highly conductive paths that as expected increase the thermal conductivity of the concrete. Figure 3-14 is a 3D image reconstructed from the 2D slices taken across the height of the specimen at 0.14mm slice spacing, in which, interconnection behaviour of copper fibres to enhance the thermal conductivity of the concrete can also be observed. Fibre orientation can also be an important factor in heat transfer; the more fibres orientated in the direction of heat flow the higher the effective thermal conductivity of the specimen.
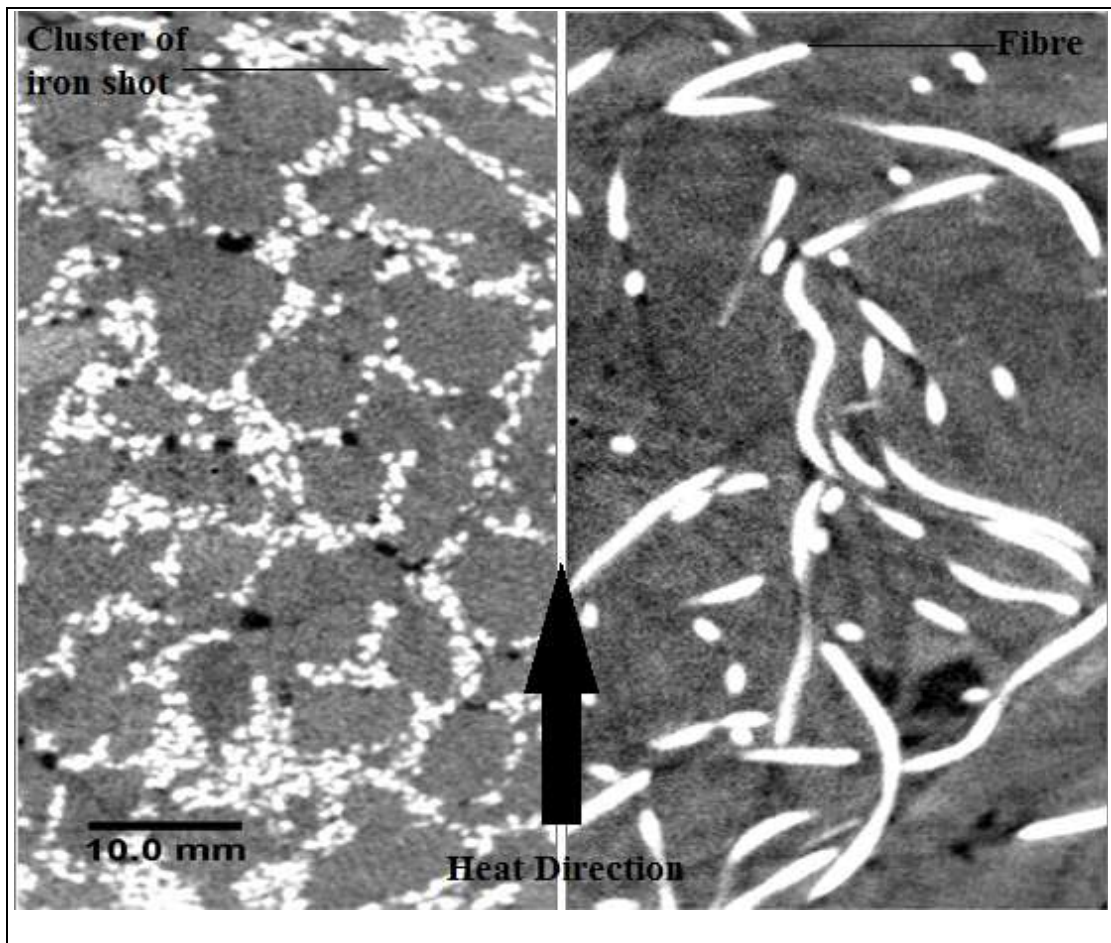
Figure 3-13 XRCT images of concrete containing iron shot (left) and 1% (by concrete volume) copper fibre (right)
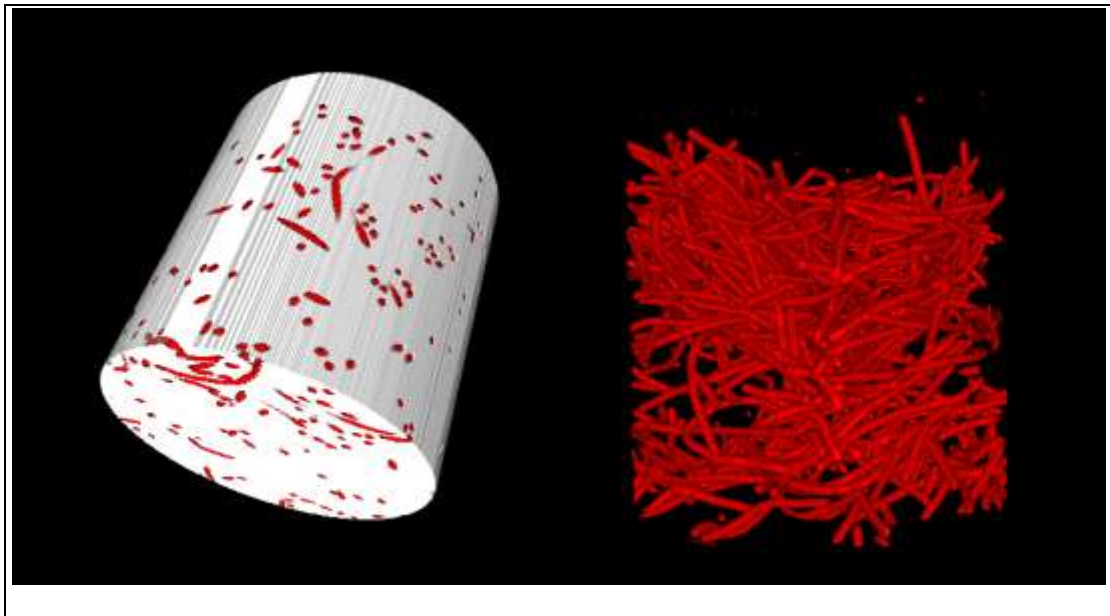
Figure 3-14 A 3D XRCT images of the formation of copper fibres in the concrete specimen

3.5.3. Test Results of PCM-modified Mixes

As mentioned in Section 2.6.1, Page 34, PCMs due to their high latent heat of solid-liquid phase change can be used in order to enhance the thermal storage. Therefore, in this section the feasibility of using PCMs in concrete mixes is investigated. This section is divided into two parts. In the first part, the thermo-physical and thermo-mechanical results of PCM-modified concrete are presented and discussed. In the second part, microstructural characterisation of PCM-modified concrete is discussed.

PCM-modified concrete

The PCM powder (see Figure 3-15) was used to replace the 0-600μm sand fraction in the concrete mix in a volume ratio of 10%, 20%, and 40%, as shown in Table 3-6. The mean values of all measured physico-mechanical and thermo-physical properties of the PCM-modified concrete mixes are presented in Table 3-7. Unfortunately, increasing PCM dosage led to significant reductions in compressive strength and flexural strength. The percentage reduction in compressive strength was approximately 35%, 65%, and 80% for 10%, 20%, and 40% PCM replacement, respectively. The reduction in flexural strength was 15%, 35%, and 45% for 10%, 20%, and 40% PCM in concrete, respectively. In addition, the overall density was also reduced which can be attributed to the particle density of the PCM (0.90 gr/cm^3) compared to that of the sand (2.65 gr/cm^3) as well as an increase of the concrete's porosity.

Table 3-6 Mix Design for PCM-modified concrete (total volume: 1m^3)

	Reference Mix		10% Mix		20% Mix		40% Mix	
	Volume (m^3)	Mass (kg)	Volume (m^3)	Mass (kg)	Volume (m^3)	Mass (kg)	Volume (m^3)	Mass (kg)
Cement	0.12	370	0.12	370	0.12	370	0.12	370
Water	0.20	200	0.20	200	0.20	200	0.20	200
Coarse Aggregate	0.37	985	0.37	985	0.37	985	0.37	985
Fine Aggregate	0.31	828	0.28	745	0.25	662	0.19	497
PCM	0	0	0.03	28	0.06	57	0.13	113
Total % of PCM in Mix	0	0	3.2	1.2	6.7	2.6	14.3	5.5
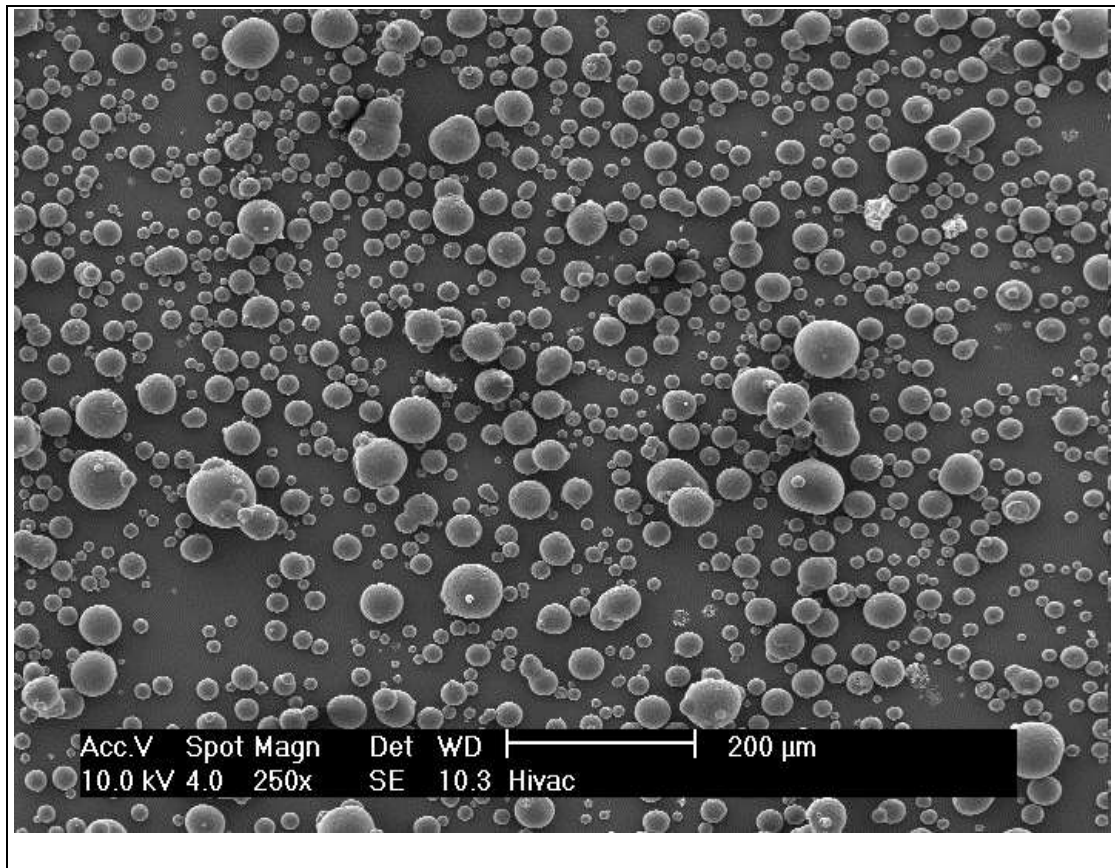
Figure 3-15 Particle size distribution of microencapsulated PCM used in this study

Table 3-7 Mean values of all measured physico-mechanical & thermo-physical properties of the PCM-modified concrete

Concrete Mixes	f_c (MPa)	f_{fl} (MPa)	ρ_d (kg/m^3)	ρ_{ssd} (kg/m^3)	AP (%)	λ (W/m K)	λ^* (W/m K)	C_p (J/ kg K)	C_p^* (J/kg K)	α ($\times 10^{-7}$) (m^2/s)	α^* ($\times 10^{-7}$) (m^2/s)	β (J/s$^{0.5}$m^{2}K)	β^* (J/s$^{0.5}$m^{2}K)
Ref	52 ±1	5.4± 0.2	2191	2320	12.9	1.12	1.36	963	1129	5.3	5.2	1537	1887
10%	34 ±3	4.5± 0.3	2039	2203	16.4	0.94	1.18	1174	1366	3.9	3.9	1500	1885
20%	19 ±4	3.5± 0.1	2006	2184	17.8	0.86	1.09	1381	1572	3.1	3.2	1544	1934
40%	10 ±1	3.0± 0.0	1835	2034	19.9	0.71	0.95	1780	1958	2.2	2.4	1523	1945

The addition of PCM resulted in a general reduction of thermal conductivity. This can be explained because the increased air void content, as a result of entrapped air from PCM addition and increasing porosity, would decrease inter-particle contact and create air pockets

and hence reducing the thermal conductivity. The reduction in thermal diffusivity of PCM-modified concrete is due to the reduction of thermal conductivity as well as the increase of specific heat capacity. Thermal effusivity fluctuates as the percentage of added PCM increases. This occurs when the decrease in thermal conductivity is partially offset by increases in heat capacity.

Figure 3-16 shows the dry-state mean specific heat capacity (c_p) of concrete across a temperature range of -10°C to 50°C. PCMs are normally defined by a mean melting temperature, in this case T_{melt} = 26°C. Due to the level of purity and varying particle diameters, phase change typically occurs across a narrow temperature range close to the mean value, which is approximately 22-30°C (see Figure 3-16). Figure 3-16 shows that clearly even a relatively small addition of PCM in concrete resulted in an increase in heat capacity. The quantity of latent energy stored in the concrete is equal to the area under the curve. The values for latent energy stored are provided on Figure 3-16 assuming a ΔT of 5ºC. In order to store 12.1 kJ/kg as sensible heat, for example, by increasing concrete temperature (with no PCM), a ΔT of >13 ºC is needed, whilst the same amount of energy can be stored in the 40% PCM mix with a ΔT of only 5ºC.
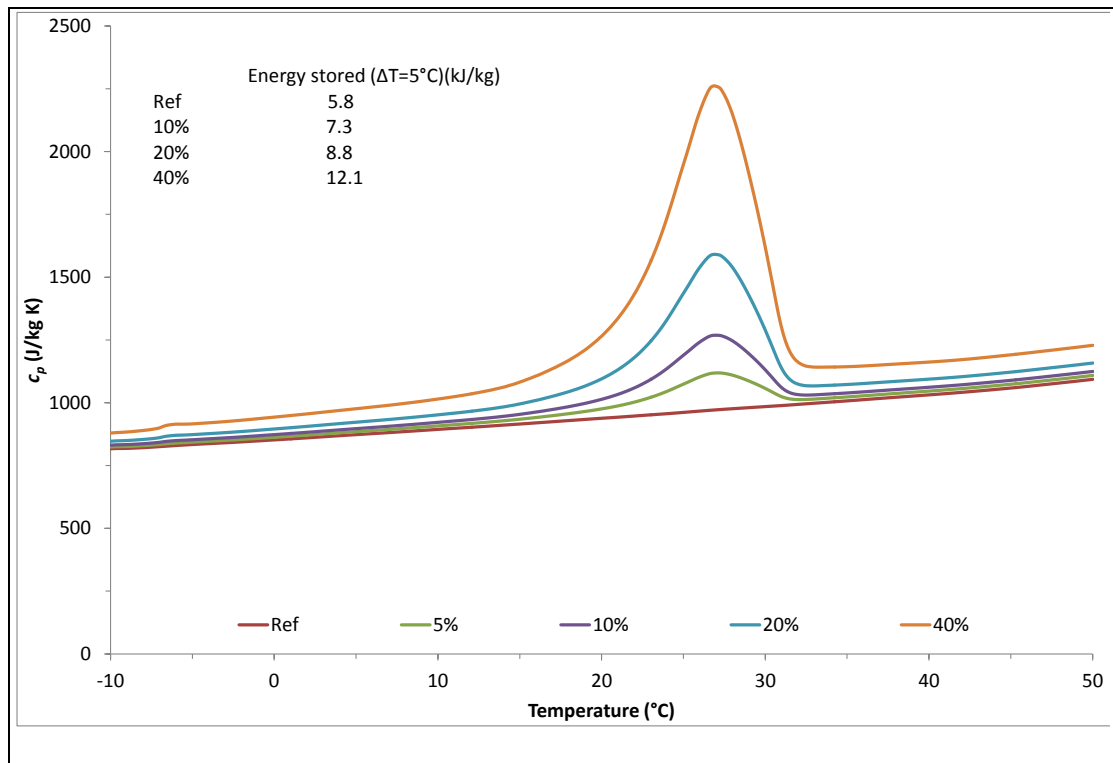
Figure 3-16 Dry-state specific heat capacity and thermal storage capacity of the PCM-modified concrete

Micro-structural characterisation of PCM-modified concrete

The benefits of PCM-modified concrete to thermo-physical behaviour appear very promising (some novel applications of PCM in pavements are discussed later in Section 6.6, Page 189). However, the large drops in strength would effectively preclude the use of these PCM as an additive to traffic-bearing concrete pavements. For this reason, the source of this unfavourable behaviour on the mechanical performance of concrete was further investigated through micro-structural analysis.

The ratio of compressive strength loss to apparent porosity increase is known to be approximately 5:1 in concrete (Neville 1995). However, Figure 3-17 shows that the relationship between apparent porosity (AP) and compressive strength of PCM-modified concrete does not follow the expected relationship (see Predicted and Data trend in Figure 3-17), suggesting that additional mechanisms contributing to strength loss are likely to be involved as discussed in the following section.
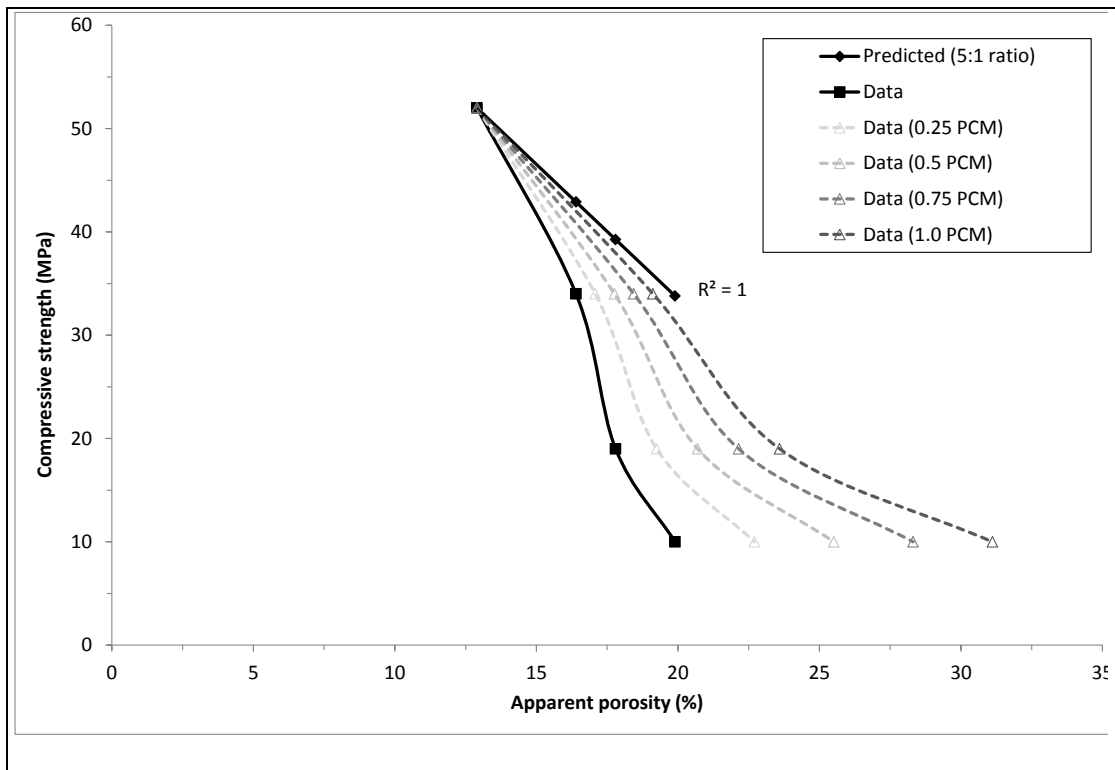
Figure 3-17 Empirical correlation between compressive strength amendments as a result of apparent porosity, with predicted effects of post-loading PCM void formation

The PCM sample, for microstructural analysis, was prepared by depositing <5mg of the dry powder onto an adhesive carbon tab attached to an Aluminium stub, and removing the surplus by compressed air followed by Platinum sputter coating. Figure 3-18 shows that the particles are spherical with the outer polymeric shell comprises gelled acrylic beads surrounding the platy paraffin core. As anticipated, EDS analysis revealed the elemental composition to be principally carbon and oxygen (acrylic and paraffin are hydrocarbons). This approach was designed to enable the author to reliably locate and identify PCM particles (as well as any ejected wax) within the highly varying textures of hardened concrete.
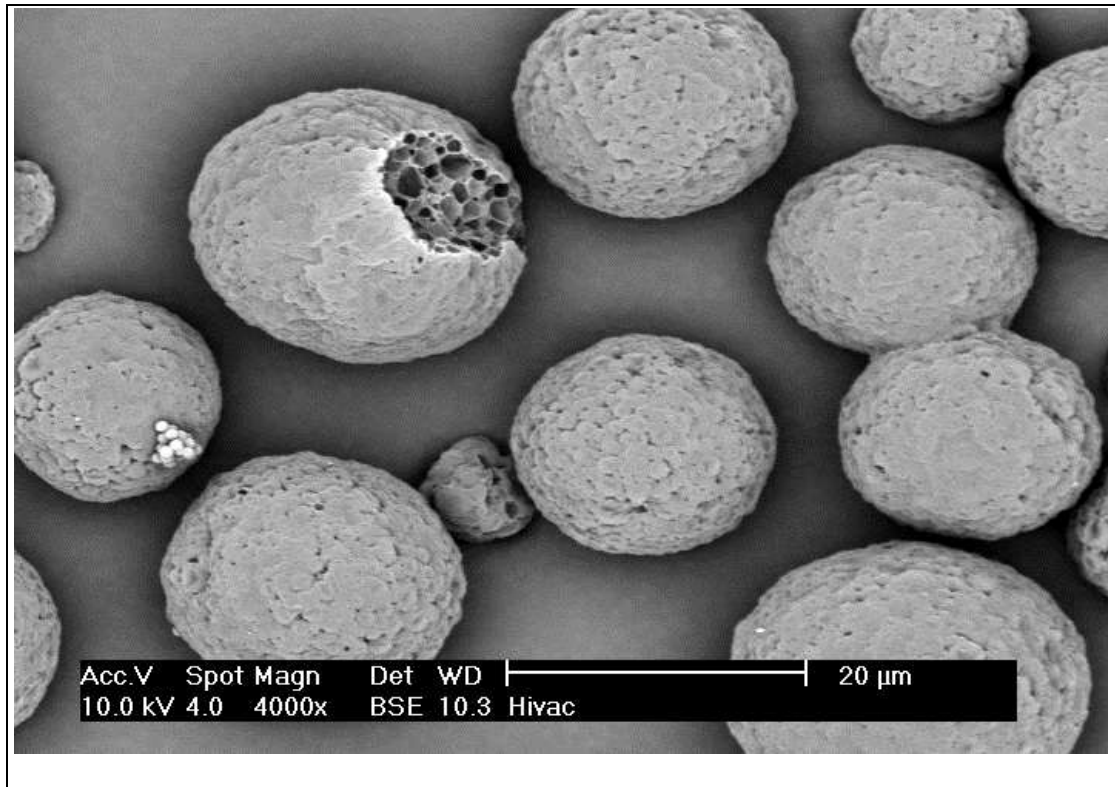
Figure 3-18 Spherical PCM particles comprising gelled acrylic beads surrounding the platy paraffin core

A concrete SEM sample was prepared as a small fragment prized away from a failed prism of the 40% PCM mix. The imaged surface was an untouched fracture surface from one of the central cracks running along the prism. The sample was mounted on an Aluminium stub with carbon cement, Platinum sputter coated, and imaged. Evidence of PCM particles was found to be well distributed throughout the hardened microstructure (see Figure 3-19).
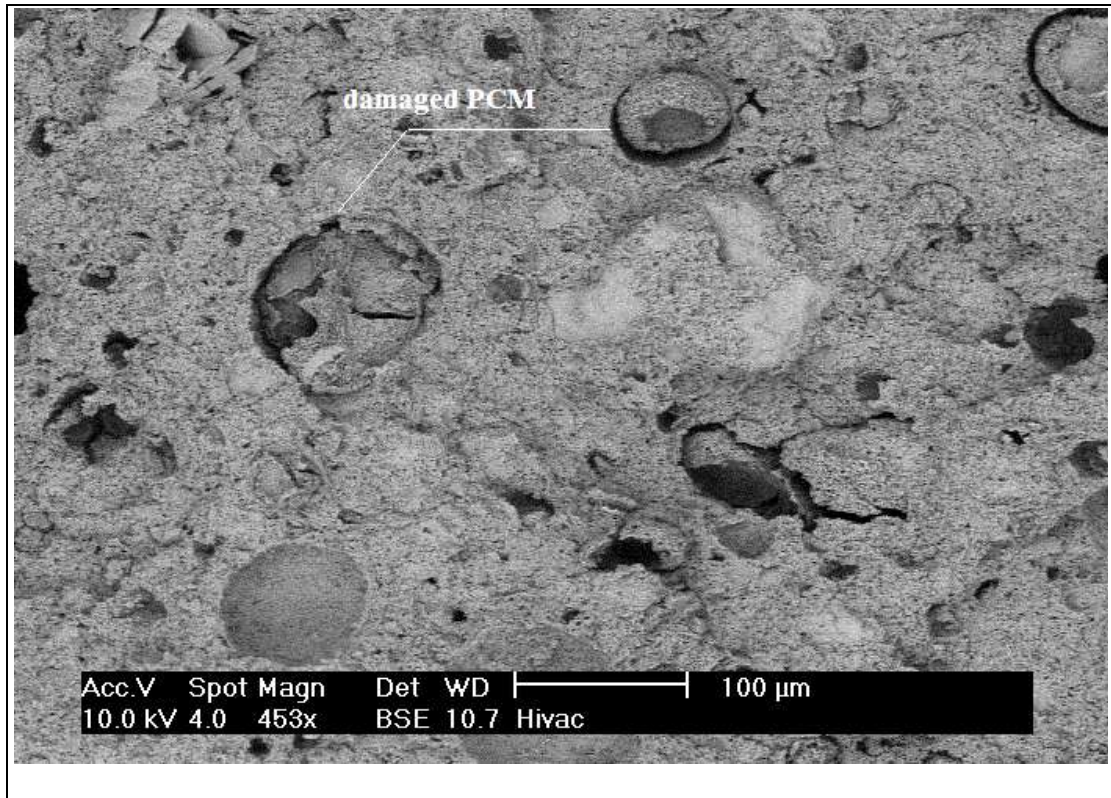
**Figure 3-19 SEM micrograph (using BSE detector) of concrete fracture surface showing
damaged/collapsed PCM particles**

Figure 3-20 shows an example of selected elemental mapping of the failed PCM particle identified with high Carbon concentrations, and adjacent cement microstructure with high Calcium and Silicon concentrations. From Figure 3-20 some evidence of wax dispersion across the adjacent sample surface can be observed. The presence of spherical voids as well as dispersed wax around the damaged PCM particle may suggest PCM particles were intact during the mixing and damage and subsequent ejection of the wax occurs during loading by bursting of PCM particles. The ejected paraffin wax from compressed PCM particles may escape into cracks and facilitate the crack propagation through their lubrication effect.
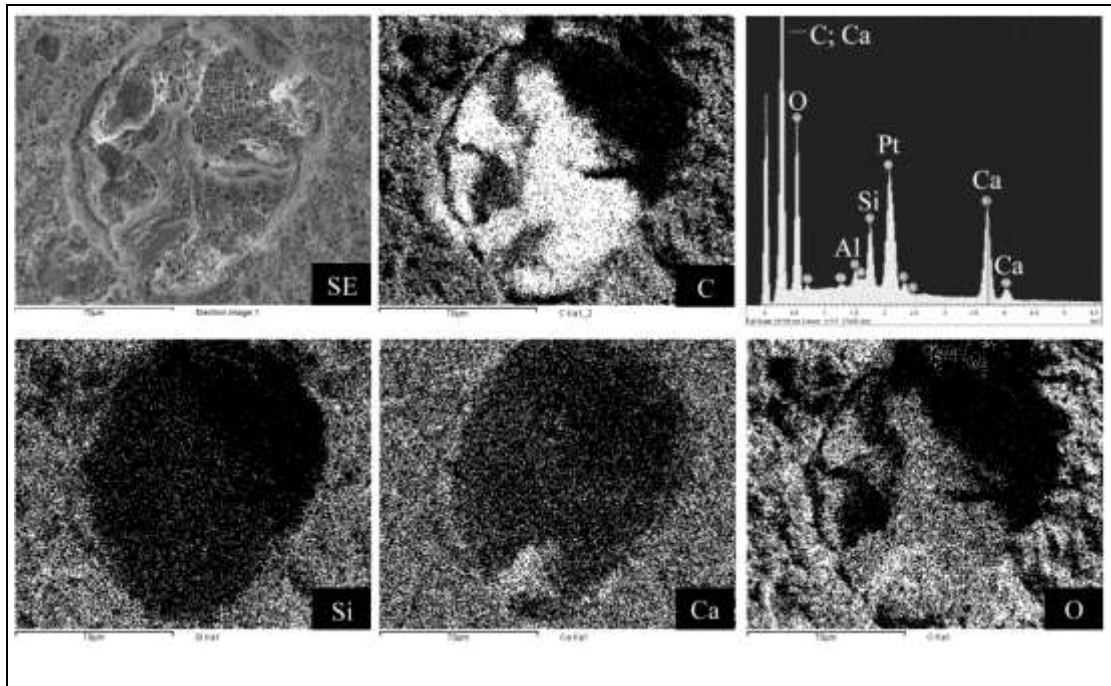
Figure 3-20 Elemental mapping using EDS spectral analysis shows a typical failed PCM particle, identified with regions of high Carbon concentration

As already shown in Figure 3-17, the relationship between apparent porosity (AP) and compressive strength of PCM-modified concrete does not follow the expected relationship. The reduction in compressive strength was predicted for different cases where 25%, 50%, 75%, and 100% of PCM capsules burst under loading and hence increase the porosity of the concrete. Figure 3-17 clearly shows that the increase in porosity as a result of PCMs bursting give a much better fit and approaches the expected porosity/strength prediction. To reduce or eliminate the reductions in mechanical strength, microencapsulated PCM particles with strong outer shells may be developed so that they will resist bursting under load. This point has also been discussed with an international industrial civil engineering company, LAFARGE, to produce artificial PCM-modified aggregates.

3.6. Asphalt Mix Design and Specimen Preparation

Four types of aggregates with different thermo-physical properties were used to produce asphalt mixes; these are Lytag, Copper slag, Quartzite, and Limestone. The aggregate gradation (see Figure 3-21) and mix design (see Table 2-3, Page 12) was selected in accordance with the Construction Support Team (Defence Estates 2008), for a wearing

course using AC. The specifications listed in Table 2-3 are particularly for limestone, there being no specification for the other aggregates used in the project. To generate alternative mix designs, the asphalt mixtures for the other aggregates were generated by replacing the limestone with the same volume of the replacement aggregates while keeping the remaining parameters (bitumen type and content, and aggregate grading) constant. All the alternative aggregates were crushed using a jaw crusher to provide the same grading as the control mix (see Figure 3-22). Due to the limited quantity of the larger sizes of Lytag and copper slag replacement aggregates, two different groups of mixes were produced as follows:

- Limestone whose nominal size is smaller than 10mm was replaced with Lytag, copper slag and quartzite.

- Two mixes were produced by fully replacing limestone aggregate with quartzite. One of the mixes in this group contained about 2% (by volume of the specimen) copper fibres.

All the aggregates were oven dried first and then mixed with bitumen in a mixer. Two slabs each, with dimensions of 300mm×300mm in area and a thickness of approximately 60 mm, were manufactured for all mixes. The slabs were compacted to the target density using a laboratory roller compactor. All the slabs were first subjected to thermal conductivity testing and then were cored and trimmed to produce ten specimens (100mm diameter with mean thickness of 40mm) for the mechanical test evaluations. The core specimens were, first, subjected to the Indirect Tensile Stiffness Modulus (ITSM) test, according to BS DD 213 (1993), which is a non-destructive test, next, the same specimens were subjected to the Indirect Tensile Fatigue Test (ITFT), according to BS DD ABF (2003), at different stress levels. In addition, two specimens (100mm diameter with mean thickness of 40mm) for each mix were also produced using gyratory compactor to perform the Repeated Load Axial Test (RLAT) according to the BS DD 226 (1996).
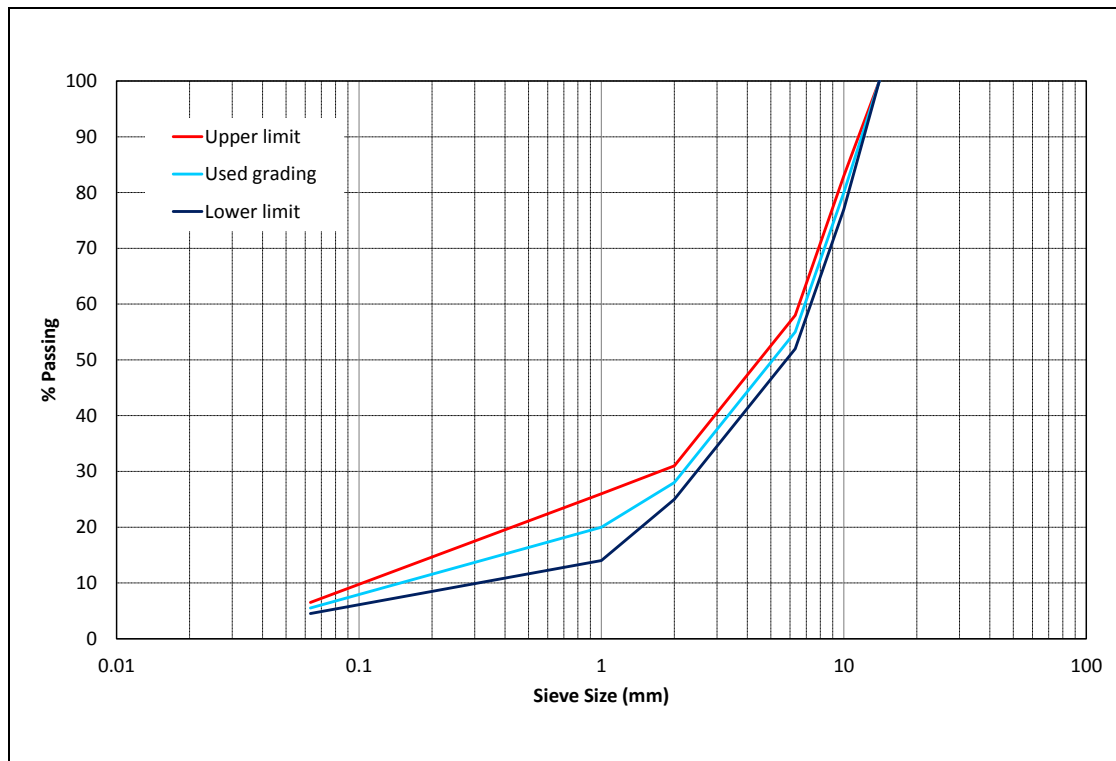
Figure 3-21 Aggregate grading used for the production of asphalt mixes
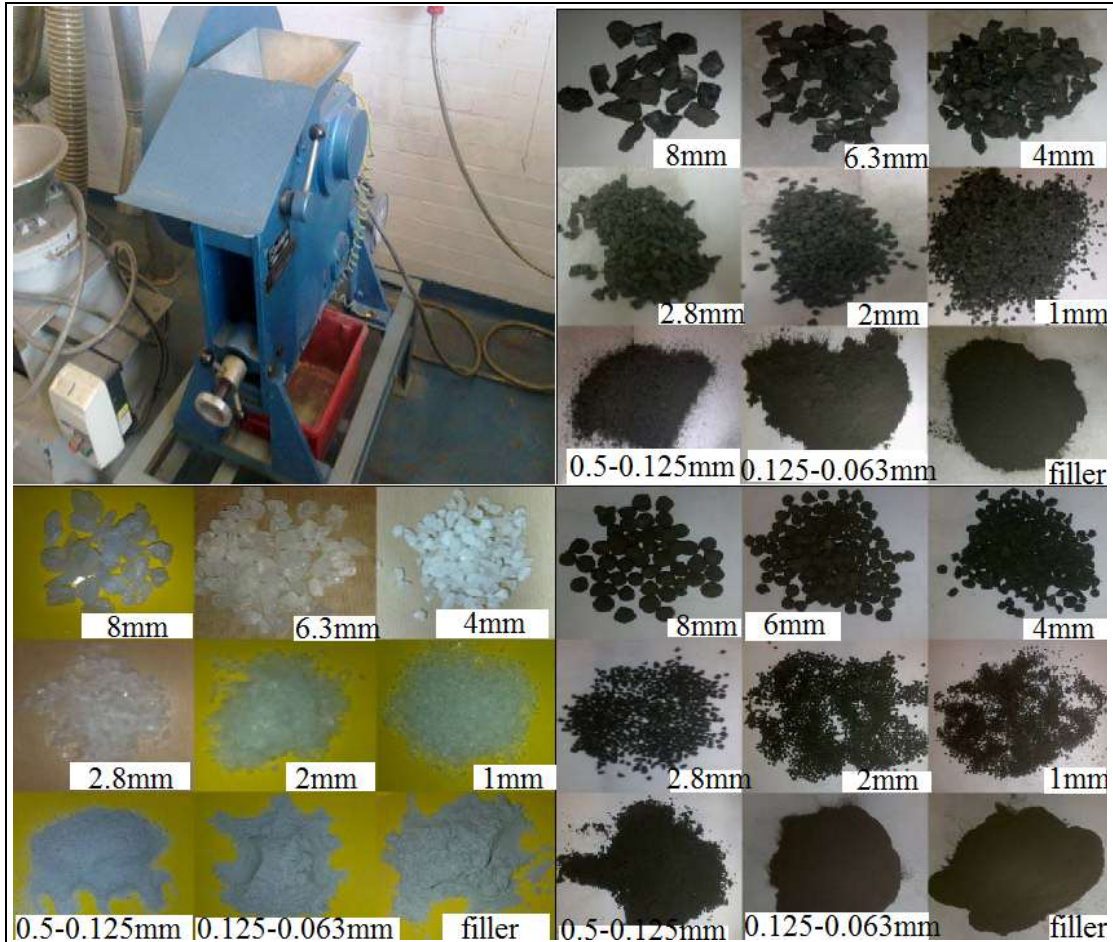
Figure 3-22 Jaw crusher used to provide grading for Copper slag (top right), Quartzite (bottom left), and Lytag (bottom right) asphalt mixes

3.7. Tests Performed on Asphalt Mixes

In this section only the results of thermo-physical tests on the asphalt mixes are presented due to their higher priority in this study as well as their use for the modelling purposes in the next chapters. The detailed mechanical testing performed on asphalt mixes is presented and discussed in the Appendix A and here only a summary of the properties are given as Table 3-8.

3.7.1. Testing Results and Discussions on the Asphalt Mixes

A variety of mechanical tests were performed on asphalt to assess stiffness, fatigue, and permanent deformation aspects. Details of tests and procedure are given in Appendix A and the results are summarised in Table 3-8. Table 3-8 shows the mean measured stiffness of all five mixes. The limestone mix has the highest stiffness modulus value of 1533MPa,

followed by the copper slag, and quartzite mixtures. The addition of metallic fibre seems to improve the stiffness by about 56% compared to the mix with no fibre. The low value for the stiffness of quartzite asphalt may be partly attributable to the relatively smooth faces of the quartzite aggregates (see Appendix A). The asphalt mix containing copper fibre showed the best resistance against fatigue (more load cycles needed to fail the specimen for the same horizontal strain). In addition, both quartzite mixes (i.e. partial and full aggregate replacement) achieved almost the same fatigue line, and the copper slag mix performed slightly better than the limestone mix. The higher fatigue life of the fibre mixture is most likely due to the high level of fibre interconnection that slows down the rate of crack propagation in the middle of specimen. The quartzite asphalt experienced by far the largest permanent strain. Once again, this could be due to its smooth surface resulting in poor bonding with bitumen and poor frictional properties.

Table 3-8 A Summary of Mechanical properties of asphalt mixtures

	Limestone (Control)	**Copper slag (partially replaced)**	**Quartzite+2%fibre**	**Quartzite (partially replaced)**	**100% Quartzite**
*Stiffness (ITSM)	1533	1022	922	740	591
*Fatigue line (ITFT), number of cycles @ 250$\mu\varepsilon$	$N_f = 2\text{E}+09\varepsilon^{-2.515}$ (1862)	$N_f = 3\text{E}+09\varepsilon^{-2.540}$ (2434)	$N_f = 2\text{E}+10\varepsilon^{-2.668}$ (8004)	$N_f = 1\text{E}+10\varepsilon^{-2.689}$ (3564)	$N_f = 1\text{E}+09\varepsilon^{-2.332}$ (2558)
*Permanent deformation (RLAT), Axial strain (%) @ 1000 cycles	0.36	0.37	0.78	0.73	0.81

 *See Appendix A for details

Table 3-9 shows that, again the thermal conductivity of asphalt mixes increases as the thermal conductivity of aggregate do so. Fully replacing limestone aggregates with quartzite can enhance the thermal conductivity by about 135%. Surprisingly, the addition of copper

fibres in asphalt mixtures did not increase the thermal conductivity as much as it did in concrete mixes and the thermal conductivity of fibre-modified asphalt was only enhanced by about 13%. This increase is unlikely to deliver a significant economic benefit given the typical cost associated with the purchase of copper fibre. This behaviour might be related to the fibre orientation in the asphalt mix. Figure 3-23 is a 3D image reconstructed from the 2D slices taken across the height of the fibre-modified asphalt specimen at 1mm slice spacing. Figure 3-23 shows many fibres, possibly during the compaction process, are lying close to the horizontal direction (perpendicular to direction of heat flow) and hence might not be able to convey heat as efficiently as possible in a fibre-modified asphalt mix.
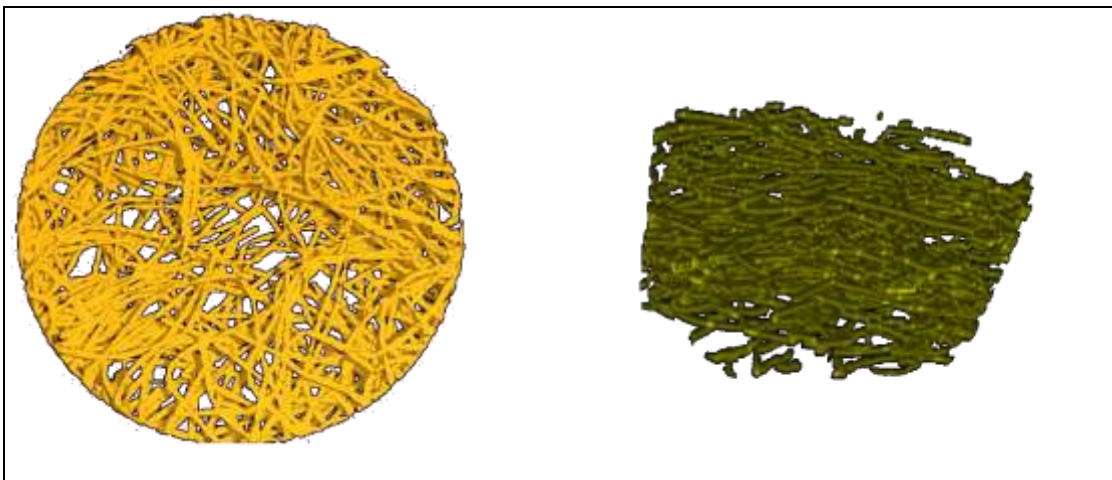
Figure 3-23 Formation of copper fibres in the asphalt specimen, X-Y view (left), 3D (right)

Table 3-9 also shows that, the thermal diffusivity of the asphalt mixes reduces due to the reduction of thermal conductivity as well as the increase in VHC (ρc_p). A thermal diffusivity of $\sim 3{\times}10^{-7}$ to $\sim 13{\times}10^{-7}$ can be achieved for asphalt pavements in this study. The slabs generated with Lytag were very weak. The aggregates did not bond well with the binder, especially at the corner of the slabs. For thermo-physical properties, one slab was tested and the results are shown in Table 3-9. The thermal conductivity was approximately half that of the value obtained for the control mix, reflecting the potential of Lytag asphalt to act as an insulating layer. Lytag asphalt might be used as an insulative layer in the lower pavement layers, where the low stiffness, short fatigue life and high deformation properties would be unlikely to hinder its use.

Table 3-9 Thermo-physical properties of asphalt mixtures

Mix No	Mix type	λ (W/m K)	c_p (J/kg K)	ρ (kg/m^3)	α ($\times 10^{-7}$) (m^2/s)	β (J/s$^{0.5}$ m^{2}K)	Air void (%)
1	Limestone (Control)	1.21±0.0	919	2382	5.5	1627	4.1
2	Quartzite (partially replaced)	1.46±0.01	880	2331	7.1	1731	4.0
3	Copper slag (partially replaced)	1.05±0.01	814	3088	4.1	1625	3.7
4	Quartzite (fully replaced)	2.40±0.07	870	2314	12.3	2230	4.2
5	Quartzite +2%Cu-fibre (fully replaced)	2.82±0.22	836	2472	13.6	2418	3.0
6	Lytag (partially replaced)	0.46	863	1504	3.5	773	-

3.8.   Summary

This chapter outlined the second objective of this study which was to determine the potential for optimisation of concrete and asphalt pavements for thermo-physical properties. The investigation in this chapter could be summarised as follows:

- The thermal conductivity of the concrete was directly and positively related to its degree of saturation as well as the thermal conductivity of its aggregates. However it was negatively related to the concrete porosity. Within the limitation of materials and mix design used in this study, it is feasible to provide mechanically acceptable PQC and LMC mixes to have a thermal conductivity range from ~0.5 to ~4 W/m K with Volumetric Heat Capacity (VHC) (ρc_p) ranging from 1.9×10^6 to 3.3×10^6 (J/m^3 K). The measured thermal conductivity and VHC can provide concrete with a thermal diffusivity ranging from ~2×10^{-7} to ~16×10^{-7} m^2/s. In addition, concrete's thermal effusivity increases with increase in the thermal conductivity and it ranges from ~1000 to ~3000 J/s$^{o.5}$ m^2 K for concrete pavements.

- Thermal diffusivity of the concrete can effectively be reduced by using the LWA and/or, to some extent, HWA. However, high conductive aggregates and/or addition of metallic fibres are the preferred way to increase the concrete's thermal conductivity and/or diffusivity.

- A relatively small addition of microencapsulated PCM results in an increase in heat capacity for modified concrete materials. However, PCM addition has a detrimental effect on the mechanical performance of concrete. The reduction in mechanical performance of concrete seems to occur as a result of PCM particles bursting under loading.

- In asphalt mixes, fully replacing limestone aggregates with quartzite can enhance the thermal conductivity by about 135%. The addition of copper fibre did not improve the thermal conductivity significantly, although it had a significant benefit on the stiffness and fatigue performance (see Appendix A). A thermal diffusivity of $\sim4\times10^{-7}$ to $\sim13\times10^{-7}$ m^2/s was achieved for asphalt pavements in this study.

4 NUMERICAL MODELLING OF HEAT TRANSFER IN PAVEMENTS

4.1. Overview

One of the objectives of this research was to develop an appropriate technique to calculate dynamic temperature profiles within pavement structures in order to simulate the performance of the Pavement Energy Systems (PESs). This chapter reports the development of a one-dimensional (1D) heat flow model using a finite difference solution method to achieve this. The model allows for a wide variety of climatic conditions and thermo-physical properties of the pavement layers to be applied. The model was validated against in-situ pavement data collected in the USA in widely differing climatic regions as well as data specifically collected, in the UK, for this study.

4.2. Modelling of Heat Transfer in Pavements

Temperature changes in pavements have been studied for many years since they have a significant impact on pavement performance under load-induced and thermal stresses and on service life. In flexible pavements (i.e. asphalt) the structural or load carrying capacity of pavement varies with temperature since hot-mix asphalt (HMA) is a 'visco-elastic' material (Solaimanian and Kennedy 1993; Hermansson 2004; Yavuzturk et al. 2005). In rigid pavements (i.e. concrete) temperature gradients across the concrete slab can cause structural defects such as warping and curling (Qin and Hiller 2011). Temperature variations in pavements can induce freeze-thaw cycles in the pavement which can often reduce their long-term stability (Dempsey and Thompson 1970; Mrawira and Luca 2002). In addition, the significant contribution that pavements can make to the Urban Heat Island (UHI) is well known, and previous studies attempted to predict this by numerically modelling near-surface temperature formation (Gui et al. 2007; Mallick et al. 2009). In this study the temperature changes in pavements were studied in order to determine the effect of pavement thermo-

physical properties and layer sequences on the performance of the PESs and other implications for pavement design.

In reality, the heat transport mechanisms in pavement materials (concrete, asphalt or unbound granular) are complex, as depicted in Figure 4-1, and can involve radiation between particles, convection in the pores, phase change processes, (vaporisation and condensation) as well as freeze-thaw processes. However, if pore sizes are negligibly small in relation to the volume of the structure under consideration, satisfactory modelling predictions can be made by reducing the complex heat transfer process to an equivalent conduction-only term (Brandl 2005). In addition, pavements represent a relatively large surface area. So, by neglecting edge effects the predictive model can be reduced to a 1D transient conduction model combined with a surface energy balance approach to predict the pavement temperature variations under given climatic variables. This simply requires the cross-sectional construction detail of the pavement and the thermo-physical properties of the materials to be known.
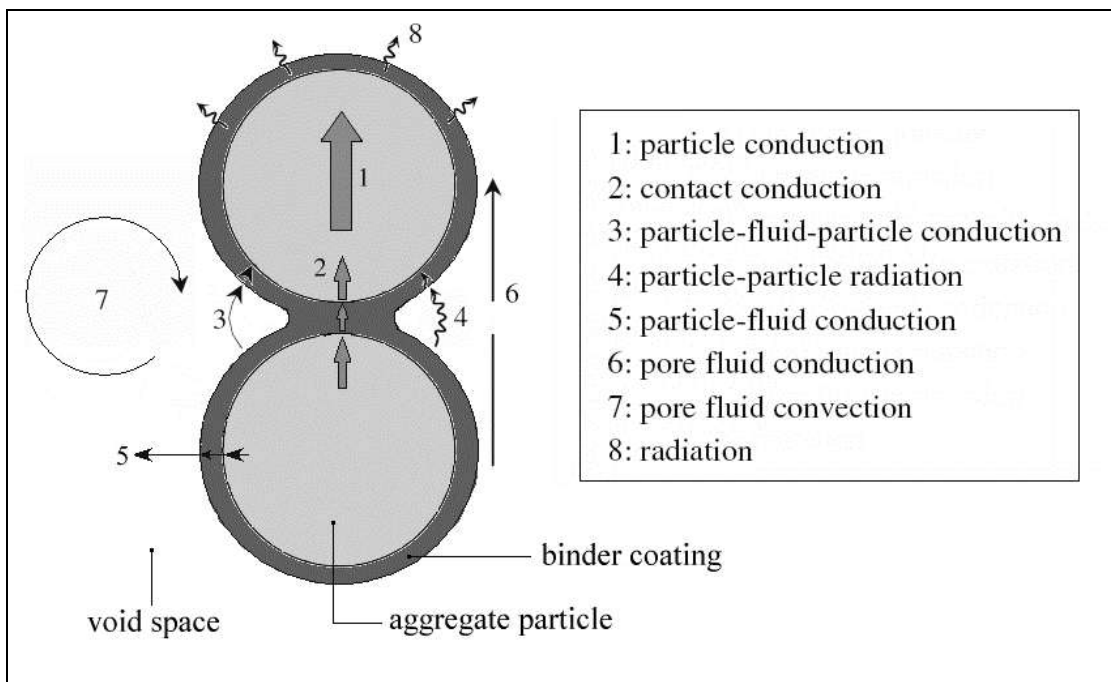
Figure 4-1 Heat transport mechanisms between binder-coated aggregate particles, Adapted from (Yun and Santamarina 2008)

4.2.1. Surface Energy Balance

The first law of thermodynamics, which is also known as the 'conservation of energy', states that energy cannot be destroyed or created, it can only change forms. The energy balance for any system undergoing any process can, therefore, be expressed as: *the net change (increase or decrease) in the total energy of the system during a process is equal to the difference between the total energy entering and the total energy leaving the system during that process* (Cengel 2002). The factors influencing the pavement surface energy balance, as well as the heat transport processes that occur within a pavement, are illustrated in Figure 4-2.
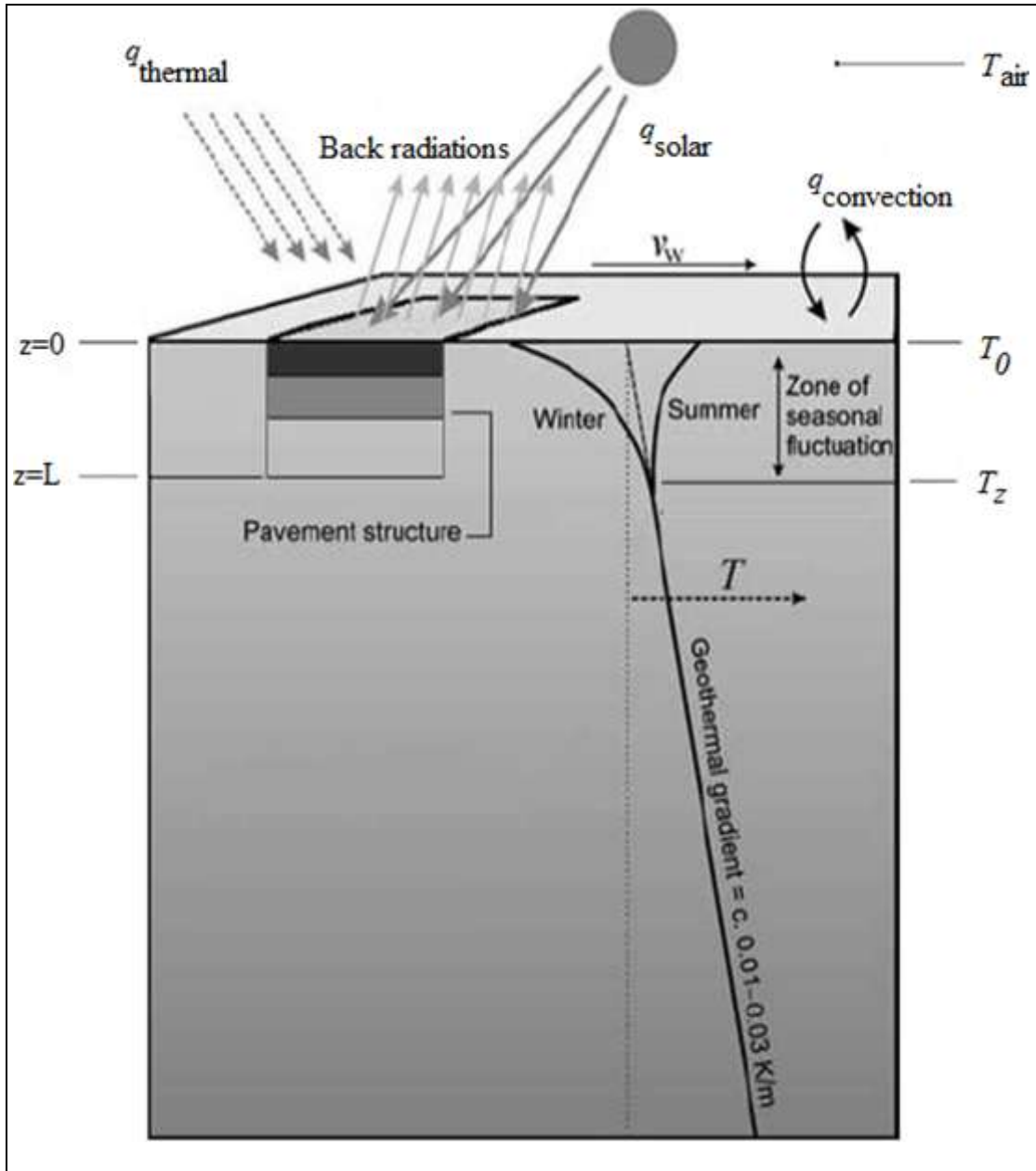
Figure 4-2 Cross-sectional illustration of surface energy balance, Adapted from (Banks 2008)

4.2.2. Solar Radiation Heat Flux

The absorbed solar (short-wave) radiation on the pavement surface can be calculated from:

$$q_{absorbed} = a q_{solar}$$

<div align="right">**Eq. 4-1**</div>

Surface absorptivity (*a*) is the fraction of solar energy that is absorbed by the surface. It is
normally a function of wavelength of the incoming radiation, surface colour, wetness,
average temperature of pavement, and age of pavement surface (Solaimanian and Kennedy
1993). The absorptivity of a pavement surface generally decreases during its lifetime as the

surface colour becomes lighter, and the reduction is quite marked in asphalt pavements (CIBSE 2006). This reduction might be due to the high susceptibility of bitumen to aging and/or aggregate polishing under traffic. Table 4-1 shows typical values used for the absorptivity of common pavement material surfaces.

Table 4-1 Solar absorptivity of pavement surfaces

Pavement types	Surface absorptivity (*a*)	References
Concrete	0.6-0.72	(Incropera et al. 2007)
Asphalt	0.82-0.93	(Solaimanian and Kennedy 1993; CIBSE 2006)

4.2.3. Thermal Radiation Heat Flux

Thermal (long-wave) radiation heat flux between the pavement surface and surrounding matter (i.e. the lower atmosphere, other buildings/objects) can be calculated as (Incropera et al. 2007):

$$q_{thermal} = \varepsilon\sigma(T_{surr}{}^4 - T_0{}^4)$$ **Eq. 4-2**

where

T_0= surface temperature (K)

T_{surr}= surrounding temperature (K)

Surface emissivity (ε) is a function of temperature, wavelength, and material type (Incropera et al. 2007). Typical values for emissivity of pavement surfaces are shown in Table 4-2.

Table 4-2 Emissivity of pavement surfaces

Pavement types	Surface emissivity (*ε*)	References
Concrete	0.85-0.95	(Bentz 2000; CIBSE 2006; Incropera et al. 2007)
Asphalt	0.85-0.98	(Solaimanian and Kennedy 1993; CIBSE 2006; Incropera et al. 2007)

T_{surr} (K) is a hypothetical temperature that represents the notional temperature of the surroundings objects and the lower atmosphere (air, clouds/water vapour). T_{surr} is normally expressed as a hypothetical temperature called 'sky temperature', T_{sky} (an approximation of T_{surr}). The value of T_{sky} depends on the atmospheric conditions and it ranges from ~230 K for

cold, clear-sky conditions to ~285 K for warm, cloudy-sky conditions (Cengel 2002). Some

researchers have simply used a reduction factor for air temperature to approximate T_{sky}

(Solaimanian and Kennedy 1993; Hermansson 2004). The modelling tool in this study

utilised the empirical Bliss equation as commonly used (Dempsey and Thompson 1970;

Bentz 2000; Chiasson et al. 2000; Yavuzturk et al. 2005; Gui et al. 2007; Qin and Hiller

2011) to calculate T_{sky} as follows:

$$T_{sky} = T_{air}(0.8 + \frac{T_{dp}}{250})^{0.25} \qquad \textbf{Eq. 4-3}$$

Where T_{dp} is the dew point temperature (°C) and can be calculated from the following

empirical relationship (Banks 2008).

$$T_{dp} = \frac{b \times \left[\frac{aT_{air}}{b + T_{air}} + \ln(\frac{RH}{100})\right]}{a - \left[\frac{aT_{air}}{b + T_{air}} + \ln(\frac{RH}{100})\right]} \qquad \textbf{Eq. 4-4}$$

a=17.271, b=237.7, RH= relative humidity (for, 0 °C< T_{air}<60 °C, 1%<RH<

100%,)

4.2.4. Convection Heat Flux at the Pavement Surface

Convection (natural and forced) accounts for heat transfer at the pavement surface and the

heat flux is calculated from:

$$q_{convection} = h_c(T_{air} - T_0) \qquad \textbf{Eq. 4-5}$$

There are many empirical models used by researchers in order to calculate convective heat

transfer coefficient (h_c) (see Palyvos (2008) for a summary). In this work, the three most

used empirical equations to predict temperature profiles in pavements, as listed in Table 4-3,

were assessed and a direct comparison between surface temperature predictions is reported

in Section 4.5.

Table 4-3 Models used to calculate convective heat transfer coefficient at pavement surface

Equations	Model	References
$h_c = 698.24 \times (0.00144 \times T_{ave}^{0.3} \times v_w^{0.7} + 0.00097 \times (T_0 - T_{air})^{0.3})$ $T_{ave} = (T_0 - T_{air})/2$	Vehrencamp	(Dempsey and Thompson 1970; Solaimanian and Kennedy 1993; Mrawira and Luca 2002; Hermansson 2004)
$h_c = 5.6 + 4.0 \times v_w$ For $v_w \leq 5 m/s$ $h_c = 7.2 \times v_w^{0.78}$ for $v_w > 5 m/s$	Jurges	(Bentz 2000; CIBSE 2006)
$h_c = \dfrac{k \times N_u}{L_c}$ $N_u = 0.664 \times Re^{0.5} \times Pr^{0.33}$ $Re = \dfrac{v_w \times L_c}{v}$	Horizontal flat plate approach	(Chiasson et al. 2000; Yavuzturk et al. 2005; Gui et al. 2007)

where; v_w: wind velocity (m/s), T_0: surface temperature (K), T_{air}: ambient air temperature (K), k: thermal conductivity of air at average air temperature (W/m K), N_u: Nusselt number (-), L_c: characteristic length, Re: Reynolds number (-), Pr: Prandtl number (-), v: Kinematic viscosity of air at average air temperature (m^2/s), h_c: convective heat transfer coefficient (W/m^2 k)

4.3. Finite Difference Grid and Boundary Conditions

The 1D vertical heat transport by transient conduction through the pavement can be modelled as a response to absorbed/desorbed energy at the pavement surface using an explicit form of the finite difference method. The cross-sectional pavement profile and the sub-soil beneath it can therefore be considered as a semi-infinite medium extending downward from z = 0 (pavement surface) to z = L, at which point seasonal temperature fluctuation is zero (see Figure 4-2). In reality, at a critical depth (usually several meters) the ground temperature is approximately constant as a result of thermal mass and so is largely unaffected by heating/cooling cycles at the pavement surface. This depth ranges approximately from 10-20m below the ground surface depending on the water content of the ground, and on the thermal properties of the soil. In the finite difference method, the pavement is comprised of a column of nodes as shown in Figure 4-3. The temperature at each boundary node is given by the energy balance equations as described below.
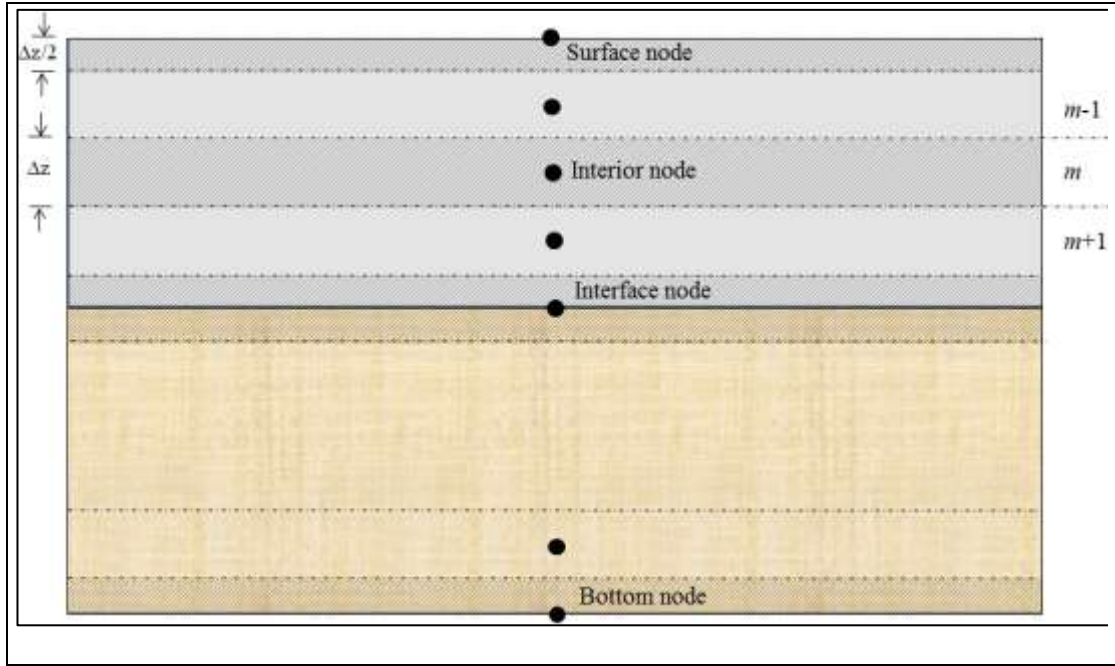
Figure 4-3 Control volume for different nodes in the Finite Difference grid

4.3.1. Surface Node

The energy balance implies that the rate of net energy (solar radiation gains, air convection gains/losses, thermal radiation gains/losses, and thermal conduction to/from pavement beneath the surface) equals the rate of change in internal energy in a control volume. Therefore, the numerical solution to the boundary condition at the pavement surface can be calculated by Eq. 4-6.

$$\rho_d c_p \frac{\Delta z}{2} \frac{T_0^{i+1} - T_0^i}{\Delta t} = q_{absorbed} + q_{convection} + q_{thermal} + q_{conduction}$$

Substituting the heat fluxes and solving for T_0^{i+1} gives:

$$T_0^{i+1} = \frac{2\Delta t}{\rho_d c_p \Delta z}\left[aq_{solar} + h_c(T_{air} - T_0) + h_{rad}(T_{sky} - T_0) + \lambda \frac{T_1^i - T_0^i}{\Delta z}\right] + T_0^i \qquad \textbf{Eq. 4-6}$$

where:

i= counter for time step (i=0 corresponding to specific initial condition)

Δt= time step (s)

ρ_d= dry density (kg/m^3)

c_p= specific heat capacity (J/kg K)

Δz= node distance

h_{rad}= radiation heat transfer coefficient (W/m^2 K)=$\varepsilon\sigma\left(T_0 + T_{sky}\right)\left(T_0^2 + T_{sky}^2\right)$

T_1= temperature at first node beneath the surface node (K)

a= solar absorptivity

4.3.2. Interior Nodes

For interior nodes, the rate of heat conduction across a volume element of thickness Δz equals the change in the energy content of the element during a time interval Δt, therefore:

$$\lambda\frac{T_{m-1}^i - T_m^i}{\Delta z} - \lambda\frac{T_m^i - T_{m+1}^i}{\Delta z} = \rho_d c_p \Delta z \frac{T_m^{i+1} - T_m^i}{\Delta t}$$

Solving for T_m^{i+1} gives:

$$T_m^{i+1} = \frac{\alpha\Delta t}{\Delta z^2}\left[T_{m-1}^i - 2T_m^i + T_{m+1}^i\right] + T_m^i \qquad \textbf{Eq. 4-7}$$

where:

α= thermal diffusivity (m^2/s)

m= number of nodal points (1, 2 …n)

4.3.3. Interface Nodes

The temperature of the interface nodes between layers of the pavement structure (e.g. the contact between surface layer and base layer) can be calculated from Eq. 4-8. It was assumed that the two different layers were in perfect contact and thus the energy balance for the interface control volume can be written as follows:

$$\lambda_1\frac{T_{m-1}^i - T_m^i}{\Delta z} - \lambda_2\frac{T_m^i - T_{m+1}^i}{\Delta z} = \rho_1 c_{p1}\left[\frac{T_m^{i+1} - T_m^i}{\Delta t}\right]\frac{\Delta z}{2} + \rho_2 c_{p2}\left[\frac{T_m^{i+1} - T_m^i}{\Delta t}\right]\frac{\Delta z}{2}$$

This can be solved for T_m^{i+1} to give:

$$T_m^{i+1} = \frac{\frac{\lambda_1}{\Delta z}T_{m-1}^i + \frac{\lambda_2}{\Delta z}T_{m+1}^i - \left[\frac{\lambda_1}{\Delta z} + \frac{\lambda_2}{\Delta z} - \frac{\rho_{d1}c_{p1}\Delta z}{2\Delta t} - \frac{\rho_{d2}c_{p2}\Delta z}{2\Delta t}\right]T_m^i}{\frac{\rho_{d1}c_{p1}\Delta z + \rho_{d2}c_{p2}\Delta z}{2\Delta t}} \qquad \textbf{Eq. 4-8}$$

4.3.4. Bottom Node

The temperature of bottom node (the last node in Finite Difference grid) can be calculated from Eq. 4-9. The energy balance for corresponding node can be written as follows:

$$\lambda \frac{T_{m-1}^{i} - T_{m}^{i}}{\Delta z} = \rho_d c_p \frac{\Delta z}{2} \frac{T_{m}^{i+1} - T_{m}^{i}}{\Delta t}$$

Solving for T_m^{i+1} gives:

$$T_m^{i+1} = \frac{2\alpha\Delta t}{\Delta z^2}\left(T_{m-1}^{i} - T_{m}^{i}\right) + T_{m}^{i} \qquad \text{Eq. 4-9}$$

4.4. Stability Criterions

The explicit method is not unconditionally stable, and the largest permissible value for the time step is limited by stability criterions. *The stability criterion is satisfied if the coefficients of all T_m^i in the T_m^{i+1} expressions (called the primary coefficients) are greater than or equal to zero for all nodes* (Cengel 2002). In the case of transient 1D heat conduction, the primary coefficients (from re-arranging Eq. 4-7) can be written as $\left(1 - \frac{2\alpha\Delta t}{\Delta z^2}\right)$. Therefore, the upper limit for all interior nodes was given by Eq. 4-10 (Cengel 2002; Incropera et al. 2007):

$$\Delta t \leq \frac{0.5\Delta z^2}{\alpha} \qquad \text{Eq. 4-10}$$

The primary coefficients for the surface node, from re-arranging Eq. 4-6, can be written as:

$$\frac{\rho_d c_p \Delta z}{2\Delta t} - \frac{\lambda}{\Delta z} - h_{rad} - h_c$$

Therefore, permissible value for the time step can be expressed as follows (Gui et al. 2007):

$$\Delta t \leq \left[\frac{\rho_d c_p \Delta z^2}{2(h_{rad}\Delta z + h_c\Delta z + \lambda)}\right] \qquad \text{Eq. 4-11}$$

In order to find the most restrictive value for Δt, first a value for Δz must be considered and then the maximum value of α (value in range of pavement materials) was inserted in Eq. 4-10. In addition, the minimum value for ρ_d and c_p as well as a maximum logical value for h_{rad}, h_c, and λ have to be inserted in Eq. 4-11. The minimum (i.e. most restrictive) value for Δt should then be used to provide the solution.

The initial condition at t = 0 assumed a constant uniform temperature distribution within the pavement. Eq. 4-6, Eq. 4-7, and Eq. 4-8 were compiled in Microsoft Excel 2010, and then solved iteratively in order to predict the temperature depth profile evolution at a given time interval. The environmental input parameters required for the model were hourly (or more frequently) solar irradiation, dry bulb air temperature, relative humidity (or dew point temperature) and mean wind velocity. The inputs were interpolated linearly across each hour period in order to achieve Δt (s) interval required for the model. In addition to surface absorptivity and surface emissivity, the pavement material thermo-physical properties and layers thickness were also required.

4.5. Model Validations

The majority of the models reported are developed to predict the pavement surface temperature (Solaimanian and Kennedy 1993; Bentz 2000; Hermansson 2004; Yavuzturk et al. 2005; Gui et al. 2007; Mallick et al. 2009; Qin and Hiller 2011) and therefore, are not validated against the temperature profiles within pavement structures. Since the model developed in this study is used for the temperature predictions within pavements therefore, it was validated at different depths (surface to 1m depth) using a large set of data (up to two years).

4.5.1. Validation Using LTPP Data

The Long-Term Pavement Performance (LTPP) program began in 1987 as part of the U.S. Strategic Highway Research Program (SHRP). It was envisioned as a comprehensive program to satisfy a wide range of pavement information needs to assess long-term performance of pavements under various loading and environmental conditions. The program involved nearly 800 pavement test sections throughout the United States and Canada. The Seasonal Monitoring Program (SMP) was part of the program performed on sixty three different test locations to measure the impact of daily and yearly temperatures on pavement structures (US Department of Transportation–Federal Highways Administration

2009). SMP data has since been used as a basis for validation of some pavement temperature prediction models (Solaimanian and Kennedy 1993; Hermansson 2004; Yavuzturk et al. 2005).

An investigation on the raw LTPP-SMP data sets showed a number of problems with individual weather and pavement data. In many cases, the time of collected weather data do not match the time of collected pavement temperature data. In addition, some weather and pavement data sets contained gaps that might be due to the failing of equipment (e.g. temperature sensors, data loggers, etc.) at the site. Most importantly, the LTPP database did not contain the thermal properties (thermal conductivity and specific heat capacity) and the thermal characteristics (surface absorptivity and emissivity) of the pavement test sections. It was therefore, somewhat unrealistic to obtain a fully satisfactory model validation and using published values for the missing data may limit the accuracy of the models only validated with LTPP data (Solaimanian and Kennedy 1993; Hermansson 2004; Yavuzturk et al. 2005). Nevertheless, an attempt was made to validate the model in four widely differing climate regions. The climatic region and mean climatic variables for each test site along with the corresponding latitude and longitude of the pavement test sections are summarised and compared in Table 4-4. The predicted temperatures were modelled at two depths within the pavement; near-surface (<25mm), and mid-depth (100-300mm). The precise value for 'z' in each of the two depth categories varied depending upon the precise position of the thermocouples at the four different LTPP project locations, as shown by the cross-sectional construction details of the test pavements in Figure 4-4. Thermo-physical material properties for each layer, shown in Figure 4-4, were selected from the results presented in Chapter 3 and other references for soil and pavement base course materials (ASHRAE 1995; Côté and Konrad 2005). The default absorptivity and emissivity values used in the modelling were taken as the average of published values. The finite difference grid consisted of a time step of $\Delta t = 30s$ and layer spacing of $\Delta z = 0.02m$.

Table 4-4 Climatic variables for the simulated test conditions in each of the four locations, data source from (US Department of Transportation–Federal Highways Administration 2009)

Pavement Location [*](latitude and longitude)	Climate type		T_{air} (°C)	RH (%)	q_{solar} (W/m^2)	v_w (m/s)
Arizona [*](33.4490, -112.7218)	Warm/hot-dry	Mean	24.9	14	536	2.0
		Max	38.1	35	1026	7.0
		Min	11.9	4	0	0.3
Alabama [*](32.6284, -85.2814)	Warm-humid	Mean	26.3	75	404	1.5
		Max	35.4	100	983	4.8
		Min	17.1	26	0	0
Delaware [*](38.7852, -75.4387)	Mixed-dry	Mean	2.1	63	202	1.4
		Max	17.8	96	513	5.4
		Min	-13.0	25	0	0
Ohio [*](40.3846, -83.0737)	Cool-dry	Mean	21.7	82	386	1.2
		Max	30.8	100	899	3.3
		Min	8.8	36	0	0.1
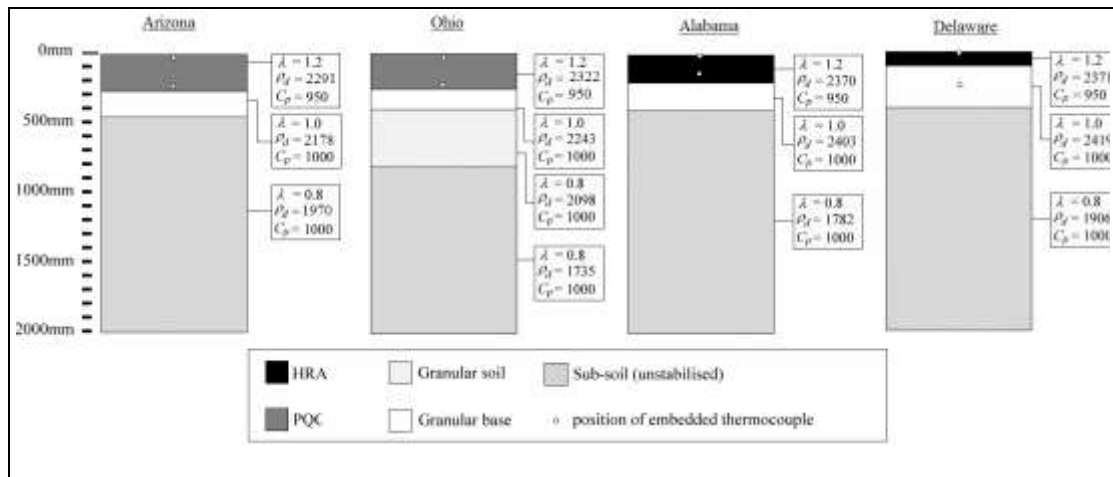
Figure 4-4 Cross-sectional designs of the four selected LTPP test pavement structures

Assessment of Convective Heat Transfer Coefficients (h_c)

Different convective heat transfer coefficients, as presented in Table 4-3, were assessed for two different regions and pavement types (i.e. concrete and asphalt). Figure 4-5 and Figure 4-6 show a direct comparison between surface temperature predictions and LTPP experimental monitoring data for Alabama and Arizona, respectively. It can be observed that the predicted temperatures using 'Jurges' and 'horizontal flat plate' estimations were very close and could achieve a slightly higher level of accuracy than that of 'Vehrencamp'. The

105

root mean-squared errors (RMSE), which is one of the most commonly used measures of success for numeric prediction, was calculated using Eq. 4-12. The RMSE show that 'Vehrencamp' estimation had the highest error and normally overestimates the temperature.

$$\text{RMSE} = \left[n^{-1} \sum_{i=1}^{n} (p_i - m_i)^2 \right]^{1/2} \qquad \textbf{Eq. 4-12}$$

where,

n= number of temperature readings for each interval

p_i= predicted temperature at each time interval (i=1,2,…,n)

m_i= measured temperature at each time interval (i=1,2,…,n)

According to heat transfer theory, convective heat transfer consists of two parts: free and forced convections (Cengel 2002). The free convection term in 'Jurges' equation is fixed at 5.6 however, this term in 'Vehrencamp' equation will be close to zero when $v_w \rightarrow 0$ (i.e. 698.24×0.00097×(T_0-T_{air})$^{0.3}$) is minimal when $v_w \rightarrow 0$). Therefore, the 'Vehrencamp' equation, in the case of free convection (no wind), over-predicted the surface temperature and increased the total error. In this project, the empirical 'Jurges' equation was applied in the modelling tool due to its slightly higher accuracy and less computational time for the model. It must be noted that when the 'horizontal flat plate' approach was used to predict h_c, a temperature-dependant function was needed for each parameter (i.e. thermal conductivity of air, Prandtl number, and kinematic viscosity of air) (see Table 4-3). The temperature-dependant functions were derived from thermo-physical properties of air at various temperatures (Incropera et al. 2007).
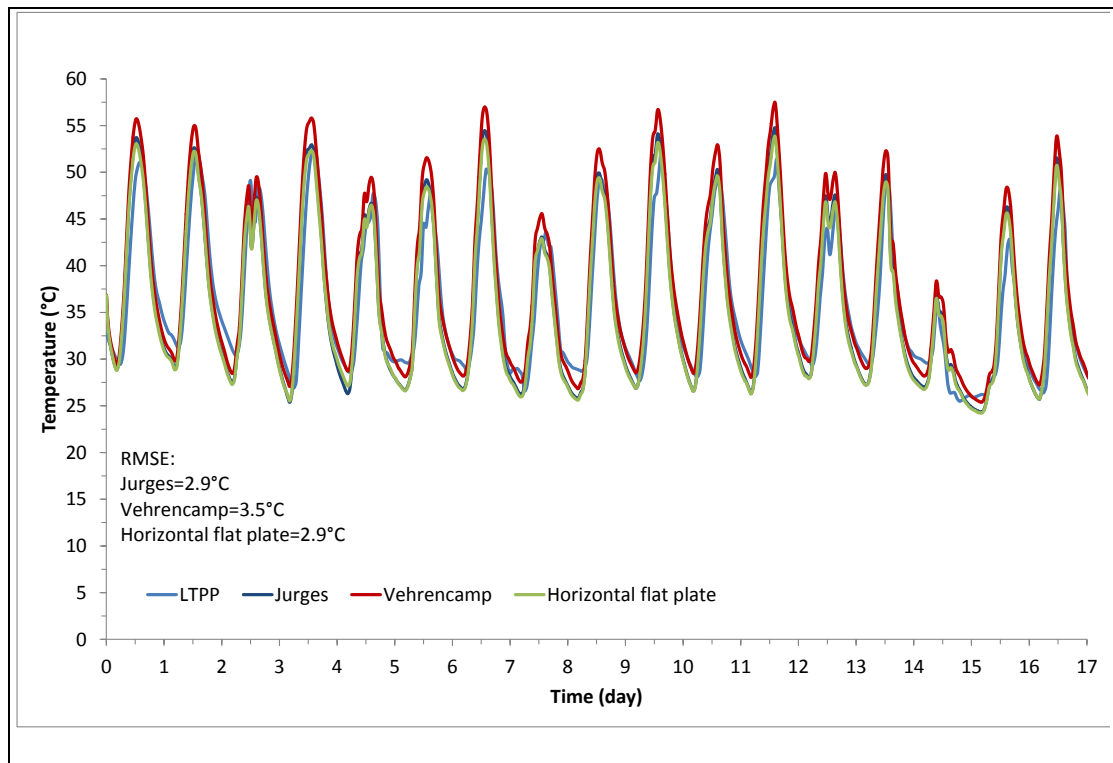
Figure 4-5 Sensitivity comparison for near-surface temperature approximations due to convective heat transport in Alabama
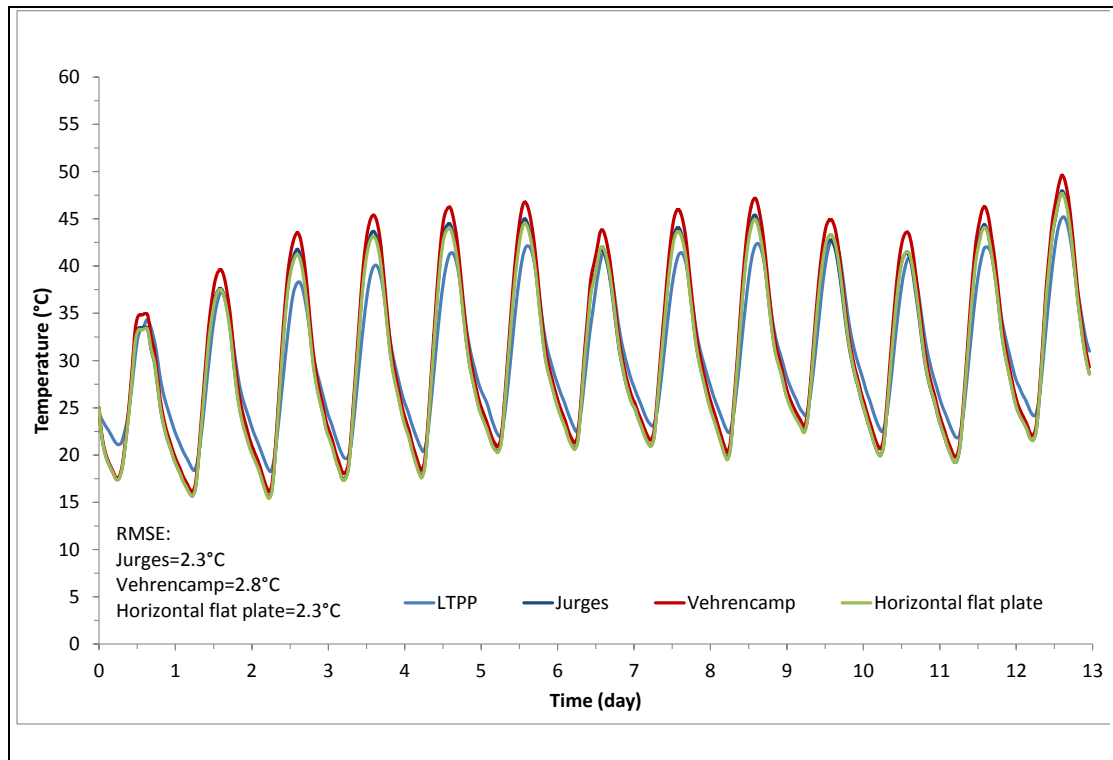
Figure 4-6 Sensitivity comparison for near-surface temperature approximations due to convective heat transport in Arizona

Validation Against LTPP Experimental Data

The comparison between the predicted near-surface and mid-depth temperature profile evolution, and the actual SMP recorded data, was made for each of the four test locations detailed above, see Figure 4-7 to Figure 4-10. Figure 4-9 and Figure 4-10 only show the mid-depth temperature profiles for Alabama and Arizona since the near-surface temperature profiles were already shown in Figure 4-5 and Figure 4-6.
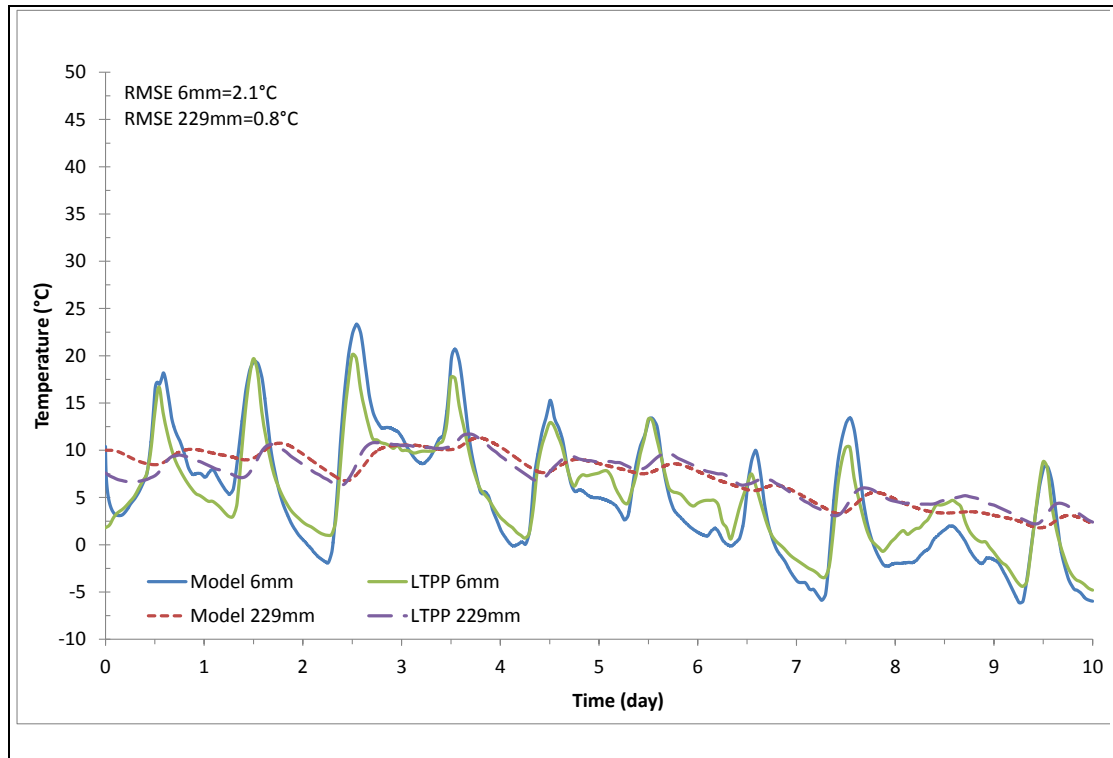
Figure 4-7 Model validation for near-surface and mid-depth temperature profile evolution against LTPP experimental data for the Delaware test site
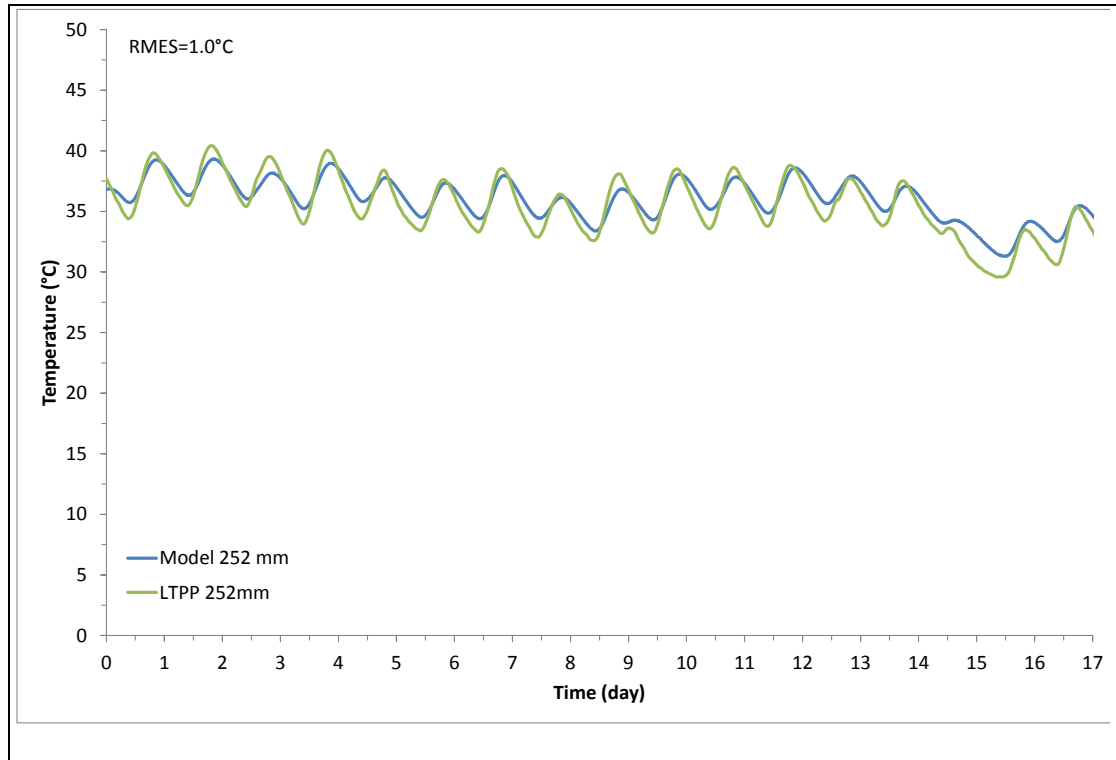
Figure 4-8 Model validation for mid-depth temperature profile evolution against LTPP experimental data for the Alabama test site
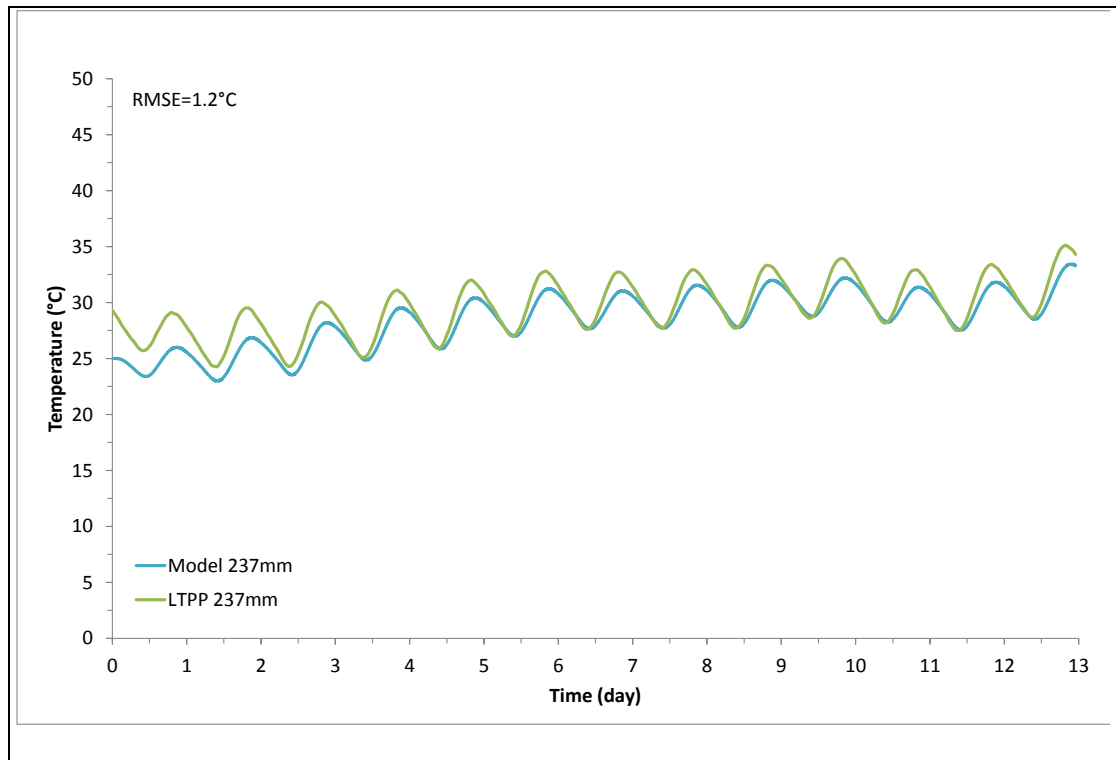
Figure 4-9 Model validation for mid-depth temperature profile evolution against LTPP experimental data for the Arizona test site
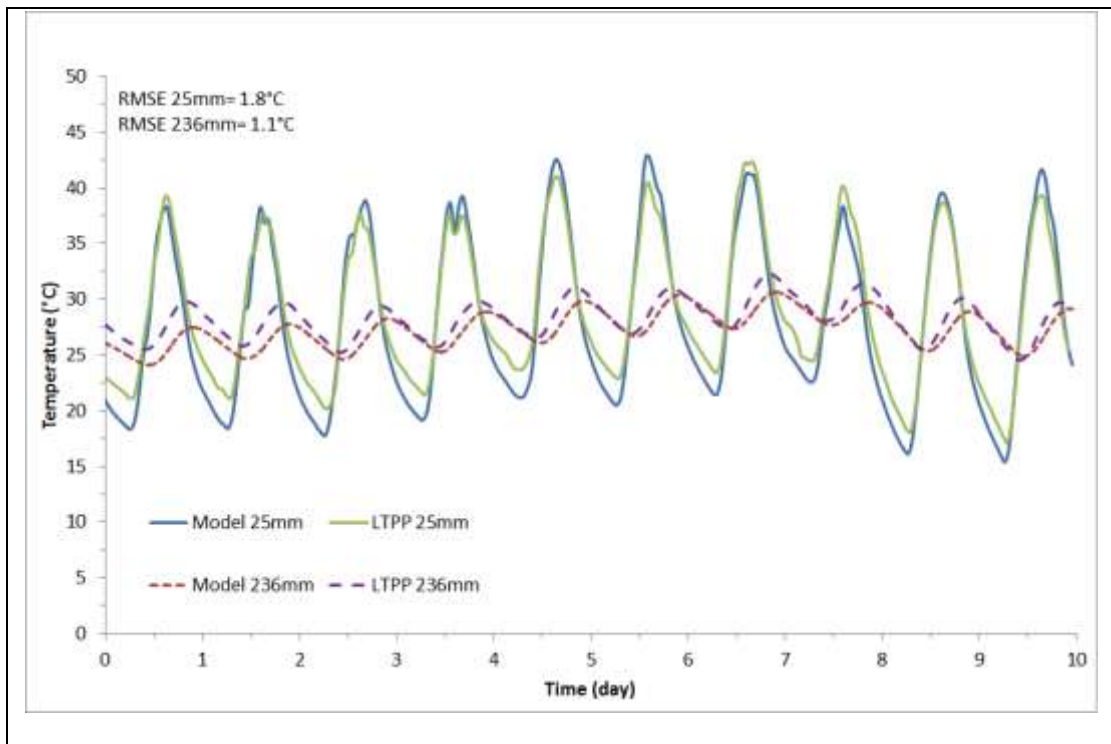
Figure 4-10 Model validation for near-surface and mid-depth temperature profile evolution against LTPP experimental data for the Ohio test site

4.5.2. Validation Using Sutton Bonington (UK) Data

The modelling tool was further validated against a more continuous set of data. Measured temperatures in the ground at depths of 100, 300, and 1000 mm below a grass-covered surface were used to validate the model (see Figure 4-11, Figure 4-12, and Figure 4-13). These temperatures along with weather data were collected from a meteorological site at the University of Nottingham, the Department of Agriculture, Sutton Bonington, UK (52.8282°N 1.2485°W). The climatic variables across a two-year period were available. The surface absorptivity and emissivity values used for a grass covered surface in the model were 0.75 (CIBSE 2006) and 0.94 (Incropera et al. 2007), respectively. The Sutton Bonington field site had a top soil which was a sandy loam (~90% sand and silt) soil with an average bulk density of 1510 kg/m³ (Atkinson et al. 2007). Therefore, the soil was modelled as ~1m top soil of sandy loam on top of clay. The thermo-physical properties used in the model for top soil were λ=0.86 W/m K, ρ=1510 Kg/m³, c_p=1000 J/kg K and for clay were

λ=1.3 W/m K, ρ=2100 kg/m^3, c_p= 1000 J/kg K as suggested by ASHRAE (1995). The finite difference grid consisted of a Δt=1800s and Δz=0.1m.

Table 4-5 Mean climatic variables across a two-year period in Sutton Bonington

	T_{air} (°C)	RH (%)	q_{solar} (W/m^2)	v_w (m/s)
Mean	10.8	3	211	3.5
Max	28.5	100	891	14.9
Min	-6.1	0	0	0.0
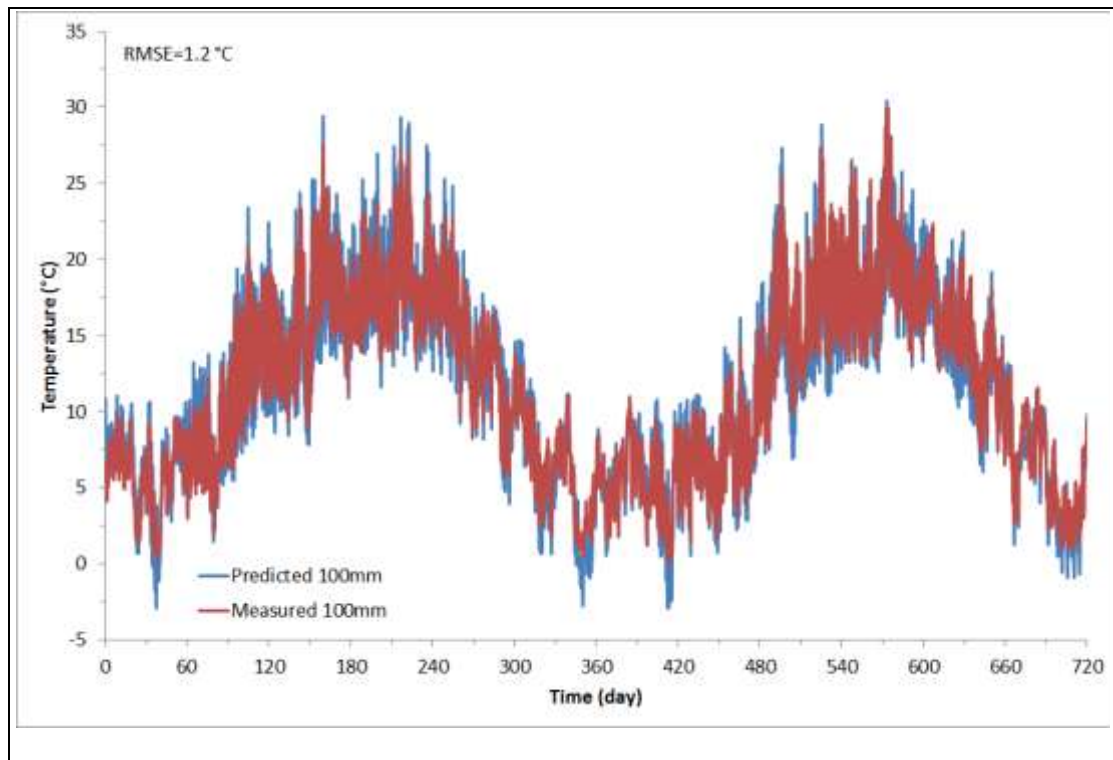
Figure 4-11 Model validation for 100 mm temperature profile evolution against Sutton Bonington experimental data
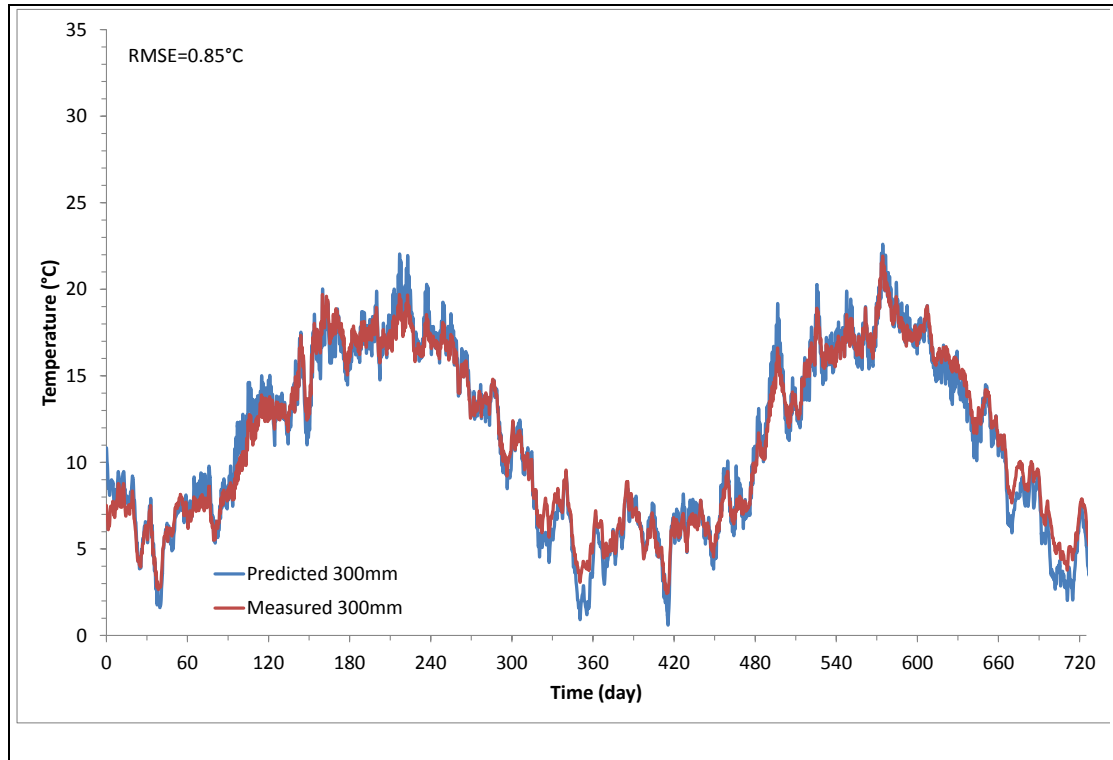
Figure 4-12 Model validation for 300 mm temperature profile evolution against Sutton Bonington experimental data
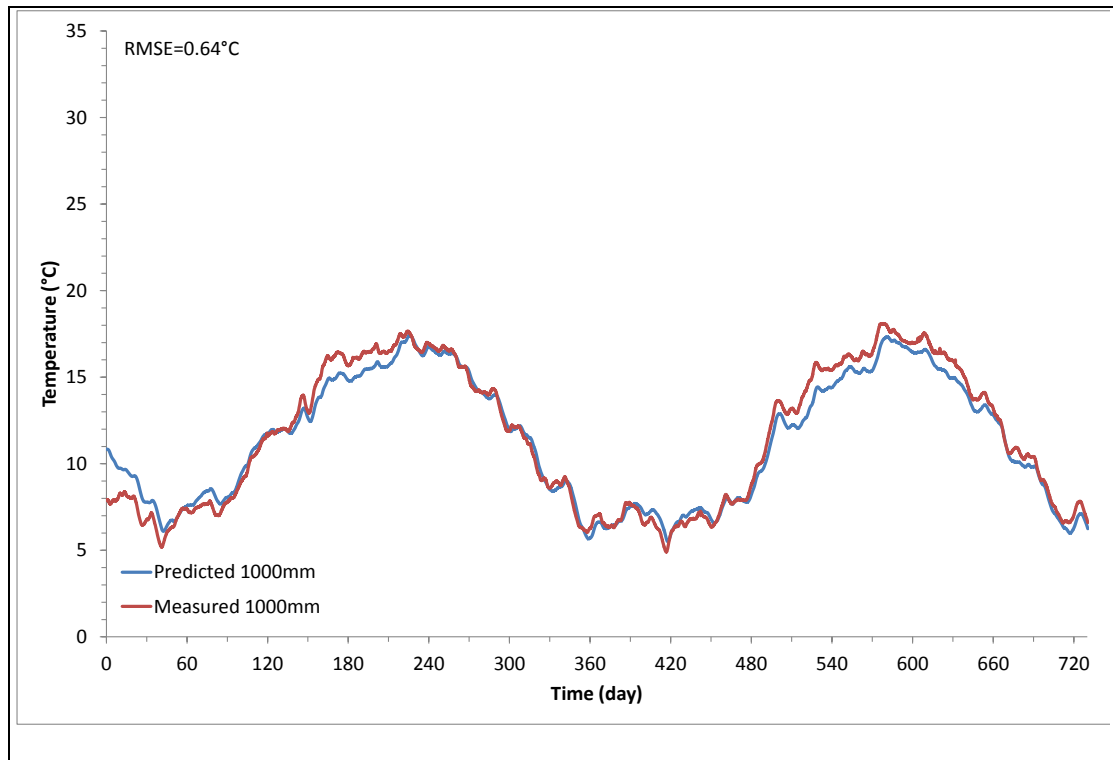
Figure 4-13 Model validation for 1000 mm temperature profile evolution against Sutton Bonington experimental data

112

4.6.   Discussions and Summary

A numerical modelling tool of 1D transient thermal conduction was presented for predicting temperature profile evolution in pavement structures. The model was well validated in four contrasting climatic regions using accepted long-term monitoring data from the SMP programme as part of the LTPP project as well as experimental field data specifically collected for this study.

When compared against these data, the model predicts the near-surface (<25mm) temperature with a RMSE of about 2°C. The accuracy of the model to predict temperatures increased with depth. With increasing depth, the uncertain effects of empirical equations (i.e. equations to predict convection and thermal radiations) were minimised and temperature variation in the ground remained more constant. Therefore, the RMES for mid-depth (100-300mm) temperature and high-depth temperature (>1000 mm) were about 1.0°C and 0.5°C, respectively. This was at least the same level of accuracy as was achieved in previous attempts to model pavement temperature profile evolution using a 1D transient conduction approach with dry state material thermo-physical properties (Dempsey and Thompson 1970; Solaimanian and Kennedy 1993; Hermansson 2004; Yavuzturk et al. 2005; Gui et al. 2007) and when using a 3D ANSYS finite element model (Minhoto et al. 2005). The numerical technique did not model moisture movement between atmosphere and pavement, nor in the pavement voids. This is an inherent limitation which may be the cause of some of the inaccuracies described earlier. Probably it would be necessary to include these aspects for further improvement.

5   PIPE-PAVEMENT HEAT EXCHANGE INVESTIGATIONS

5.1.   Overview

The model presented in the previous chapter has been shown to be a good tool for predicting the temperature distributions within the pavement. However, in order to simulate the performance of the PESs (see Figure 1-1) for quantifying the transfer of heat from the pavement to the working fluid in the pipe, the model needs to be modified to take account for the internal fluid flow through the pipes. Therefore, the first part of this chapter details development of a heat flow model that allows for any configurations of the PES to be simulated under any climate. The second part of this chapter includes the design and construction of a large-scale physical model of the PESs to carry out laboratory testing in order to validate the model.

In addition to the model development, the performance of the thermally modified concrete and asphalt pavement structures were compared with those of conventional ones. The Interfacial Zone (IZ) between embedded pipes and the pavement's materials in the PESs were investigated using X-Ray Computed Tomography (XRCT) and the observations were correlated to the performance of the PES.

5.2.   Model Development

The main heat transfer mechanisms acting upon a pavement slab were already shown in Figure 4-2, Page 96. However, to model the performance of the different PES, the mechanism of heat transfer from the pavement to the working fluid flow, as shown in Figure 5-1, must be considered.
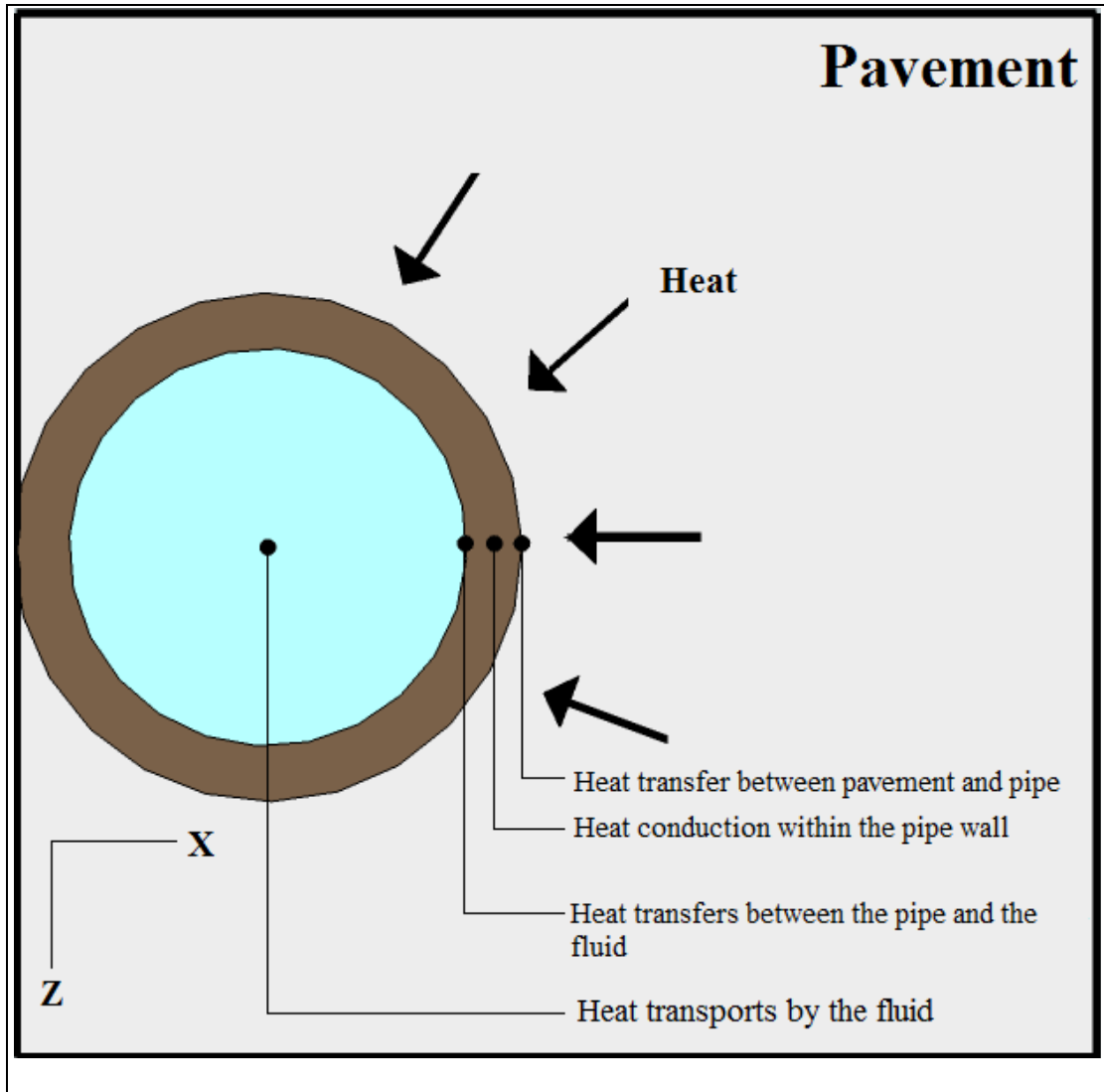
Figure 5-1 Heat transfer from pavement to working fluid within the pipe, Adapted from (Brandl 2005)

Considering fluid flow in the pipe, heat transfer in the pavement is not strictly a 1D problem anymore, although some researchers have modelled it one dimensionally (Turner 1987). In general, heat transfer is a 3D heat conduction problem however, previous study showed that, the temperature gradient along the pipe axis (Y axis) in the pavement is so small that it can be neglected (Bopshetty et al. 1992; Sokolov and Reshef 1992; Chiasson et al. 2000; Esen et al. 2007; Demir et al. 2009). Therefore, heat conduction in the pavement can be modelled using dynamical boundary conditions in 2D (X and Z axis, see Figure 5-1) geometry. The following simplifying assumptions were also made in the analysis:

- The ground thermal properties are uniform and ground type does not change along the pipe,

- For the interfaces between the pavement layers, continuity of heat flux is assumed,

- The fluid temperature inside the pipe does not change in a section perpendicular to the pipe axis,

- Convection heat transfer in the pavements pores are neglected,

- The pavement represents a large surface area and edge effects are neglected,

Such a model was developed by Bopshetty et al. (1992), Sokolov and Reshef (1992), Chiasson et al. (2000), Esen et al. (2007), and Demir et al. (2009) for thermal energy analysis of roof solar concrete collectors and for GSHP applications. The proposed model in this study has many advantages over the other similar models that can be summarised as follows:

1) The previous models can only cope with one pipe cross section, while in this model up to two series of pipes (i.e. collector and storage) can be considered in the pavement cross section. Therefore, the performance of the 'hybrid system' can also be modelled (see Appendix B). For the hybrid simulation, the outlet temperature from the collector pipes served as the inlet temperature for the storage pipes.

2) The previous models were either applied to a single layer (Bopshetty et al. 1992; Sokolov and Reshef 1992; Esen et al. 2007; Demir et al. 2009) or a maximum of two layers (Chiasson et al. 2000). In contrast, in this model, there is no limit on the number of layers, and users can simply define the number of layers in the pavement (see Appendix B).

3) In this model, not only the outlet temperature but also the temperature profile along the pipe and pavement (Y axis) can be predicted. Therefore, the proposed model in this study can be considered as a pseudo 3D transient explicit finite-difference model.

4) Since the proposed model is developed and coded in MS Excel (see Appendix B), it can simply be accessed and applied by the user and does not require a significant investment in learning effort as might be the case with a costly commercial software.

5.2.1. Governing Equations

The finite difference grid used in the model is shown in Figure 5-2. A uniform square nodal spacing equal to the pipe radius has been used. Because of symmetry, the model domain was reduced to a width equivalent to one-half of the pipe spacing as shown in Figure 5-2. In the Z direction, the domain corresponds to the top and bottom of the pavement. In the X direction, the domain corresponds to a distance from the centre-line of a pipe to half the distance to the adjacent pipe. All the heat fluxes are already defined in the Chapter 4 (except heat transfer due to working fluid). Nodal equations in the finite difference grid for node (x,z) are presented in Table 5-1.
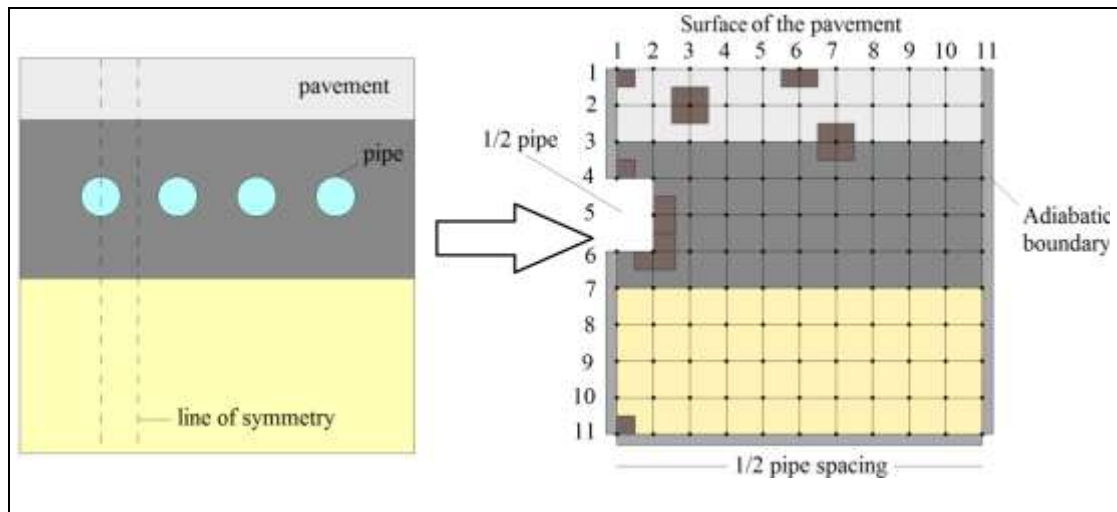
Figure 5-2 Finite difference grid and control volume for different types of grid node geometries

Table 5-1 Nodal equations in the finite difference grid

$T_{(1,1)}^{i+1} = 2F_o \left[\dfrac{q_{Convection}l}{\lambda} + \dfrac{q_{absorbed}l}{\lambda} + \dfrac{q_{thermal}l}{\lambda} + T_{(1,2)}^i - 2T_{(1,1)}^i + T_{(2,1)}^i \right] + T_{(1,1)}^i$	**Eq. 5-1**
$T_{(1,6)}^{i+1} = F_o \left[\dfrac{2q_{Convection}l}{\lambda} + \dfrac{2q_{absorbed}l}{\lambda} + \dfrac{2q_{thermal}l}{\lambda} + 2T_{(2,6)}^i - 4T_{(1,6)}^i + T_{(1,5)}^i + T_{(1,7)}^i \right]$ $+ T_{(1,6)}^i$	**Eq. 5-2**
$T_{(2,3)}^{i+1} = F_o \left[T_{(1,3)}^i + T_{(3,3)}^i + T_{(2,2)}^i + T_{(2,4)}^i - 4T_{(2,3)}^i \right] + T_{(2,3)}^i$	**Eq. 5-3**
$T_{(11,1)}^{i+1} = 2F_o \left[T_{(11,2)}^i + T_{(10,1)}^i - 2T_{(11,1)}^i \right] + T_{(11,1)}^i$	**Eq. 5-4**
$T_{(4,1)}^{i+1} = 2F_o \left[\dfrac{U_{pipe}(T_{fluid} - T_{(4,1)})l}{\lambda} + T_{(4,2)}^i - 2T_{(4,1)}^i + T_{(3,1)}^i \right] + T_{(4,1)}^i$	**Eq. 5-5**
$T_{(5,2)}^{i+1} = F_o \left[\dfrac{2U_{pipe}(T_{fluid} - T_{(5,2)})l}{\lambda} + T_{(4,2)}^i - 4T_{(5,2)}^i + T_{(6,2)}^i + 2T_{(5,3)}^i \right] + T_{(5,2)}^i$	**Eq. 5-6**
$T_{(6,2)}^{i+1} = \dfrac{4F_o}{3} \left[\dfrac{U_{pipe}(T_{fluid} - T_{(6,2)})l}{\lambda} + T_{(7,2)}^i - 3T_{(6,2)}^i + T_{(6,3)}^i + \dfrac{T_{(6,1)}^i + T_{(5,2)}^i}{2} \right] + T_{(6,2)}^i$	**Eq. 5-7**
$T_{(3,7)}^{i+1} = \dfrac{\dfrac{2\Delta t}{l^2} \left[\lambda_1 \left(\dfrac{T_{(3,6)}}{2} + \dfrac{T_{(3,8)}}{2} + T_{(2,7)} - 2T_{(3,7)} \right) + \lambda_2 \left(\dfrac{T_{(3,6)}}{2} + \dfrac{T_{(3,8)}}{2} + T_{(4,7)} - 2T_{(3,7)} \right) \right]}{\rho_1 c_{p1} + \rho_2 c_{p2}}$ $+ T_{(3,7)}$	**Eq. 5-8**

Where in Table 5-1, F_o (Fourier number) $= \dfrac{\alpha \times \Delta t}{l^2}$ and $l = \Delta x = \Delta z$. For numerical stability

requirements, $F_o < 0.25$ (Cengel 2002).

Heat transfer due to working fluid

The mechanism of heat transfer from the pavement to the pipe is already shown in

Figure 5-1. In the absence of any work interactions, the conservation of energy equation for

the flow of a fluid in a pipe can be expressed as (Cengel 2002):

$$Q = \dot{m}c_p(T_{outlet} - T_{inlet})$$

<div align="right">

Eq. 5-9
</div>

where

Q= extracted/rejected heat (W)

$\dot{m}$= mass flow rate (kg/s)

T_{inlet} = inlet fluid temperature (K)

T_{outlet} = outlet fluid temperature (K)

On the other hand, from 'Newton's law of cooling', the rate of heat transfer to or from a

fluid in a pipe can be explained as (Chiasson et al. 2000; Cengel 2002):

$$Q = u_{pipe} A_{pipe} (T_{pipe} - T_{fluid})$$

Eq. 5-10

where

A_{pipe} = inside surface area of the pipe (m^2)

U_{pipe}= overall heat transfer coefficient for the pipe (see Eq. 5-11)

T_{pipe} = average temperature surrounding the pipe (K)

T_{fluid} = Mean fluid temperature ($\frac{T_{inlet}+T_{outlet}}{2}$)

$$U_{pipe} = \frac{1}{\frac{1}{h_{pipe}} + \frac{d_{pipe}}{\lambda_{pipe}}}$$

Eq. 5-11

h_{pipe} = convection coefficient due to fluid flow in the pipe (W/m^2 K)

d_{pipe} = wall thickness of the pipe (m)

λ_{pipe} = thermal conductivity of pipe materials (W/m K)

The convection coefficient due to fluid flow in the pipe (h_{pipe}) is determined using correlations for the Nusselt Number in flow through a horizontal cylinder. For laminar flow in the pipe (Re<2300) or turbulent flow, the convection coefficient can be calculated by Eq. 5-12, Eq. 5-13 , respectively (Chiasson et al. 2000; Cengel 2002).

$$h_{pipe} = \frac{4.36\, \lambda_{fluid}}{D_i}$$

Eq. 5-12

$$h_{pipe} = \frac{0.023 Re^{0.8} Pr^n \lambda_{fluid}}{D_i}$$

Eq. 5-13

where

n= 0.4 for heating and 0.3 for cooling of the fluid flowing through the pipe

λ_{fluid} = thermal conductivity of fluid (W/m K),

Re = Reynolds number (-) ($=\frac{\dot{m} D_i}{\nu A \rho_{water}}$)

Pr = Prandtl number (defined as: $\frac{c_{fluid}\mu}{\lambda_{fluid}}$, μ is the dynamic viscosity of fluid)

D_i = internal pipe diameter (m)

From Eq. 5-9 to Eq. 5-13, the outlet temperature can be calculated from Eq. 5-14:

$$T_{outlet} = T_{inlet} - \left[\frac{U_{pipe}(T_{fluid} - T_{pipe})A_{pipe}}{\dot{m}c_{fluid}} \right]$$

Eq. 5-14

In order to calculate the outlet water temperature and water temperature along the pipe length, the pipe length is divided into a number of sections with a known length (*dl*). The outlet fluid temperature of one section serves as the inlet fluid temperature for the next section and this procedure is carried on until one reaches the end of the pipe. Since the outlet temperatures for the sections are not known, the inlet fluid temperature (T_{inlet}) is set as the fluid temperature (T_{fluid}) for the section, and the outlet fluid temperature (T_{outlet}) of the section is then calculated from Eq. 5-14. An iterative process for each section will then be employed by computing the fluid temperature (T_{fluid}) from the new outlet fluid temperature (T_{outlet}) and the process continued until the values for the outlet fluid temperature (T_{outlet}) converge in a defined tolerance (e.g. <0.1K).

Computer implementation

Figure 5-3 shows the inputs and outputs data for the PES model. All the equations were coded in the Visual Basic for Applications (VBA) in MS Excel 2010. In order to develop a user-friendly and highly flexible model, the compilation of the model was performed with the help of an expert modeller (see Acknowledgment). An explanation of the model's procedures is described and illustrated in Appendix B.

Air temperature	Irradiation	Wind speed	Humidity

1. Thickness of pavement layers
2. Pipe spacing
3. Pipe cross section (i.e. collector, storage)
4. Pipe depth below surface
5. Pipe diameter, wall thickness, and thermal conductivity
6. Pipe length and number of sections (*dl*) along the pipe

7. Thermo-physical properties of layers
8. Surface absorptivity and emissivity
9. Inlet fluid temperature
10. flow rate
11. Average thermal properties of fluid
12. Finite difference mesh size

Outlet fluid temperature profile along the pipe length

Pavement temperature distributions in X, Y, and Z

Figure 5-3 Inputs and outputs data for the PES model

5.3. Experimental Setup and Apparatus

This section outlines the procedures for design and construction of the large-scale experimental setup. The apparatus used to measure the model parameters (e.g. temperature, solar irradiation, etc.) are also described.

5.3.1. Experimental Setup

Figure 5-4 shows a schematic of the experimental setup used to carry out laboratory testing on the PES applications in order to validate the model. Test sections were designed and constructed in a laboratory at the Nottingham Transportation Engineering Centre (NTEC). The pavement cross-section and the position of thermocoples in the pavement are shown in Figure 5-5.
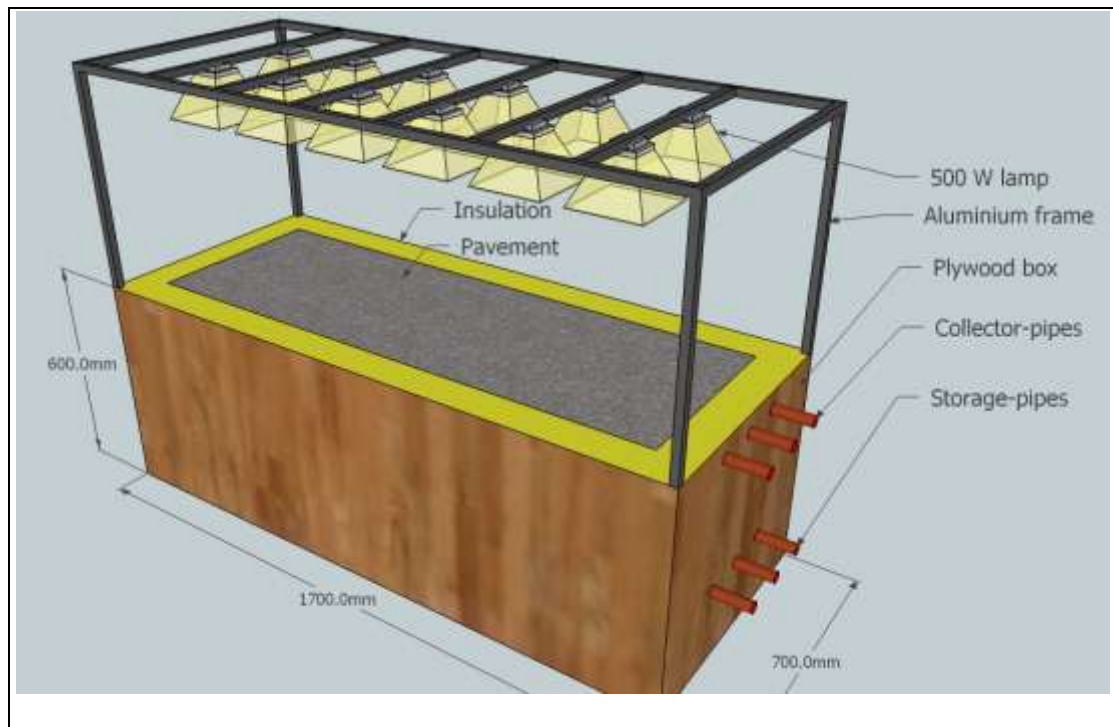
Figure 5-4 Schematic of the experimental setup
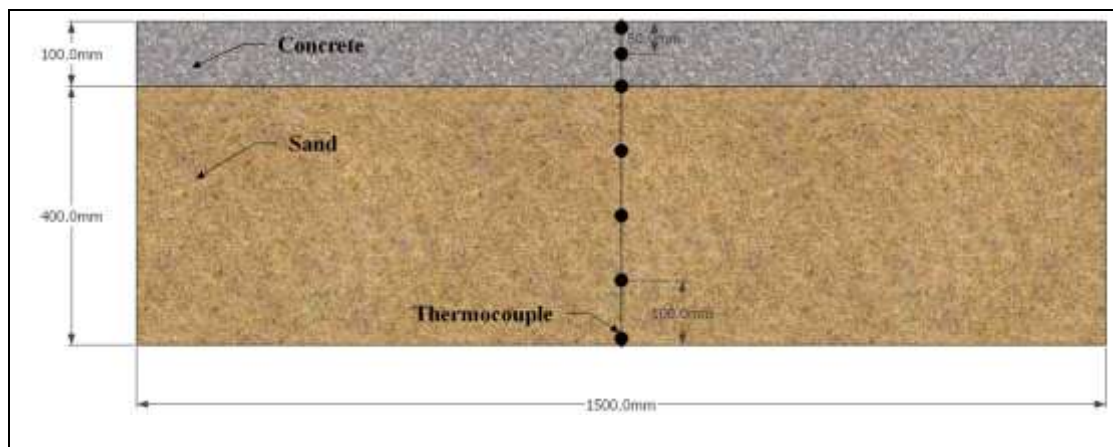
Figure 5-5 Pavement cross-section and thermocouples' positions

Details and procedures for the construction of the experimental setup are summarised as follows:

1) A rectangular box, made of plywood, with a plan area of 1700mm ×700mm and a height of 600mm was constructed.

2) The bottom and all four edges of the box were insulated using 100 mm Polyisocyanurate insulation boards (or PIR foam) in order to minimise heat

loses/gains. This gives a pavement area of 1500mm×500mm with a thickness of 500mm (see Figure 5-5).

3) Collector (i.e. top) and storage (i.e.bottom) pipes were installed into the box. The collector and storage pipes are made of copper with a nominal diameter of 15mm and were embedded at depths of 50mm and 400mm from the slab surface on 125mm centres. Although, copper pipes have been reported to be used for GSHP applications (Banks 2008), they, under some geochemical conditions, may be liable to corrosion. In addition, they are likely to increase the project cost. However, since the size of the experimental design in this study is relatively small, thus, in order to increase the system performance, it was decided to use copper pipes that have a lower thermal resistance (i.e. higher conductivity). The effect of any pipe materials such as Polyethylene on the performance of the PES can be investigated, nevertheless, using the numerical model.

4) Each of the storage pipes was rested on three supports along its length, which were screwed to the bottom of the box (see Figure 5-6). This has been done to avoid buckling and damaging of the pipes during the pavement construction.

5) The top pipes were also supported by harnessing the pipes with a piece of plywood, which was in turn designed to hold the box together during the pavement construction (see Figure 5-7).

6) All the pipes were levelled by loosening/tightening of the support nuts that are holding the pipes (see Figure 5-7).
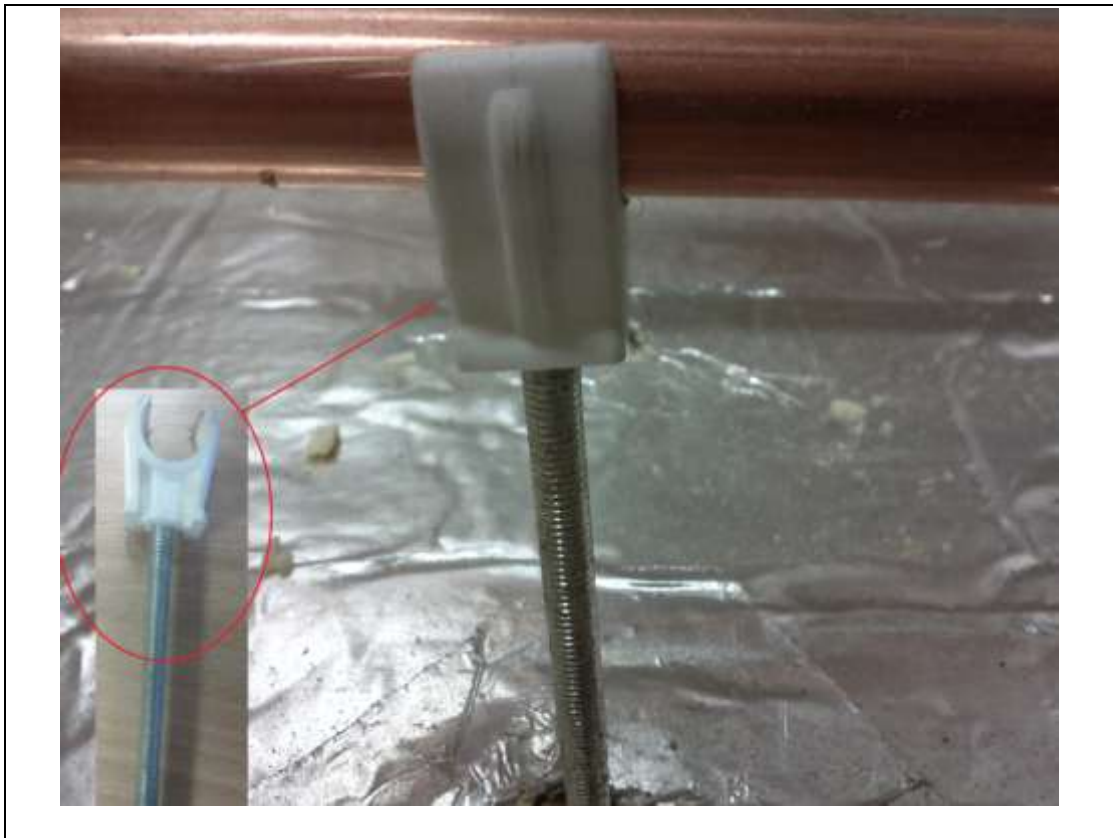
Figure 5-6 Storage pipes rested on supports

Figure 5-7 Supporting and levelling the collector pipes

7) Two arrays of thermocouples were assembled by fastening the thermocouples with an epoxy resin to a PVC conduit at different depths (see Figure 5-8). The thermocouples were fastened such that the tip of thermocouple is in direct contact with the pavement, and were positioned at depths of 500 mm (bottom), 400 mm, 300 mm, 200 mm, 100 mm, 50 mm, and 0 (surface). The thermocouples were labelled and inserted into the pavement prior to its construction.

Figure 5-8 Thermocouples were fastened on a conduit

8) The thermocouple arrays were placed inside the box, and sand was then poured in three layers and compacted up to 400mm level. The sand was compacted by placing a flat wooden board on top of the sand to which a Kango Hammer was applied.

9) Concrete containing coarse quartzite aggregates and natural sand as fine aggregates was mixed, according to the mix design given in Table 3-1, Page 57, using a drum concrete mixer. The concrete was poured into the box, on top of the sand, and well compacted using a poker vibrator. Slab specimens were also prepared from the concrete mix and the sand in order to test the thermal conductivity.

10) After finishing the pavement construction, the pipes were connected together in different ways such that any of the PES applications can be tested. 'Plastic Push Fit' connectors (see Figure 5-9) were used to connect the pipes in different

arrangements. Pipes were connected together in series mode to produce a total pipe length of 4.5m (see Figure 5-10).

11) Tap water was used as an inlet water to the system and its temperature was measured using two thermocouples. To ensure that the pipes are full of water, and also to achieve a more constant and uniform flow, the flow was controlled on the outlet pipe using a regulator tap. The outlet water temperature was also measured using two thermocouples.

12) The heat source comprised twelve 500W halogen linear lamps installed in two rows at ~500 mm above the concrete surface, covering the whole pavement area. The halogen lamps were connected to a dimmer switch that allows control of the heat flux density incident upon the pavement surface. It is known that radiation produced by halogen lamps has a spectral distribution similar to solar radiation in the wavelength range of 0.2-2.7 μm, which contains 97% of the energy in solar radiation (Bilgen and Richard 2002).
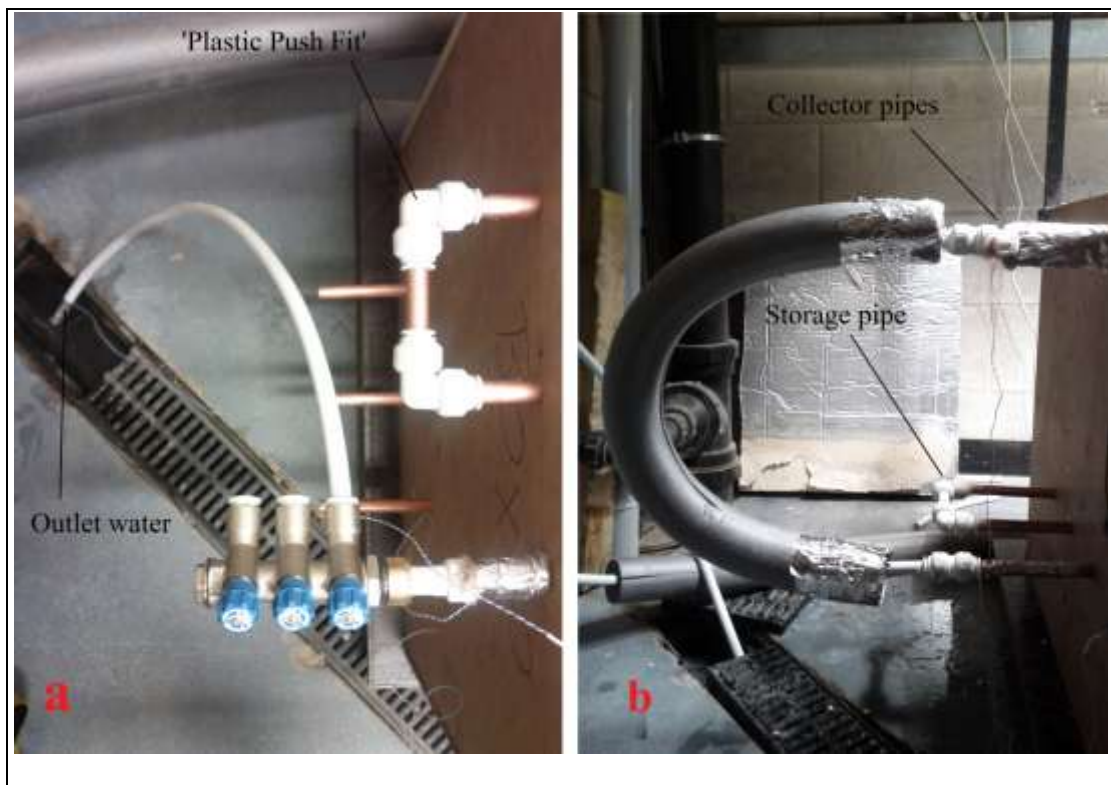
Figure 5-9 Different pipe configuration collector (a), connecting collector and storage pipe for hybrid simulation (b)
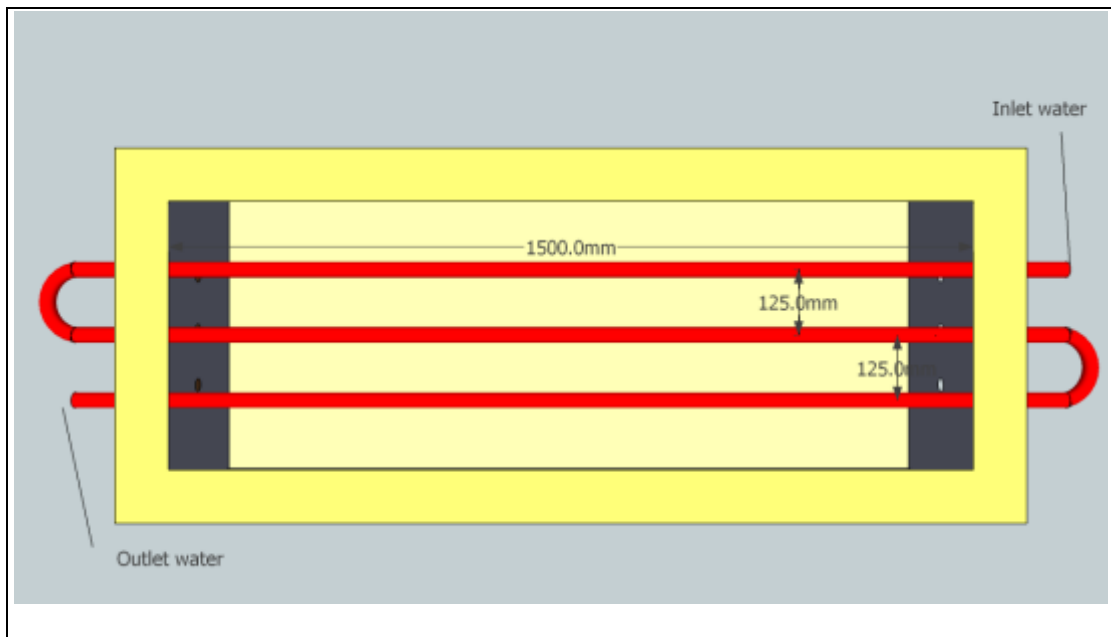
Figure 5-10 Pipe connections and flow direction

5.3.2. Apparatus

Solar intensity

Solar intensity was measured using a pyranometer (Kipp & Zonen CMP 3) that measures the

solar intensity up to 2000 W/m^2 with an accuracy of ±3%. The pyranometer was levelled and

positioned at different points along the pavement surface to measure the average solar

intensity. Since the pyranometer sensor was ~70 mm higher than the pavement surface (see

Figure 5-11), the values measured were not exactly equal to the solar radiation received by

the pavement surface. For this reason, before the construction of pavement, the relationship

between solar intensity when the pyranometer sensor is on the surface (i.e. the body of

pyranometer was lower than the pavement surface and the pyranometer sensor was levelled

with the pavement surface) and also when the pyranometer sensor is at ~70mm height (i.e.

the pyranometer was placed on the pavement surface so that the sensor was at ~70mm height

from the pavement surface (see Figure 5-11)) were experimentally determined. From this

linear relationship (see Figure 5-12), the actual solar intensities (i.e. solar intensity received

by the pavement surface) were calculated accordingly.

<u>Surface absorptivity</u>

The pavement surface absorptivity was measured using the 'pyranometer method' (Levinson et al. 2010), which includes measuring the absorbed and reflected solar radiation by the pavement. The reflected solar radiation is measured using an inverted pyranometer (see Figure 5-11). A disadvantage of this method is shadow cast of the inverted pyranometer on the pavement surface when the reflected radiation is being measured (Levinson et al. 2010). To minimise this effect, the pyranometer was lifted upward from the pavement surface until the shadow disappeared. The reflected intensity was measured by placing the pyranometer at a depth of 150mm, 200mm, and 250mm from the pavement surface. Finally, the mean solar absorptivity was computed as the ratio of solar radiation absorbed by the pavement to the incident value.
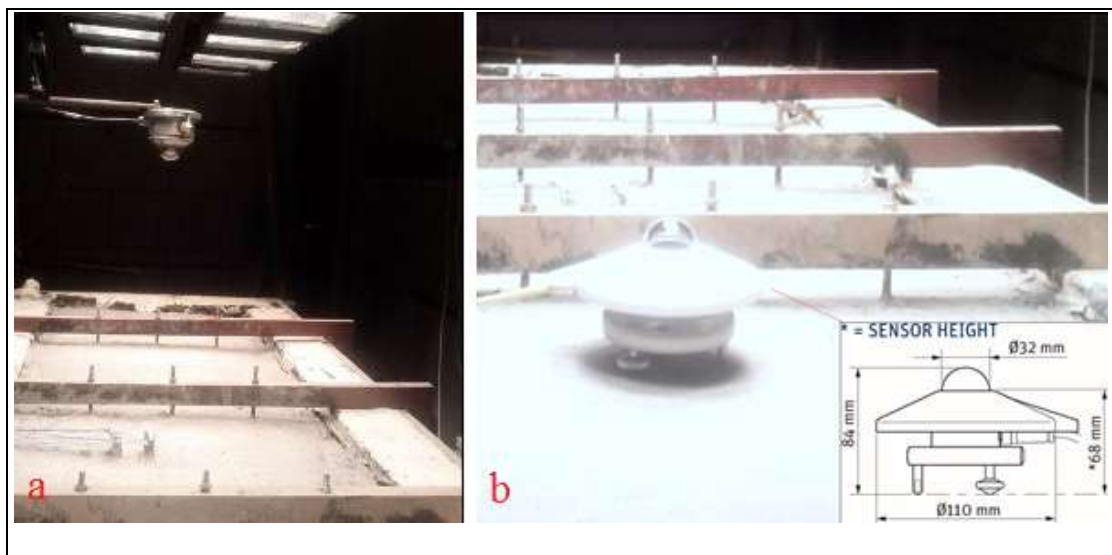
Figure 5-11 Pyranometer measures reflected (a) and received (b) radiation from/by the pavement surface
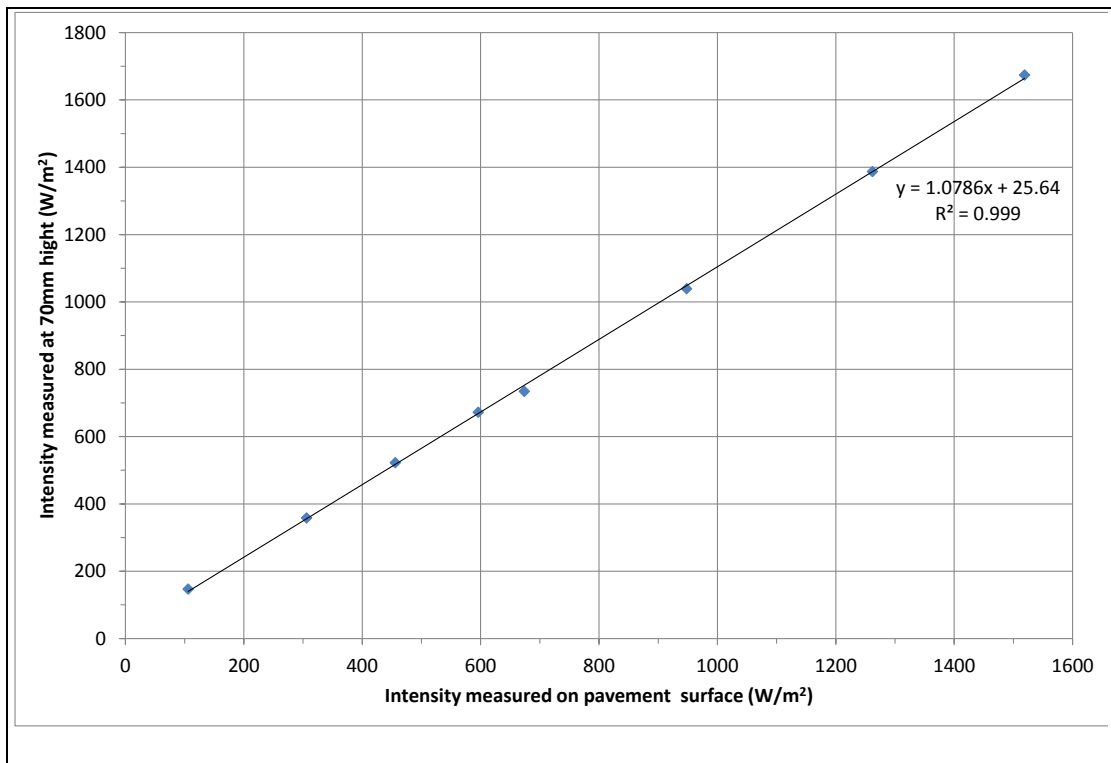
Figure 5-12 Relationship between solar intensity received on the pavement surface and at 70mm height

Surface emissivity

Surface emissivity of the pavement was measured using a high resolution infrared camera (FLIR SC7000) (see Figure 5-13), with a spectral range of 3.5-5.0 μm and a sensitivity of 0.07°C, connected to the FLIR system software (ALTAIR). The value of surface emissivity in the software was varied until the mean temperature reading from the infrared camera matched the mean surface temperature readings from the thermocouples.

Wind speed

To evaluate the performance of the model in windy conditions, two rotary fans were used to generate wind over the pavement surface. The mean wind speed on the pavement surface was measured using a handheld Anemometer (TESTOTERM 4400) capable of measuring 0.6-40 m/s.

Temperature

All the temperature readings (e.g. temperature distribution in the pavements, inlet and outlet water temperature, and ambient temperature) were taken using T-type thermocouples (copper/constantan) with an accuracy of ±0.5°C.

Data acquisition system

The thermocouples and pyranometer were connected to a datalogger (Data Taker DT800), and data were recorded at 10s intervals.
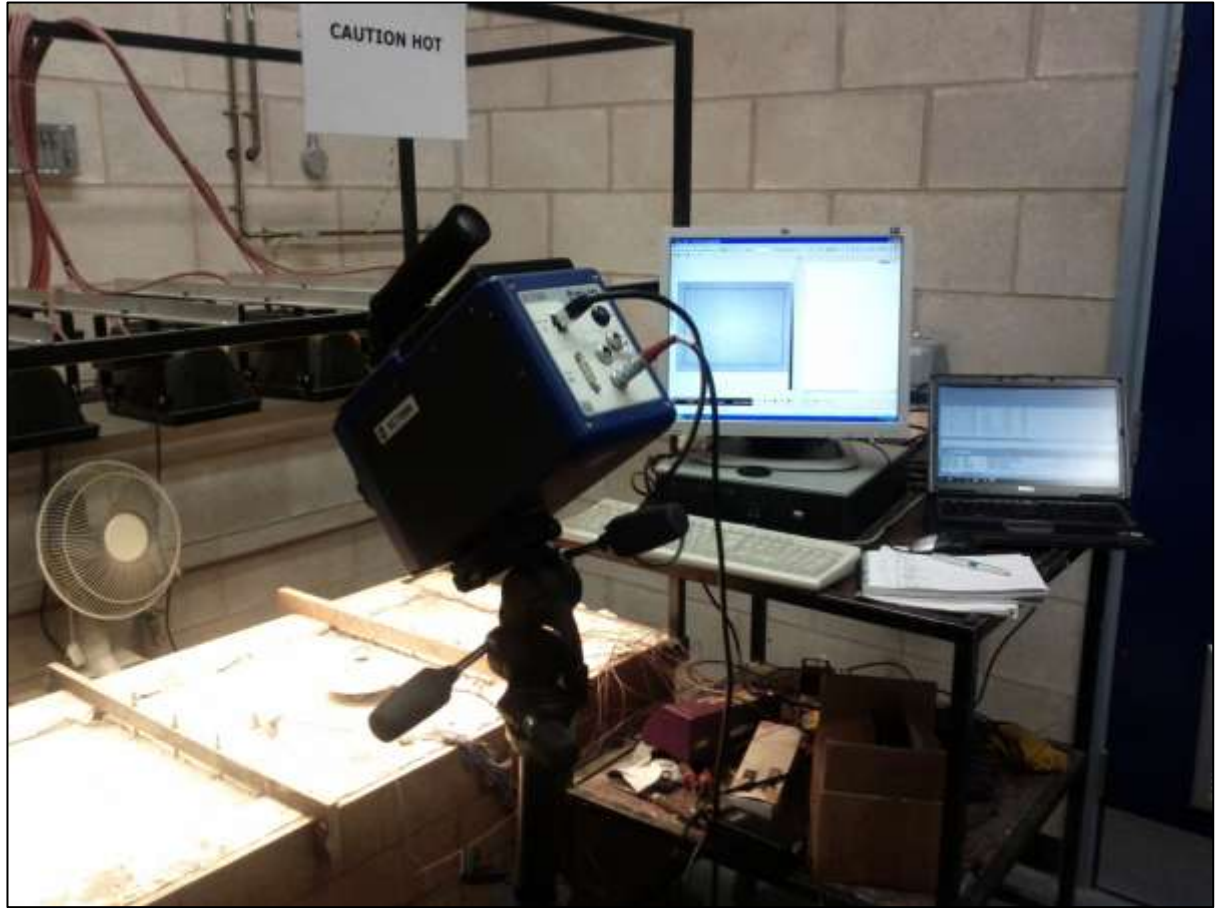
Figure 5-13 Infrared camera used to measure surface emissivity of the pavements

5.4. Validation of the Model

The model was validated by comparing simulation results to experimental data that were obtained under different conditions (e.g. mass flow rate, solar radiation, and surface absorptivity). The results, for similar experiments, are reduced and, together with the theoretical ones, are presented in Figure 5-14 to Figure 5-20. The finite difference grid parameters for all simulations consisted of a time step $\Delta t = 10s$ and nodal spacing $\Delta z = \Delta x = 0.0075m$.

5.4.1. **Validation with no Water Circulating**

In order to validate the ability of the model to predict temperature profiles within the pavement, the following cases were analysed without any heat addition or removal thorough the loops.

- ✓ Normal concrete was tested (Figure 5-14)

- ✓ Black-top concrete was tested (Figure 5-15)

- ✓ Black-top concrete + wind applied on the surface (Figure 5-16)

Figure 5-14, Figure 5-15 and Figure 5-16 show typical experimental and theoretical temperatures at various depths in the pavement as a function of time, when no water was circulated through the pipes. Each experiment consisted of a heating period (i.e. the heat source was turned on) and a cooling period (i.e. the heat source was turned off).

Figure 5-14, Figure 5-15 and Figure 5-16 show that temperature cyclic variation reduces with the pavement depth and the temperature at 400mm remains almost constant at a value close to the mean ambient temperature throughout the experiment period. It can also be observed that due to the thermal inertia of the pavement, temperature cycles lagged behind. For instance, at 200mm depth maximum temperature lagged behind the surface temperature by about 2 hours. The reductions in temperature amplitude with depth and temperature lags are the principle of the GSHP technology (see 2.5.1, Page 22).

Figure 5-14 and Figure 5-15 show that, as expected, the black-top concrete increases the absorption of heat energy such that for the same heating period (after about 6.3 h), the normal concrete and black painted concrete will reach 52°C and 64°C, respectively. In addition, a comparison between Figure 5-15 and Figure 5-16 shows that the pavement surface temperature has reduced by up to 13°C as a result of wind applied on the surface which suggests surface convection heat transfer plays an important role in near-surface temperature profile.
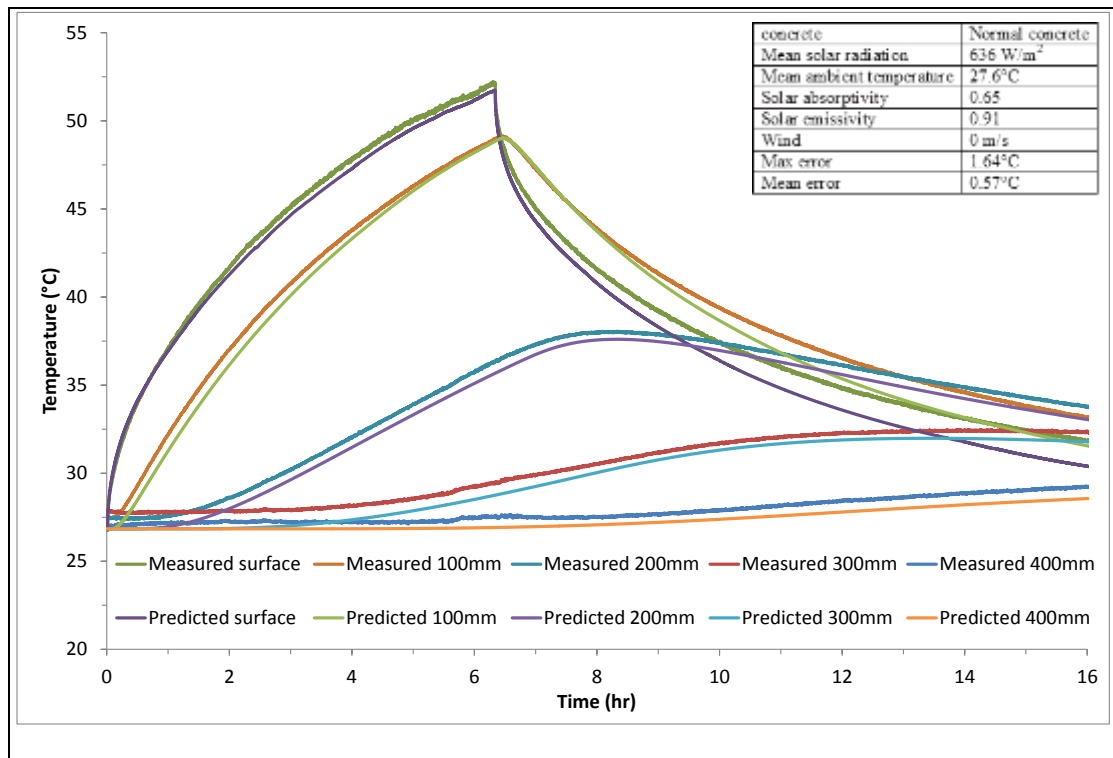
Figure 5-14 Experimental and theoretical results of normal concrete
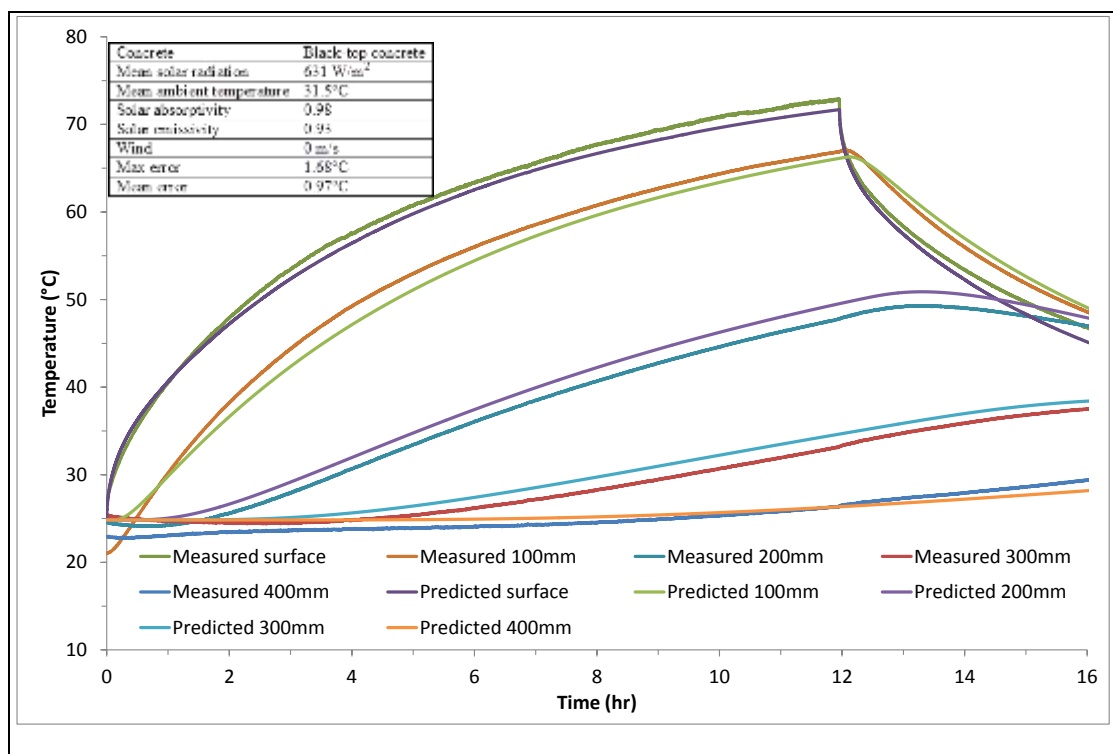
Figure 5-15 Experimental and theoretical results of black painted concrete
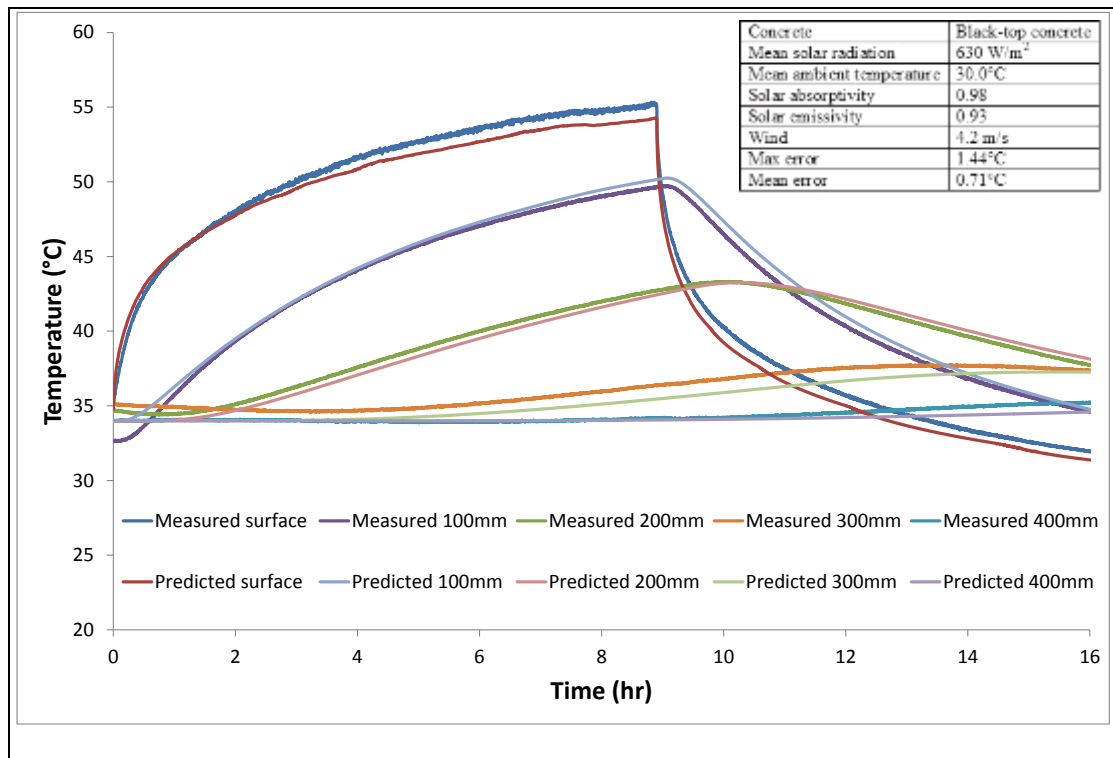
Figure 5-16 Experimental and theoretical results of black painted concrete with wind applied on the pavement surface

From Figure 5-14, Figure 5-15 and Figure 5-16, the numerical model gives reasonable time-dependent temperature profile within the pavement but with some errors. The maximum and mean errors were ~1.6°C and ~0.75°C, respectively, which can be related to a couple of assumptions in the model and material property inputs. There can be errors associated with the uncertain effects of empirical equations (i.e. equations to predict convection and thermal radiations) applied on the pavement surface boundary. Furthermore, the pavement material thermo-physical properties were considered uniform and homogeneous in the model, whereas these properties might not be uniform within the pavement. Finally, the assumption of 1D heat transfer across the pavement and neglecting edge effects as well as the assumption of perfect bonding between the pavement layers may lead to error in the numerical model.

5.4.2. Validation with Water Circulating

In order to validate the model for different PES applications (i.e. heat collection or heat storage) the following experiments were performed.

✓ Normal concrete pavement in collection mode (Figure 5-17)

✓ Black-top concrete pavement in collector mode (Figure 5-18)

✓ Concrete pavement in storage mode (Figure 5-19)

✓ Water circulated through the collector and storage pipes simultaneously at two different flow rates and temperatures (Figure 5-20)

Figure 5-17 to Figure 5-20 show the results for these cases with heat being extracted/rejected from/to the pavement (i.e. water was circulated in the system). Figure 5-17 and Figure 5-18 show the mean surface temperature and outlet water temperature in a normal and black painted concrete pavement, respectively. From the simulated results, it can be seen that the model average pavement surface temperature and outlet water temperature projected the experimentally measured values and were in good agreement with them. The simulated temperatures were generally lower than the measured values by a mean error of 0.91°C. In addition, despite the lower flow rate and inlet water temperature of the normal concrete, the mean temperature rises in normal concrete and black-painted concrete were 2.7°C and 4.6°C, respectively, which shows the effect of surface absorptivity on the heat collection from the pavement.

Figure 5-19 shows a case where water was circulated through the storage pipes that were buried in the sand. This case simulates the performance of a GSHP in the winter (i.e. heating mode). The water in the pipes absorbed heat and its temperature increased by ~1.5°C. The outlet water was predicted satisfactorily with a mean temperature error of ~0.41°C.

Figure 5-20 shows a case where water circulated through the collector and storage pipes simultaneously at two different flow rates and temperatures. Figure 5-20 shows that water at ~40°C and ~20°C entered the storage and collection pipes, respectively. The water temperature in the collector pipes heated up whilst the water temperature in the storage pipes rejected heat to the pavement and began to cool down. The ability of the model to accurately

predict temperatures in such a challenging case was very good where the mean temperature

discrepancy between simulated and measured values was ~1.0°C.
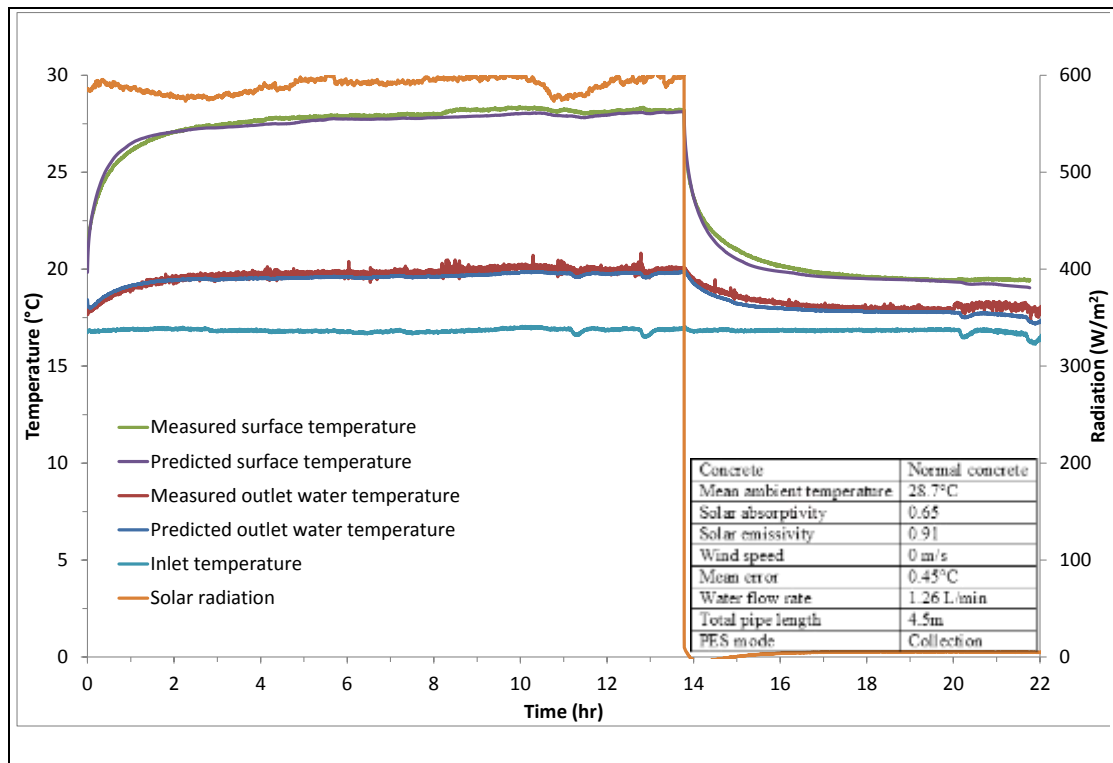
Figure 5-17 Comparison of measured and simulated mean slab surface temperatures and outlet water temperatures for normal concrete
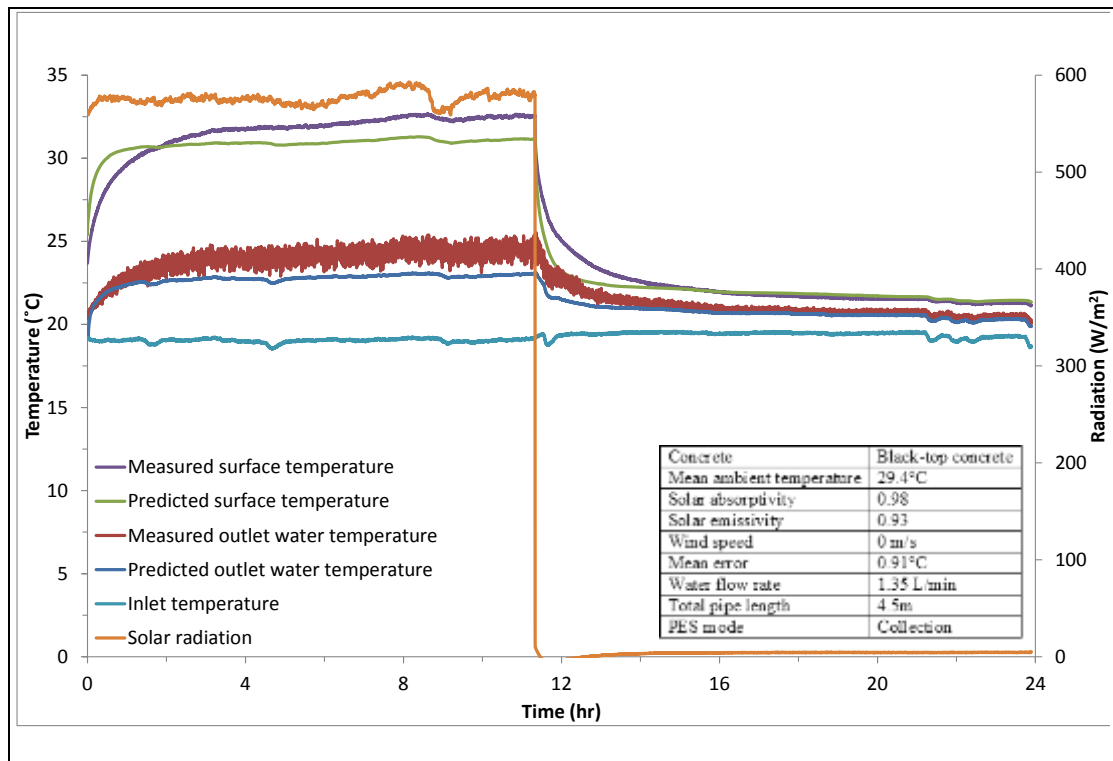
Figure 5-18 Comparison of observed and simulated mean slab surface temperatures and outlet water temperatures for black painted concrete
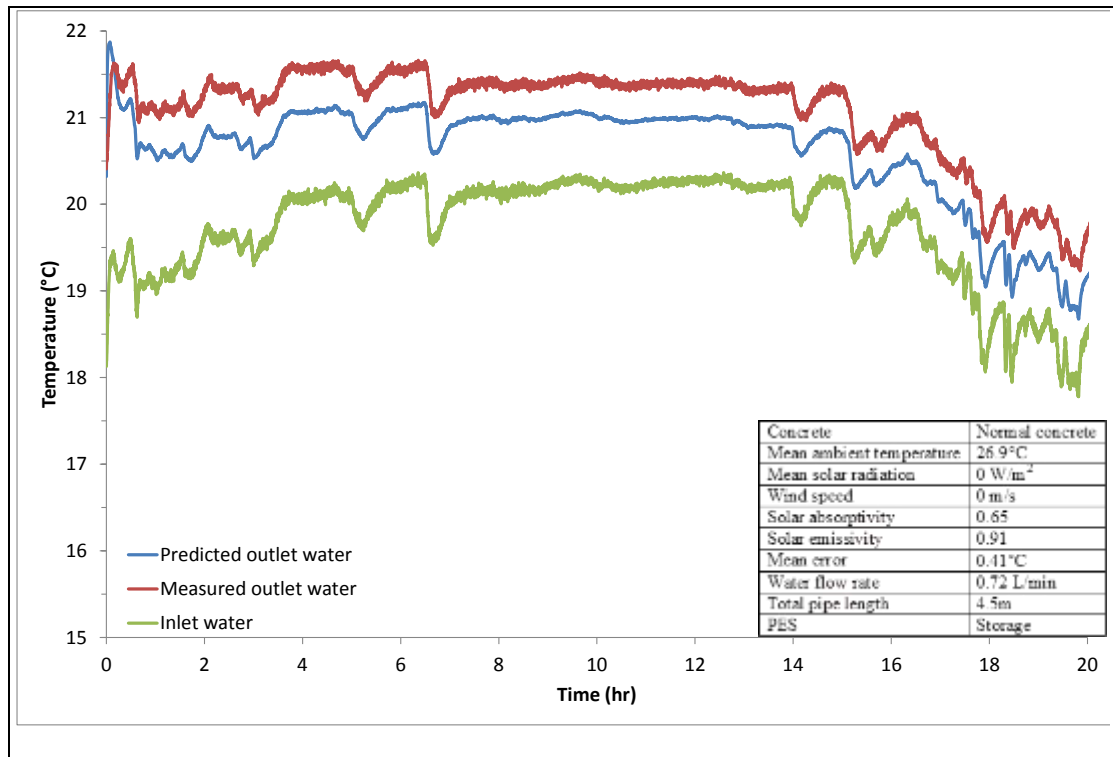
Figure 5-19 Comparison of observed and simulated outlet water temperature for storage mode
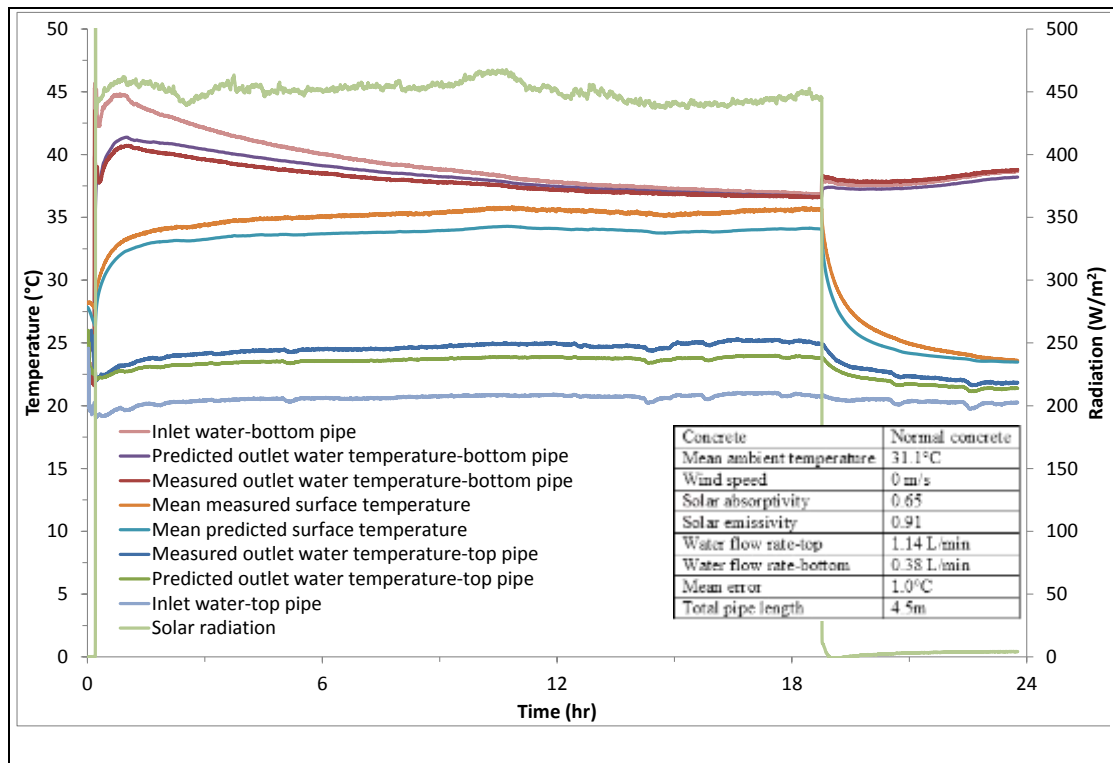
Figure 5-20 Comparison of observed and simulated mean slab surface temperatures and water outlet temperatures for variable inlet temperatures and flow rate

5.4.3. Validation of the PCM Model

In order to simulate the relative effect of PCM addition on the temperature profile evolution in pavements, the model needed to be modified to include the latent heat of the phase transition (H_{melt}) of the PCM at its melting temperature (T_{melt}). In this study, the 'apparent heat capacity method' (Mehling and Cabeza 2008) was incorporated within the numerical model, which accounts for the latent heat capacity of the PCM by adding a heat capacity function to the model (see Figure 3-16). Therefore, the latent heat is accounted for by applying the temperature-dependant heat capacity function to the model.

To validate the PCM model, two concrete slabs; one containing 0% PCM (i.e. control) and one with 40% PCM (see Table 3-6, page 78, for mix design) were instrumented by attaching two thermocouples to their surfaces. The concrete specimens were insulated by encasing them in the insulation boards, leaving only one face exposed. The exposed surface was covered in aluminium foil to ensure that both specimens had the same surface absorptivity

and that changes in surface temperatures were not affected by albedo. The specimens were pre-conditioned at an air temperature of 5°C±0.5 before being placed under the halogen lamp array. Solar intensity along with concrete surface temperatures and ambient air temperature were measured and recorded at 10s intervals.

Figure 5-21 shows the experimental data for mean surface temperature evolution for the two concrete samples as a function of time. The influence of the PCM can be clearly observed, producing a 'shoulder' in the curve that corresponds to the median melting temperature (~26°C). The temporary increase in heat capacity due to the addition of PCM causes a surface temperature reduction of up to 4°C throughout the melting temperature range (approx. 22-30°C). Figure 5-22 shows that the model predicted the surface temperature of the PCM-modified concrete favourably with a mean temperature error of 0.65°C. The error might be due to the ignoring the convectional heat transfer as a result of PCM melting.
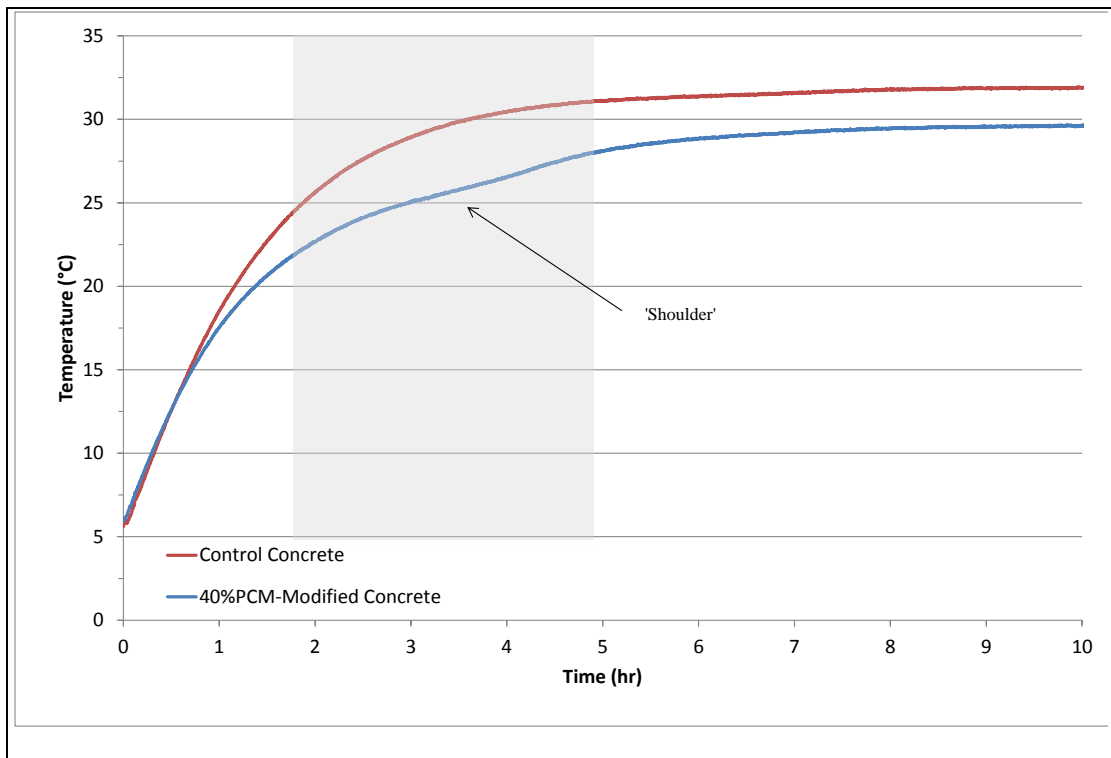
Figure 5-21 Mean measured surface temperature evolution for control & PCM-modified concrete
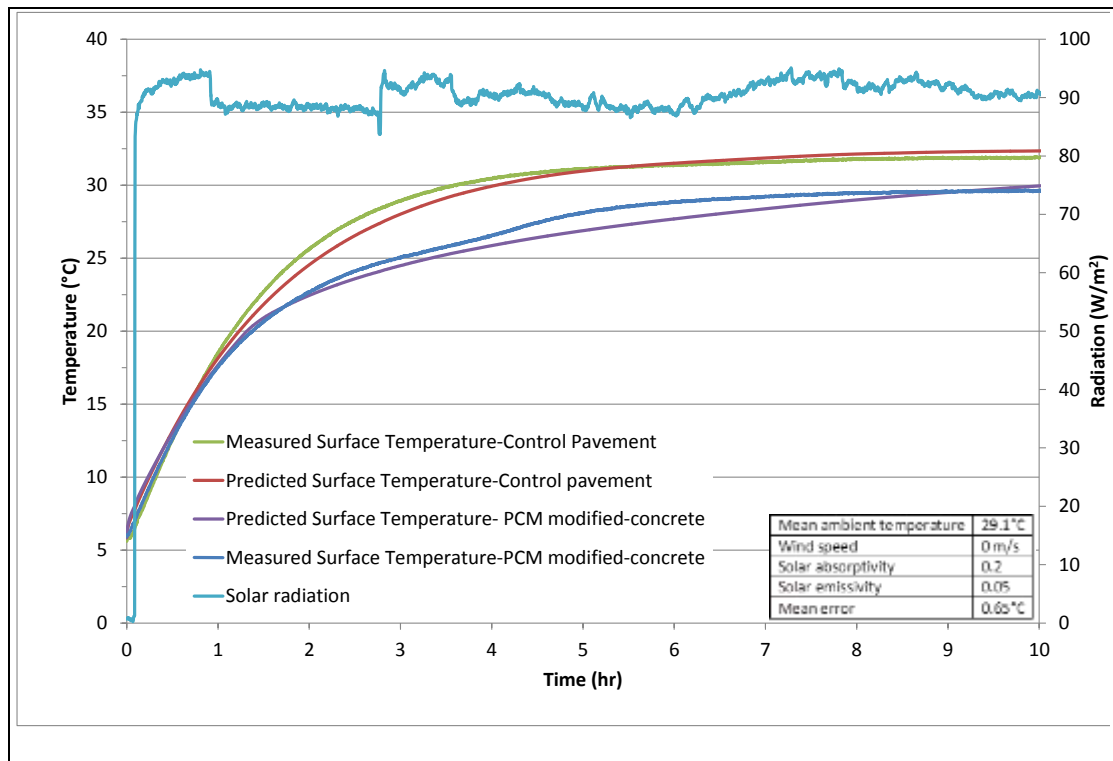
Figure 5-22 Predicted surface temperature for control concrete and 40% PCM-modified concrete

5.5. Experimental Comparison between Normal & Modified Pavements for Different Applications

In this section, the experimental setup was re-designed in order to compare the performance of normal pavement constructions with thermally modified ones. The experimental setup was designed to accommodate two pavements side by side (see Figure 5-23) so that they can be tested simultaneously and under similar conditions (e.g. water flow rate, environmental conditions). Two different setups were constructed for concrete-and asphalt-normal and modified pavements. The inlet and outlet water temperature, pavement and ambient temperatures, and solar intensity were recorded at 10s interval.
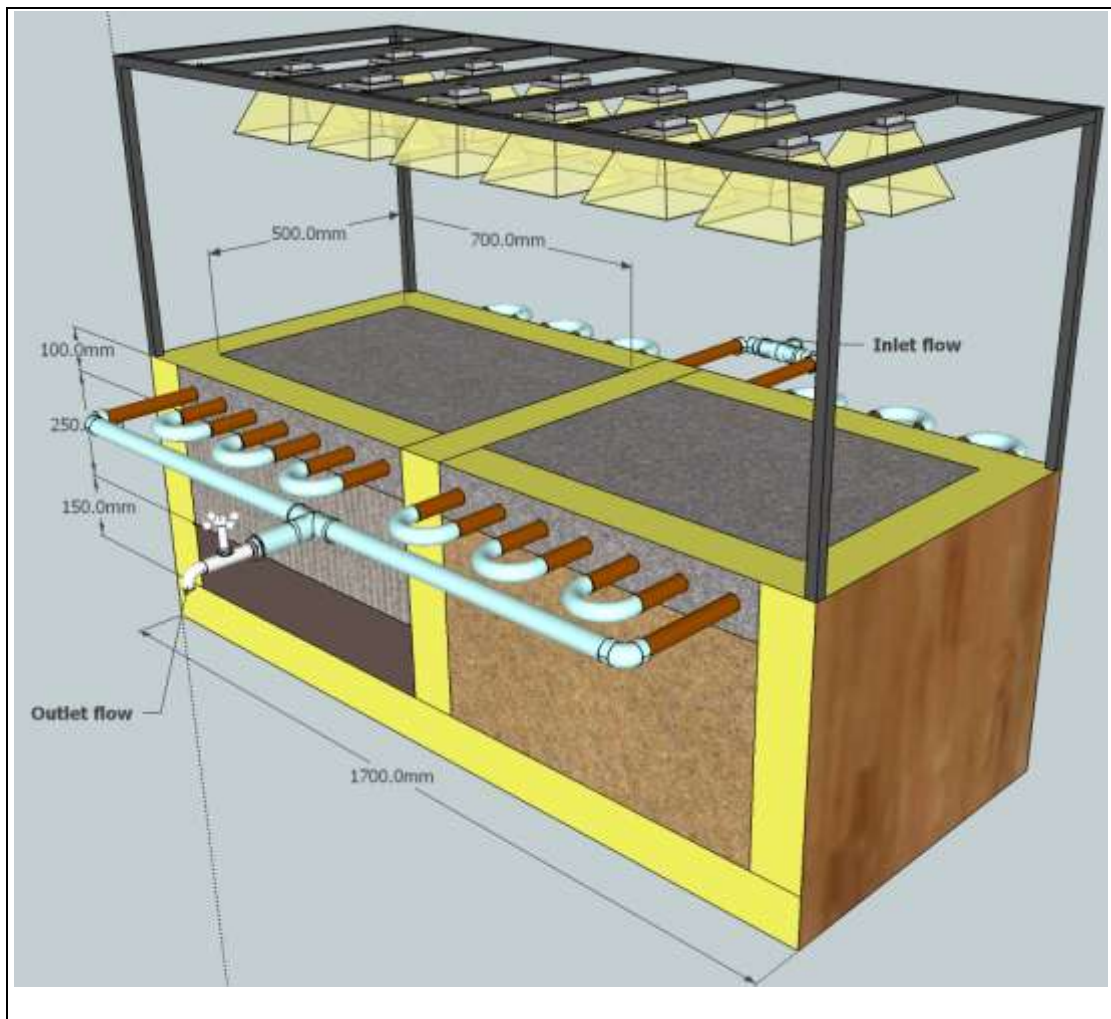
Figure 5-23 Experimental setup to test normal and modified concrete pavements

5.5.1. Concrete Pavements

Concrete pavements comprised a reference concrete, and a modified concrete pavement. The reference concrete was a 100 mm limestone Pavement Quality Concrete (PQC) mix (Mix#1 in Table 3-4) on top of a compacted sandy soil to represent a conventional construction whilst the modified concrete comprised three different layers to simulate a Pavement Source Heat Store (i.e. PSHS) system. The layers in the modified pavement were a 100mm conductive quartzite PQC on top (Mix#3 in Table 3-4), a 250 mm Lytag PQC (Mix#12 in Table 3-4) in the middle to minimise heat loss, and finally a 150mm Lean Mix Concrete (LMC) quartzite (Mix#16 in Table 3-4) at the bottom. Pipes were spaced at 100mm intervals and connected together in series to produce a total pipe length of 3.5m. Prior to the experiment flow rate from each pavement was controlled separately to ensure that the flows

are the same. The pipes from two pavements were then connected together and the flow was controlled on the outlet pipe using a regulator tap in order to ensure that the pipes are full of water, and also to achieve a more constant and uniform flow. Three modes of operation were evaluated; i) heat collection only, ii) storage only, and iii) combined collection and storage (hybrid).

Collector-only mode

Figure 5-24 shows the measured and predicted outlet water temperature from the reference and modified concrete pavements in the collector mode. Figure 5-24 clearly shows that the outlet water temperature of the modified pavement is higher than that of the reference one by an average value of ~1.1°C. In addition to the experimental observations, the outlet water temperatures were also predicted and the model showed a difference of 1.4°C between the modified and the reference outlet water. The results from the experiment and the numerical model were in good agreement and they proved that application of a pavement with high thermal diffusivity (i.e. quartzite mix) on top of a pavement with low thermal diffusivity (i.e. Lytag mix) can increase the temperature at the pipe location and facilitate heat transport to the fluid.
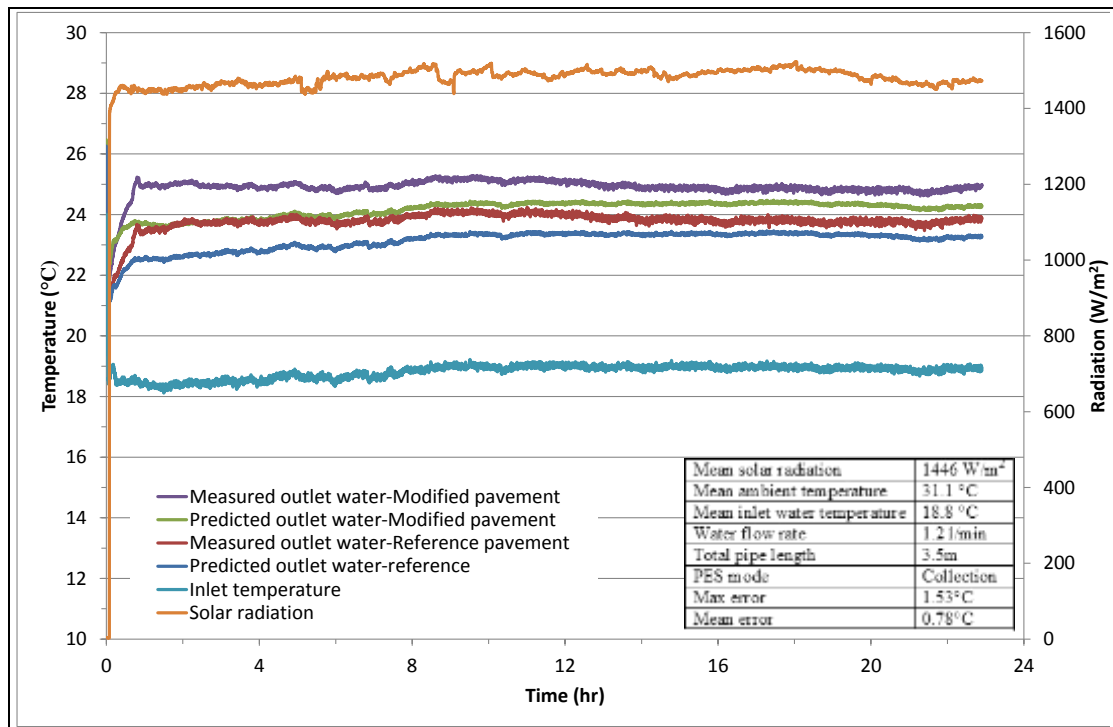
Figure 5-24 Measured and predicted outlet water temperature from the reference and modified concrete pavements in collector mode

Figure 5-25 shows the measured (two readings for each pavement) and predicted surface temperatures for the same experiment. From Figure 5-25, it can be observed that the surface temperature of the reference concrete remains higher compared to that of the modified one. The difference between the reference and modified pavement surface temperatures is about 8°C and it was in good agreement with the predicted ones. The lower surface temperature of the modified pavement can be attributed to its higher thermal diffusivity (see Mix#1 and Mix#3 in Table 3-4) resulting in a greater ability to exchange thermal energy between the water and the pavement.
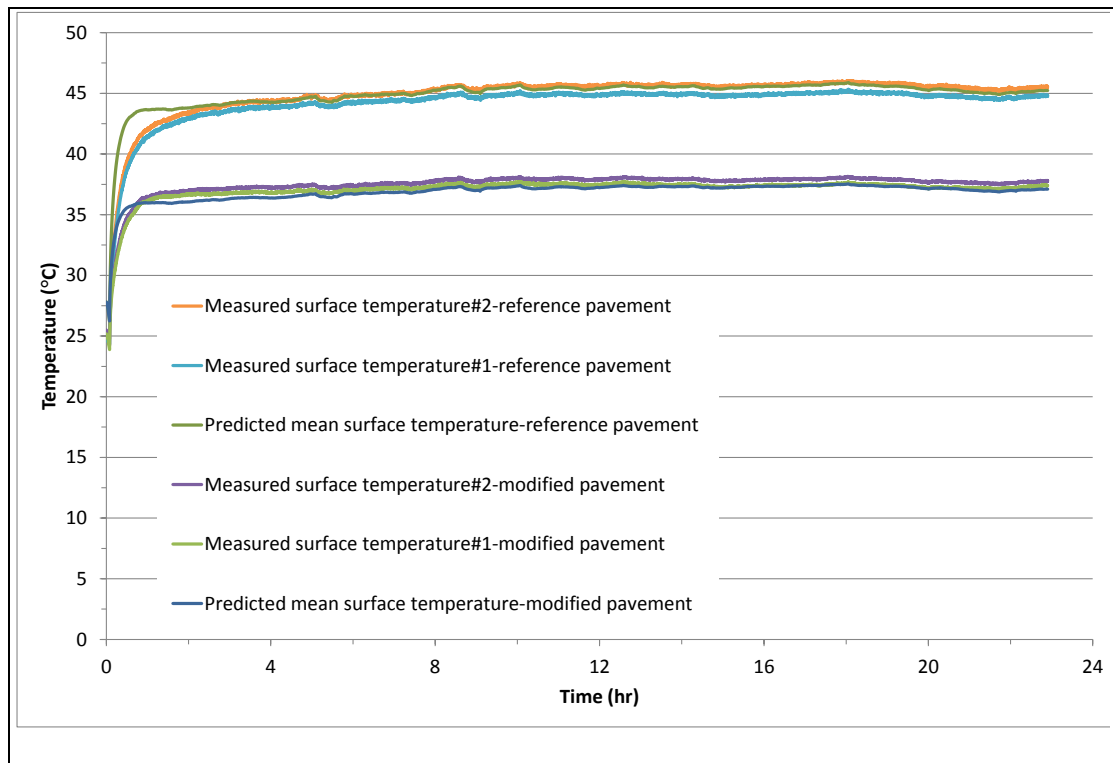
Figure 5-25 Measured and predicted surface temperature of the modified and the reference concrete pavement in collector mode

The above experiment has also been performed for different conditions (e.g. solar radiation and flow rate), and all the results are summarised in Table 5-2.

Table 5-2 Summary of the test results performed on the concrete pavements in the collector-only mode

	Experiment#1	Experiment#2	Experiment#3
Mean solar radiation	1446 W/m^2	669 W/m^2	439 W/m^2
Mean ambient temperature	31.1 °C	28.2 °C	28.2 °C
Mean inlet water temperature	18.8 °C	19.4 °C	19.1 °C
Water flow rate	1.21 L/min	0.5 L/min	0.7 L/min
Mean measured outlet water temperature difference	1.1 °C	0.9°C	0.7°C
Mean measured surface temperature difference	7.9 °C	2.9°C	2.1°C

Storage-only mode

Cool water from a tap and warm water from a storage tank were circulated through the storage pipes in order to simulate heat extraction (i.e. winter mode) and heat rejection (i.e. summer mode) to the pavements.

Figure 5-26 shows a case where warm water was circulated through the pipes, and it shows the inlet water temperature, outlet water temperature from each pavement, the pavement temperatures at the pipe locations, and initial temperature distributions in the pavements. From Figure 5-26, it can be observed that the modified pavement, in spite of having higher temperatures initially, shows a greater ability to absorb heat and, hence, to reduce the outlet water temperature compared to that of the reference pavement. This can also be seen from the higher temperature of the modified pavement compared to that of the reference. The inlet/outlet temperature difference, after running the system for approximately 1h, was about 5°C and 10°C for the reference and the modified pavements, respectively. The temperature difference was reduced as the inlet water temperature decreased and approached the pavement temperature. After running the system for 21h, the inlet/outlet temperature difference was about 2°C and 4°C for the reference and modified pavements, respectively.

The heat rejection rate (W/m) to the pavements was calculated using Eq. 5-9 (Page 118) and is shown in Figure 5-27 (negative values mean lower outlet temperature than inlet temperature, i.e. heat rejected to the pavement). From Figure 5-27, it can be seen that the heat rejection rate to the LMC concrete (i.e. the modified pavement) was higher to the soil (i.e. the reference pavement). Respectively for the modified and the reference pavements, heat rejection was approximately at 81 W/m and 40 W/m after 1h operation, decreasing to approximately 40 W/m and 20 W/m after continuously running the system for 21h. Thus, it can be concluded that the heat rejection decreases with running time due to the reduction in the temperature difference between the inlet water and pavement. However, the ratio of heat rejection between the modified and the reference pavement was fixed. The higher ability of heat extraction/rejection of the ground materials, in practice, can lead to a shorter pipe installation and reduction in land surface area required for system installation. For a 10 kW heat pump, for example, it can be calculated that with an average heat rejection of about 20 W/m for the reference pavement, the pipe length requirement is about 500m (i.e. 10000W/20W), whilst this value is halved for the modified pavement assuming an average

heat rejection of 40 W/m. It is emphasized that, in these experiments, the modified pavement was compared to the best reference pavement since the pipes were buried in highly conductive quartz sand, as recommended for GSHP installations.

Figure 5-28 shows a case where cool tap water was circulated through the pipes to simulate the heat extraction from the pavement. Figure 5-28 shows that, for a similar initial temperature distribution within the pavements, the outlet water temperature of the modified pavement was higher than that of the reference pavement. The mean heat extraction rate was calculated to be ~9 W/m and ~4 W/m for the modified and the reference pavements, respectively. The lower value of heat extraction rate, compared to the heat rejection, was due to the small temperature difference between the inlet water and the pavement temperature. In practice for GSHP systems, the inlet temperature should be 11°C-17°C higher than the ground temperature for cooling (i.e. summer mode) and 6°C -12°C lower than the ground for heating (i.e. winter mode) period (ASHRAE 1995; Banks 2008).
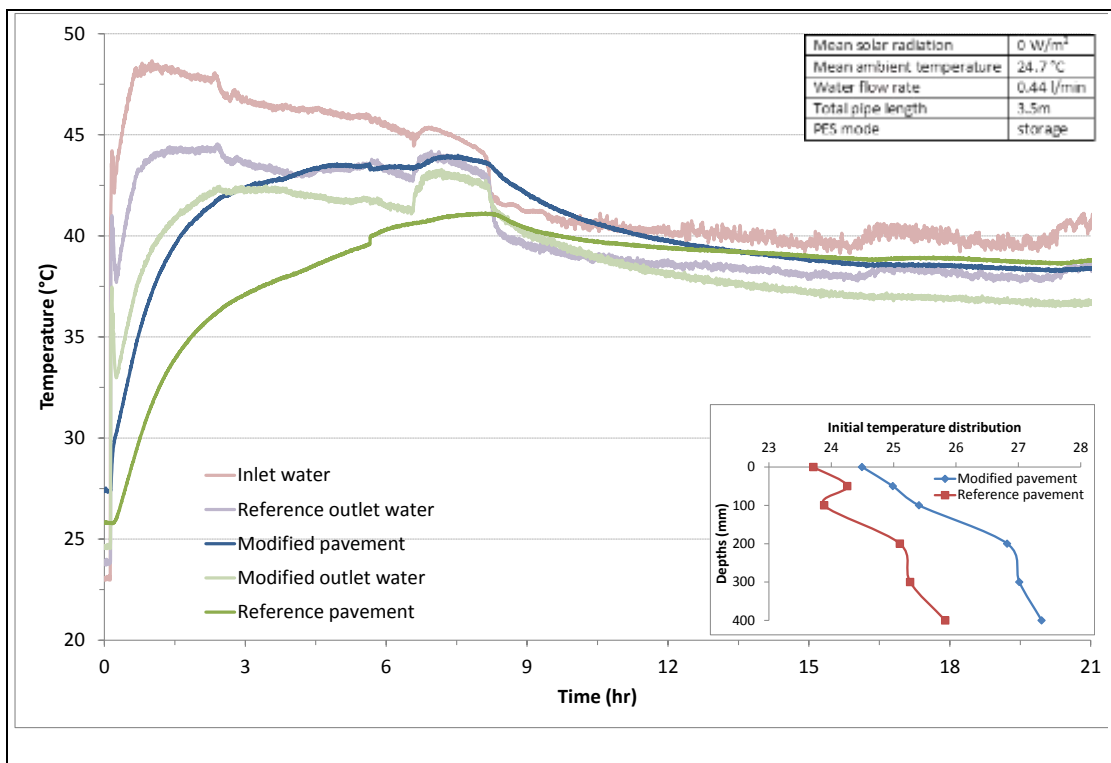
Figure 5-26 Warm water circulation within the reference and modified concrete pavements

145
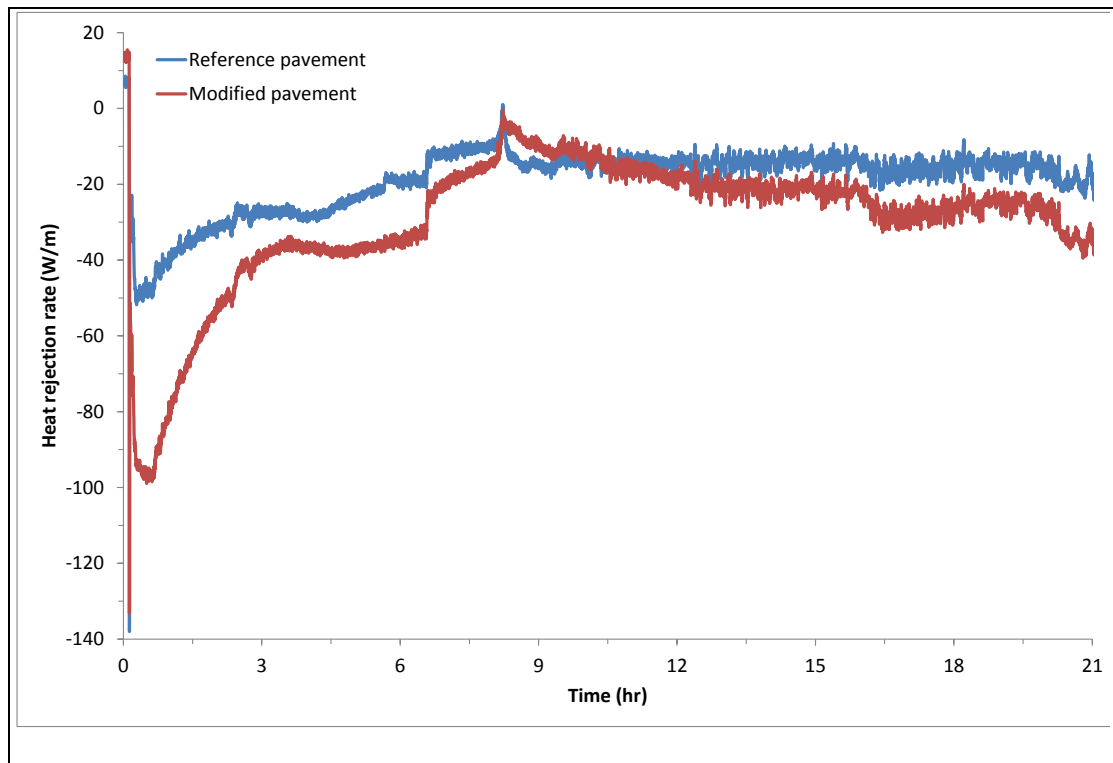
Figure 5-27 Heat rejection rate (W/m) to the reference and modified concrete pavements
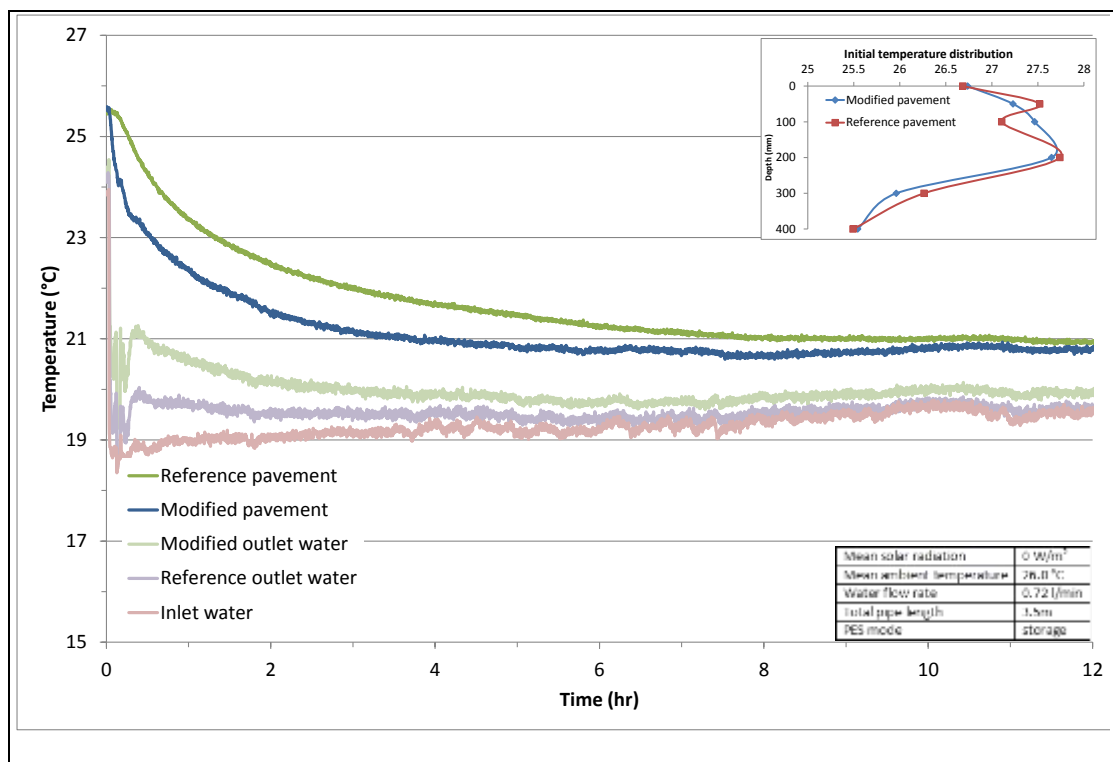
Figure 5-28 Cool water circulation within the reference and modified concrete pavements

Hybrid mode

146

Hybrid systems are designed to collect the summer heat by the collection loops and to store it at shallow depth through the storage loops. Figure 5-29 and Figure 5-30 show the performance of both pavements in the hybrid mode. In both experiments, the pavement temperature at the storage pipes was initially at a relatively high temperature (~ 30-35°C). Therefore, the collected heat from the top pipes could not reach a temperature to be greater than the pavement temperature at the storage pipes. For this reason, the storage of heat in the pavement did not happen and the water further absorbed heat from the lower layers of the pavements. Although the collected heat by the collection loops was not stored in the bottom layers through the storage pipes, Figure 5-29 and Figure 5-30 suggests that the ability of the concrete (i.e. modified pavement) was superior to that of soil (i.e. reference pavement) in rejecting heat from the pavement to the water. The outlet water temperature from the storage pipes was higher than that of the reference pavement by ~1.5°C in Experiment#1 (see Figure 5-29) and ~1.2°C in Experiment#2 (see Figure 5-30). In addition, in both experiments the predicted outlet water temperatures were in good agreement with the measured ones with a mean error of 0.4°C.
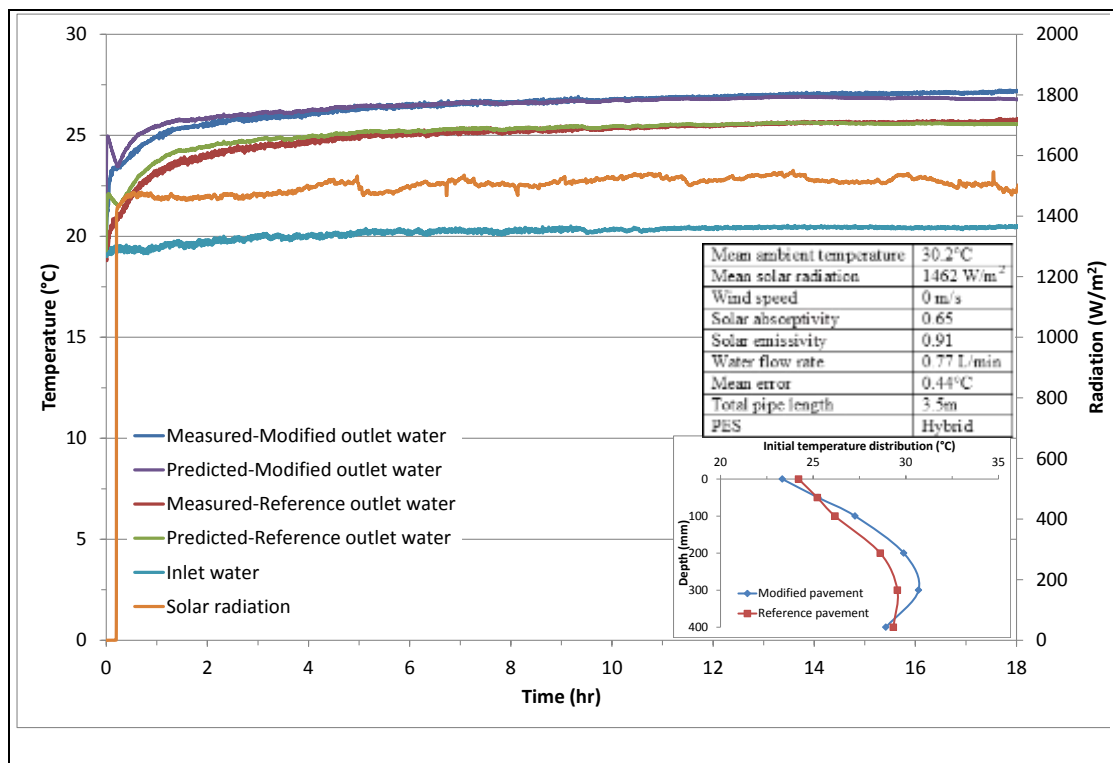
Figure 5-29 Hybrid performance of the reference and modified pavement, experiment#1
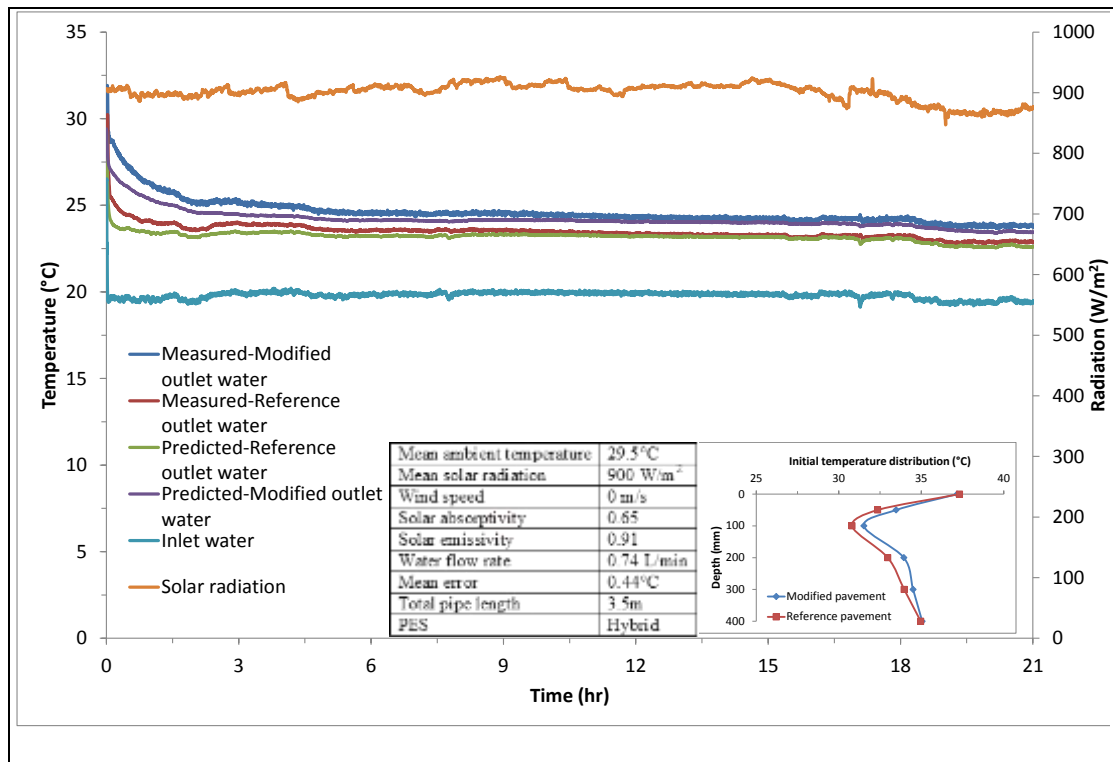
Figure 5-30 Hybrid performance of the reference and modified pavement, experiment#2

5.5.2. Asphalt Pavements

The asphalt pavements consisted of a reference asphalt, 100 mm limestone (see Mix#1 in Table 3-9), and a conductive asphalt pavement, 100 mm quartzite (see Mix#4 in Table 3-9). Since the in-situ compactions of the asphalt pavements were difficult, asphalt mixes were compacted in a special designed box (500mm×700mm, with a thickness of 100mm). The asphalt pavements were mixed (see the procedure in Section 3.6, page 85) and compacted, using a Kango hammer, in two layers. They were then transferred from the box to the solar pavement rig and placed on top of the soil. The heat collection ability of the asphalt pavements was evaluated.

Figure 5-31 shows the predicted and measured outlet water temperature from the reference and modified asphalt pavements. The experimental results show that the temperature rise in the reference and modified pavement was ~3.3°C and ~3.1°C, respectively. The predicted

temperature rise from the modified and reference pavements was ~4.2°C and ~3.5°C, respectively.
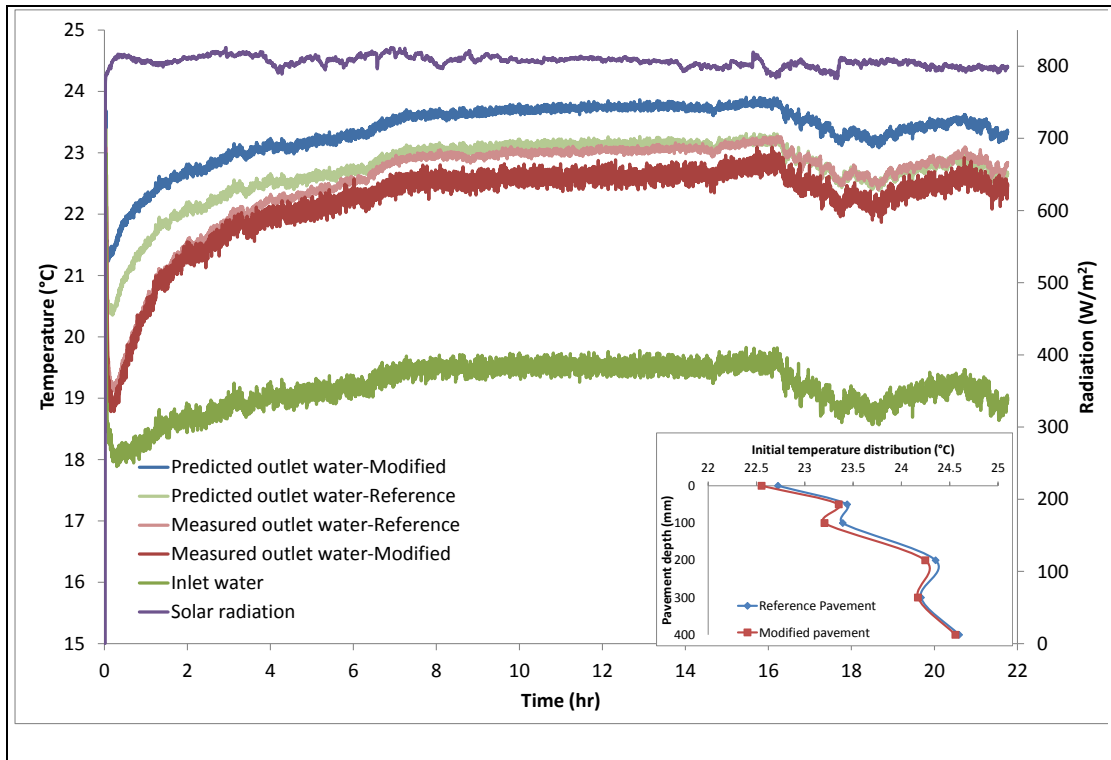
Figure 5-31 Measured and predicted outlet water temperature from the reference and modified asphalt pavements

Figure 5-32 shows the mean measured and predicted surface temperature of the reference and modified asphalt pavements for the same experiment. Although the mean measured and predicted surface temperature of the modified pavement was lower than that of the reference pavement by ~8°C, there were significant discrepancies between the measured and predicted surface temperature for both pavements. From Figure 5-32 can be observed that, the model under-predicts the surface temperature by ~14°C for both reference and modified pavements.
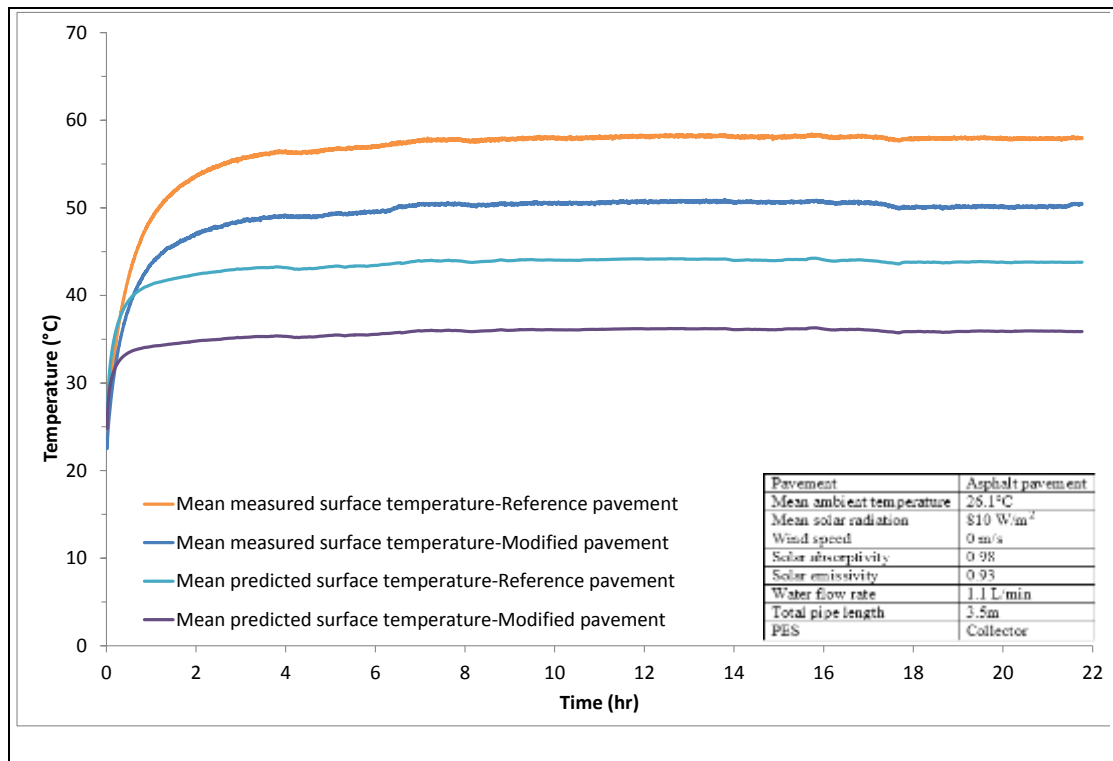
Figure 5-32 Measured and predicted surface temperature of the reference and modified asphalt pavement, experiment#1

A similar experiment with different flow rate and solar intensity was performed (see Figure 5-33) and similar results were obtained. Figure 5-33 shows that, the modified pavement has maintained the pavement surface temperature at ~5°C lower than the reference pavement. However, Figure 5-33 also shows that, there exists a significant temperature difference of ~11°C between the measured and predicted surface temperatures for both pavements.
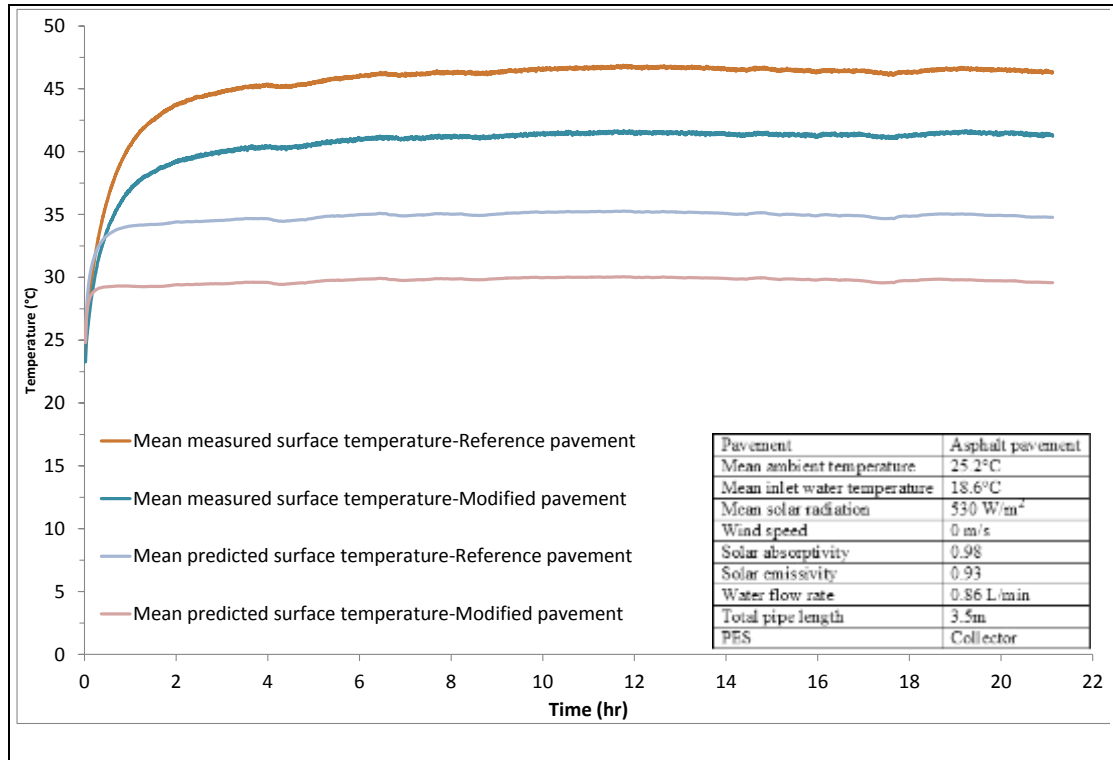
Figure 5-33 Measured and predicted surface temperature of the reference and modified asphalt pavement, experiment#2

The fact that the surface temperature of pavements was under-predicted by the model may indicate that, in the experiment, thermal energy was not effectively exchanged between the pipes and the asphalt pavement and therefore, the solar radiation absorbed by the asphalt pavements may not be transferred to the pipe efficiently, the asphalt thereby reaching a higher temperature than anticipated. It was suspected that the problem could have been arisen at the microstructure level where the pipe and pavement are bonded together.

5.6.   X-Ray Analysis

The Interfacial Zone (IZ) between the embedded pipes and the asphalt pavement was investigated using X-Ray Computed Tomography (XRCT). An asphalt slab, with dimensions of 300×300mm and a thickness of 100mm, with an embedded pipe in the middle was manufactured from the same mix design as the reference pavement. A cylinder, 300mm height and 100mm in diameter, with the embedded pipe in its centre was cored out of the slab. The cylinder was X-rayed across the height of the specimen at ~3mm slice spacing to give 100 slices.

Figure 5-34 shows some typical XRCT slices of the asphalt specimen with embedded copper pipe (more XRCT images are available in Appendix C). Improper bonding between the pavement's materials and the pipe can be clearly observed by the presence of air voids around the pipe. Air with a thermal conductivity of 0.024 W/m K has a high thermal resistance compared to pavement materials. Therefore, the existence of air voids around the pipe could limit the effective heat exchange between the pipes and the asphalt pavement, and could explain the significant discrepancies between the predicted and measured temperatures by the model.
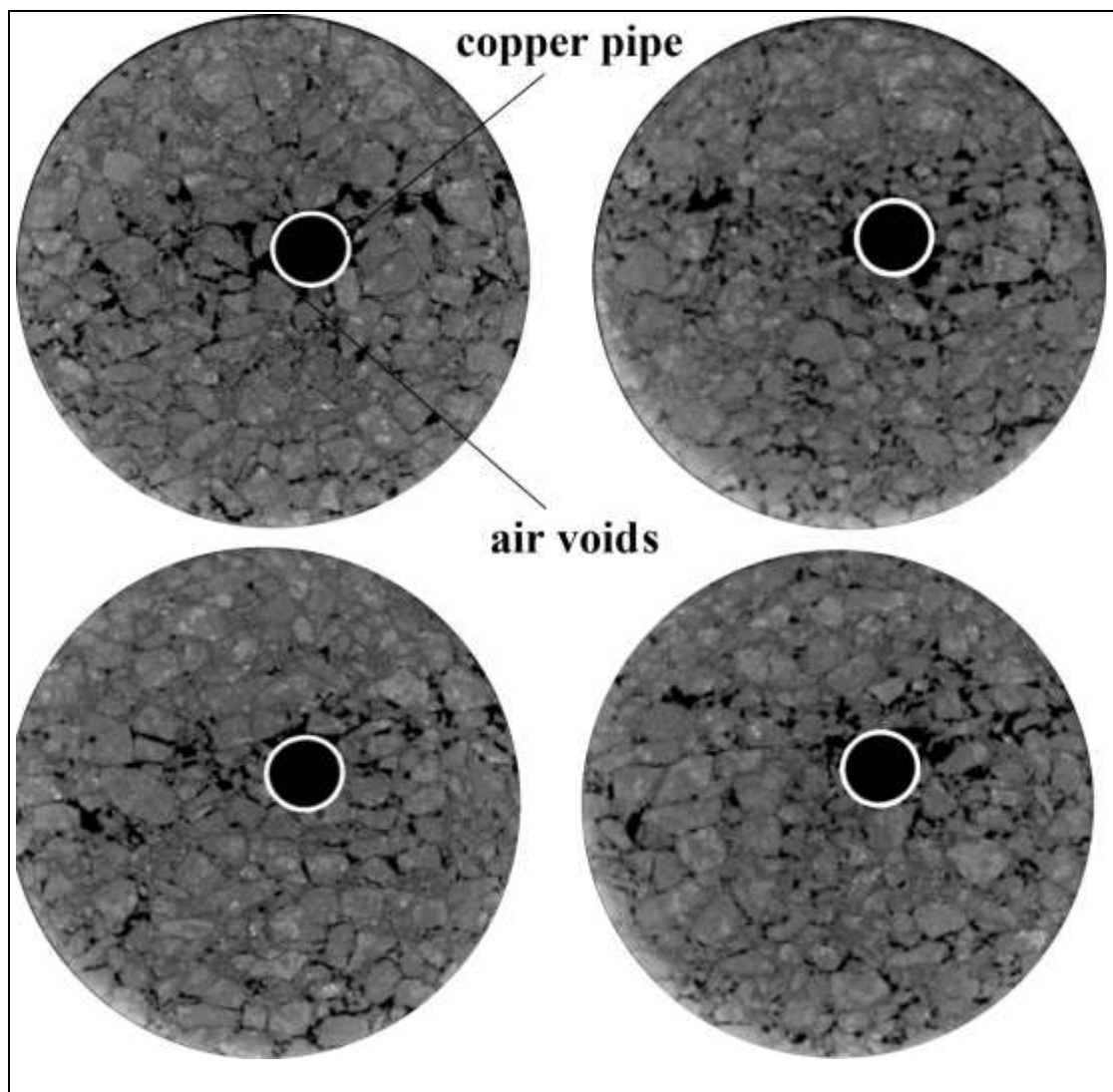
Figure 5-34 XRCT images of asphalt specimen with embedded copper pipe

The effect of the IZ on the surface temperature of asphalt pavement was simulated. For this reason, the predictive model simulations shown in Figure 5-32 and Figure 5-33 were

reproduced for cases when the effect of high thermal resistance of the air void around the pipe was considered in the model. This effect was replicated by introducing the air void thermal resistance (i.e. d_{air}/λ_{air}) to the equation of overall pipe heat transfer coefficient (U_{pipe}) (see Eq. 5-11, Page 119), so that the equation changed to:

$$U_{pipe} = \frac{1}{\frac{1}{h_{pipe}} + \frac{d_{pipe}}{\lambda_{pipe}} + \frac{d_{air}}{\lambda_{air}}} \qquad \textbf{Eq. 5-15}$$

Where, d_{air} =air void thickness around the pipe (mm), λ_{air} = thermal conductivity of air (W/m K)

Since the air void distribution around the pipe was not uniform therefore, the simulation was performed for three different values of d_{air}/λ_{air}. Figure 5-35 and Figure 5-36 show the predicted surface temperature when the IZ effect was considered in the model. From Figure 5-35 and Figure 5-36 can be clearly observed that, once the IZ phenomenon are considered in the model, the surface temperature predictions were in much better agreement with the measured values, and the ratio of d_{air}/λ_{air}=0.002/0.024 found to give a better fit in both experiments.
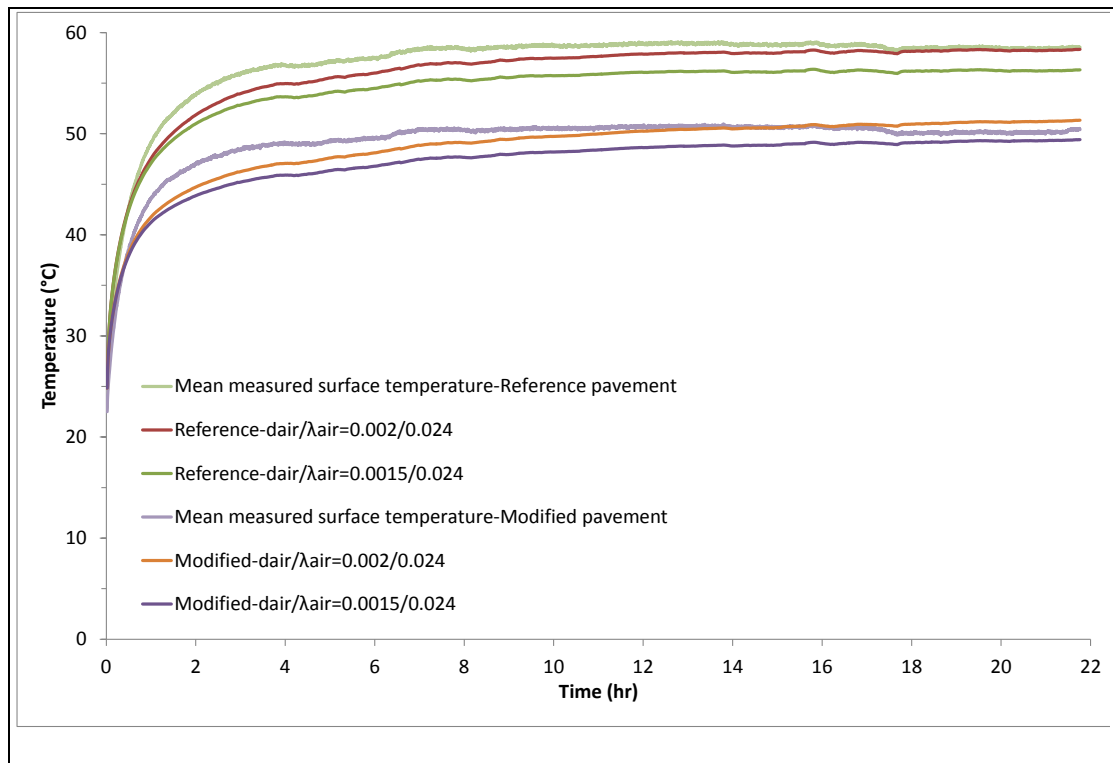
Figure 5-35 Predicted surface temperature with IZ consideration, experiment#1
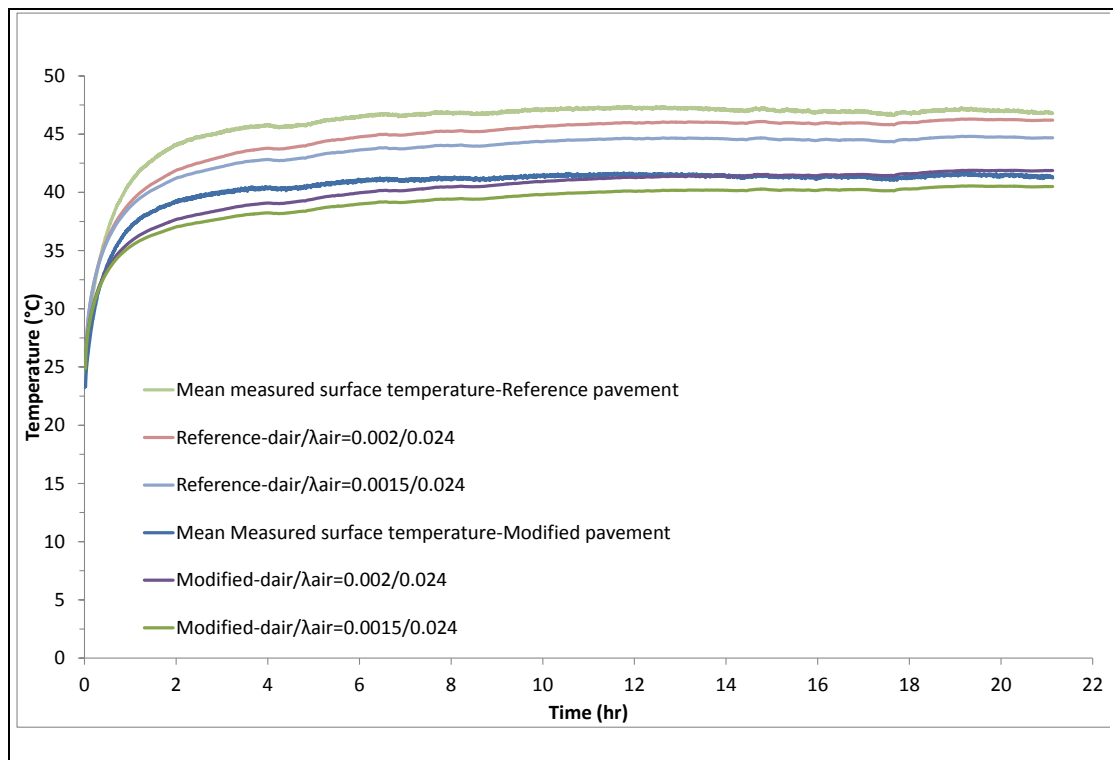
Figure 5-36 Predicted surface temperature with IZ consideration, experiment#2

Due to the importance of the IZ on the thermal energy exchange of the PES applications, different pavements and pipes materials were also investigated for such a problematic phenomenon. XRCT images were taken across concrete, sand, and asphalt samples with embedded copper and polyethylene pipes.

Figure 5-37 and Figure 5-38 show representative XRCT images of the concrete specimen with embedded copper and polyethylene pipes respectively. Concrete, because of its higher fluidity during placing compared with asphalt, showed good bonding with both copper and polyethylene pipes, and no sign on the IZ was observed. The close agreement between predicted and measured temperatures for concrete pavement, whilst not accounting for additional resistance of the IZ air voids, supports the theory that this phenomenon could be responsible for the significant inaccuracy of some predictions in the model, e.g. for asphalt. Therefore, concrete pavements (assuming the same solar absorptivity) are likely to perform better than asphalt in collecting heat energy due to i) their minimal limitation of heat transfer at the pipe/pavement IZ region ,ii) due to their higher thermal conductivity. The solar absorptivity of concrete pavements could be improved with the addition of a high-absorptivity coloured surface coating, or by addition of a dark additive such as fly ash which is commonly used in concrete production, or by addition of a thin bituminous overlay.

Figure 5-39 and Figure 5-40 show some XRCT images of a sand specimen with embedded copper and polyethylene pipes, respectively. Figure 5-39 shows no sign of the IZ in the sample with copper pipe, however a small IZ can be observed between the sand and the polyethylene pipe in Figure 5-40. The air void around the pipe might be caused by electro-static repulsion by the charged surface of the polyethylene pipe. The IZ between the sand and the polyethylene pipe may have some negative effect on the fluid heat extraction/rejection rate in the GSHP application where such pipes are used in highly conductive sand.

Figure 5-41 show some XRCT images of the asphalt specimen with embedded polyethylene pipe. Deformation of the pipe, as a result of pipe softening due to the hot asphalt as well as compaction, can be seen. Figure 5-41, clearly shows the IZ between the asphalt pavement and the polyethylene pipe. In addition, several cracks that are orientated perpendicular to the pipe can also be observed. The cracks were possibly caused because of the pipe recovery after it was being compacted so that the pipe will push the mixture apart and hence cracks appeared. In practice, cooling water is normally circulated to minimise such damages to the pipes during compaction (de Bondt 2003; Carder et al. 2007), however reduction in temperature around the pipes may also induce cracking as well as improper compaction of the asphalt mixture.
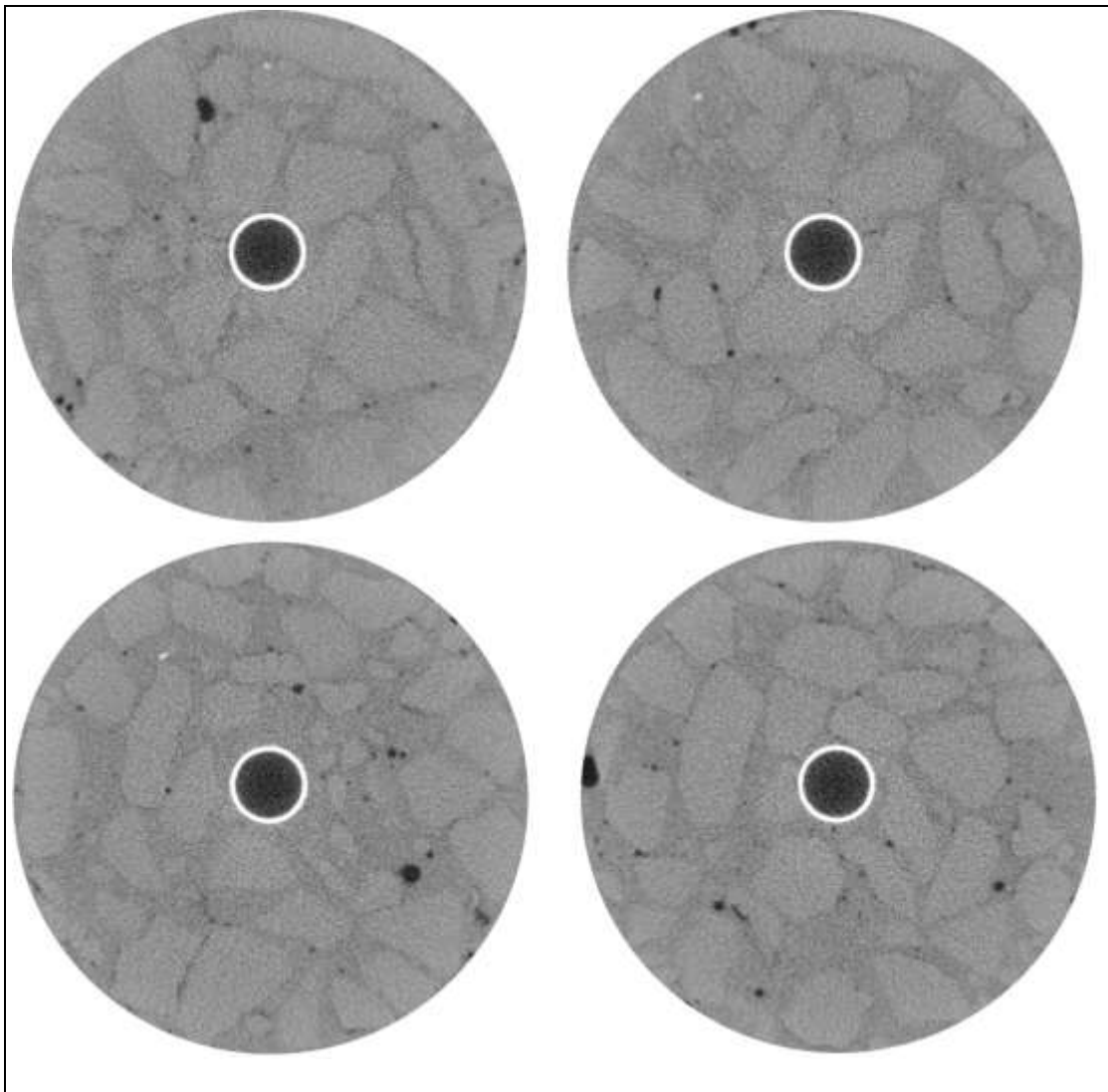
Figure 5-37 XRCT images of concrete specimen with embedded copper pipe
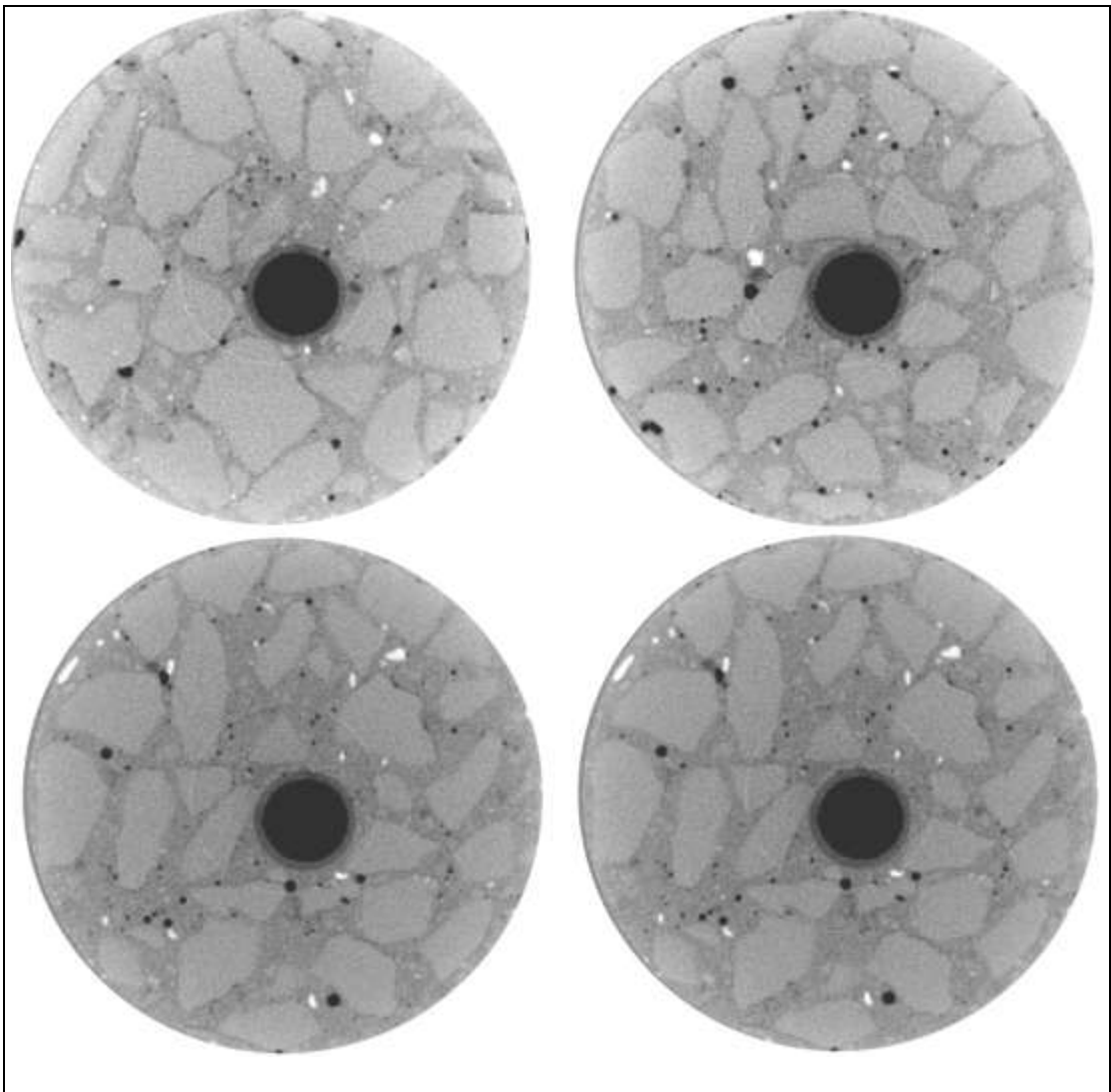
Figure 5-38 XRCT images of concrete specimen with embedded polyethylene pipe
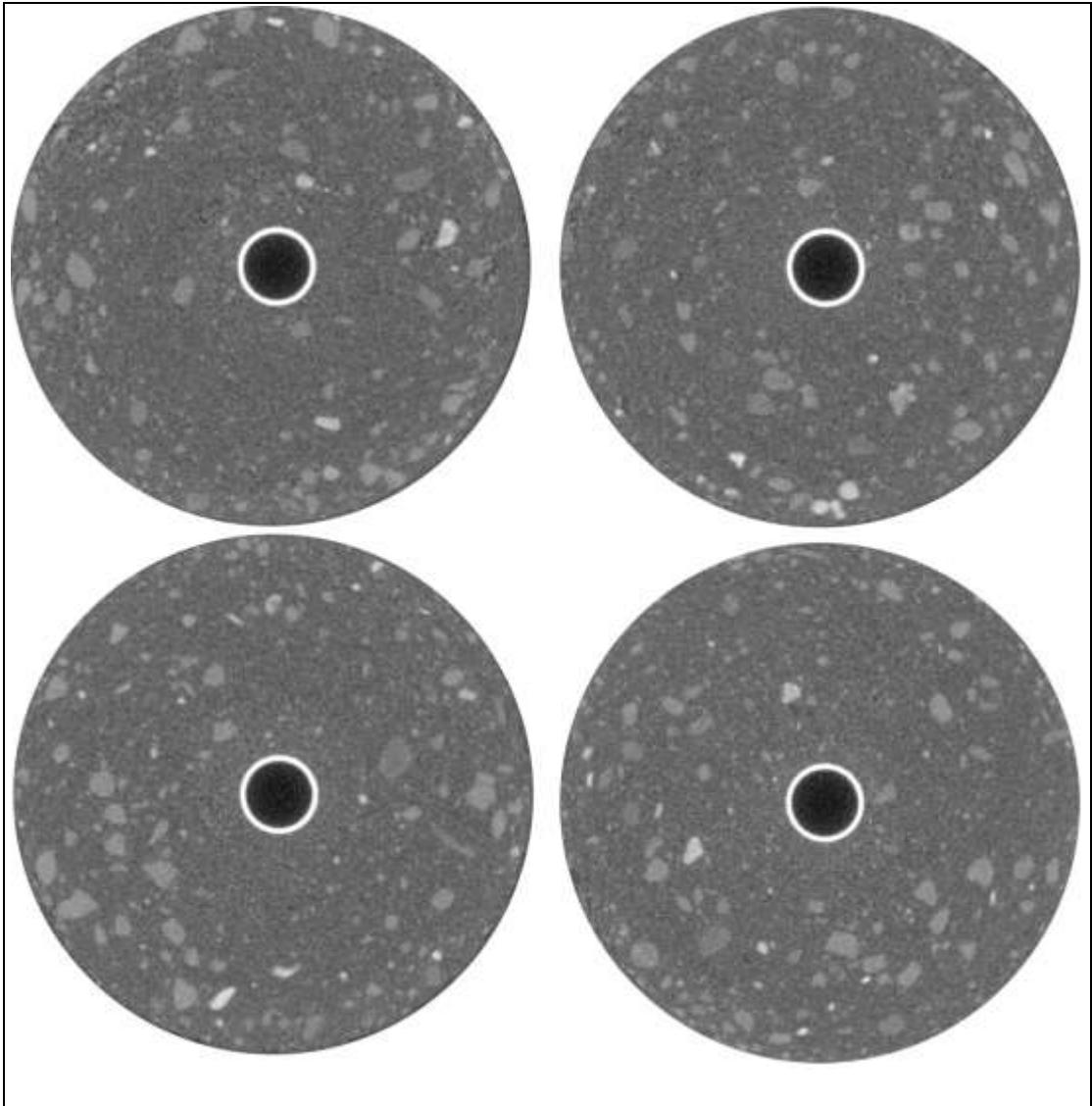
Figure 5-39 XRCT images of sand specimen with embedded copper pipe
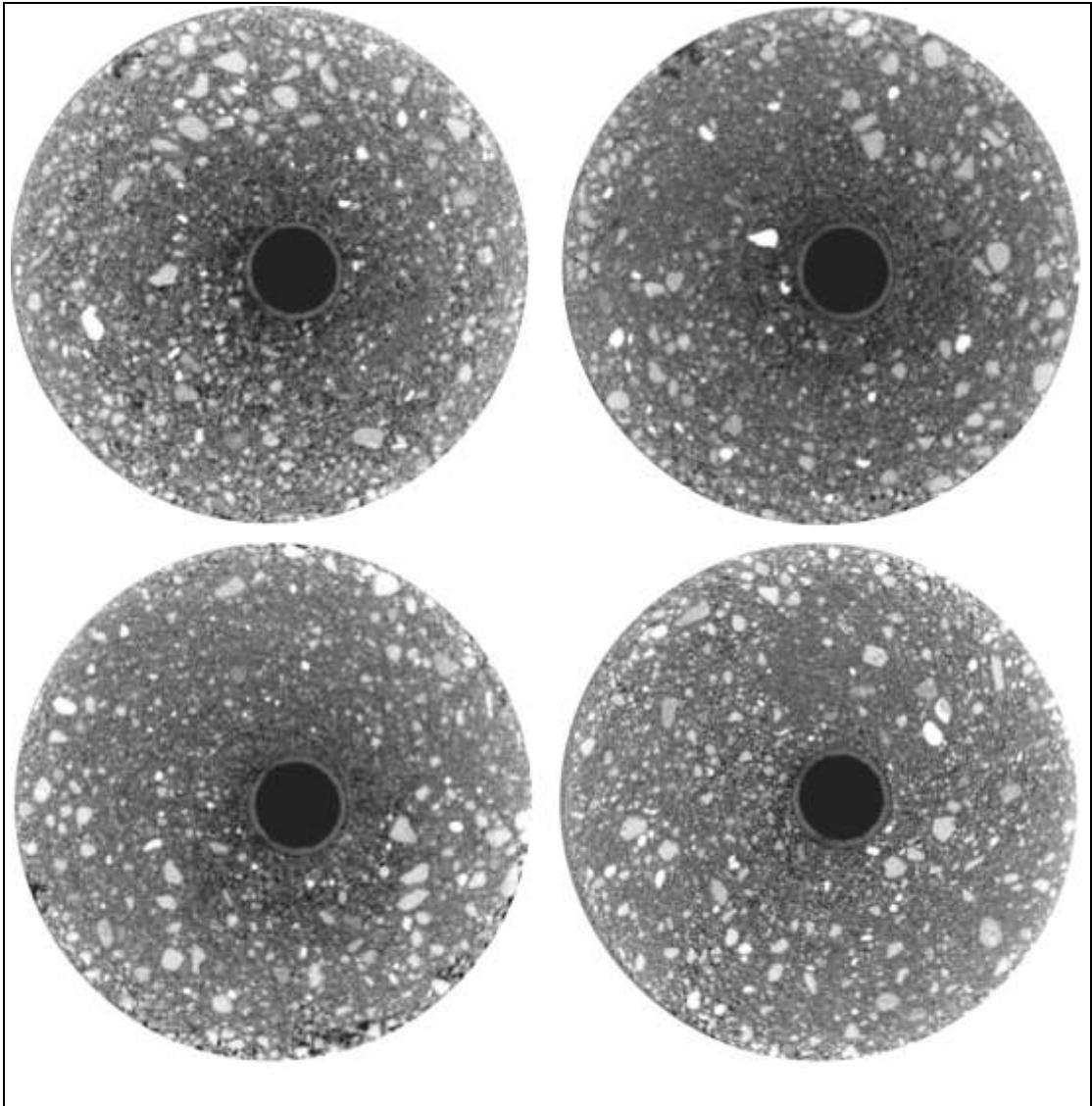
Figure 5-40 XRCT images of sand specimen with embedded polyethylene pipe
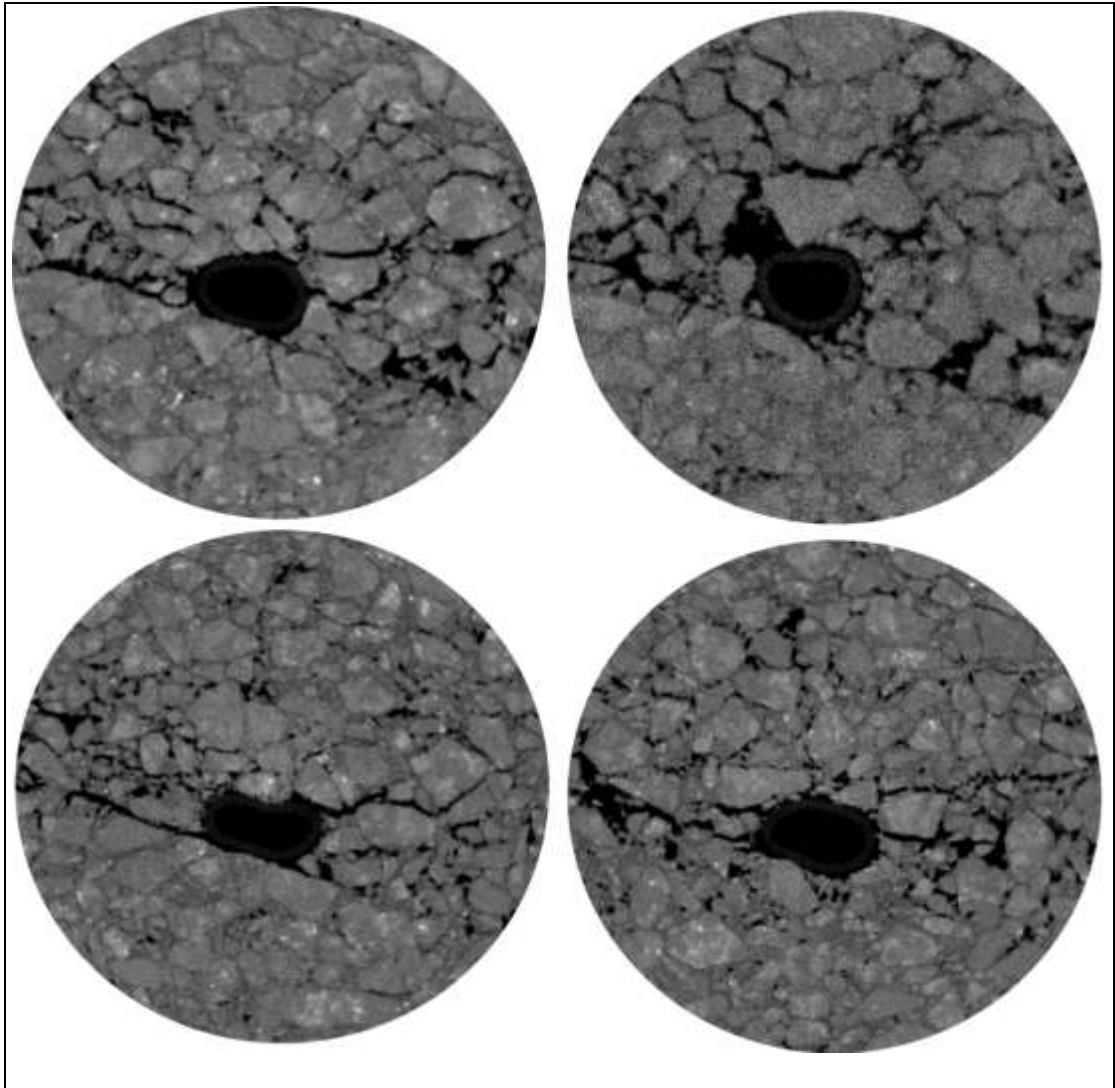
Figure 5-41 XRCT images of asphalt specimen with embedded polyethylene pipe

5.7.   Summary

- This chapter addressed 4th objective of this study that was; to develop and validate a numerical tool in order to simulate the performance of the PES.

- A pseudo 3D computer program was developed such that any applications of the PES can be simply evaluated. The model can cope with any number of pavement layers and up to two pipes cross-section can be modelled. The model's user friendliness, flexibility, operational simplicity, and acceptable accuracy, makes the model a suitable tool for the simulation of PES applications and also as an open-source/programmable alternative to costly commercial software.

- A large-scale physical model of the PES was designed and constructed to determine the performance of the PES and to validate the numerical model. The physical model consisted of copper pipes embedded in a pavement which was irradiated (causing surface heating) using halogen lamps. The pipes connected in various arrangements so that any of the PES applications could be tested. Temperatures predicted numerically were generally in close agreement with the experimental values from the physical model, with a mean error of less than 1℃.

- The PCM model was also validated by comparing the surface temperature changes of a reference concrete and a PCM-modified concrete. The experimental results show that, the addition of the PCM caused a surface temperature reduction of ~4℃ throughout its melting temperature range that was successfully predicted by the model.

- Using the physical model, the performance of modified asphalt and concrete pavements were compared with those of conventional ones. Comparison between a modified pavement (i.e. with quartzite concrete) and a reference pavement (i.e. with limestone concrete) revealed that the modified pavement, due to its higher thermal diffusivity, could produce higher outlet water temperatures in collection mode, which is desirable for such a system and improves its efficiency. In addition, quartzite-rich pavements, due to their greater ability to conduct thermal energy within the pavement, show that they have a much greater ability to reduce the pavement surface temperature compared to that of limestone-rich pavements. A maximum difference of ~8°C was observed between the reference and modified concrete pavement surface temperatures under the conditions of this study.

- The heat storage ability of a PSHS (i.e. concrete pavement) was compared with that of a GSHP (i.e. soil) by entering cool and hot water through the pipe. It was found that the PSHSs have greater abilities in heat extraction and heat rejection. The rate of

heat extraction and heat rejection was almost double in the PSHS compared to that of the GSHP.

- The heat collection ability of the modified (i.e. quartzite mix) and reference (i.e. limestone) asphalt mixtures was also investigated. The experimental results showed the surface temperature of the modified pavement was lower than that of the reference pavement. However, there were significant discrepancies between the measured and predicted surface temperatures for both pavements. The model under-predicted the surface temperature by ~14°C for both reference and modified pavements. The Interfacial Zone (IZ) between the embedded pipes and the asphalt pavement was investigated using X-Ray Computed Tomography (XRCT). XRCT images showed improper bonding between the pavement's materials and the pipe due to the presence of air voids around the pipe. The IZ effect was approximated in the numerical model and, subsequently, the surface temperature predictions were in much better agreement with the measured values.

- Different pavements and pipes materials were also investigated for the IZ. XRCT images were taken across concrete, sand, and asphalt samples with embedded copper and polyethylene pipe. Concrete, because of its higher fluidity during placement than asphalt, showed good bonding with both copper and polyethylene pipes, and no sign of the IZ was observed in the XRCT images. A small IZ was observed between sand and the polyethylene pipe. Polyethylene pipes in the asphalt mixture were deformed as a result of pipe softening due to the hot asphalt as well as due to compaction, and the IZ was observed between the asphalt pavement and the pipe. In addition, crack development was observed in the XRCT images that possibly occurred because of the pipe recovery after the mix had been compacted.

6   MATERIALS DESIGN OPTIMISATION FOR DIFFERENT APPLICATIONS

6.1. Overview

The most important advantage of the numerical model developed in Chapter 4 and 5 is the ability to implement meteorological data. In this chapter the performance of the PES under various conditions (e.g. pavements' thermo-physical properties, layer sequence, climatic conditions, etc.) are evaluated using the validated model.

6.2. Material Design Optimisation for Pavement Heat Collector (PHC) Applications

6.2.1. Temperature Distributions in Pavements

In this section the temperature distribution in pavements were predicted for cases when no fluid was circulating through the pipes. Figure 6-1 shows the cross-section of an existing pavement (US Department of Transportation–Federal Highways Administration 2009) with different thermo-physical properties obtained from Table 3-5 for concrete pavements and from Table 3-9 for asphalt pavements. For concrete pavements, the thermo-physical properties were considered as the average value of dry and wet states. The surface absorptivity/emissivity values used in the model were 0.9/0.91 for asphalt and 0.65/0.91 for concrete.

Figure from the page showing pavement cross-section and tables:

Cross-section diagram:
- ○=Loops
- Layer A — 40mm
- Layer B — 120mm
- Layer C — 320mm

Asphalt pavement Code	Layer A	Layer B	Layer C
Reference Pavement-A0	*Mix#1 (Limestone Mix)	**Granular base	***Compacted soil
PHC Design#A1	*Mix#4 (Quartzite Mix with high conductivity)	*Mix#6 (Lytag mix with low conductivity)	*** Compacted soil

*Refer to Table 3-8

**=(Côté and Konrad 2005) λ=1.0, c_p=1000, ρ=2100

***=(ASHRAE 1995) λ=1.0, c_p=1000, ρ=2000

Concrete Pavement Code	Layer A	Layer B	Layer C
Reference Pavement-C0	*Mix#1 (Limestone_PQC mix)	*Mix#14 (Limestone_LMC mix)	Compacted soil
PHC Design#C1	*Mix#3 (Quartzite mix with higher conductivity than reference concrete)	*Mix#15 (Lytag mix with lower conductivity than reference concrete)	Compacted soil
PHC Design#C2	*Mix#4 (Quartzite mix+fibre with higher conductivity than Mix#3)	*Mix#15	Compacted soil
PHC Design#C3	**extremely conductive concrete	*Mix#15	Compacted soil

*=Average of wet and dry values from Table 3-5

**= (Cook and Uher 1974) λ=10.71, c_p= 920, ρ=2590

Figure 6-1 Cross-section of modified pavements for the PHC applications

The simulation was performed for asphalt and concrete pavements in two different climates; Arizona, USA and Sutton Bonington, UK. The Arizona state was chosen as it is a prime location for a PHC installation where solar radiation exceeds 1000 W/m² in summer, and so approaching a 'best case' performance scenario for PHC system. The Arizona LTPP climatic data were collected at weather station number 0100, between 01/01/1996 to 31/12/1996 (US Department of Transportation–Federal Highways Administration 2009). The UK climatic data were collected from the University of Nottingham weather station at Sutton Bonington, Leicestershire, UK (52.58˚N, 1.38˚W), between 01/01/2007 to 26/12/2007.

164

By applying the thermo-physical properties of pavement layers in the thermal model, the mean maximum temperature for each month in Arizona and in Sutton Bonington has been plotted at two depths; 40mm and 120mm. These depths were chosen based on the embedded pipe depths in previous full-scale PES trials by Ooms Avenhorn Holding (de Bondt 2003) and the Transport Research Laboratory (Carder et al. 2007), respectively.

Asphalt pavements

Figure 6-2 and Figure 6-3 show the mean maximum monthly temperatures at depths of 40mm and 120mm for different asphalt PHC designs in Arizona and Sutton Bonington, respectively. Installing the pipe network very close to the surface of the pavement (e.g. <50mm depth) obviously provides higher temperature heat energy for absorption by the working fluid as can be seen in Figure 6-2 and Figure 6-3. For the reference pavement in Arizona (see Figure 6-2), the average summer and winter temperatures at depth of 40mm was about 8°C and 4°C higher than those at 120mm depth, respectively. Whilst, for Sutton Bonington (see Figure 6-3) with a lower mean solar radiation, the average summer and winter temperatures at a depth of 40mm was about 4°C and 2°C higher than those at 120mm depth. Ideally, sufficient depth for pipe burial is required in order to avoid 'reflective cracking' under traffic loading, which has a detrimental effect on the lifespan of the pavement, and also to enable future resurfacing without damaging the pipe network. Pavement resurfacing is currently a problem that Ooms Avenhorn Holding (de Bondt 2003) has encountered in practice where the pipes were installed at 40mm depths (see Section 2.4.2, Page 19).

Figure 6-2 and Figure 6-3 shows that by using PHC Design#A1 the same temperature can be achieved at a depth of 120mm, as the temperature at 40mm depth in the unmodified reference pavement. The presence of a high thermal conductivity pavement layer (i.e. Mix#4, Table 3-9) above a depth of 120mm, combined with a high thermal resistance pavement layer below this depth, (i.e. Mix#6, Table 3-9) can significantly increase the temperature at deeper pipe locations. Loop installation deeper within the pavement is

expected to reduce 'reflective cracking' under traffic loading as well as enabling future

resurfacing of the pavement without damaging the pipe network.
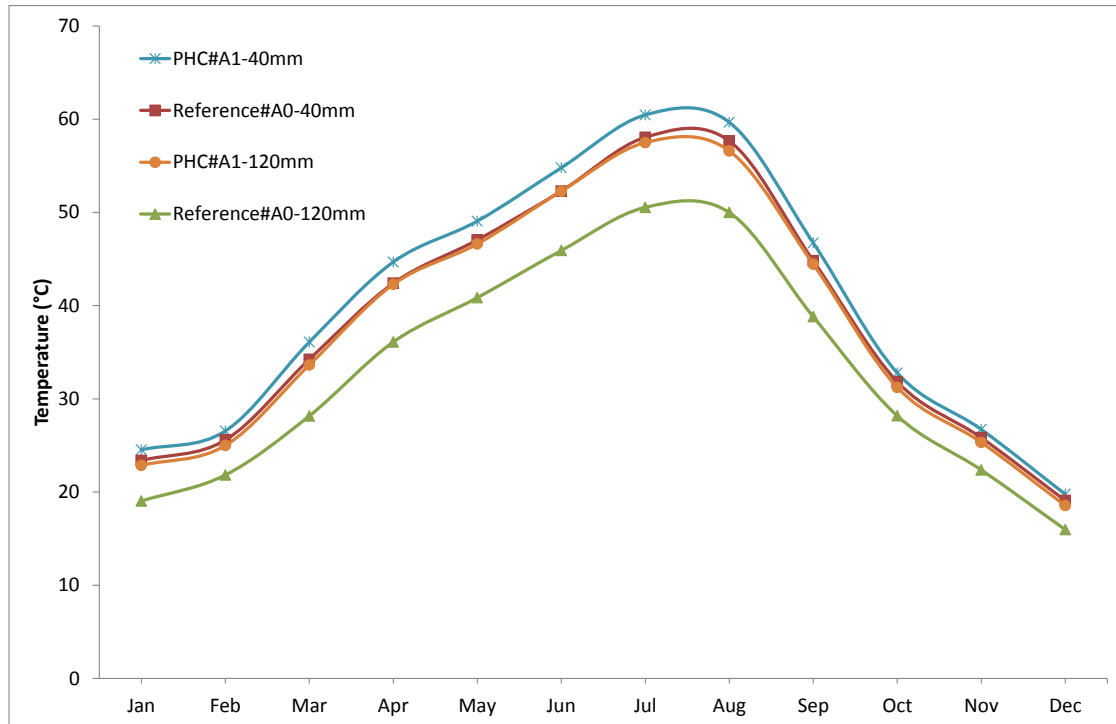
**Figure 6-2 Mean maximum monthly temperatures at depths of 40mm and 120mm in Arizona
for asphalt PHC designs (no water was circulated)**
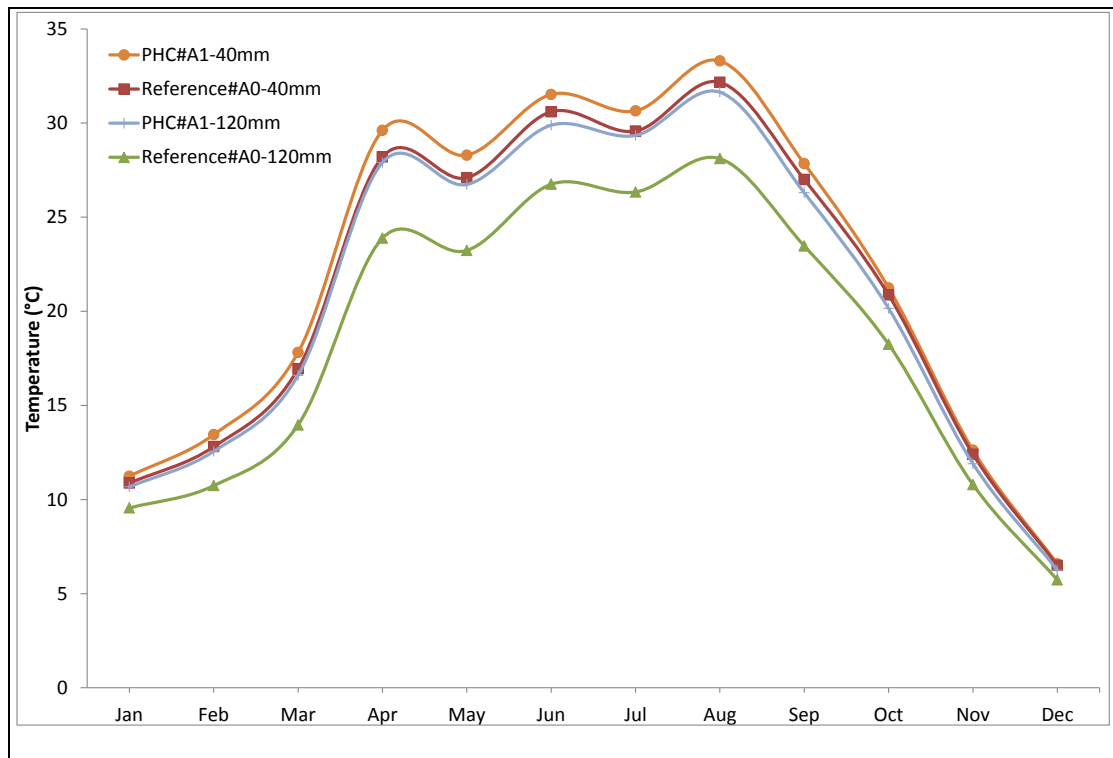
Figure 6-3 Mean maximum monthly temperatures at depths of 40mm and 120mm in Sutton Bonington for asphalt PHC designs (no water was circulated)

Concrete pavements

Concrete pavements produce a lower temperature at the pipe location due to their lighter surface colour than asphalt pavements (i.e. surface absorptivity of 0.65 compared to 0.9). Figure 6-4 shows that at depth of 40mm the maximum temperature of the asphalt pavement is over 30°C whilst this value for the concrete pavement is ~25°C. However, concrete pavements with the addition of a high-absorptivity coloured surface coating and/or addition of fly ash can achieve a surface absorptivity in excess of 0.9 (Christine and Rochelle 2003; Pomerantz et al. 2003). Furthermore, as mentioned in the Chapter 5, concrete pavement PES can achieve a higher efficiency due to their higher conductivity and better bonding with pipes.
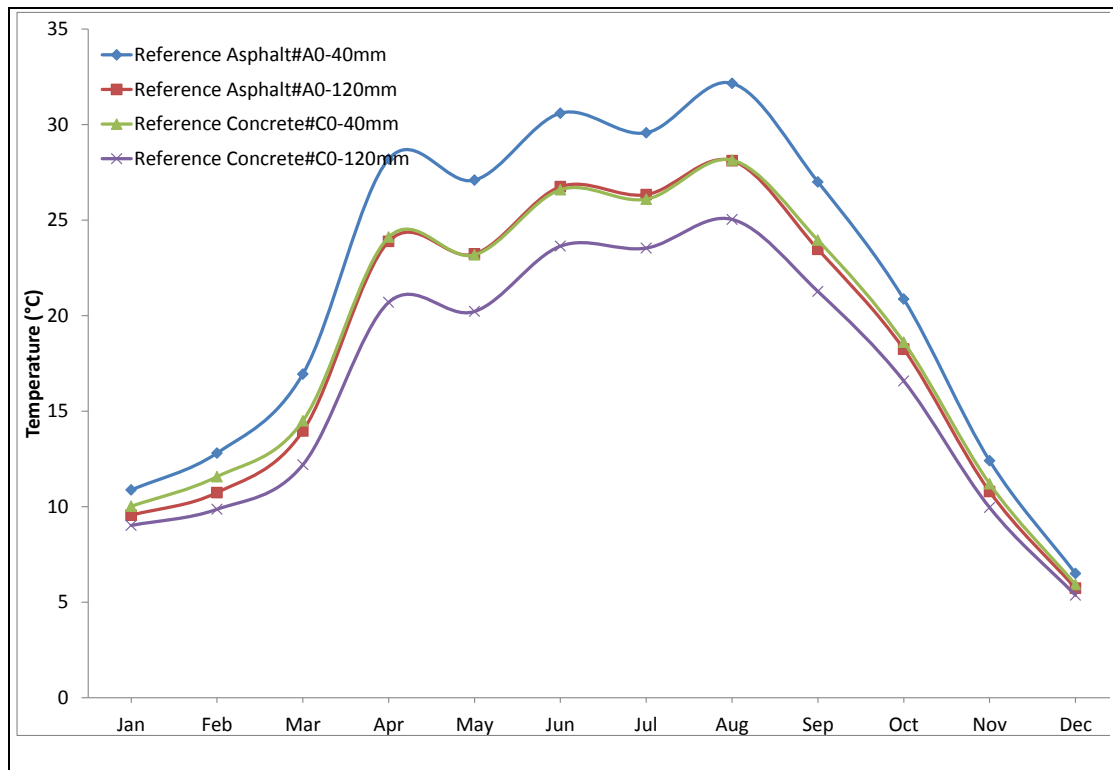
Figure 6-4 Comparison between asphalt and concrete mean maximum monthly temperatures at depths of 40mm and 120mm in Sutton Bonington (no water was circulated)

The mean maximum temperatures in Arizona for concrete with an enhanced solar absorptivity (i.e. 0.9) were predicted. Figure 6-5 shows that applying a high thermal conductivity pavement layer (i.e. Mix#3, Table 3-5) combined with a low thermal conductivity pavement layer below this depth (Mix#16, Table 3-5) can significantly increase the rate of heat transfer to the bottom layers of the pavement. Therefore, the temperature at 120mm in PHC#C1 was about 6°C higher than that in the reference pavement at similar depth, and it was similar to the reference pavement temperature at 40mm depth.

Additionally, Figure 6-5 shows that the average temperature at 40mm has increased by more than 2°C when the reference pavement was replaced with PHC#C1. However, increasing the thermal conductivity of pavement materials further, by applying the PHC#C2 and PHC#C3, has showed no significant increase in the temperature at pipe locations. Therefore, it can be concluded that there is a critical value for a pavement's thermal conductivity beyond which the pavement does not experience any significant temperature increase at sensible pipe installation depths.
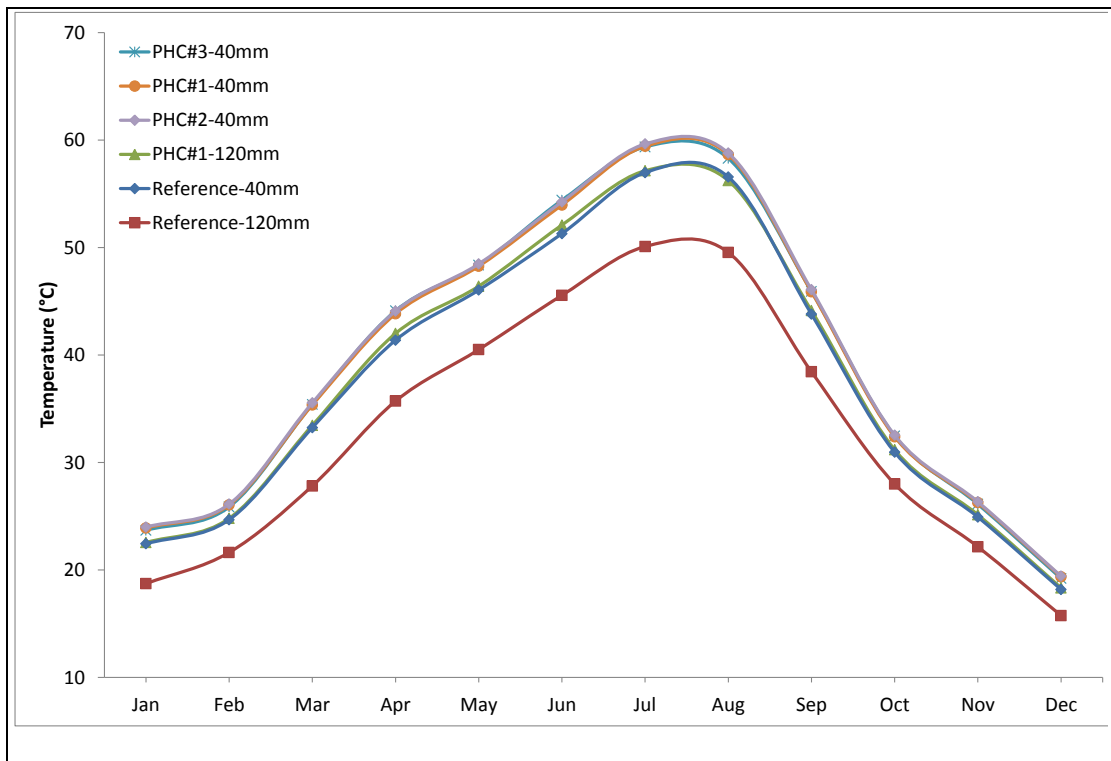
Figure 6-5 Mean maximum monthly temperatures at depths of 40mm and 120mm in Arizona for concrete PHC designs (no water was circulated)

6.2.2. Outlet Water Temperature and Surface Temperature of PHC Systems

In the previous section the temperature distribution in pavements, which consisted of materials with different thermo-physical properties, were investigated. It was shown that, pavement material optimisation and pavement layer sequences can enhance the temperatures at pipe locations and could solve some of the problems associated with the PES technologies (e.g. future re-surfacing, minimising reflective cracking). In this section the outlet fluid temperature as well as the capability of the PHC to increase or decrease surface temperature was predicted when a working fluid is circulating within the pipes. Simulations were performed for two climates; Arizona and Sutton Bonington where the climatic variables for the simulations are shown in Figure 6-6 and Figure 6-7, respectively. Parameters used in the numerical simulation were obtained from other similar experimental works (Carder et al. 2007; Mallick et al. 2009) and are shown on Figure 6-8 and Figure 6-9.
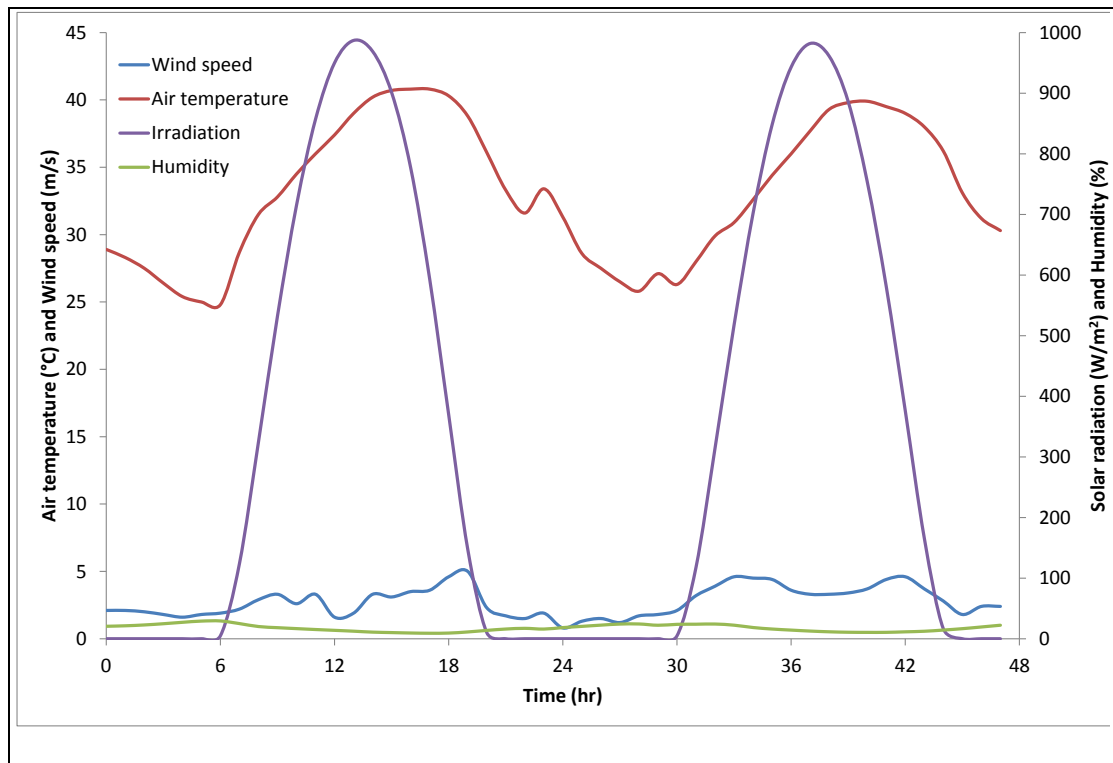
Figure 6-6 Summer climatic inputs for a 2-day period in Arizona (US Department of Transportation–Federal Highways Administration 2009)
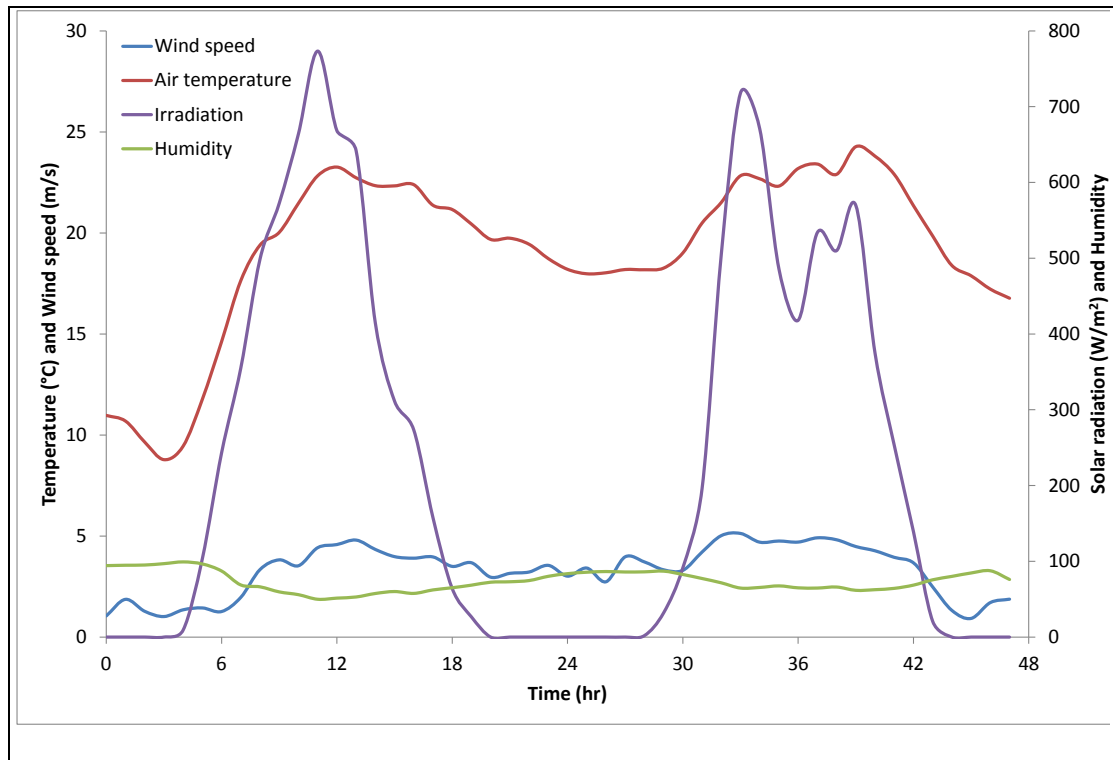
Figure 6-7 Summer climatic inputs for a 2-day period in Sutton Bonington

Outlet fluid temperature

Outlet water temperatures at depths of 40mm and 120mm in Arizona and Sutton Bonington

for asphalt PHC designs were simulated as shown in Figure 6-8 and Figure 6-9, respectively.

Figure 6-8 represents how pavement materials' modification can significantly increase the

outlet water temperature under identified operating conditions. The water temperature in the

modified pavement (i.e. PHC#A1) compared to the reference pavement has increased by

about 8°C and 10°C at depths of 40mm and 120mm, respectively. In addition, loops

installed at 120mm depths in the modified pavement can perform even better than the loops

installed at 40mm depth in the reference pavement in terms of water heating. In high solar

irradiation areas (>1000 W/m^2) the low-grade heat energy absorbed by the working fluid in

the embedded pipes may be upgraded by a heat pump and converted to a transmittable form

by exploiting binary-type energy conversion systems such as Kalina cycles that are typically

used to exploit low-temperature geothermal resources, typically 85˚ C or less (Banks 2008).

Figure 6-9 shows that in a sunny summer in the UK water can heat up to a temperature over

30°C under the conditions used for this simulation (see Figure 6-9). Water circulating in a

pipe network can be used directly or as a heating system for swimming pools, which are

usually operated at between 20°C and 27°C in the UK (Sedgwick and Patrick 1981). In

addition, Figure 6-9 also shows that the optimisation of a pavement materials can allow the

pipes to be installed deeper (i.e. at 120mm) in the pavement and operate as good as (or better

than) the pipes installed at shallower depths (i.e. 40mm) in the reference pavement.
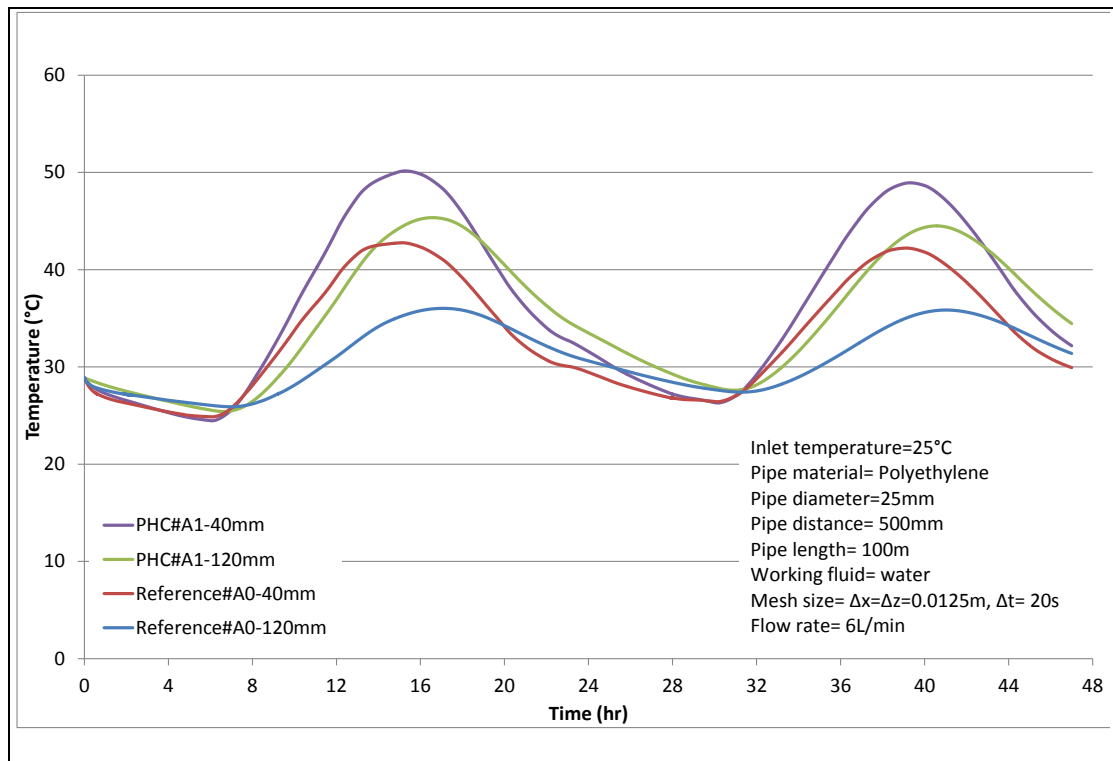
Figure 6-8 Predicted outlet water temperatures at depths of 40mm and 120mm in Arizona for asphalt PHC designs
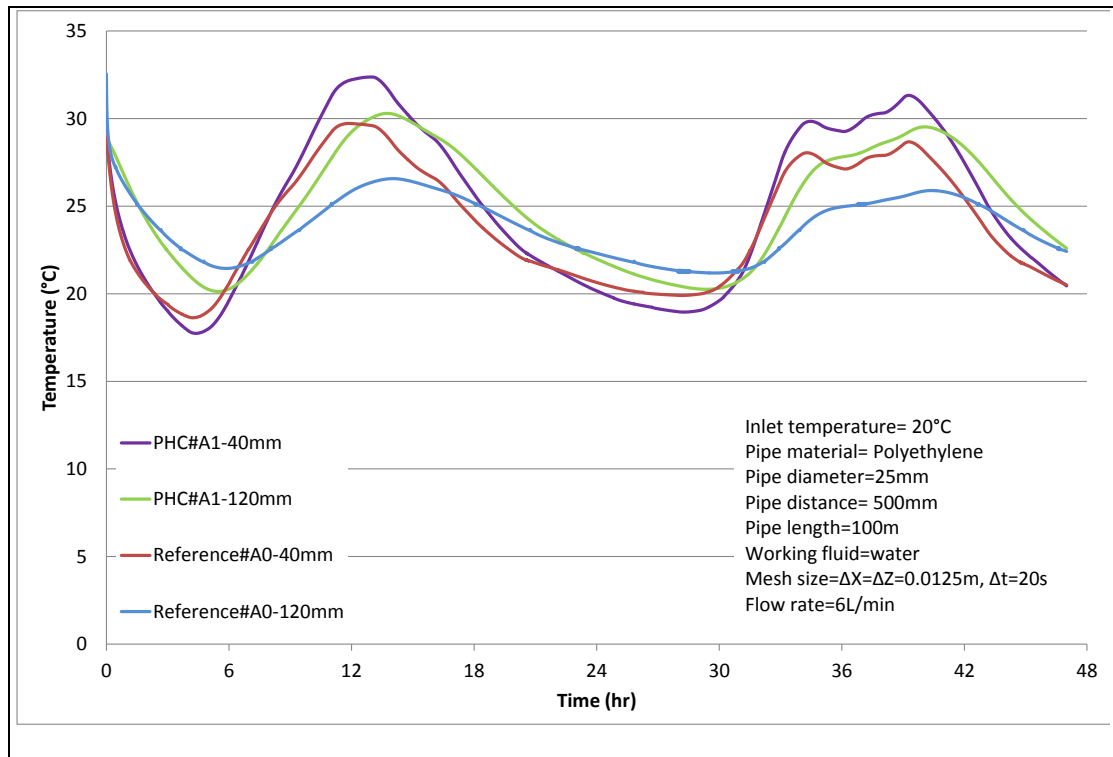
Figure 6-9 Predicted outlet water temperatures at depths of 40mm and 120mm in Sutton Bonington for asphalt PHC designs

Pavement surface temperature reduction

The ability of different PHC designs to reduce the pavement surface temperature was evaluated. Figure 6-10 illustrates mean pavement surface temperature reduction (i.e. the difference between the maximum surface temperature when no water was running through the pipe and the maximum surface temperature when water was running through the pipe) as a function of flow rate in Arizona (i.e. hot climate). Mean temperatures were calculated as the average of maximum temperature (i.e. pavement section above the pipes) and minimum temperature (i.e. pavement section between two pipes). As indicated in Figure 6-10, the results show that, in all cases, the pavement surface was cooled. This is generally good both for reduction of rutting and for the UHI effect in hot climates. The results also show that, as expected, the pavement surface temperature reduction was greater for cases where the pipes were installed at 40mm depth compared to 120mm.

Importantly, the influence of the pavement modification on the surface temperature reduction can be clearly observed in Figure 6-10. At a flow rate of 6 L/min, the pavement surface temperature reduction when changing from the reference pavement to PHC#A1 was about 80% and 210%, for pipes installed at 40mm and 120mm respectively. In addition, Figure 6-10 indicates that, as the flow rate increases, the reduction in pavement surface temperature also increases as more heat is extracted from the pavement (see Eq. 5-9, Page 118). However, increase in the flow rate has a limited influence on the reduction of the pavement surface temperature. At a relatively low flow rate of 1 L/min, the average temperature reduction at 40mm depth in the modified pavement was ~5°C, and increased sharply to ~9°C when the flow rate increased to 3 L/min. The sharp increase in temperature reduction occurred as a result of change in the flow regime where flow changed from laminar flow at 1 L/min (Reynolds number ~1351) to turbulent flow at 3 L/min (Reynolds number ~4053). Doubling the flow rate from 6 L/min to 12 L/min only resulted in ~1.5°C reduction in the pavement maximum surface temperature. Therefore, it can be concluded that the reduction in pavement surface temperature become much less significant after a

certain value of the flow rate. The increase of working fluid flow rate in PES systems will

lead to a higher energy required for pumping to circulate the fluid. Under the climatic

conditions and parameters used in the model, a relationship between the surface temperature

reduction as a function of flow rate was suggested that may be used in similar situations (see

Figure 6-10).
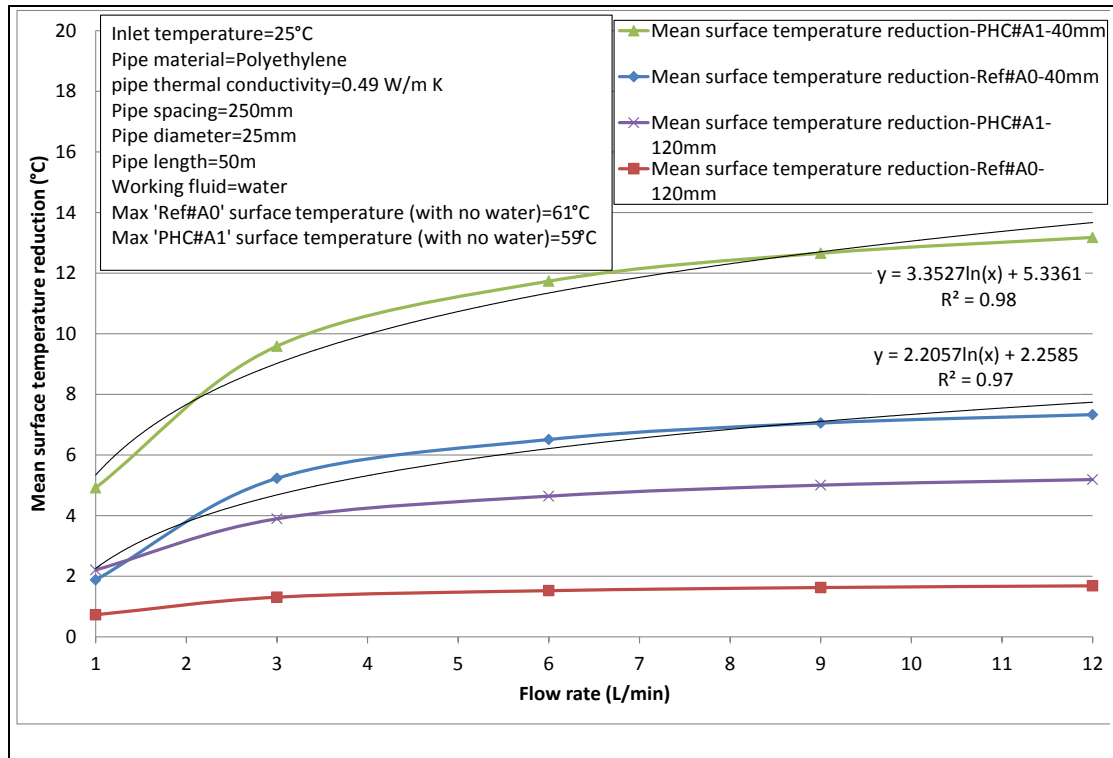
Figure 6-10 Surface temperature reduction as a function of flow rate for 'Reference#A0' and PHC#A1 in Arizona

Pavement surface temperature increase

The ability of the PHC designs to increase the pavement surface temperature in winter, so as

to maintain a temperature above 0°C, was evaluated. A weather pattern was chosen where

air temperature and pavement surface temperatures fell below 0°C overnight, as shown in

Figure 6-11. Figure 6-12 and Figure 6-13 show the mean pavement surface temperature for

the reference and modified asphalt pavements in Sutton Bonington for an inlet temperature

of 10°C and 5°C. The working fluid for winter simulation was an anti-freeze mix (30%

Ethylene glycol) to provide frost protection (Carder et al. 2007; Wu et al. 2010b), and its

thermal properties were extracted from data provided by Banks (2008). From Figure 6-12 it

can be observed that, in all cases, the pavement surface temperature has increased when the fluid was circulated through the pipes. The mean pavement surface temperature remained above 0°C for all cases except for the reference pavement where pipes were installed at 120mm. Figure 6-13 shows that the pavement surface was maintained above freezing for the modified pavement only where pipes were installed at 40mm and the flow rate was greater than 9 L/min.

Once again, the importance of optimising pavement materials can be evidenced where the use of PHC#A1, for an inlet of 10°C, could allow the pipes to be installed at 120mm and still keep the pavement surface temperature above freezing point. In addition, Figure 6-12 shows that a minimum flow rate of 6 L/min was required to keep the modified pavement surface temperature above 0°C where the pipes were installed at 120mm. It is interesting to notice the sudden rise in the pavement surface temperature when the flow rate increased from laminar flow at 9 L/min (Reynolds number ~1921) to turbulent flow at 12 L/min (Reynolds number ~2561).
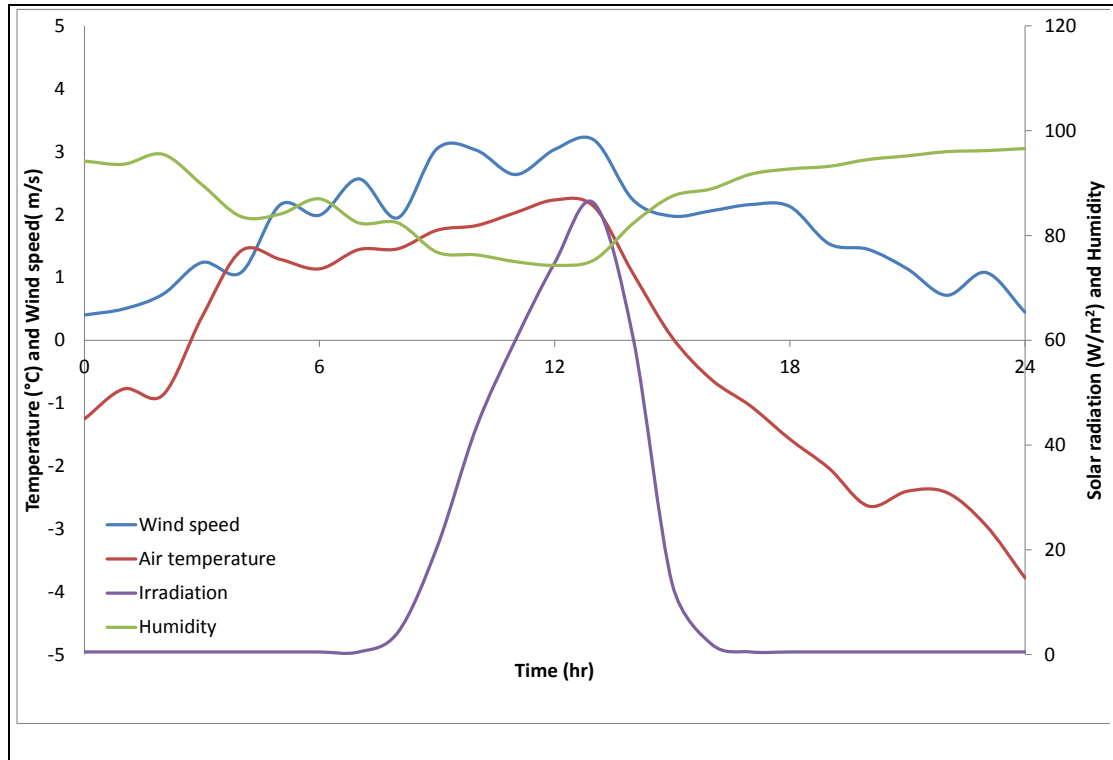
Figure 6-11 Winter climatic inputs to simulate the maintenance of winter road surface for ice prevention
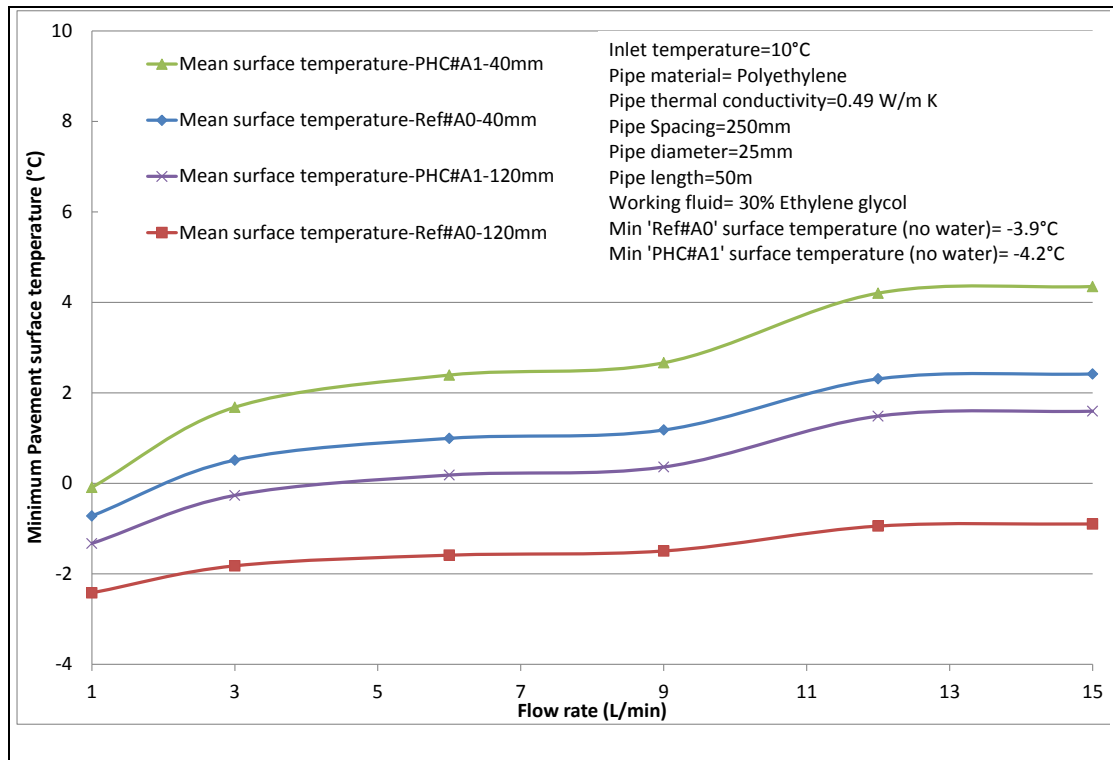
Figure 6-12 Mean winter surface temperature of 'Reference' and 'PHC#A1'as a function of flow rate in Sutton Bonington, inlet temperature 10°C
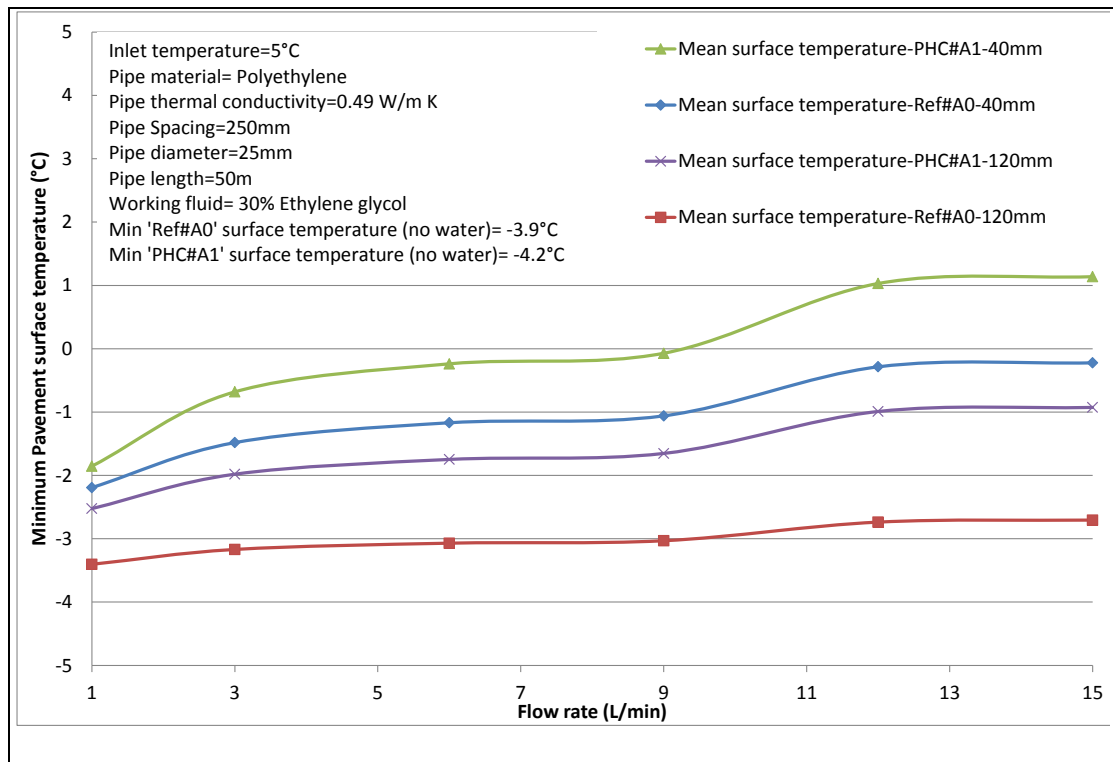
Figure 6-13 Mean winter surface temperature of 'Reference' and 'PHC#1'as a function of flow rate in Sutton Bonington, inlet temperature 5°C

6.3. Materials Design Optimisation for Pavement Source Heat Store (PSHS) Applications

This section aims to show how the thermo-physical optimisation of pavement materials affects the performance of Pavement Source Heat Store (PSHS) systems. Figure 6-14 shows the cross-section of an airport apron where the pavements consisted of varying concrete types with different thermo-physical properties, obtained from Table 3-5, Page 73. The performance of the PSHS was compared to that of the conventional system (i.e. ground source heat pump systems, GSHP#3, GSHP#4). As mentioned in Chapter 1, airport pavements are key potential application for the PSHS technology. Airport buildings typically have high cooling loads and energy demands and are immediately adjacent to large areas of pavement surface area. They are also of a similar arrangement throughout the world.

Concrete pavement Code	Layer A	Layer B	Layer C
PSHS Design#1 (Reference)	*Mix#1 Limestone_PQC	**Mix#14** Limestone_LMC	Compacted soil
PSHS Design#2	**Mix#3** Limestone_PQC	**Mix#16** Quartzite_LMC with higher effusivity than the Reference mix	Compacted soil
GSHP Design#3	**Dry soil	**Dry soil	Compacted soil
GSHP Design#4	***Wet soil	***Wet soil	Compacted soil

*=Refer to Table 3-5

**=Dry sand (used in the previous chapter). λ=0.28, c_p=692, ρ=1510

***= (ASHRAE 1995; Wu et al.2010). λ=1, c_p=1400, ρ=1510

Figure 6-14 Pavement's cross-section considered for the PSHS simulation

The parameters used in the numerical simulation were obtained from similar experimental works (ASHRAE 1995; Banks 2008; Wu et al. 2010b) and are shown on Figure 6-17 and Figure 6-18. A flow rate was selected in order to obtain a turbulent flow in the loops and enhance convention heat transfer (Banks 2008). The inlet fluid temperature was based on the recommendation given by ASHRAE (1995) and Banks (2008); that is 11°C and 17°C higher than the ground temperature for cooling, and between 6°C and 12°C lower than the ground for heating (the summer and winter ground temperature at the pipe locations when no water was circulating through the pipes was predicted to be 17°C and 7°C, respectively). The outlet temperature and the rate of heat extraction from the pavements were predicted over a period of 5 days at Sutton Bonington. Figure 6-15 and Figure 6-16 show the summer and winter climatic data that were used in the simulations.

The outlet temperature is the most representative parameter of the loop effectiveness and design (Banks 2008). In other words, the performance of the PSHS is a function of the fluid temperature produced by the loops. A greater temperature difference between the inlet and outlet fluid from the loop will result in a higher Coefficient of Performance (COP) of the system. Figure 6-17 and Figure 6-18 show the outlet fluid temperature from the PSHS designs in summer (i.e. cooling mode) and winter (i.e. heating mode), respectively.
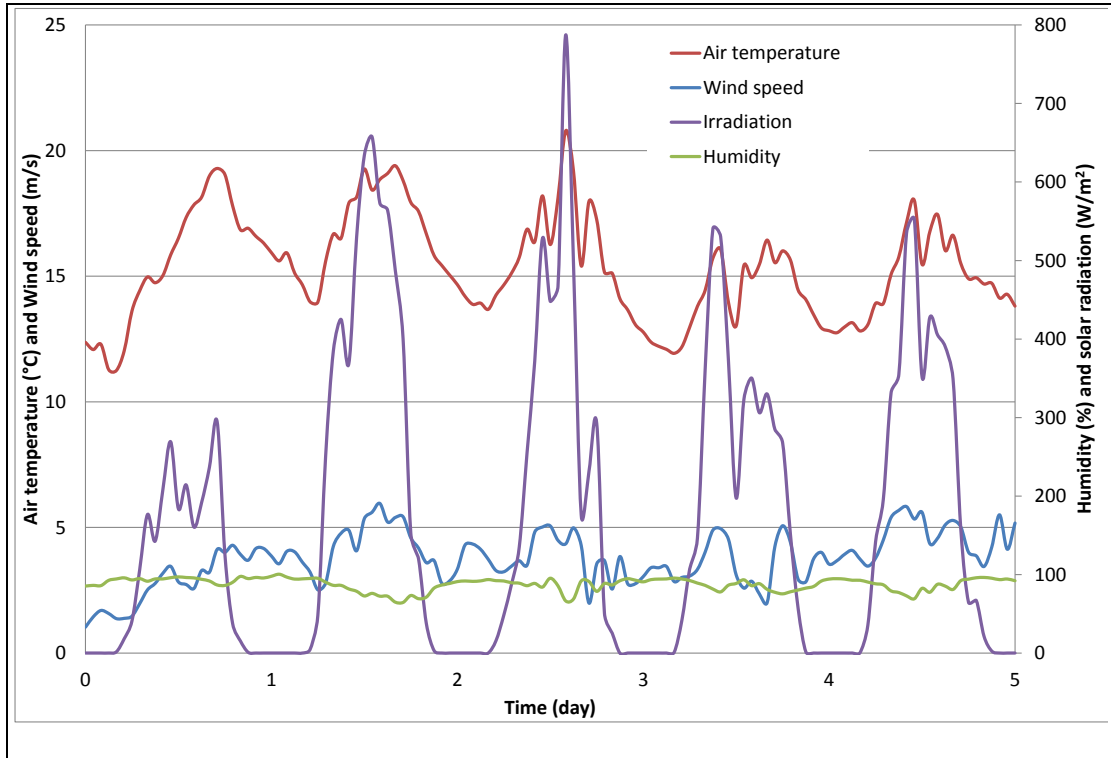
Figure 6-15 Summer climatic inputs for the PSHS simulation
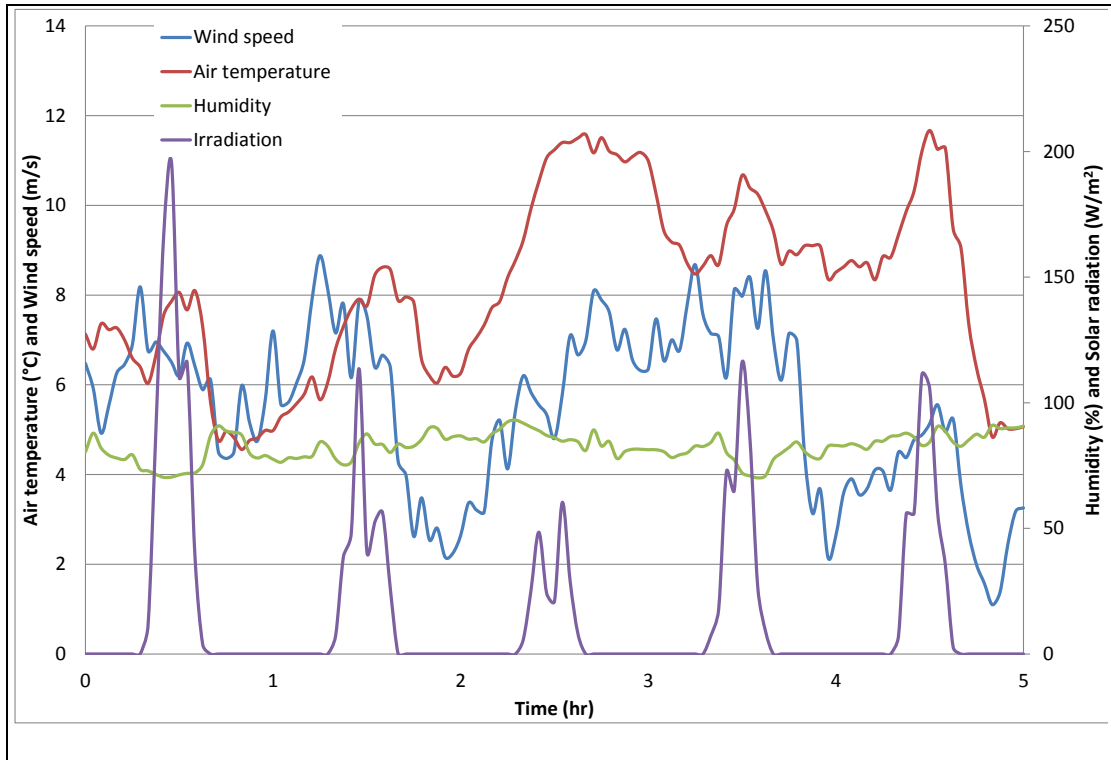
Figure 6-16 Winter climatic inputs for the PSHS simulation

Figure 6-17 and Figure 6-18 clearly show that the GSHP#3 installation, which is a conventional system installed in dry soil, had the poorest performance among the other designs as it provided the lowest temperature difference between the inlet and outlet fluid. The performance of the GSHP system was enhanced as the loops were buried in the wet soil (i.e. GSHP#4). Figure 6-17 and Figure 6-18 showed the burial of pipes in the concrete pavement (i.e. PSHS #1, PSHS #2) can enhance the performance of the system compared to that of the conventional ones (i.e. GSHPs). In addition, the performance of the PSHSs was enhanced as the thermal effusivity of the materials surrounding the pipes increased (PSHS#2). Materials with higher thermal effusivity allow rapid heat transfer from the pipes.
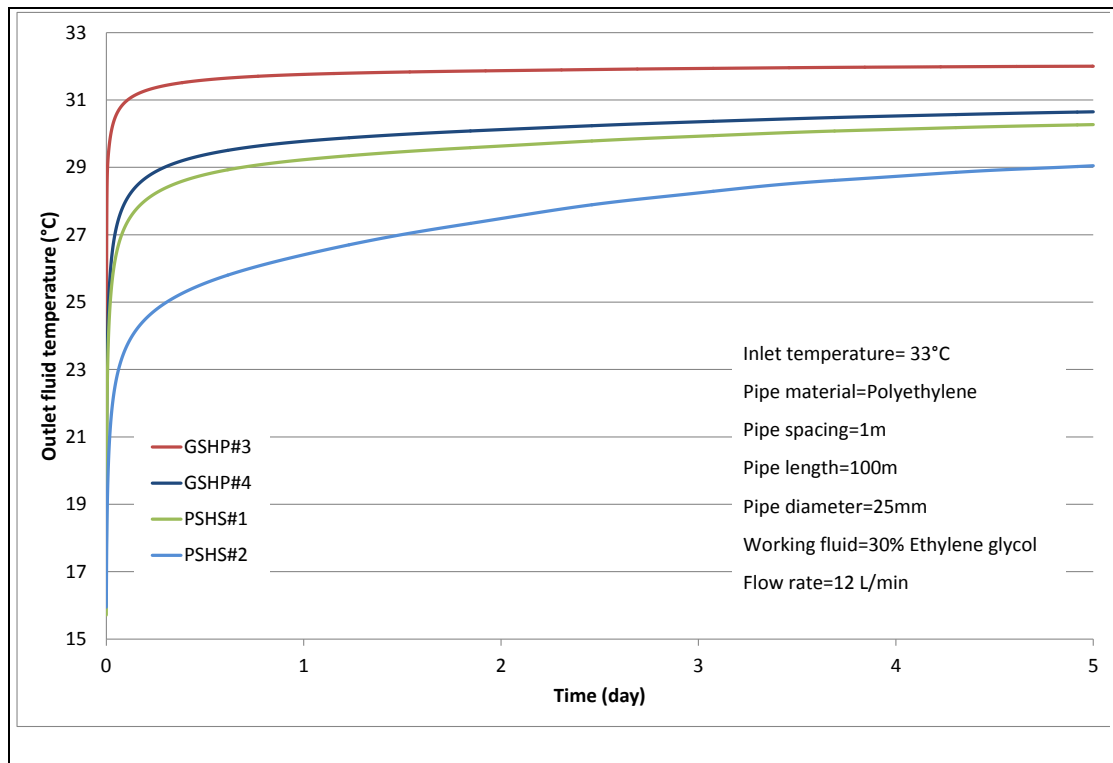
Figure 6-17 Outlet fluid temperature of PSHSs for summer (i.e. cooling mode) simulation
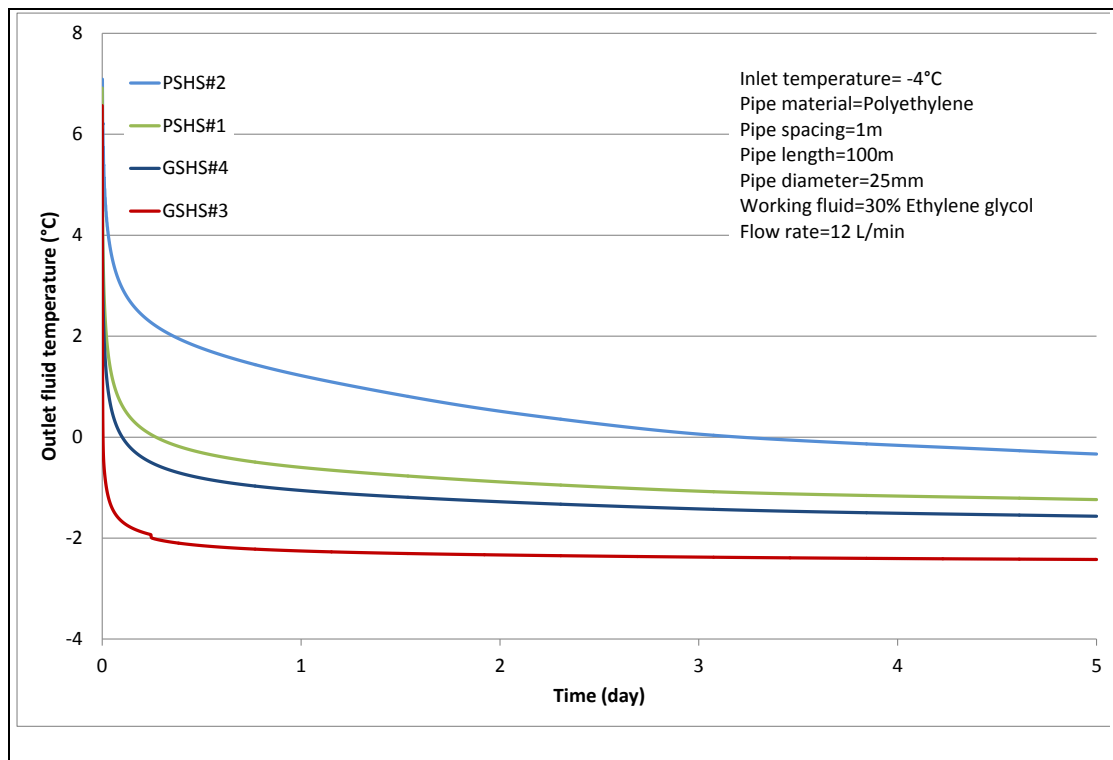
Figure 6-18 Outlet fluid temperature of PSHSs for winter (i.e. heating mode) simulation

Specific heat extraction/rejection is a parameter that is used to calculate the required length of trench in which the pipes are buried (see Section 2.5.3, Page 25). It can be seen from Figure 6-19 that the specific heat rejection for all the designs was initially at its highest at ~130 W/m due to the relative high and uniform temperatures in the ground. After running the system continuously for five days the specific heat rejection nearly reached steady-state and values decreased to approximately 30, 21, 18, 8 W/m for the PSHS#2, PSHS#1, GSHP#4, GSHP#3, respectively. In comparison the heat extraction/rejection rate from dry soil is about 8W/m (Inalli and Esen 2004; Banks 2008) and from normal soil between 15 to 30 W/m (see Figure 2-12 and Figure 2-13, Page 28). Figure 6-19 shows that the reduction of heat rejection rate occurs sharply in the systems having a lower thermal effusivity value (i.e. GSHP#3, GSHP#4). This can be attributed to the fact that such systems cannot effectively dissipate the fluid heat away from the pipes and hence the temperature around the pipes will rapidly increase and minimise the effective heat transfer from the pipe to the surrounding materials.
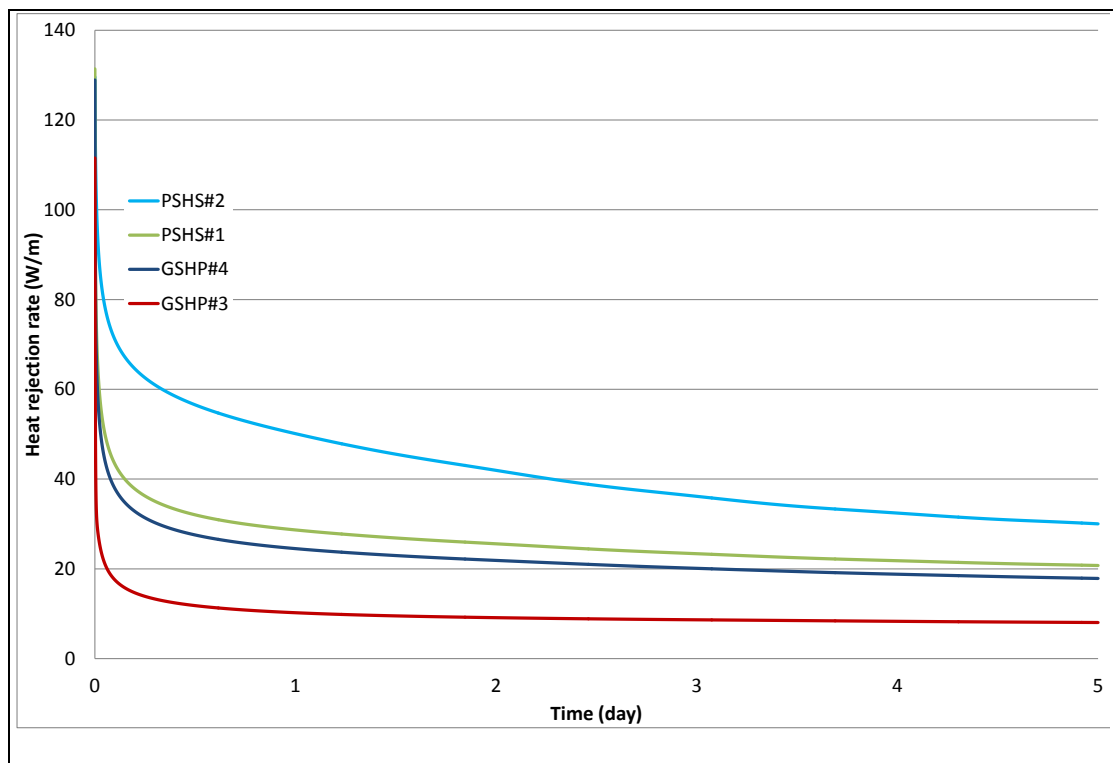
Figure 6-19 Heat rejection rate to the PSHS in summer

The initial heat extraction rate was about 75 W/m and decreased to approximately 21, 13, 11, 4 W/m for the PSHS#2, PSHS#1, GSHP#4, GSHP#3, respectively, as shown by Figure 6-20.
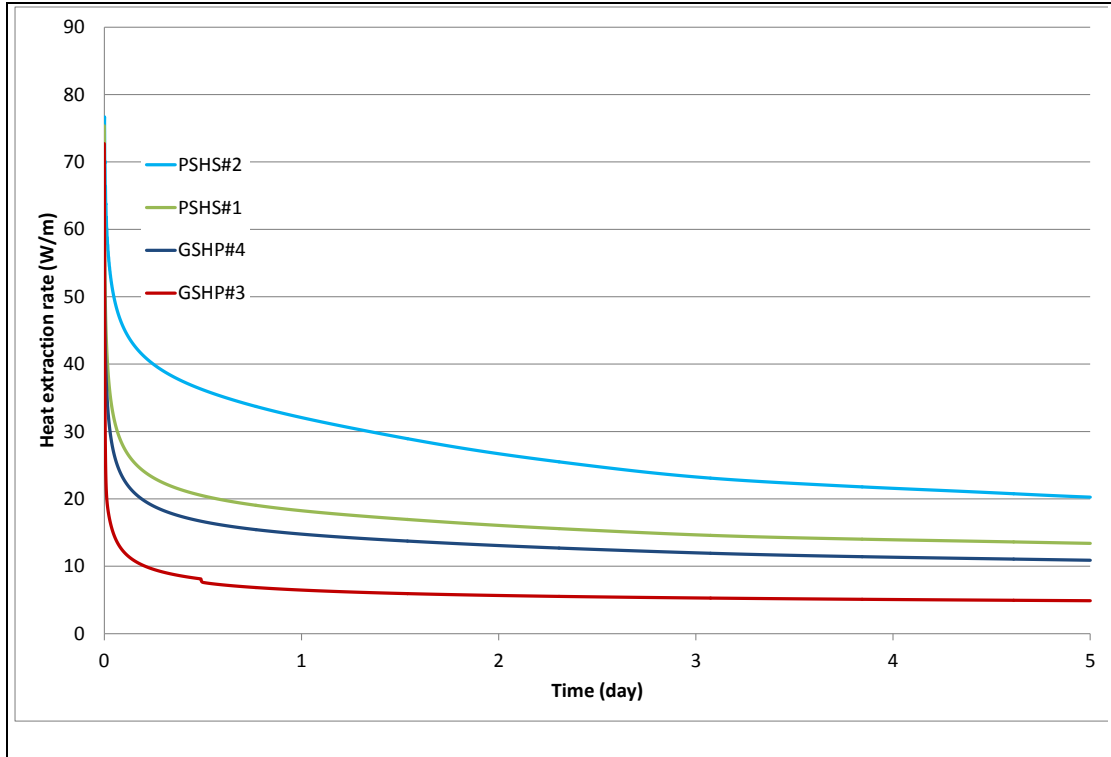
Figure 6-20 Heat extraction rate from the PSHS in winter

Figure 6-19 and Figure 6-20 clearly show that a modified PSHS (i.e. PSHS#2) can increase the heat extraction/rejection rate by ~425% and ~90% compared to GSHP#3 (i.e. pipes installed in dry soil) and GSHP#4 (i.e. pipes installed in wet soil). As mentioned in Section 2.5.3, Page 25, specific heat extraction rate is the parameter that controls the required length of pipe and area needed for the installation of the loops. Therefore, for the same heat pump capacity, doubling the heat extraction rate simply means halving the pipe length and the area requirements for the loop installation.

Figure 6-21 shows the relationship between the heat extraction rates from different pavements and their thermal conductivity. Using data from Table 3-5, the PSHS cross section was evaluated for a range of potential materials and the heat extraction was computed at the end of the 5-day simulations. Figure 6-21 suggests that there is a strong

logarithmic relationship, with an $R^2 = 0.99$, between the thermal conductivity of pavements surrounding the pipes and the heat extracted from the pavement. From Figure 6-21it can also be seen that, for two pavements having similar thermal conductivity (i.e. Ferag and PQC_Limestone), the one with higher thermal effusivity (i.e. Ferag, with higher VHC) resulted in a slightly higher heat extraction.
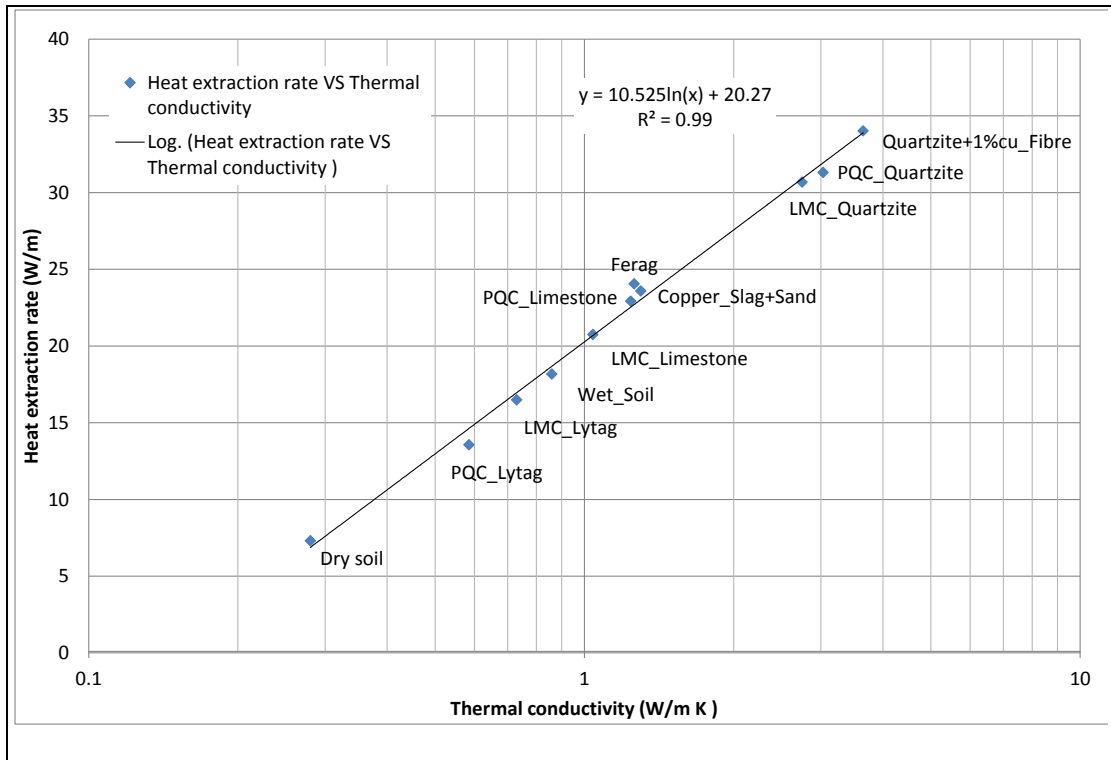
Figure 6-21 Heat extraction rate from the concrete pavements as a function of thermal conductivity

Another important point that must be considered in the PSHS designs is the pipe spacing which dictates the required ground surface area (for a given heat pump capacity). Figure 6-22 suggests that, for parameters used in the model, there a strong positive hyperbolic relationship, with a $R^2 = 0.98$, between the pipe spacing and the heat extraction rate from the pavement.
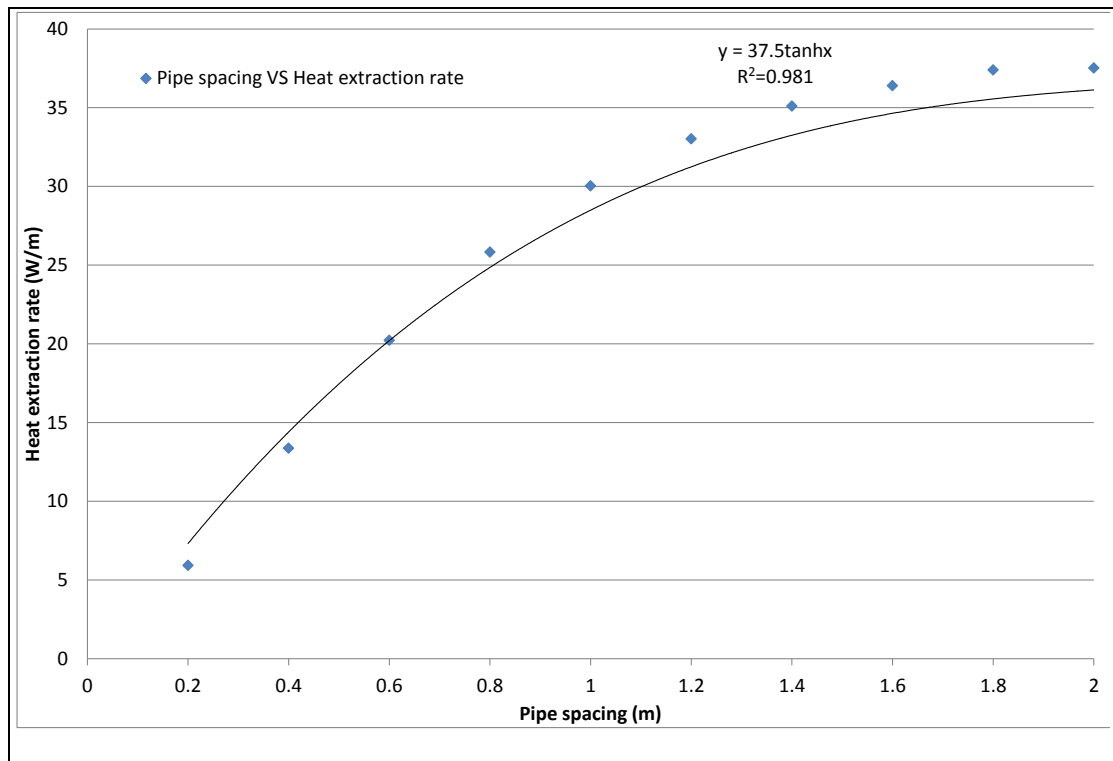
**Figure 6-22 Rate of heat extraction from the modified concrete pavement (i.e.PSHS#2) as a
function of pipe spacing**

6.4.   Materials Design Optimisation for a Hybrid System

Although it is obvious that a combination of a modified collector system (i.e. PHC) and a
modified storage system (i.e. PSHS) will enhance the performance of the hybrid systems,
this section, for completeness, show how the thermo-physical optimisation of pavement
materials affects the performance of the hybrid systems. The effect of thermo-physical
optimisation of pavement materials on the heat collection and storage ability of the hybrid
system was simulated for an inlet fluid temperature lower than pavement temperature at
collector pipes and higher than pavement temperature at storage pipes so that both heat
collection and storage can occur in the pavement.

Figure 6-23 gives details of pavements comprising of different thermo-physical properties,
where the simulations were performed for cases where the collector pipes were installed at
depths of 40mm and 120mm. The maximum difference between the outlet fluid temperature
for collection and storage was predicted as a measure of performance and the results are

185

given in Table 6-1. In order to simulate the best case scenario, a value of 0.9 was assumed

for the concrete's solar absorptivity. Climatic data and parameters used in the model were

the same as those already shown in Figure 6-7 and Figure 6-9, respectively. As might be

anticipated, the highest temperature difference was achieved by the Hybrid#2, which

consists of a modified PHC and a concrete PSHS. Higher temperature differences suggest

that more heat was recovered from the collector pipes and was placed in the storage bank.

Hybrid#3 showed the lowest value because; the storage pipes were surrounded by a low

thermal effusivity material which consequently reduces the effectiveness of heat transfer. As

a result of greater heat recovery from the collector pipes, the pipes installed at a depth of

40mm showed higher temperature differences compared to those installed at 120mm. The

importance of a pavement material optimisation is also evidenced from Table 6-1 where

Hybrid#2 could allow pipes to be installed at 120mm and yet provide a higher temperature

difference (i.e. higher heat recovery) than Hybrid#1, where pipes were installed at 40mm. In

general, the modified hybrid system (i.e. Hybrid#2) for 120 and 40mm pipe installations

were 500% and 310% more efficient, respectively, in heat recovery than the conventional

hybrid system (Hybrid#3) (see Table 6-1).
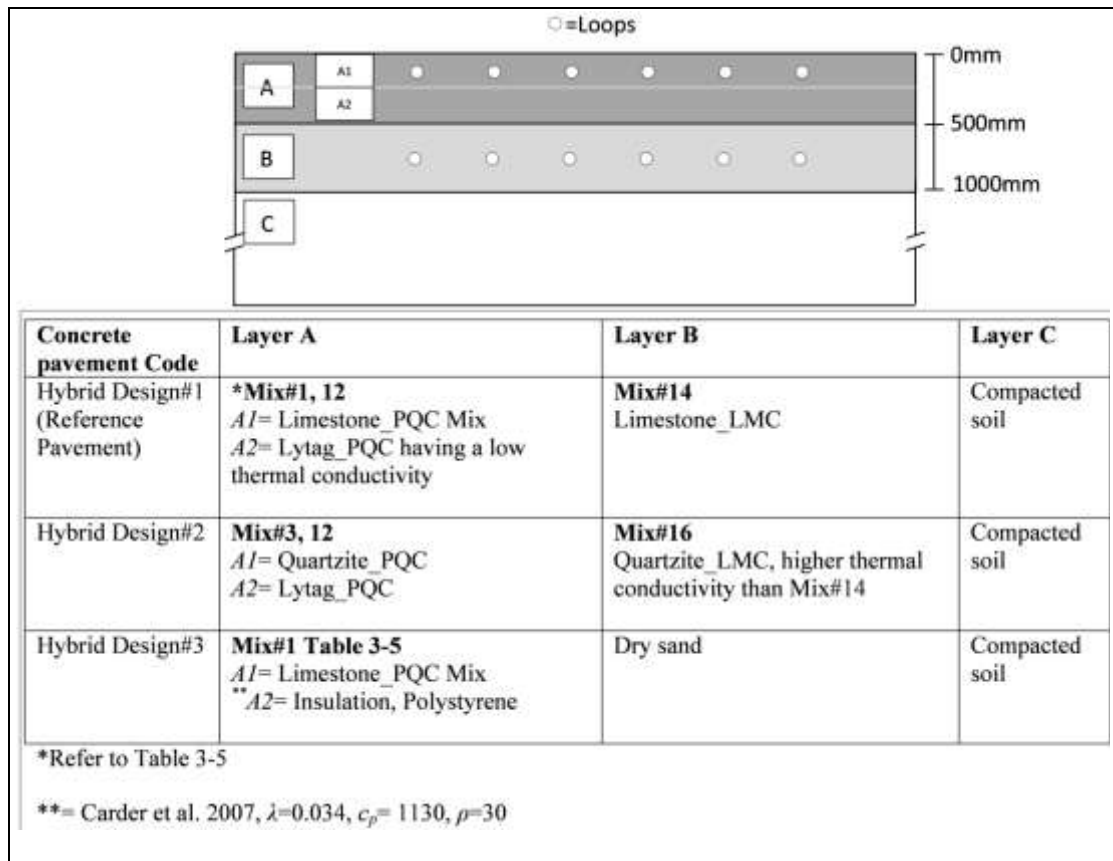
Figure 6-23 Pavement's cross-section considered for the Hybrid simulation

Table 6-1 Outlet fluid temperature difference in the Hybrid systems

Hybrid designs	Hybrid#1-120	Hybrid#2-120	Hybrid#3-120	Hybrid#1-40	Hybrid#2-40	Hybrid#3-40
Temperature difference (°C)	2.7	5.3	0.9	4.6	7.4	1.8

6.5.   Other Implications for Pavement Design

In this section, the relative influence of different pavement thermo-physical properties on the thermal response of pavement cross-sections is presented. A better understanding of how material selection can affect the pavement temperature profile evolution could allow intelligent design and material specification leading to improved performance and longevity of pavements.

Figure 6-24, shows the surface temperature for the asphalt reference pavement and PHC#A1 (see Figure 6-1, Page 164) in Arizona (climatic data are shown in Figure 6-24). Figure 6-24 clearly shows that the maximum surface temperature can be reduced when quartzite aggregates are used in the wearing course of the pavement. The maximum surface reduction is approximately 4ºC with an average reduction of more than 2ºC at the peak temperature. The reduction in surface temperature is because of the higher thermal conductivity of the quartzite mix increasing the rate of heat transfer to the bottom layers of the pavement. Reductions of pavement surface temperature could, potentially, minimise the rutting in asphalt pavements and extend their life. The UHI effect could also be minimised as a result of pavement surface temperature reduction and, consequently, air temperature reduction in the adjacent urban area.

	Air Temperature (°C)	Wind (m/s)	Humidity	Solar (W/m^2)
Max	40.8	11.6	75	1066
Min	21.8	0.5	8	0
Mean	30.5	3.1	30	510
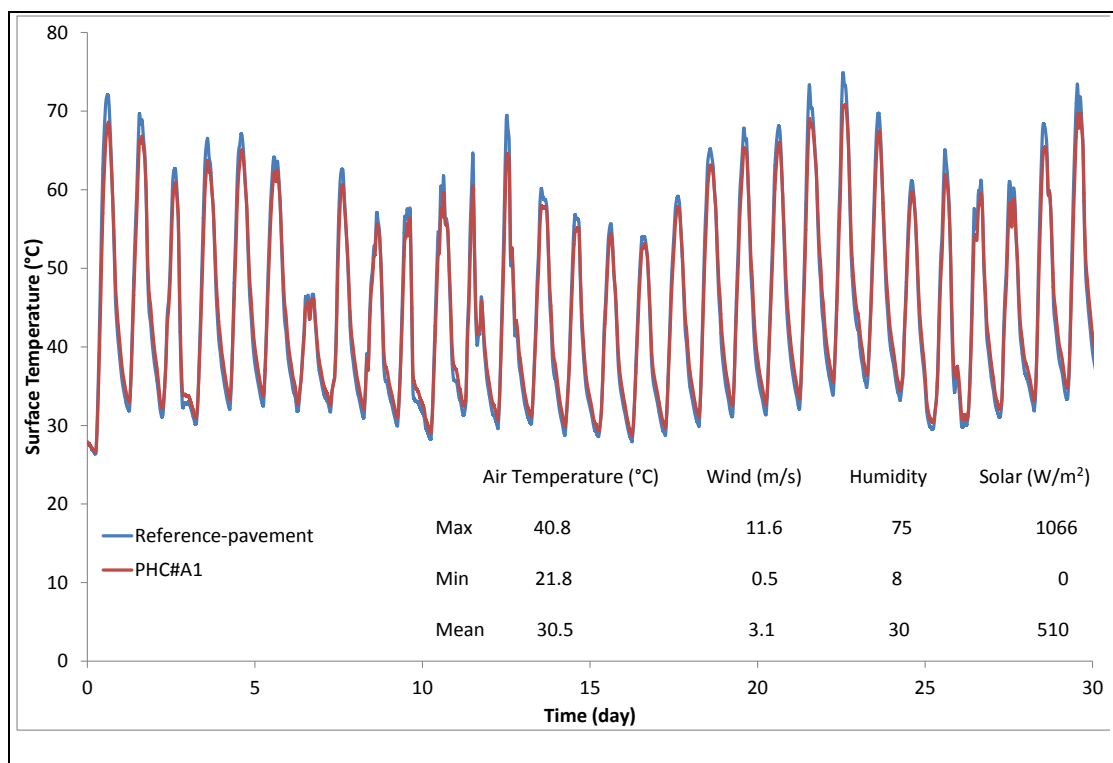
Figure 6-24 Predicted surface temperatures for the reference (i.e. limestone) and PHC#A1 (i.e. Quartzite)

Figure 6-25 compares the temperature distribution within the concrete reference pavement, with PHC#C1 and PHC#C3 (see Figure 6-1, Page 164) at 4am and 4pm in July in Arizona. It can be seen that as the concrete thermal conductivity increases, the temperature gradient range across the slab (120mm thickness) will decrease considerably. The temperature

gradient reduction in a concrete slab can reduce the warping stresses that occur due to temperature differences between the top and bottom of the slab (Griffiths and Thom 2007). Therefore, the service life of the pavement can be prolonged due to the reduction of these thermal stresses in this case. The temperature differences across the concrete slab are about 8°C, 3°C, and 1°C for the reference, PHC#C1, and PHC#C3 pavements, respectively. In addition, the total temperature variations between 4 am and 4 pm reduce as thermal conductivity increases, which could minimise the likelihood of thermal cracking due to the expansion and contraction of concrete pavements.
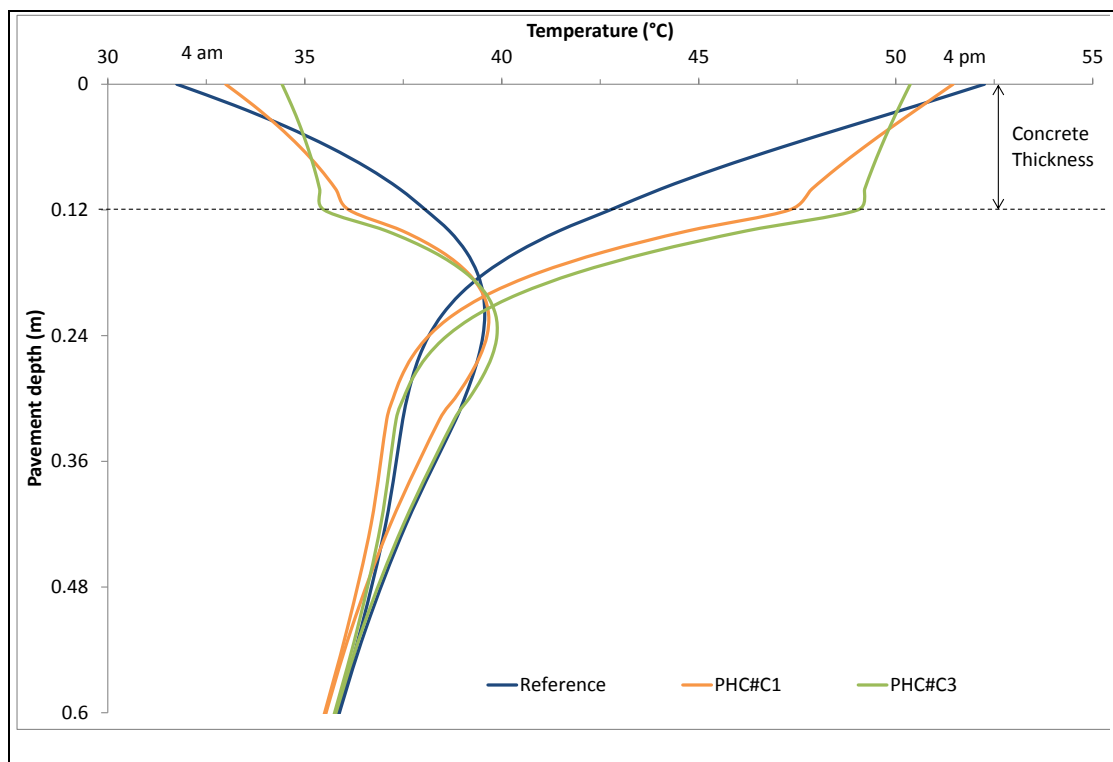
Figure 6-25 Comparison of the average temperature distribution across 120 mm concrete slabs at 4am and 4pm in July in Arizona

6.6. Benefits of PCM in Pavements

The large drops in strength, and potential questions regarding durability, would effectively preclude the use of microencapsulated PCM, at this stage, as an additive to traffic-bearing concrete pavements. Furthermore, PCM-modified concretes not only did not improve the performance of the PSHS but in fact can diminish its performance. Figure 6-26 compares the performance of the reference pavement (i.e. PSHS#1) with the 40% PCM-modified concrete

(see Table 3-7). In the model of the pavement with PCM-modified concrete, the peak

specific heat capacity was considered to simulate the best-case scenario. Figure 6-26 shows

that the burial of pipes in the PCM-modified concrete resulted in a 16% reduction in the heat

extracted from the pavement. This can be attributed to the fact that a marginal increase of the

VHC of the PCM-modified concrete, intended to enhance heat extraction from the

pavement, was offset by the reduction in thermal conductivity (see Table 3-7).
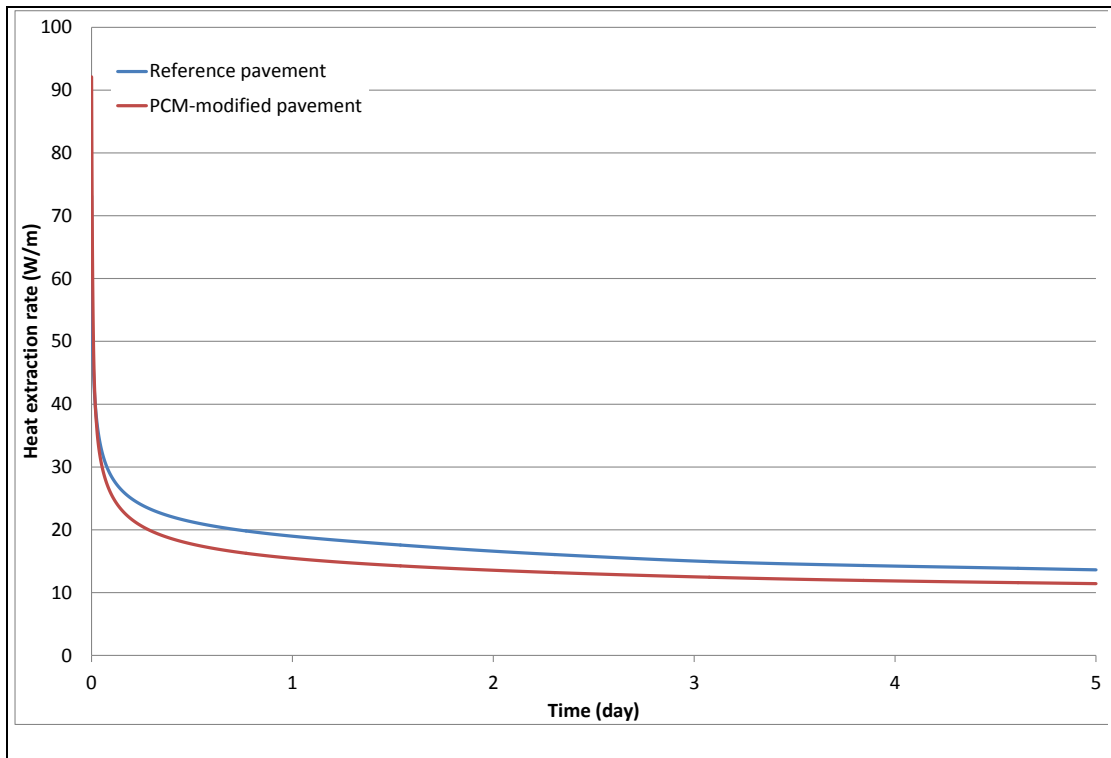
Figure 6-26 Heat extraction rate from the reference and PCM-modified concrete

Nevertheless, in Section 5.4.3, Page 137, it was observed that PCM-modified concretes can

reduce the pavement surface temperature in some cases. Further numerical simulation was

performed in order to evaluate the behaviour of PCM-modified concrete under genuine

weather conditions. The modelling was conducted for a typical pavement cross-section

where comparative surface temperature predictions were made for pavements using a

surface layer comprising the reference mix (see Figure 6-1) and a 40% PCM-modified

concrete (see Table 3-6 and Table 3-7). The climatic data was for Sutton Bonington between

1/06/2008 and 1/07/2008 when day time conventional pavement surface temperatures can be

expected to rise above T_{melt} (i.e. ~26 ºC) but fall beneath this value at night. From

Figure 6-27, it can be clearly observed that the maximum concrete surface temperature can be reduced by approximately 3.5ºC, under these climatic conditions, as a result of higher VHC of the PCM-modified concrete. Reduction of summer surface temperatures could theoretically reduce shrinkage and thermal stresses (e.g. curling, warping, etc.) in concrete pavements thus extending their service lives. However, PCM-modified concrete could be applied to other applications such as concrete roofs or other precast concrete panels. In addition, it would also be interesting to apply PCMs to asphalt mixes where the reduction in surface temperature is beneficial in hindering rutting. It may be noted that although, in this study, PCMs with a melting temperature of ~26°C were used, various commercial PCMs are readily available, offering a wide range of melting temperatures (Mehling and Cabeza 2008), which can be used for other climates.
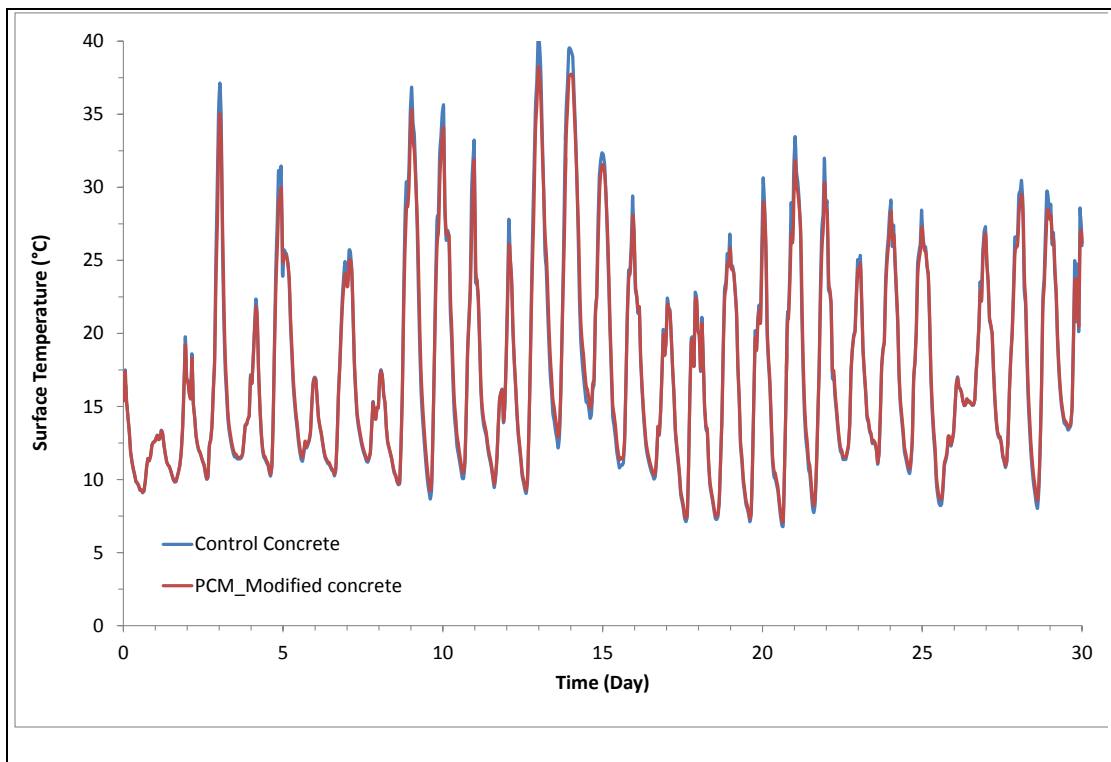
Figure 6-27 Predicted surface temperature for a concrete pavement comprising the control mix and PCM-modified concrete

6.7. Summary

- This chapter has addressed the last objective of the study which was to investigate the influence of the thermo-physical properties of pavement materials and pavement layer sequences on the performance of PES and other implications for pavement design. Simulations were carried out, for genuine temperature patterns, on the conventional pavements and those with modified thermo-physical properties using the previously validated model.

- The presence of a high thermal conductivity pavement layer above pipes, combined with a high thermal resistance pavement layer below the pipes, can significantly increase the temperature at pipe locations and the outlet water temperature from those pipes.

- Modification of pavement materials can allow the pipes to be installed deeper within the pavement without having any negative effect on their thermal performance. Pipe installation deeper within the pavement may avoid 'reflective cracking' under traffic loading as well as enabling future resurfacing of the pavement without damaging the pipe network.

- The circulation of the working fluid in the pipes in a PHC can reduce the pavement surface temperature in hot climates with implications for the reduction of rutting and the UHI effect. In addition, the pavement surface temperature in winter can be kept above freezing temperatures and icy road conditions can be minimised.

- Comparison between a conventional Ground Source Heat Pump (GSHP) and a Pavement Source Heat Store (PSHS) revealed that the PSHSs have a higher efficiency in terms of the heat extraction/rejection rates to and from the pavement. The modified PSHSs compared to the modified GSHPs, showed ~90% increase in the heat extraction rate. In addition, there was a strong positive logarithmic relationship between the pavement's thermal conductivity and the heat extraction rate from the pavement. Moreover, there was a strong positive hyperbolic

relationship between the pipe spacing and the heat extraction rate from the pavement.

- In the hybrid systems, the maximum temperature difference between the outlet fluids from the collector and storage was predicted as a measure of the system efficiency. The results showed that the performance of the enhanced hybrid system was superior to that of the conventional hybrid system (i.e. storage pipes buried in sand). The thermally modified hybrid system for 120 and 40mm pipe installations was ~500% and ~310% more efficient in heat recovery, respectively, than the conventional systems.

- From the pavement design point of interest, concrete pavements with higher thermal conductivity can reduce the warping stresses by the reduction of temperature gradients between the top and bottom of the concrete pavement. In addition, asphalt pavements with higher thermal conductivity can reduce the pavement surface temperature and could, potentially, minimise rutting and the UHI effect in asphalt pavements.

- The result of the numerical simulation showed that, by adding ~5wt.% microencapsulated PCM in concrete; the concrete surface temperature can be reduced by approximately 3.5ºC.

7 CONCLUSIONS AND RECOMMENDATIONS FOR FUTURE RESEARCH WORK

7.1. Introduction

Renewable energy technologies are likely to become more important as other energy sources become depleted and the cost of power generation using fossil fuels rises. However, in most cases, renewable energy technologies require high initial investments that may deter potential users. Pavement Energy Systems (PESs) potentially offer a low-cost solution to sustainable and clean energy generation by utilising the thermo-physical properties and design features of pavement infrastructure.

In the PES, pavement structures are equipped with loops, which consist of fluid-filled pipes buried in the pavement, in order to serve as a solar energy collector and/or storage media. The fluid in the pipes can absorb/reject heat to the pavement and deliver useful energy to nearby buildings as well as benefiting the pavement structure and pavement users. A significant advantage of such systems is that the pipes are installed within pavements that are already needed for structural reasons and need not to be specially constructed as do conventional thermal energy utilisation systems.

The use of pavements to collect and/or store solar energy is a relatively new subject that is still at an early age of development. Very little work has been reported (experimental or theoretical), on the PES or determination of factors affecting their performances, especially those related to the design of civil engineering materials. This research is, in general, intended to investigate the feasibility of using pavement materials and structures as solar energy collectors and/or thermal storage media.

7.2. Main Conclusions

The conclusions deal with the general aim and the specific objectives of this research as stated in Chapter 1. The main body of work and conclusions are summarised as follows:

<u>Potential of asphalt and concrete pavement materials for combined thermo-physical and mechanical use.</u>

Within the limitation of materials and mix design used in this study, it can be concluded that, it is possible to achieve a wide range of thermally modified pavements with an acceptable mechanical performance that, at least, meet the rigorous functional requirements of an airfield pavement. The results of this study showed that it was feasible to achieve mechanically acceptable concrete and asphalt pavement mixes having thermal conductivity in the range ~0.5 to ~4 W/m K and ~1.2 to ~2.4 W/m K, respectively.

<u>Numerical model development</u>

A transient explicit finite-difference model was developed to predict the temperature distribution as a function of time and depth within the pavement structure. The model was later advanced to a pseudo 3D for performance analysis of the PES under various operating conditions and configurations. The software developed is capable of predicting the outlet fluid temperatures and pavement temperature depth profiles. It can therefore be used as a tool for calculating the optimum dimensions of loops and pipe burial depths, as well as assessing the relative effects of thermo-physical properties on the PES performance for a given location if meteorological data are available.

Large-scale physical models of the PES

Large-scale physical models were designed and constructed to compare the performance of the thermally-modified pavement structures with those of conventional ones, and also to validate the model predictions. The physical model consisted of pavements in which copper pipes were embedded. These were irradiated (causing surface heating) using halogen lamps. The experimental comparison between the thermally-modified and unmodified concrete pavements revealed that there was potential to significantly enhance both the heat collection and storage capability of concrete pavement structures. In addition the model predicted temperature depth profiles and outlet water temperatures were in good agreement with the experimental ones with a mean error of less than 1°C. A similar comparison on asphalt pavements showed that, although the surface temperature was altered by asphalt modification, there were significant discrepancies between the measured and predicted surface temperatures for both modified and unmodified pavements. Further study was conducted on the pipe/pavement Interfacial Zone (IZ) using X-Ray Computed Tomography (XRCT). The X-ray images revealed improper bonding between the pavement's matrix and the pipe, which was evidenced by the presence of air void accumulation around the pipe perimeter in the case of asphalt. This was not observed for the concrete samples and so could explain the significant discrepancy in the modelled temperatures, although more research is needed to quantify the effect as a model input parameter.

Simulation of the relative influence of thermo-physical material properties and pavement structure

The validated model was used, under different climates, to simulate the performance of the PES and to determine the implications for pavement design. It was concluded

that, for the heat collector systems, pavement material enhancements could allow pipes to be installed deeper within the pavement without having any negative effect on their thermal performances when compared to conventional materials. Greater pipe installation depth is expected to reduce 'reflective cracking' under traffic loading as well as enabling future resurfacing of the pavement without potential damage to the pipe network. In addition, comparison between different Pavement Source Heat Store (PSHS) systems revealed that their performance, in terms of heat extraction/rejection from and to the pavements, significantly depends on the pavement materials surrounding the loops. The loops installed in the conventional Ground Source Heat Pump (GSHP) system (i.e. soils) had the poorest performance compared to the systems where the loops where installed in concrete. In addition, the performance of the PSHS systems was enhanced as the thermal effusivity of the concrete pavements surrounding the loops increased. Also, there was a strong positive logarithmic relationship between the pavement's thermal conductivity and the heat extraction rate. Furthermore, it was concluded that concrete pavements with higher thermal conductivity have a smaller top-bottom temperature difference that could potentially reduce the warping and thermal stresses of concrete pavements. In addition, asphalt pavements with higher thermal conductivity can reduce the pavement surface temperature. This could potentially minimise rutting in asphalt pavements and also the Urban Heat Island (UHI) effect.

7.3. Recommendations for Future Research

According to the literature review and the findings obtained from this research, suggestions for further work might encompass the following items:

- ✓ Although there are many theoretical and numerical models to simulate the effective thermal conductivity of composite (e.g. pavement) mixtures, most researchers concluded that no single model can provide accurate prediction for all materials considered in their reviews. In addition, comprehensive experimental thermal

conductivity data for concrete is generally scarce. Therefore, the thermo-physical results provided in Chapter 3 of this study might be used for further study to predict the influence of various variables (e.g. aggregate types, porosity, and moisture content) on the effective thermal conductivity of the concrete mixtures.

✓ Both numerical and experimental results of this study revealed that, the modification of concrete pavements using PCM can reduce their surface temperature. However, the large reductions in strength would effectively preclude the use of microencapsulated PCM at this stage. Future studies can focus on the utilisation of microencapsulated PCM particles with stronger outer shells. The use of PCM capsules with stronger shells might also allow higher amounts of PCM to be mixed into concrete. Future work could also study the potential of using PCM in asphalt mixtures.

✓ Further research is needed to improve the prediction accuracy of the model proposed in this study. The effect of convection heat transfer as a result of moisture transport and storage in the pore networks of pavements should be investigated. In addition, field validation of the PES model, using data collected under a wider range of weather conditions, would be useful.

✓ The PESs are likely to operate more cost-effectively than conventional systems (e.g. GSHP systems) as the cost of the pavement construction would probably be already funded from a separate infrastructure budget. However, marginal additional costs are likely to be incurred in order to provide the necessary thermal enhancements. Future work is needed to compare the whole cost of operation of a PES with that of conventional systems.

✓ Pavement Heat Collector (PHC) loops are installed relatively close to the pavement surface to absorb solar energy and to benefit pavement structures in terms of reduction in pavement surface temperature in summer and increase in winter. However, there might be a compromise between the benefit delivered by loops for the pavements and the likely detrimental effect of the loops on the long term

performance of the pavement under the traffic loading. The conflict between these two aims might be studied in the future.

✓ There was strong evidence to suggest that pipe/pavement interfaces can significantly influence the performance of the PES, as discussed in Section 5.6. This was good enough for early investigations but additional experiments should be performed to quantitatively assess the effect of air voids around the loops on the PES performance.

✓ Further study could be carried out to improve the efficiency of heat transfer between pipe and pavement. The effect of finned pipe on the performance of the PES can be studied in the future.

✓ The presence of pipe in pavements, especially asphalt pavements, influences the durability of the structure negatively. This research showed that modification of pavement material and structure can allow the pipe to be installed deeper in the pavement. However, the effect of traffic loading on the pipe survivability, especially in heavy-duty applications like airfield platforms, can be studied in the future.

✓ This research showed that the temperature gradient across the concrete pavement was significantly influenced by its thermo-physical properties. Future study can investigate the effect of reduction in the top-bottom temperature differences on the likely reduction of maximum tensile stresses within the pavement and also on the likely reduction of concrete pavement thickness. This can be done, for example, by using Finite Element stress analysis packages such as EVERFE 3D.

REFERENCES

Al-Jabri, K. S., R. A. Taha, A. Al-Hashmi and A. S. Al-Harthy (2006). "Effect of copper slag and cement by-pass dust addition on mechanical properties of concrete." Construction and Building Materials **20**(5): 322-331.

Armstrong, F. and K. Blundell (2007). Energy... Beyond Oil. Oxford, Oxford University Press.

Asaeda, T., V. T. Ca and A. Wake (1996). "Heat storage of pavement and its effect on the lower atmosphere." Atmospheric Environment **30**(3): 413-427.

ASHRAE (1995). Commercial/institutional ground source heat pump engineering manual. Atlanta, American Society of Heating, Refrigerating and Air-Conditioning Engineers, Inc.

Athienitis, A. K., C. Liu, D. Hawes, D. Banu and D. Feldman (1997). "Investigation of the thermal performance of a passive solar test-room with wall latent heat storage." Building and Environment **32**(5): 405-410.

Atkinson, B. S., D. L. Sparkes and S. J. Mooney (2007). "Using selected soil physical properties of seedbeds to predict crop establishment." Soil and Tillage Research **97**(2): 218-228.

Banks, D. (2008). An Introduction to Thermogeology: Ground Source Heating and Cooling. Oxford, Blackwell Publishing Ltd.

Benazzouk, A., O. Douzane, K. Mezreb, B. Laidoudi and M. Quéneudec (2008). "Thermal conductivity of cement composites containing rubber waste particles: Experimental study and modelling." Construction and Building Materials **22**(4): 573-579.

Bentz, D. P. (2000). A Computer Model to Predict the Surface Temperature and Time-of-Wetness of Concrete Pavements and Bridge Decks. NISTIR 6551, U.S. Department of Commerce.

Bentz, D. P. and R. Turpin (2007). "Potential applications of phase change materials in concrete technology." Cement and Concrete Composites **29**(7): 527-532.

Beshr, H., A. A. Almusallam and M. Maslehuddin (2003). "Effect of coarse aggregate quality on the mechanical properties of high strength concrete." Construction and Building Materials **17**(2): 97-103.

Bilgen, E. and M. A. Richard (2002). "Horizontal concrete slabs as passive solar collectors." Solar Energy **72**(5): 405-413.

Bopshetty, S. V., J. K. Nayak and S. P. Sukhatme (1992). "Performance Analysis of a Solar Concrete Collector." Energy Conversion and Management **33**(11): 1007-1016.

Brandl, H. (2005). "Energy Foundations and other thermo-active ground structures." Geotechnique **56**(2): 81 -122.

British Geological Survey (2006). Mineral Planning Factsheet: Limestone, Available online: http://www.bgs.ac.uk/downloads/start.cfm?id=1361.

British Standards Institution (1993). Method for Determination of the Indirect Tensile Stiffness Modulus of Bituminous Mixtures, Draft for Development DD 213.

British Standards Institution (1996). Method for Determining Resistance to Permanent Deformation of Bituminous Mixtures Subject to Unconfined Dynamic Loading. Draft for development DD 226.

British Standards Institution (2003). Method for Determination of Fatigue Characteristics of Bituminous Mixtures Using Indirect Tensile Fatigue. Draft for development, DD ABF.

BS EN (2000). British Standard Institute, Tests for mechanical and physical properties of aggregates-Determination of particle density and water absorbsion, BS EN 1097-6:2000.

BS EN (2008). British Standard Institute, Aggregates for Concrete, BS EN 12620:2002+A1.

BS EN (2009a). British Standards Institution, Testing hardened concrete, Part 3: Compressive strength of test specimens, BS EN 12390-3:2009.

BS EN (2009b). British Standards Institution, Testing hardened concrete, Part 5: Flexural strength of test specimens, BS EN 12390-5:2009.

BS EN ISO (2009). Differential scaning calorimetry (DSC), Part1:General principles, 11357-1:2009.

BS ISO (2005). "Differential scaning calorimetry (DSC), Part4: Determination of specific heat capacity, 11357-4:2005.".

Budikova, D., M. Hall-Beyer and G. Hassan (2010). "Albedo", in Encyclopedia of Earth. Washington, D. C., Environmental Information Coalition, National Council for Science and the Environment.

Busby, J., M. Lewis, H. Reeves and R. Lawley (2009). "Initial geological consideration before installing ground source heat pump systems." Journal of Engineering Geology and Hydrogeology **42**: 295-306.

Cabeza, L. F., C. Castellón, M. Nogués, M. Medrano, R. Leppers and O. Zubillaga (2007). "Use of microencapsulated PCM in concrete walls for energy savings." Energy and Buildings **39**(2): 113-119.

Canakci, H., R. Demirboga, M. Burhan Каракоз and O. Sirin (2007). "Thermal conductivity of limestone from Gaziantep (Turkey)." Building and Environment **42**(4): 1777-1782.

Carder, D. R., K. J. Barker, M. G. Hewitt, D. Ritter and A. Kiff (2007). "Performance of an interseasonal heat transfer facility for collection, storage, and re-use of solar heat from the road surface." Transport Research Laboratory, Poblished Project Report PPR 302.

Cengel, Y. (2002). Heat Transfer: A Practical Approach. New York, McGraw-Hill Comapnies, Inc.

Chaurasia, P. B. L. (2000). "Solar water heaters based on concrete collectors." Energy **25**(8): 703-716.

Cheeseman, C. R., A. Makinde and S. Bethanis (2005). "Properties of lightweight aggregate produced by rapid sintering of incinerator bottom ash." Resources, Conservation and Recycling **43**(2): 147-162.

Chiasson, A. D., J. D. Spitler, S. J. Rees and M. D. Smith (2000). "A Model for Simulating the Performance of a Pavement Heating System as a Supplemental Heat Rejecter With Closed-Loop Ground-Source Heat Pump Systems." Journal of Solar Energy Engineering **122**(4): 183-191.

Christine, B. and J. Rochelle (2003). concrete and masonry databook. New York, McGraw-Hill Publishing Co.

CIBSE (2006). Guide A: Environmental Design. London, Chartered Institution of Building Services Engineers.

Cook, D. J. and C. Uher (1974). "The Thermal Conductivity of Fibre-Reinforced Concrete." Cement and Concrete Research **4**: 497-509.

Côté, J. and J. M. Konrad (2005). "Thermal conductivity of base-course materials." Canadian Geotechnical Journal **42**(1): 61-78.

de Bondt, A. (2003). "Generation of Energy Via Asphalt Pavement Surfaces, Prepared for Asphaltica Padova, Netherland, 2003. Also available online at: http://www.roadenergysystems.nl/pdf/Fachbeitrag%20in%20OIB%20-%20de%20Bondt%20-%20English%20version%2013-11-2006.pdf."

Defence Estates (2005). Pavement Quality Concrete for Airfields, Specification 033. UK, Ministry of Defence.

Defence Estates (2006). Design and Maintenance guide 20, A Guide to Airfield Pavement Design and Evaluation. UK, Ministry of Defence.

Defence Estates (2008). Hot Rolled Asphalt and Asphalt Concrete (Macadam) for Airfields. UK, Ministry of Defence.

Delatte, N. (2008). Concrete Pavement Design, Construction, and Performance. London, Taylor & Francis.

Demir, H., A. Koyun and G. Temir (2009). "Heat transfer of horizontal parallel pipe ground heat exchanger and experimental verification." Applied Thermal Engineering **29**(2-3): 224-233.

Demirboga, R. (2007). "Thermal conductivity and compressive strength of concrete incorporation with mineral admixtures." Building and Environment **42**(7): 2467-2471.

Demirboga, R. and R. Gül (2003). "The effects of expanded perlite aggregate, silica fume and fly ash on the thermal conductivity of lightweight concrete." Cement and Concrete Research **33**(5): 723-727.

Dempsey, B. J. and M. R. Thompson (1970). "A Heat-Transfer Model for Evaluating Frost Action Temperature-Related Effects in Multilayered Pavement System." Transportation Research Record: Journal of the Transportation Research Board **342**: 39-56.

dos Santos, W. N. (2003). "Effect of moisture and porosity on the thermal properties of a conventional refractory concrete." Journal of the European Ceramic Society **23**(5): 745-755.

Edberg, O., N. Barker and J. Stambaugh (2011). Review of technical information on renewable heat technologies, Report for the Department of Energy and Climate Change.

http://www.rhincentive.co.uk/library/regulation/1103AEA_Update.pdf. Oxford, AEA Technology plc.

Egg, J. and B. C. Howard (2011). Geothermal HVAC, Green Heating and Cooling. New York, McGraw-Hill Companies, Inc.

Entrop, A. G., H. J. H. Brouwers and A. H. M. E. Reinders (2011). "Experimental research on the use of micro-encapsulated Phase Change Materials to store solar energy in concrete floors and to save energy in Dutch houses." Solar Energy **85**(5): 1007-1020.

Erdem, S., A. R. Dawson and N. H. Thom (2011). "Impact load-induced micro-structural damage and micro-structure associated mechanical response of concrete made with different surface roughness and porosity aggregates." Cement and Concrete Research **42**(2): 291-305.

Esen, H., M. Inalli and M. Esen (2007). "Numerical and experimental analysis of a horizontal ground-coupled heat pump system." Building and Environment **42**(3): 1126-1134.

European Geothermal Energy Council (2008). Ground Source Heat Pump: A Guide Book.

Ewing, R. P. and R. Horton (2007). "Thermal conductivity of a cubic lattice of spheres with capillary bridges." Journal of Physics D: Applied Physics; **40**(16).

FHWA (2011). User Guidelines for Waste and Byproduct Materials in Pavement Construction. http://www.fhwa.dot.gov/publications/research/infrastructure/pavements/97148/043.cfm.

Fu, X. and D. D. L. Chung (1997). "Effects of silica fume, latex, methylcellulose, and carbon fibers on the thermal conductivity and specific heat of cement paste." Cement and Concrete Research **27**(12): 1799-1804.

Gorai, B., R. K. Jana and Premchand (2003). "Characteristics and utilisation of copper slag--a review." Resources, Conservation and Recycling **39**(4): 299-313.

Griffiths, G. and N. Thom (2007). Concrete Pavement Design Guidance Notes. London, Taylor &Francis.

Gui, J., P. E. Phelan, K. E. Kaloush and J. S. Golden (2007). "Impact of Pavement Thermophysical Properties on Surface Temperatures." Journal of Materials in Civil Engineering **19**(8): 683-690.

Hall, M. and D. Allinson (2008). "Assessing the moisture-content-dependent parameters of stabilised earth materials using the cyclic-response admittance method." Energy and Buildings **40**(11): 2044-2051.

Hall, M. and D. Allinson (2009). "Assessing the effects of soil grading on the moisture content-dependent thermal conductivity of stabilised rammed earth materials." Applied Thermal Engineering **29**(4): 740-747.

Harris, A. and D. Sorensen (2007). "Thermal Conductivity Testing of Minimal Volumes of Energetic Powders." Journal of Pyrotechnics **1**(25): 49-54.

Hasebe, M., Y. Kamikawa and S. Meiarashi (2006). Thermoelectric Generators using Solar Thermal Energy in Heated Road Pavement. Thermoelectrics, 2006. ICT '06. 25th International Conference on.

Hermansson, E. (2004). "Mathematical model for paved surface summer and winter temperature: comparison of calculated and measured temperatures." Cold Regions Science and Technology **40**(1-2): 1-17.

Hilton Ltd, P. A. (1994). Experimental Operating and Maintenance Manual, Thermal conductivity of Building and Insulating Materials Unit. Hampshire, P. A. Hilton Ltd.

Hossam, F. H. and K. Al-Jabri (2011). "Laboratory Evaluation of Hot-Mix Asphalt Concrete Containing Copper Slag Aggregate." Journal of Materials in Civil Engineering.

Hunger, M., A. G. Entrop, I. Mandilaras, H. J. H. Brouwers and M. Founti (2009). "The behavior of self-compacting concrete containing micro-encapsulated Phase Change Materials." Cement and Concrete Composites **31**(10): 731-743.

Inalli, M. and H. Esen (2004). "Experimental thermal performance evaluation of a horizontal ground-source heat pump system." Applied Thermal Engineering **24**(14-15): 2219-2232.

Incropera, F. P., D. P. DeWitt, Bergman and Lavine (2007). Fundamentals of Heat and Mass Transfer. New York, John Wiley &Sons, Inc.

ISO 8301 (1996). Thermal Insulation – Determination of Steady-State Thermal Resistance and Related Properties – Heat Flow Meter Apparatus, International Organization for tandardization, Genève, Switzerland.

Kan, Y.-C., K.-C. Pei and C.-L. Chang (2004). "Strength and fracture toughness of heavy concrete with various iron aggregate inclusions." Nuclear Engineering and Design **228**(1-3): 119-127.

Kayali, O., M. N. Haque and B. Zhu (2003). "Some characteristics of high strength fiber reinforced lightweight aggregate concrete." Cement and Concrete Composites **25**(2): 207-213.

Khan, M. I. (2002). "Factors affecting the thermal properties of concrete and applicability of its prediction models." Building and Environment **37**(6): 607-614.

Kim, K.-H., S.-E. Jeon, J.-K. Kim and S. Yang (2003). "An experimental study on thermal conductivity of concrete." Cement and Concrete Research **33**(3): 363-371.

Kridan, F. A. M., A. K. Arshad and M. Y. A. Rahman (2010). "Development of Warm Mix Asphalt and Compliance with the Requirements Set by Specifications." European Journal of Scientific Research **48**(1): 118-128.

Leong, W. H., V. R. Tarnawski and A. Aittomäki (1998). "Effect of soil type and moisture content on ground heat pump performance: Effet du type et de l'humidité du sol sur la performance des pompes à chaleur à capteurs enterrés." International Journal of Refrigeration **21**(8): 595-606.

Levinson, R., H. Akbari and P. Berdahl (2010). "Measuring solar reflectance—Part II: Review of practical methods." Solar Energy **84**(9): 1745-1759.

Lie, T. T. and V. K. R. Kodur (1996). "Thermal and mechanical properties of steel-fibre-reinforced concrete at elevated temperatures." Canadian journal of civil engineering **23**(2): 511-517.

Mallick, R. B., B.-L. Chen and S. Bhowmick (2009). "Harvesting energy from asphalt pavements and reducing the heat island effect." International Journal of Sustainable Engineering **2**(3): 214-228.

Mallick, R. B., B.-L. Chen, S. Bhowmick and M. S. Hulen (2008). Capturing Solar Energy from Asphalt Pavements. International ISAP Symposium on Asphalt Pavements and Environment. Zurich, Switzerland**:** 161-172.

Masad, E., A.M.ASCE, V. K. Jandhyala, N. Dasgupta, N. Somadevan, S.M.ASCE and N. Shashidhar (2002). "Characterization of Air Void Distribution in Asphalt Mixes using X-ray Computed Tomography." JOURNAL OF MATERIALS IN CIVIL ENGINEERING **14**(2): 122-129.

Mehling, H. and L. F. Cabeza (2008). Heat and cold storage with PCM. Berlin, Springer.

Minhoto, M. J. C., J. C. Pais, P. A. A. Pereira and L. G. Picado-Santos (2005). "Predicting Asphalt Pavement Temperature with a Three-Dimensional Finite Element Method." Journal of the Transportation Research Board, : 96-110.

Mrawira, D. M. and J. Luca (2002). "Thermal properties and transient temperature responses of full-depth asphalt pavements." Transportation Research Record **1809**(1): 160.

Nayak, J. K., S. P. Sukhatme, R. G. Limaye and S. V. Bopshetty (1989). "Performance studies on solar concrete collectors." Solar Energy **42**(1): 45-56.

Neville, A. M. (1995). Properties of Concrete. Essex, Longman Group Limited.

O'Flaherty, C. A. (2002). Highways, The location, design, construction and maintenance of road pavements. Oxford, Butterworth-Heinemann.

Palyvos, J. A. (2008). "A survey of wind convection coefficient correlations for building envelope energy systems' modeling." Applied Thermal Engineering **28**(8-9): 801-808.

Phillipps, P. (2007). Optimising Pavement Materials to Collect the Solar Energy By Asphalt. Civil Engineering, School of the Built Environment. Nottingham, University of Nottingham. **Msc dissertation**.

Pomerantz, M., H. Akbari, S.-C. Chang, R. Levinson and B. Pon (2003). Example of Cooler Reflective Streets for Urban Heat-Island Mitigation: Portland Cement Concrete and Chip Seal, Lawrence Berkeley National Laboratory, LBNL No. 49283.

PTB (2010). "Comparing Emissivity Evaluation Methods for Infrared Sources. Available online at: http://www.ptbmagazine.com/features/2009/feat1_0909.html." Retrieved [13/09/2011].

Pundhir, N., C. Kamaraj and P. Nanda (2005). "Use of copper slag as construction materials in bituminous pavements." Journal of Scientific & Industrial Research **64**: 997-1002.

Qin, Y. and J. E. Hiller (2011). "Modeling temperature distribution in rigid pavement slabs: Impact of air temperature." Construction and Building Materials **25**(9): 3753-3761.

Rabl, A. (1985). Active Solar Collectors and Their Applications. Oxford.

Rawlings, R. H. D. and J. R. Sykulski (1999). "Ground source heat pumps: A technology review." Building Services Engineering Research and Technology **20**(3): 119-129.

Read, J. and D. Whiteoak (2003). <u>The Shell Bitumen Handbook</u>. London, Thomas Telford Publishing.

Sánchez, P., M. V. Sánchez-Fernandez, A. Romero, J. F. Rodríguez and L. Sánchez-Silva (2010). "Development of thermo-regulating textiles using paraffin wax microcapsules." <u>Thermochimica Acta</u> **498**(1-2): 16-21.

Sedgwick, R. H. D. and M. A. Patrick (1981). <u>The Use of a Ground Solar Collector for Swimming Pool Heating</u>. Proceedings of ISES, Brighton, England.

Segre, N. and I. Joekes (2000). "Use of tire rubber particles as addition to cement paste." <u>Cement and Concrete Research</u> **30**(9): 1421-1425.

Smith, M. R. and L. Collis. (2001). <u>Aggregates: sand, gravel and crushed rock aggregates for construction purposes</u>. Geological Society, London, Engineering Geology Special Publication No. 17.

Sokolov, M. and M. Reshef (1992). "Performance Simulation of Solar Collectors Made of Concrete with Embedded Conduit Lattice." <u>Solar Energy</u> **48**(6): 403-411.

Solaimanian, M. and T. W. Kennedy (1993). "Predicting Maximum Pavement Surface Temperature Using Maximum Air Temperature and Hourly Solar Radiation." <u>Transportation Research Record: Journal of the Transportation Research Board</u> **1417**: 1-11.

Somerton, W. H. (1992). <u>Thermal properties and temperature-related behavior of rock/fluid systems</u>. New York, Elsevier Science Publishers.

Sullivan, C., A. H. de Bondt, R. Jansen and H. Verweijmeren (2007). Innovation in the Production and Commercial Use of Energy Extracted from Asphalt Pavements. <u>6th Annual International Conference on Sustainable Aggregates, Asphalt Technology and Pavement Engineering</u>. Liverpool.

Sundberg, J. (1988). <u>Thermal properties of soil and rocks</u>. Sweden, Swedish Geotechnical Institute.

Tarnawski, R., T. Momose and W. H. Leong (2009a). "Assessing the impact of quartz content on the prediction of soil thermal conductivity." <u>Geotechnique</u> **59**(4): 331-338.

Tarnawski, V. R., W. H. Leong, T. Momose and Y. Hamada (2009b). "Analysis of ground source heat pumps with horizontal ground heat exchangers for northern Japan." <u>Renewable Energy</u> **34**(1): 127-134.

Thom, N. (2008). <u>Principles of Pavement Engineering</u>. London, Thomas Telford Ltd.

Tixier, R., R. Devaguptapu and B. Mobasher (1997). "The effect of copper slag on the hydration and mechanical properties of cementitious mixtures." <u>Cement and Concrete Research</u> **27**(10): 1569-1580.

Turner, R. H. (1986). <u>Concrete slabs as winter solar collectors</u>. Proceedings of the ASME Solar Energy Conference (SED), California.

Turner, R. H. (1987). <u>Concrete Slabs as Summer Solar Collectors</u>. Proceedings of the International Heat Transfer Conference, California.

Ünal, O., T. Uygunoglu and A. Yildiz (2007). "Investigation of properties of low-strength lightweight concrete for thermal insulation." Building and Environment **42**(2): 584-590.

US Department of Transportation–Federal Highways Administration (2009). LTPP Seasonal Monitoring Programme (SMP): Pavement Performance Database (PPDB), DVD Version, Standard Data Release 23.0, USA.

Uysal, H., R. Demirboga, R. Sahin and R. Gül (2004). "The effects of different cement dosages, slumps, and pumice aggregate ratios on the thermal conductivity and density of concrete." Cement and Concrete Research **34**(5): 845-848.

van Bijsterveld, W. T. and A. H. de Bondt (2002). Structural Aspects of Asphalt Pavement Heating and Cooling Systems. Third International Symposium on 3D Finite Element Modeling, Design and Research. Amsterdam, Netherland.

Vosteen, H.-D. and R. Schellschmidt (2003). "Influence of temperature on thermal conductivity, thermal capacity and thermal diffusivity for different types of rock." Physics and Chemistry of the Earth, Parts A/B/C **28**(9-11): 499-509.

Williams, R. I. T. (1986). Cement-Treated Pavements, Materials, Design and Construction. UK, Elsevier Applied Science Publishers.

Wong, N. H. and Y. Chen (2009). Tropical Urban Heat Islands. Abingdon, Taylor & Francis.

Wu, K., B. Chen, W. Yao and D. Zhang (2001). "Effect of coarse aggregate type on mechanical properties of high-performance concrete." Cement and Concrete Research **31**(10): 1421-1425.

Wu, S., M. Chen, H. Wang and J. Zhang (2009). "Laboratory Study on Solar Collector of Thermal Conductive Asphalt Concrete." International Journal of Pavement Research and Technology **2**(4): 130-136.

Wu, S., M. Chen and J. Zhang (2011). "Laboratory investigation into thermal response of asphalt pavements as solar collector by application of small-scale slabs." Applied Thermal Engineering **31**(10): 1582-1587.

Wu, W., W. Zhang and G. Ma (2010a). "Optimum content of copper slag as a fine aggregate in high strength concrete." Materials & Design **31**(6): 2878-2883.

Wu, Y., G. Gan, A. Verhoef, P. L. Vidale and R. G. Gonzalez (2010b). "Experimental measurement and numerical simulation of horizontal-coupled slinky ground source heat exchangers." Applied Thermal Engineering **30**(16): 2574-2583.

Xu, Y. and D. D. L. Chung (2000). "Effect of sand addition on the specific heat and thermal conductivity of cement." Cement and Concrete Research **30**(1): 59-61.

Yavuzturk, C., K. Ksaibati and A. D. Chiasson (2005). "Assessment of Temperature Fluctuations in Asphalt Pavements Due to Thermal Environmental Conditions Using a Two-Dimensional, Transient Finite-Difference Approach." Journal of Materials in Civil Engineering **17**(4): 465-475.

Yun, T. and J. Santamarina (2008). "Fundamental study of thermal conduction in dry soils." Granular Matter **10**(3): 197-207.

Zhang, D., Z. Li, J. Zhou and K. Wu (2004). "Development of thermal energy storage concrete." <u>Cement and Concrete Research</u> **34**(6): 927-934.

APPENDICES

Appendix A: Mechanical Tests Performed on Asphalt Mixes

Three important fundamental properties of flexible pavement (i.e. asphalt) design are; stiffness modulus, resistance to fatigue cracking, and resistance to permanent deformation. These properties were measured using Nottingham Asphalt Tester (NAT) (see Figure A-1), developed at the University of Nottingham. It consists of a temperature-controlled cabinet containing a load frame, a sample support and instrumentation cradle, and a loading system comprising a pneumatic load actuator with load cell. The test system is capable of imparting 0 to 4kN through a spherical seating with a rise time of between 80 to 160 ms. Diametral extension or axial deformation may be measured at right angles to the direction of diametral load application by two Linear Variable Differential Transformers (LVDTs). The instruments' response, and that of the load cell, is passed through an interface unit to a personal computer which controls the test, monitors and records the outputs of the instrumentation and formats a test report.
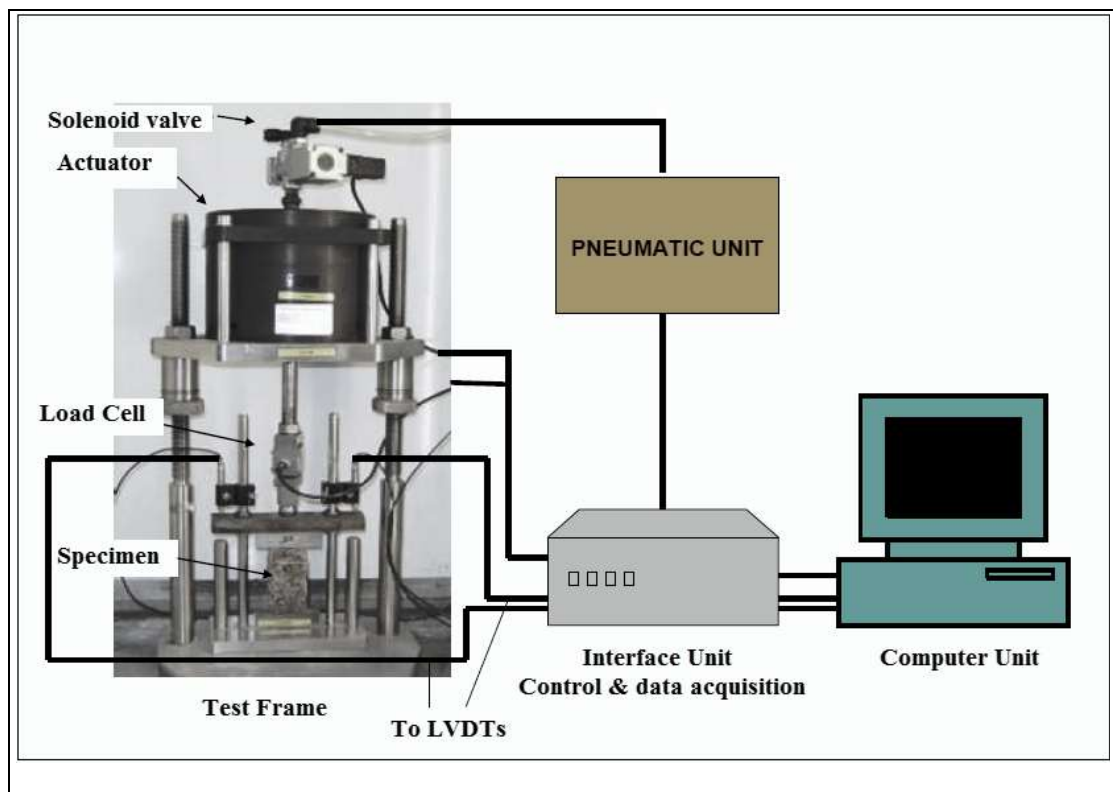
Figure A-1 Nottingham Asphalt Tester (NAT) configuration for testing bituminous mixtures

Indirect Tensile Stiffness Modulus (ITSM)

Stiffness in a pavement material is the principal measurement used to indicate the ability of a material to spread the traffic loading over an area. For comparative purposes a fixed temperature of 20°C was used and the test performed according to BS DD 213 (1993). The standard target parameters pertaining throughout testing are as follows:

- ✓ Test temperature= 20±0.5 **°C**

- ✓ Rise time= (124 ± 4) ms

- ✓ Horizontal deformation= (5 ± 2) μm

- ✓ Poisson ratio= 0.35

- ✓ Test orientation: 0˚ and 90˚

- ✓ Specimen size= 100mm diameter with mean thickness of 40mm

Prior to testing, all specimens were conditioned in an environmental cabinet at the test temperature of 20**°C** for at least two hours. Figure A-2 shows the typical test configuration of ITSM. Based on the ITSM test, the stiffness modulus of bituminous mixtures, S_m, can be determined using Eq. A-1 (British Standards Institution 1993):

$$S_m = \frac{L}{(D \times t)} \times (v + 0.27)$$ **Eq. A-1**

where

L= the peak value of the applied vertical load (N)

D= the peak horizontal diametral deformation resulting from the applied load pulse (mm)

t= mean thickness of the test specimen (mm)

v = value of Poisson's ratio,

Indirect Tensile Fatigue Test (ITFT)

Fatigue is the condition whereby a material cracks or fails as a result of repeated (cyclic) stresses applied below the ultimate strength of the material. For the purposes of evaluating the asphaltic specimens in this study, the test was performed according to BS DD ABF (2003) using the stress mode. The testing procedure is briefly described as follows:

- The 100mm diameter specimens were conditioned at the test temperature (20±0.5°C) at least two hours prior to positioning in between the loading strips of the test frame as shown in Figure A-2.

- 10 specimens (cored out from 2 slabs) from each mixture were tested at a range of applied loads resulting in different target stress levels at the centre of each specimen.

- The maximum horizontal tensile stress and the maximum horizontal tensile strain at the centre of each specimen were then calculated from Eq. A-2 and Eq. A-3, respectively.

- The results were plotted as the maximum tensile strains against the number of cycles to failure (N_f) using logarithmic scales. Linear regression analysis was used to describe the resultant fatigue relationship.

The results obtained from ITFT tests can be expressed in the form of a relationship between the maximum horizontal tensile strain and the number of cycles to failure. The maximum horizontal tensile stress and the maximum horizontal strain for each specimen can be calculated.

$$\sigma_{max} = \frac{2P}{\pi dt}$$

Eq. A-2

$$\varepsilon_{max} = \frac{\sigma_{max} \times (1 + 3v)}{S_m}$$

Eq. A-3

where

P= maximum applied load (N)

d= specimen diameter (mm)

Repeated Load Axial Test (RLAT)

The ability to resist the development of permanent deformation due to repeated load application is an important indicator of pavement performance. It is a property that is directly related to the stability of the aggregate skeleton; it being impossible to produce a high deformation-resistant mixture without an appropriate aggregate skeleton. In this study,

the repeated load axial test was performed according to the BS DD 226 (1996). The test is carried out as follows:

- All specimens were treated with graphite powder to ensure smooth, friction free surfaces for uniform load application.

- The specimens were conditioned at a standard testing temperature of 30°C for at least two hours prior to positioning on the loading plate (see Figure A-2).

- The specimen was centred on the bottom plate and a top-loading plate was then placed on top of the specimen.

- The specimen was then subjected to a pre-test conditioning regime consisting of the application of a 10kPa static stress for duration of 10 minutes. The main purpose of this conditioning period is to ensure that the loading platens are firmly seated on the specimen prior to the commencement of deformation measurement.

- In total 3,600 load pulses were applied to each specimen, each cycle consists of the application of 100kPa vertical axial stress for one second.

- The axial cumulative deformations were continuously measured during the test. The test results were then expressed as a relationship between the accumulated axial strain and number of load cycles.


Figure A-2 Different Modes of Testing in the NAT, (A) ITSM, (B) ITFT, (C) RLAT

Aggregate surface roughness (Ra)

Surface roughness (Ra) of the aggregates was measured by stylus profilometry using a 2D Mitutoyo Surftest SV profiler with a 5 μm stylus (see Figure A-3). An auto drive unit was used to measure the evaluation length at a speed of 0.2 mm/s. Ra is calculated as the total of

the average height of the entire surface from the mean line within the sampling length. It should be noted that the equipment is normally used for the roughness measurement of metallic surfaces.
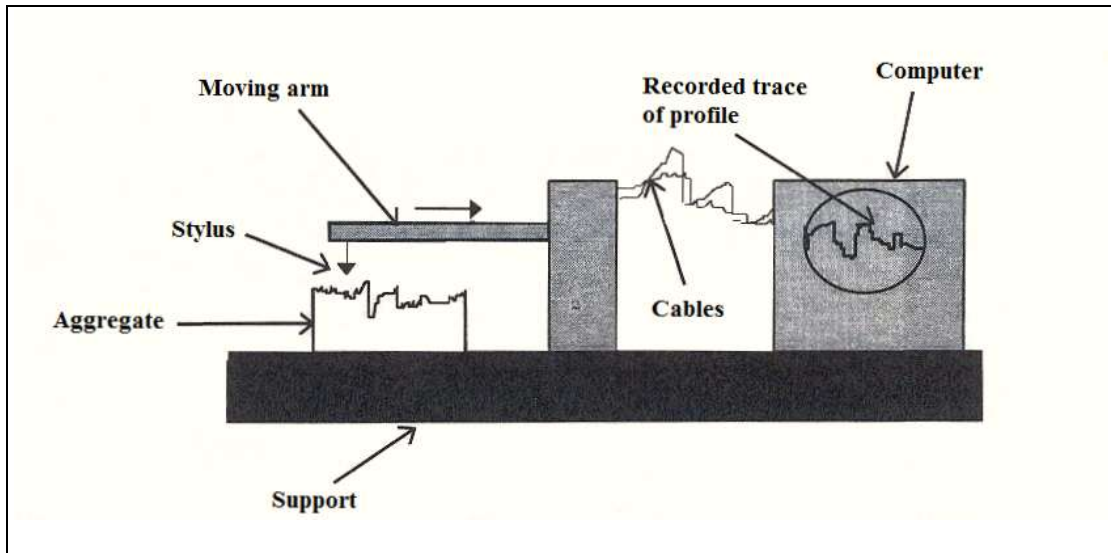
**Figure A-3 Surface profilometer to measure aggregate roughness**

Results and Discussions on the Asphalt Mixes

The test results of asphalt mixtures made with the limestone, copper slag, and quartzite are presented and analysed as a group, while the results for Lytag mix, due to its poor performance, are discussed separately.

<u>ITSM Results</u>

Figure A-4 shows the mean measured stiffness of all five mixes. The limestone mix has the highest stiffness modulus value of 1533MPa, followed by the copper slag, and quartzite mixtures. The addition of metallic fibre seems to improve the stiffness by about 56% compared to the mix with no fibre (i.e. 100% quartzite mix). There were no literature found that reports the mechanical properties of unconventional coarse aggregates used in this study. However, criteria and limits for asphaltic concrete wearing course AC14 (i.e. maximum aggregate size of 14mm) with conventional aggregates requires a value for stiffness ranges 1500 to 2000 MPa at 20°C (Thom 2008; Kridan et al. 2010). Thus all alternative mixtures perform rather poorly compared with this value. The average readings for five profiles of the roughness (Ra) values for limestone, copper slag, and quartzite were

10.87μm, 8.63μm, and 5.52μm, respectively. The low value for the stiffness of quartzite asphalt may be partly attributable to the relatively smooth faces of the quartzite aggregates as revealed by its low roughness value. In addition, O'Flaherty (2002) also added that: *quartzite aggregates having a tendency to strip because of poor adhesion to bitumen, however, they make good road aggregates due to their high resistance to polishing* (high resistance of quartzite aggregate to polishing was also observed by the author during the aggregate's preparation for thermal conductivity test). The effect of copper fibres on the stiffness improvement of the mix may be due to the increased interconnection between fibres (the same effect as shown in Figure 3-14, Page 77, for concrete mixes).
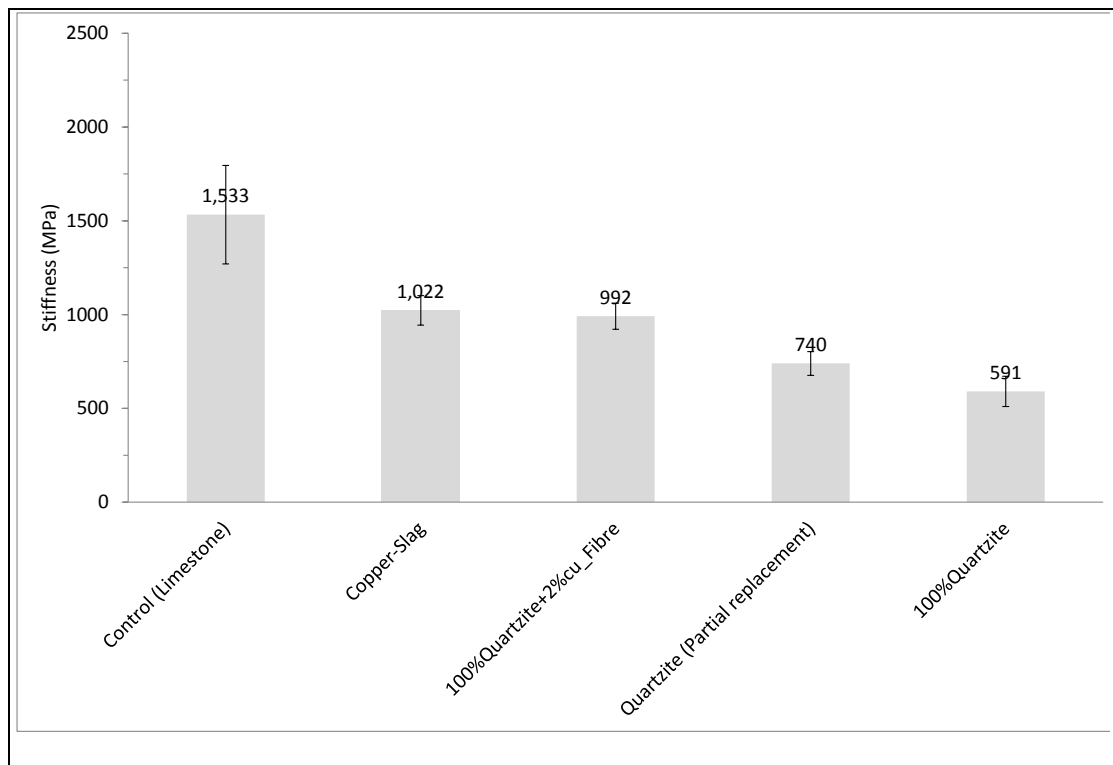
Figure A-4 Mean stiffness of different mixtures, including 95% confidence limit

ITFT Results

Fatigue life is commonly defined as the number of load cycles to fail the asphalt specimen at a certain stress level. A fatigue regression analysis was performed using the relationship:

$$N_f = k_1 \left\{ \frac{1}{\varepsilon} \right\}^{k_2}$$
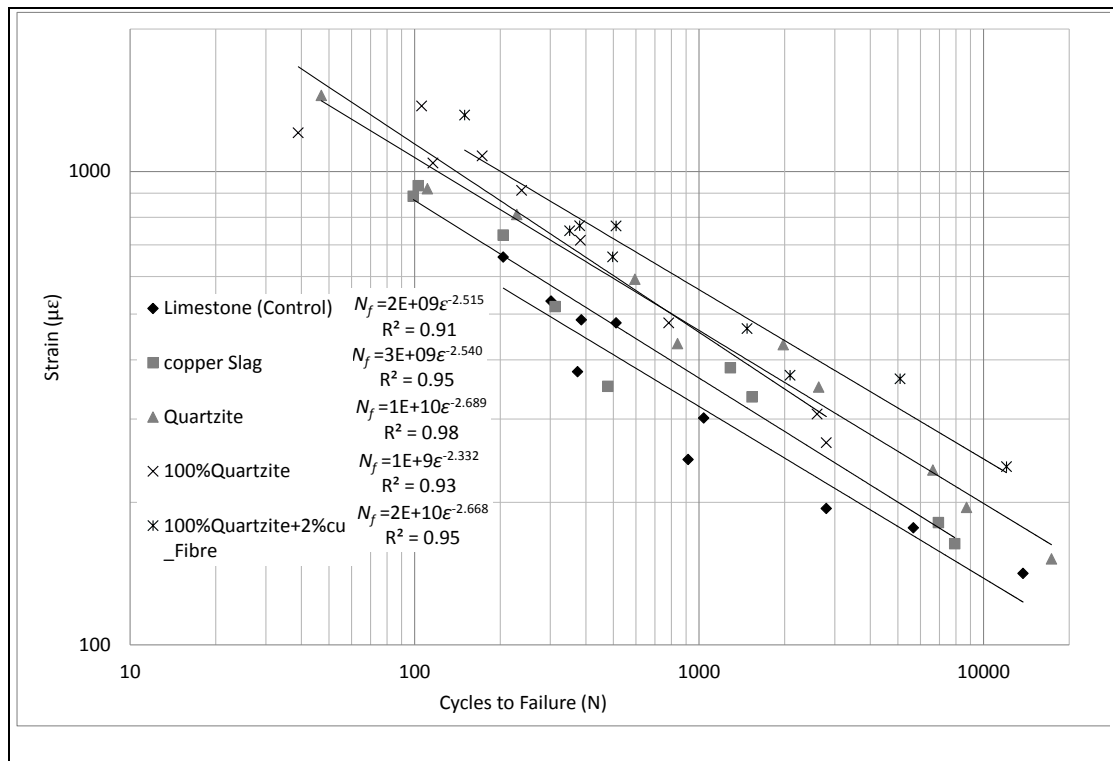
Eq. A-4

where:

N_f= Number of Load application to failure;

215

k_1 ,k_2= Constants depending on the mixture characteristics;

ε= Applied strain

The fatigue lines are plotted as Figure A-5, with the enumerated forms of Eq. A-4 for the five materials given on the figure. The similarity of the values of k_2 reflect the parallel nature of the five lines while the small differences in k_1 reflect the small spacing of the lines with respect to each other. Based on the regression lines it can be seen that the ITFT is a suitable test for analysing these mixtures due to the reasonable value of correlation coefficient obtained from the experiments compared to the BS DD ABF (2003) recommended R^2 value of 0.90.

From Figure A-5 it can be seen that the asphalt mix containing copper fibre showed the best resistance against fatigue (more load cycles needed to fail the specimen for the same horizontal strain). Both quartzite mixes (i.e. partial & full aggregate replacement) achieved almost the same fatigue line, and the copper slag mix performed slightly better than the limestone mix. The higher fatigue life of the fibre mixture is most likely due to the high level of fibre interconnection that slow down the rate of crack propagation in the middle of specimen. Thus all of the unconventional mixtures show a fatigue relationship that is likely to represent satisfactory in-situ performance.

Figure A-5 Number of load cycles to failure versus strain

The figure contains the following legend and equations:

- ◆ Limestone (Control) $N_f = 2E+09\varepsilon^{-2.515}$ $R^2 = 0.91$
- ■ copper Slag $N_f = 3E+09\varepsilon^{-2.540}$ $R^2 = 0.95$
- ▲ Quartzite $N_f = 1E+10\varepsilon^{-2.689}$ $R^2 = 0.98$
- ✕ 100%Quartzite $N_f = 1E+9\varepsilon^{-2.332}$ $R^2 = 0.93$
- ✳ 100%Quartzite+2%cu_Fibre $N_f = 2E+10\varepsilon^{-2.668}$ $R^2 = 0.95$

Axis labels: Strain (μɛ) [vertical], Cycles to Failure (N) [horizontal]

RLAT Results

Figure A-6 presents the average axial permanent strain curves obtained from the results of the RLAT tests for the five mix materials. It can be seen that they exhibit a similar response during the loading. The permanent strains all increase rapidly at the beginning, followed by a progressively reducing strain rate per cycle. The deformation occurring in the first 500 cycles is 69%, 69%, 85%, 82% and 83%, respectively for the limestone, copper slag, quartzite (partially replaced), quartzite+2%fibre, and quartzite (fully replaced) asphalts. The quartzite asphalt experienced by far the largest permanent strain. Once again, this could be due to its smooth surface resulting in poor bonding with bitumen and poor frictional properties. Although the addition of fibres in the asphalt mix slightly improved the permanent deformation, compared with the mix with no fibres, it did not result in a significant reduction of permanent deformation. This may be due to the horizontal fibre orientation (perpendicular to the direction of loading) in the asphalt mix, as shown by Figure 3-23, Page 90.

217
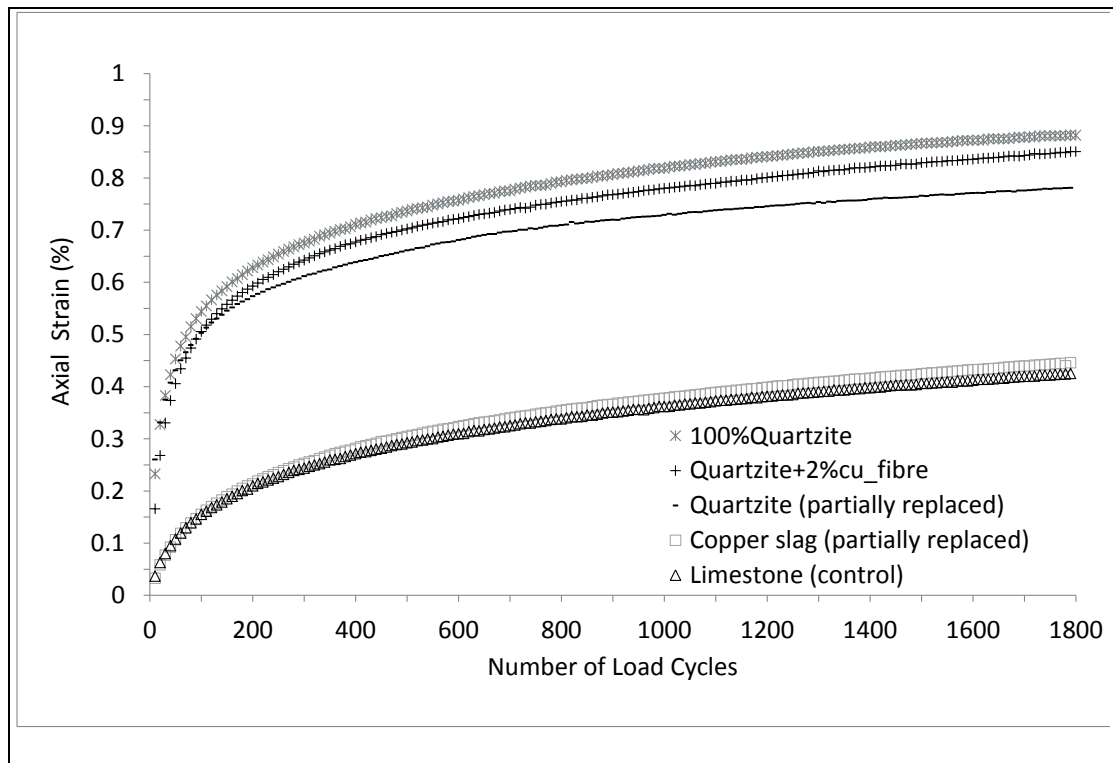
Figure A-6 Vertical permanent strain variations with number of cycles

Tests Results of Lytag

The slabs generated with Lytag were very weak. The aggregates did not bond well with the binder, especially at the corner of the slabs. Due to the poor quality, there were no meaningful results obtained for the ITSM. A sample was selected and tested under 100kPa for fatigue in order to give a general idea about the fatigue resistance of this mixture. As shown in Table A-1, its performance is far behind the other materials. In terms of RLAT, the Lytag experienced a deformation of 0.98% in strain at the end of 1800 cycles, only a little higher than that of the quartzite asphalt. Though it is still the poorest performing, in terms of mechanical properties, it might have a useful role in forming a stabilized sub-base layer. One possibility to improve the performance of Lytag could be to increase the binder content, since due to the higher porosity of Lytag, a binder content of 4.9% (used in this study) seems not enough to provide an appropriate bond in the asphalt mixture.

Table A-1 Cycles to failure under 100kPa stress level

Limestone	Copper slag	100% Quartzite	Quartzite+2%fibre	Quartzite (partially replaced)	Lytag
13781	7924	2603	12045	8728	738

Appendix B: Illustration of Heat transfer model

The pseudo 3D transient explicit finite-difference model was coded in the VBA in MS Excel 2010. An explanation of the model's procedures can be described and illustrated as follows:

The first step is to insert the required inputs (e.g. surface characteristics, thermo-physical properties, climatic data, pipe thermal data and length, etc.) in the Excel spread sheet and define the mesh size and time step (see Figure B-1).
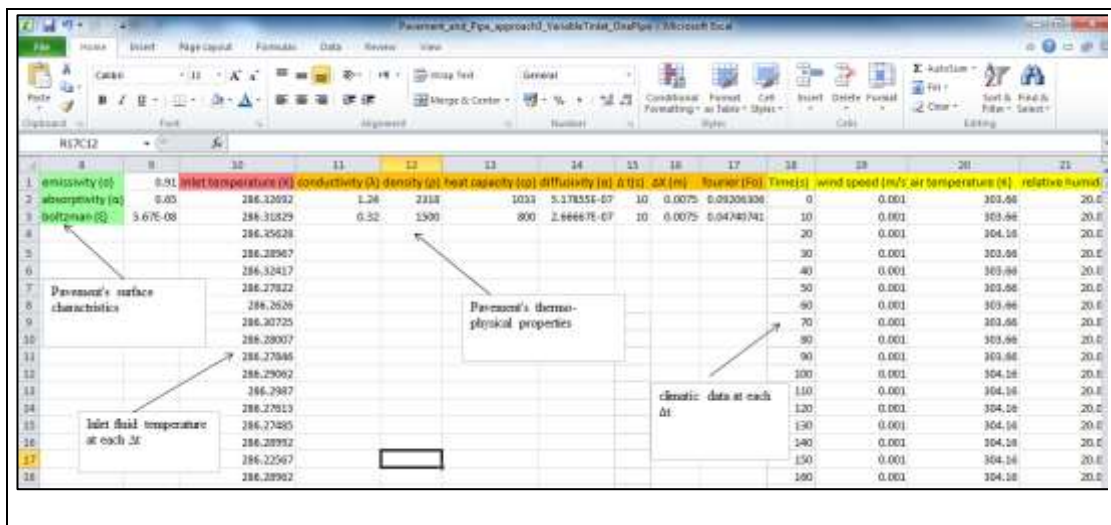

Figure B-1 Inserting the input data into the model

The second step is to construct the finite difference grid (see Figure B-2). The finite difference grid, in the Z direction (i.e. top to bottom of the spread sheet) and X direction (i.e. left to right of the spread sheet) corresponds to the thickness of the pavement layers and to half the distance to the adjacent pipe, respectively. In the model, each pavement layer is identified by a specific font colour as shown in Figure B-2. The pipe position in the domain is identified by a different background colour. For the pavement-only temperature distibution (i.e. no pipe installed in the pavement) or the hybrid simulation, no pipe and two pipes cross section will be installed in the finite difference domain, respectively (see Figure B-3). Once the code was executed, the temperature distribution in the pavement and outlet water temperatures at each time step are calculated.
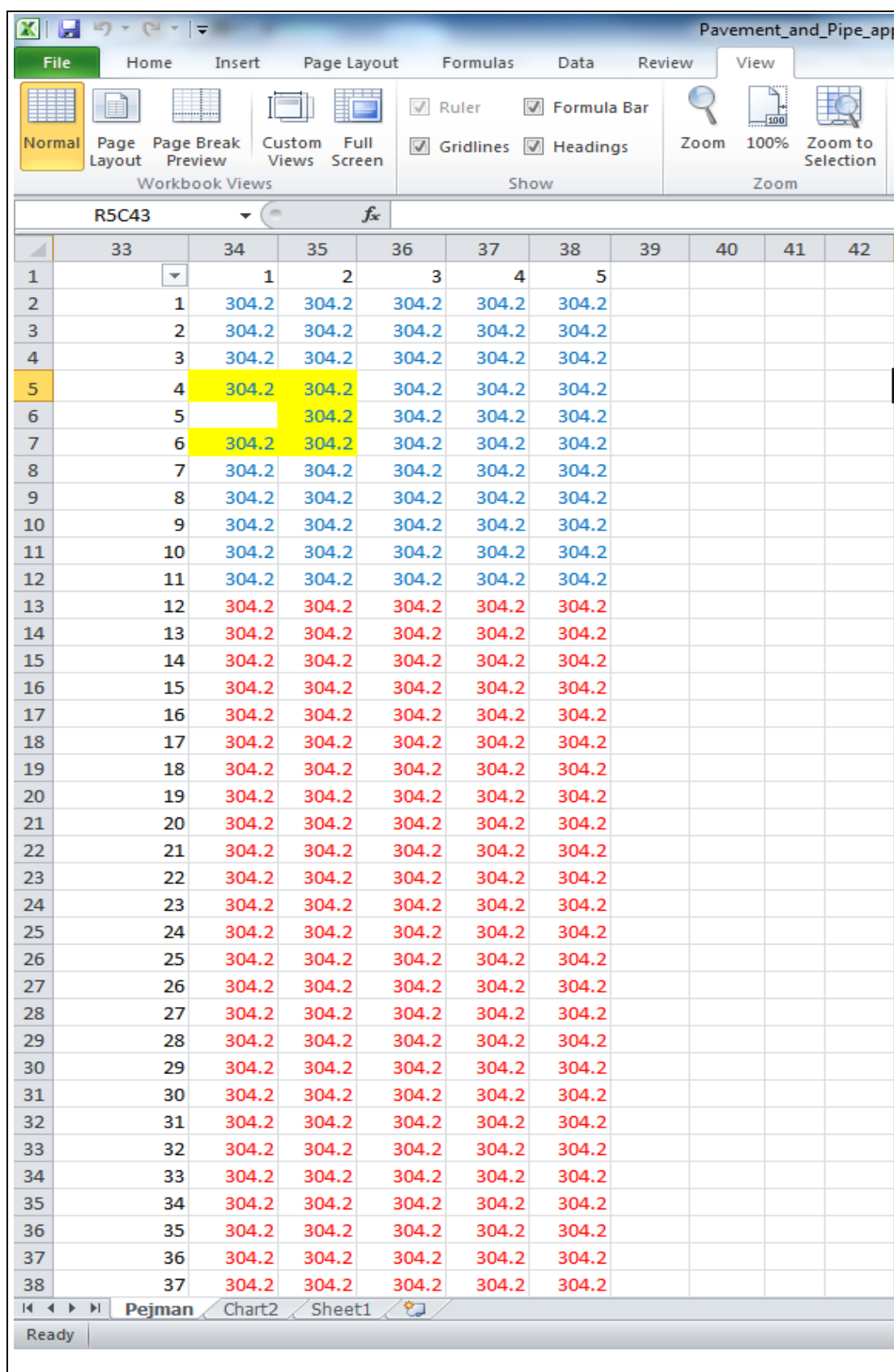
Figure B-2 Construction of the finite difference grid, pavement layers and pipe are identified by different font colour and background colour, respectively
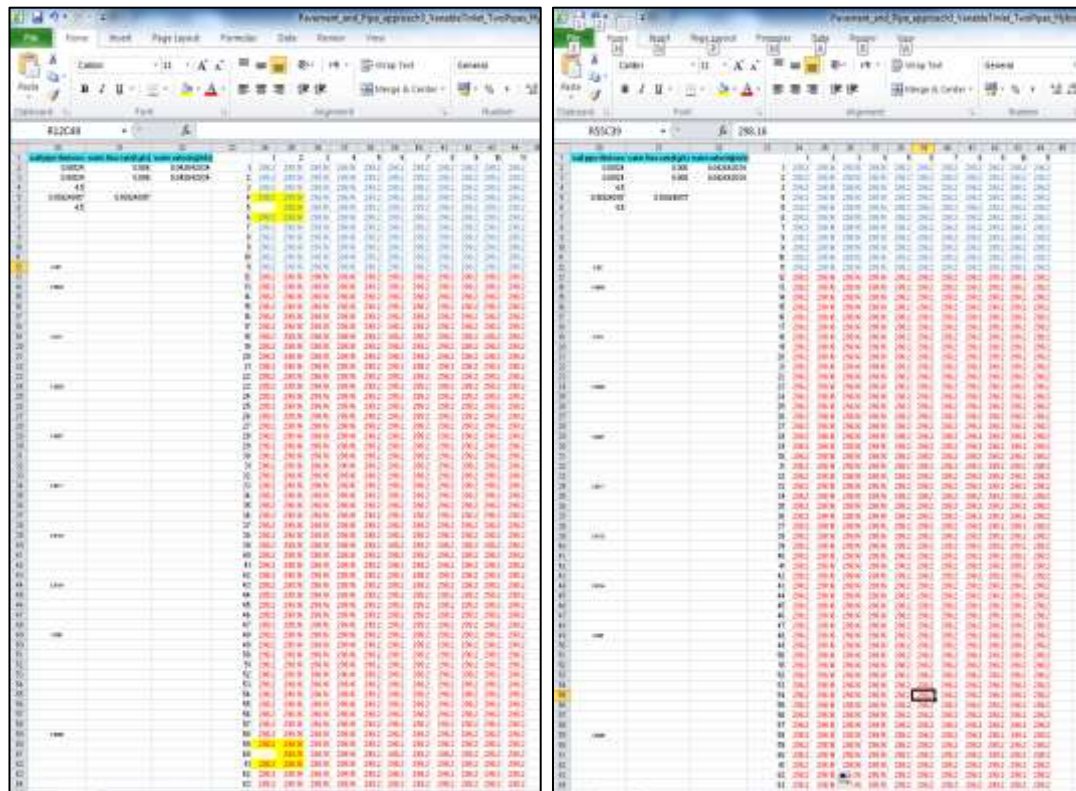
Figure B-3 Hybrid simulation (left) and pavement-only temperature simulation (right)

Appendix C: XRCT images of the asphalt specimen with embedded copper pipe